# Infrared Spectroscopy
## Anharmonicity of Biomolecules, Crosslinking of Biopolymers, Food Quality and Medical Applications

*Edited by Theophanides Theophile*

# INFRARED SPECTROSCOPY - ANHARMONICITY OF BIOMOLECULES, CROSSLINKING OF BIOPOLYMERS, FOOD QUALITY AND MEDICAL APPLICATIONS

Edited by **Theophanides Theophile**

**Infrared Spectroscopy - Anharmonicity of Biomolecules, Crosslinking of Biopolymers, Food Quality and Medical Applications**

Edited by Theophanides Theophile

## Contributors

Jianping Wang, Jose Luis Rivera Armenta, Beatriz Adriana Salazar-Cruz, Alejandro Esquivel De La Garza, Sergio Moctezuma Espiricueto, Ana Maria Mendoza Martinez, Alexander Gersten, Yankun Peng, Wenxiu Wang, Eugen Sheregii, Vasiliki Dritsa, Jane Anastassopoulou, Theophanides Theophile

## Notice

Statements and opinions expressed in the chapters are these of the individual contributors and not necessarily those of the editors or publisher. No responsibility is accepted for the accuracy of information contained in the published chapters. The publisher assumes no responsibility for any damage or injury to persons or property arising out of the use of any materials, instructions, methods or ideas contained in the book.

# We are IntechOpen,
# the world's leading publisher of
# Open Access books
# Built by scientists, for scientists

## 3,800+
Open access books available

## 116,000+
International authors and editors

## 120M+
Downloads

## 151
Countries delivered to

Our authors are among the
## Top 1%
most cited scientists

## 12.2%
Contributors from top 500 universities

CLARIVATE ANALYTICS
BOOK CITATION INDEX
INDEXED

WEB OF SCIENCE™

Selection of our books indexed in the Book Citation Index
in Web of Science™ Core Collection (BKCI)

## Interested in publishing with us?
## Contact book.department@intechopen.com

Numbers displayed above are based on latest data collected.
For more information visit www.intechopen.com

# Meet the editor

Professor Theophile Theophanides was born in Platamon, Kavala, Greece and is known for his ground-breaking research in the field of Metal Coordination Chemistry and Infrared Spectroscopy. In particular, his research focus has been in the areas of life metal ions, bioinorganic chemistry and in his pioneering work in anti-tumor drugs, such as cis-Platinum, commonly employed in chemotherapy. He has authored over 300 peer-reviewed scientific publications in international journals, penned numerous articles and book chapters and served on the board of many Scientific Associations and Committees. He has been invited speaker in many Universities, Institutions and Media. Prof. Theophanides has been honored many times for his research. He is an Honorary Professor of the University of Montreal and the National Technical University of Athens, Doctor Honoris Causa of the University of Reims and Silver Medalist of the National French Academy of Medicine for his outstanding work on magnesium research. Additionally, he has received medals from Universities, Media and other Associations for his research and communications on Environmental and Public Health issues.

# Contents

# Preface

In this book you can find studies on Infrared Spectroscopy and Near Infrared Spectroscopy, Anharmonicity of biomolecules (proteins), biopolymers food quality and safety as well as Infrared Spectra of human tissues from diseases like Down syndrome tooth disorders and metastatic cancer of bones.

The book contains four sections:

**1) Introduction**

**2) Anharmonicity in protein vibrations and biopolymers.** The two chapters in this section are skillfully describing the calculation of anharmonicities for signature bands of proteins and the molecular cross-linking of a biopolymer.

**3) Food quality.** In this section one can find applications of MIRS and NIRS in food industry and research. These include quality control of food, e.g. the structure and dynamics of carotenoid and chlorophyll triplets in photosynthetic light-harvesting complexes in fruits and in farms in order to determine the amounts of carbon and nitrogen at a farm scale.

**4) Medical applications.** This section contains 3 chapters of MIRS and NIRS on medical applications including the role of β-antagonists on the structure of human cancerous bone and characterization of bone-based graft materials; brain-computer interface in rehabilitation and brain oxygenation; and tooth disorders found in Down syndrome. Overall they provide a review of FT-IR on biomedical research in cells and biopolymer modifications in biomedical applications.

**Theophile Theophanides**
Emeritus Professor of Chemical Engineering
National Technical University of Athens
Chemical Engineering Department
Greece

# Introduction

# Introduction to the Book

Theophile Theophanides

Additional information is available at the end of the chapter

http://dx.doi.org/10.5772/60123

Infrared (IR) Spectroscopy is the most used tool today for the characterization and identification of materials, and biomaterials. In the last 20 years, its applications have been extended to large biological materials, such as proteins, DNA and membranes [1] and to healthy or diseased human tissue (e.g. cancer, atheromatic plaques, etc) [2, 3]. The technique is extensively used not only for organic compounds but almost all substances and is popular because it is simple, easy to perform, accurate and cost effective. It is hoped that in the very near future, affordable small IR instruments will be build to assist in fast pre-diagnosis and diagnosis, in clinical settings.

Functional groups like $-CH_2$, $-CH_3$, -NH, -OH, etc are easily identified from an IR spectrum and the material and biomaterial that contains them can be detected and conveniently compared with library spectra. Modern Fourier Transform Infrared (FT-IR) Spectrometers, can obtain an average of 100 to 150 spectra in the mid-infrared region, in a few seconds and with excellent resolution, a vast improvement from the past. FT-IR Spectrometers are now available at low cost (~€40,000) for the analytical chemist and the structural chemical spectroscopist. [4].

The aim of this book is to assist the chemist, spectroscopist and any other scientist interested in applying FT-IR. Presented herein are signature bands at high frequency regions (4,000-1,500 $cm^{-1}$), capable of giving structural information [5-10]. The positions and intensities of the absorption bands can be used to characterize a compound from library spectra and to confirm the presence of a particular group in order to obtain information as to the structure and conformation of the molecule and its microenvironment. Skeletal vibrations of molecules (1,500-400 $cm^{-1}$) can change substantially with conformational changes. However these should be used with caution and cannot be applied with a high degree of confidence to structural modifications taking place to large biomolecules. It is in assisting the IR spectroscopist in determining with confidence any particular identification and characterization of a molecule from "signature bands", that this monograph aims to be of value.

## Author details

Theophile Theophanides

Emeritus Professor of NTUA

## References

[1] Theophanides, T, Angiboust, J.P. Manfait, M.In::Spectroscopic and Structural Studies of Biomaterials, I. Proteins, ed., Twardowski, Sigma Press, Wilmslow, UK, p. 3 (1988).

[2] Theophanides,T. (1984), *Fourier Transform Infrared Spectroscopy*, D. Reidel Publishing Co. Dodrecht,The Netherlands.

[3] Theophanides, T.&Rizzarelli, E. (1991).*Chemistry and Properties of Biomolecular Systems, Topics in Molecular Organisation and Engineering*, Kluwer Academic Publishers, Dodrecht, The Netherlands.

[4] Theophanides, T.,Anastassopoulou,J.& Fotopoulos,N. (1997).*Fifth International Conference on the Spectroscopy of Biological Molecules*, Kluwer Academic Publishers, Dodrecht,The Netherlands.

[5] Theophanides, T. (2012).*Infrared Spectroscopy-Life and Biomedical Sciences*, Vol.I InTech, open science.

[6] Theophanides, T. (2012).*Infrared Spectroscopy Materials Science, Engineering and Technology*, Vol. II, InTech open science.

[7] Petra, M. Anastassopoulou, J.Theologis, T. &Theophanides, T.(2005) Synchrotron micro-FT-IR spectroscopic evaluation of normal paediatric human bone, *J. Mol Structure*, Vo 733, pp. 101-110.

[8] L.J. Bellamy, *The Infrared Spectra of Complex Molecules*, Wiley, New York, 1958

[9] Goormaghtigh E, Raussens V, Ruysschaert JM, Attenuated total reflection infrared spectroscopy of proteins and lipids in biological membranes, Biochim Biophys Acta, 1999 Jul 6;1422(2):105-85.

[10] Ferraro JR, Basile L.*Fourier Transform Infrared Spectroscopy,Academic Press, 1979, New York.*

# Infrared Anharmonic Vibrational Spectroscopy of Biomolecules

# Anharmonic Vibrational Signatures of Peptides — Methods and Applications

Jianping Wang

Additional information is available at the end of the chapter

## 1. Introduction

Understanding the structure of proteins is a key to understanding their functions. Infrared (IR) spectroscopy is a very sensitive tool for studying three-dimensional molecular structures of proteins [1,2] in conditions relevant to biology, for example, in solution phase. This is because the vibrational frequency is determined by the chemical structure of the chromophore. However, both intra- and intermolecular force fields are involved. For the intramolecular aspect, the frequency of a specific vibration is influenced by the collective interaction of this mode with the rest 3N-7 (or 3N-6 for linear molecule) modes, where N is the total number of atoms in the molecular system. As for the intermolecular aspect, the frequency of a specific vibration is also influenced by its neighboring solvent molecules. Further, the IR spectroscopy is essentially a label-free method. There are a variety of intrinsic vibrational modes that can be used to characterize protein structures, thus the use of external chromophore, as is obligatory in some other spectroscopic methods, is not absolutely necessary for the IR method.

Commercial Fourier-transform infrared (FTIR) spectrometer allows the measurement of the IR absorption spectra for a large number of vibrational transitions in proteins in the mid-IR frequency range (4000 – 650 cm$^{-1}$). Certain key vibrational modes are well studied, and empirical relationship between their frequency and protein structure has been established. A well-known example of such is the amide-I mode, which is mainly the C=O stretching vibration. It is usually used as a protein/peptide backbone conformational reporter, because the amide unit is the linkage between amino acid residues and appears periodically on the peptide chain. The well-known linear IR signature of the $\alpha$-helix, although appears to be a single absorption peak at 1640-1658 cm$^{-1}$, has a two-component (a low-frequency A-mode and a high-frequency E-mode) band structure [3]. For the anti-parallel $\beta$-sheet, there is a major sharp absorption band appearing at 1620-1640 cm$^{-1}$ and a weak peak at 1680-1696 cm$^{-1}$ [4-8],

**INTECH**
open science | open minds

while the parallel β-sheet only exhibits a major sharp absorption band at 1620-1640 cm$^{-1}$ [6,8,9]. Whereas the IR signature of other conformations, such as the β-turn and random coil, usually appears to be a single band at 1640-1658 cm$^{-1}$ for random coil, or at higher frequency for the β-turn.

Assuming a harmonic potential, quantum chemical calculations can yield a complete set of vibrational frequencies of mid-sized polypeptide molecules. Good performance of the Kohn-Sham formulation of density functional theory (DFT) for predicting molecular geometries and harmonic vibrational frequencies has been established. For example, the fundamental vibrational frequencies for nine amide modes (amide-I to -VII, and amide-A and -B) in simple peptides using the hybrid density functional B3LYP are found to be in reasonable agreement with measurements in the gas phase. In certain cases the results are even better than those from strictly *ab initio* approaches, such as second-order Moller-Plesset perturbation theory (MP2) [10]. However, because of the crudeness of the harmonic approximation, a frequency scaling factor is often needed in order to better match the theoretical prediction with experimental measurement. The frequency scaling factor is dependent on the level of theory used. A typical scaling factor is 0.9914 at the level of B3LYP/6-31G(d) [11]. However, a single scaling factor cannot scale multiple vibrational frequencies satisfactorily for a given molecule.

In reality, molecular vibrations are intrinsically anharmonic. Because of this, experimentally measured IR spectra are often complicated: it contains not only absorption peaks coming from fundamental transitions, but also those from overtone and combination transitions. For a given vibrational chromophore, the frequency difference between its fundamental transition and its overtone transition is known as the (diagonal) anharmonicity. For a pair of vibrational chromophores, the frequency difference between the sum of their fundamental transitions and that of the combinational transition is known as the off-diagonal anharmonicity. The measurement and assignment of overtone and combination bands in conventional linear IR spectroscopy have been known to be trouble some. This is because for the low-frequency modes, their overtone and combination bands fall into the high-frequency region that could be already very crowded; and for the high-frequency modes, their overtone and combination bands will fall into the high-frequency region of the mid-IR or even into the near-IR regime.

Using the two-dimensional infrared (2D IR) spectroscopy developed in recent years, measurement of anharmonic frequencies in the mid-IR region has been made easier. In this method, a typical two-frequency 2D IR spectrum containing a set of anharmonic vibrators can be obtained, and from which the anharmonic frequencies, diagonal- and off-diagonal anharmonicities can be measured.

With the aid of modern laser technology, 2D IR spectroscopic studies in the 3-μm wavelength region (frequency = 3300 cm$^{-1}$) [12], 4-μm (2500 cm$^{-1}$) [13], 5-μm (2000 cm$^{-1}$) [14-17], 6-μm (1666 cm$^{-1}$) [18-20] and 8-μm (1250 cm$^{-1}$) [21] have been reported. This method is expected to be more powerful with the use of broadband laser sources in the future. Further, the 2D IR spectroscopic method also allows additional anharmonic vibrational parameters to be acquired, for example, diagonal and off-diagonal anharmonicities, and anharmonic couplings. Recent studies have shown that these parameters are also sensitive to molecular structures. In addition, the distributions of these vibrational parameters can also be experimentally determined by 2D IR.

It is of great importance to computationally predict the anharmonic vibrational properties of biomolecules, so that they can be used to interpret experimental IR results. The second-order perturbative vibrational treatment (PT2) [22,23] allows such computations. In this method, a full cubic and a semidiagonal quartic force field is obtained by central numerical differentiation of analytical second derivatives [24]. Un-scaled anharmonic vibrational frequencies of medium size molecules can be obtained quite efficiently. A previous study [25] has shown that the performance of B3LYP functional with reasonable basis sets in computing anharmonic vibrational frequencies of semirigid molecules is quite satisfactory. In addition, high-perform‐ance computer clusters can be utilized to compute the cubic and quartic derivatives for a given molecular system so that the anharmonic vibrational frequencies can be obtained efficiently using the DFT/PT2 combination. Very recently, the chain-length dependent anharmonicity and mode-delocalization of the amide-I mode [26], and that of the amide-A mode [27], in typical peptide conformations, have been reported.

In this chapter, we present a review of our recent works in studying the anharmonic vibrations of peptide oligomers. Methods to predict the anharmonic parameters are reviewed followed by results and discussions, mainly on the amide-I modes of peptides. The conformational dependence of the obtained anharmonic parameters is discussed. Results are useful in gaining more insights into the structural basis of the anharmonic vibrations of proteins and peptides.

# 2. Methods

## 2.1. Anharmonic vibrational frequency and anharmonicity

In the normal mode picture, the vibrational energy of fundamentals, overtones and combina‐tion bands for an $N$-atom molecular system can be generally written in the following form:

$$E\left(n_i, n_j\right) = E_0 + hc\sum_i^{3N-6}\omega_i\left(n_i + \frac{1}{2}\right) + hc\sum_{i \leq j}^{3N-6} x_{ij}\left(n_i + \frac{1}{2}\right)\left(n_j + \frac{1}{2}\right), \qquad (1)$$

where $\omega_i$ is the harmonic frequency, $n_i$ is the vibrational quantum number of the $i$th mode, $x_{ij}$ is the anharmonic correction term. Applying the perturbation theory to the second-order [22-24], one can obtain $x_{ij}$ in terms of the cubic and quartic force constants. The resulting anharmonic fundamental, the overtone and the combination band frequencies are $v_i = \omega_i + 2x_{ii} + \frac{1}{2}\sum_{j \neq i} x_{ij}$, $v_{2i} = 2v_i + 2x_{ii}$ and $v_{ij} = v_i + v_j + x_{ij}$ respectively, from which one obtains the diagonal anharmonicity: $\Delta_{ii} = 2v_i - v_{2i} = -2x_{ii}$, and the mixed-mode off-diagonal anharmonicity $\Delta_{ij} = v_i + v_j - v_{ij} = -x_{ij}$. The diagonal anharmonicity can be written as [22-24]:

$$\Delta_{ii} = \frac{1}{8}\left[-\Phi_{iiii} + \frac{5\Phi_{iii}^2}{3\omega_i} + \sum_{k \neq i=1}^{3N-7}\frac{\Phi_{iik}^2\left(8\omega_i^2 - 3\omega_k^2\right)}{\omega_k\left(4\omega_i^2 - \omega_k^2\right)}\right]. \qquad (2)$$

The first two terms of equation (2) incorporates exclusively energy derivatives with respect to the $i$th mode whose diagonal anharmonicity is being considered. The coefficients $\Phi_{ijk}$ and $\Phi_{ijkl}$ are the third and fourth derivatives of the potential that involve other normal coordinates. The off-diagonal anharmonicity for any two vibrators $i$ and $j$ can also be expressed in terms of the cubic and quartic force constants and harmonic frequencies:

$$\Delta_{ij} = \frac{1}{4}\left(-\Phi_{iijj} + \frac{\Phi_{iii}\Phi_{ijj}}{\omega_i} + \frac{\Phi_{jjj}\Phi_{iij}}{\omega_j} + \frac{2\Phi_{iij}^2\omega_i}{4\omega_i^2 - \omega_j^2} + \frac{2\Phi_{jji}^2\omega_j}{4\omega_j^2 - \omega_i^2}\right)$$

$$+\frac{1}{4}\sum_{k \neq j \neq i=1}^{3N-8}\left[\frac{\Phi_{iik}\Phi_{jjk}}{\omega_k} - \frac{2\Phi_{ijk}^2\left(\omega_i^2 + \omega_j^2 - \omega_k^2\right)\omega_k}{\omega_i^4 + \omega_j^4 + \omega_k^4 - 2\left(\omega_i^2\omega_j^2 + \omega_i^2\omega_k^2 + \omega_j^2\omega_k^2\right)}\right].$$

(3)

The first bracket contains the interaction between mode $i$ and $j$, while the second line is due to the interaction of mode $i$ and $j$ with the remaining *3N-8* modes. In addition, the composition of $\Delta_{ii}$ and $\Delta_{ij}$ can be examined for a given vibrational mode to investigate the localization degree of the anharmonic forces [28]. Examples of such calculations have been given previously [24,29,30].

## 2.2. Anharmonic vibrational coupling and local modes

The through bond and through space interactions amongst vibrational chromophore units cause the anharmonic vibrational excitations to exchange from site to site. This is the physical origin of vibrational coupling. There are several ways to assess the vibrational coupling. The first approach is through *ab initio* computations. Wavefunction de-mixing of a *N*-unit coupled system can yield *N* local mode frequencies and 1/2*N*(*N*-1) bilinear couplings [29]. This method is ideal for a collection of vibrational chromophores of the same kind. Taken the amide-I mode for example, a collection of normal modes can be treated as a linear combination of uncoupled local modes, whose mixing angle $\xi$ defined below can be obtained from the normal mode eigenvectors [29]:

$$\xi = 1/2 \cdot \tan^{-1}[2|\beta_{ij}| / (v_i^0 - v_j^0)],$$

(4)

where $\beta_{ij}$ is the coupling of two local states with frequencies $v_i^0$ and $v_j^0$. Normal-mode displacement in the basis of the entire 3*N*-6 normal modes can be obtained by a frequency calculation, from which the vibrational wave functions of the amide-I normal mode in the reduced normal mode basis can be reconstructed. For the amide-I modes in a peptide system such a calculation is straightforward if the mode is assumed to be mainly a C=O stretching vibration. In this way an *N* by *N* matrix (thus a reduced amide-I subspace from the entire 3*N*-6 normal modes) was obtained for a system containing *N* amide units. Through such a procedure, the transition frequency of the local modes, the wave function mixing angle, and intermode coupling are obtained together. This method is particularly useful for assessing the coupling strength between the nearest neighboring chromophores that are covalently-bonded.

The second approach is to use transition multipole interaction. Bilinear term in the expansion of the normal mode displacement of vibrational oscillator is the lowest order of the through space interaction potential [3]. The couplings can be evaluated conveniently either by using an electrostatic transition dipole coupling (TDC) scheme [31,32], or using the transition charge and charge flux interaction [3,33], or using the distributed transition-charge density derivative interaction proposed previously [34]. In these methods, the couplings of different vibrational modes were assumed to depend solely on the molecular structure. For the amide-I mode in peptides, if the two amide units are covalently bonded, the transition charge-based approaches have advantages over the transition dipole approach. However, as the inter unit distance increases, all the approaches tend to give the same answer.

The TDC is computed by using the following formula:

$$\beta_{ij} = \left[ \left( \mu_i \cdot \mu_j \right) - 3 \left( \mu_i \cdot e_{ij} \right) \left( \mu_j \cdot e_{ij} \right) \right] / r_{ij}^3, \tag{5}$$

where $\mu_i$ is the transition dipole in (DÅ$^{-1}$amu$^{-1/2}$) units, $r_{ij}$ is the distance between dipoles (in Å), $e_{ij}$ is the unit vector connecting $i$th and $j$th vibrators.

The transition charge interaction approach has also been formulated for the amide-I mode in peptides [35]. In this method, atomic partial charge and transition charge are needed, which can be evaluated using the Mulliken charges and charge-fluxes via *ab initio* calculations [33,35-38]. The inter-site potential is approximated by the second-order expansion in terms of the normal modes [3]:

$$\beta_{ij} = \frac{1}{4\pi\varepsilon_0} \sum_{i,j} Q_i Q_j \left[ \frac{1}{2} \sum_{a_i,b_j} \frac{\partial^2}{\partial Q_i \partial Q_j} \left( \frac{(q_{a_i}^0 + \delta q_{a_i} Q_i)(q_{b_j}^0 + \delta q_{b_j} Q_j)}{r_{a_i,b_j}} \right) \right]_{Q_i = Q_j = 0}. \tag{6}$$

In equation (6), $\beta_{ij}$ is the so-called pair-wise vibrational coupling for the $i$th and $j$th amide groups; $a_i$, $b_j$ are the atoms that involved in the two amide-I normal mode displacement, which are C, O, N and H atoms here; $q_{a_i}^0$ is the atomic partial charge of the $a_i$th atom; $\delta q_{a_i}$ is the transition charge for the $a_i$th atom in the normal mode $Q_i$; $r_{a_i,b_j}$ is the distance between the two atoms; and $\varepsilon_0$ is the dielectric constant. We use a monopeptide model compound, namely *N*-methylace-tamide (NMA), for parameterization, as also previously described [33,35]. Here, the charges and charge fluxes can be refined to produce the desired transition dipole strength for the amide-I band [37], or to fit IR and Raman signals [40,41]. For NMA, the charges and charge fluxes obtained at the B3LYP/6-31+G* level yields a transition dipole magnitude of 0.38 *D*, in fair agreement with a previous report [31]. Further, as pointed out earlier [3], other charges schemes, such as Merz-Kollman [42], CHELP [43], CHELPG [44], NPA [45] and dipole-derivative derived charges [39] are also potential choices for this purpose.

In the TDC approach, the angle between the transition dipole and amide C=O bond is usually set to between 15° and 23° to fit experimental IR spectra. In the TCI approach, the calculated orientation of the transition dipole is found to be ~ 20° with respect to the C=O bond axis and towards the nitrogen atom. This angle falls into the experimentally determined range (15° to 25°) for the model compound NMA [46]. However, various values of this angle have been obtained theoretically (between -19° and 20°) when using different force fields even for the same model compound [32,47-49].

When the through bond interaction is important, the *ab initio* computation approach has to be used. For peptides in conformation covering the entire Ramachandran space, vibrational coupling maps for the amide-I mode based *ab initio* computations have been documented in literature [38,50-52], A more detailed *ab initio* computation based coupling map for the amide-I mode is also available for peptides in helical conformations [3], or in the region of the polyproline-II conformations [53]. The local-mode frequency map for the amide-I modes of peptides has also been made available [51].

### 2.3. Potential energy distribution

To evaluate how much a normal mode is delocalized onto its neighboring unit of the same kind, the potential energy distribution (PED) analysis can be carried out on the basis of the internal coordinates. This method has been recognized for some time [32]. The obtained PED value can be used to describe the relative contributions of various displacement coordinates to the total change in potential energy during a specific vibrational motion. When a normal mode $Q_k$ is excited, the potential energy $V_k$ of the molecule can be expressed as [32]

$$V_k = \tfrac{1}{2} Q_k^2 \lambda_k, \tag{7}$$

where $\lambda_k$ measures the potential energy change for unit displacement of $Q_k$, and

$$\lambda_k = \sum_{ij} F_{ij} L_{ik} L_{jk}. \tag{8}$$

Here $F_{ij}$ is the force constant in internal coordinates, and $L_{ik}$ is the element of the eigenvector of the GF matrix [23]. The PED values are obtained using the vibrational energy distribution analysis (VEDA) [54]. The information on the coordinate orientation, force constants in Cartesian coordinates and frequencies with atom displacement matrix are extracted from *ab initio* computations.

### 2.4. Simulation of 1D IR spectra

In the following, we introduce two simple frequency-domain methods for simulating 1D IR spectra of peptides. First, for the entire 3$N$-6 normal modes of a given molecule, a straightforward way of simulating its 1D IR spectra is to use the *ab initio* computed (anharmonic) frequencies and intensities. Assuming certain line broadening functions, one can obtain the

simulated broadband 1D IR spectra. A combination of Lorentzian and Gaussian functions is usually used for homogeneous and inhomogeneous contributions to the line broadening. Even though the widths of these two functions can be set flexibly for each vibration in order to compare with experimental IR spectra, the obtained line width is not physically meaningful.

The excitonic modeling, on the other hand, is particularly useful for simulating the linear IR spectra of a set of identical vibrational modes in the frequency domain. It has been used effectively to the amide-I mode of peptides. The excitonic band structure is illustrated in Figure 1, in which site states and excitonic states are shown. A set of coupled anharmonic oscillators, i.e., the site states $\{|m\rangle\}$, forms the one-quantum states $\{|k\rangle\}$. *The so-called one-exciton Hamiltonian for a particular polypeptide labeled by the index* n, *was chosen as* M *coupled harmonic oscillators* [3]*:*

$$H_n = \sum_m^M (\varepsilon + \xi_m^{(n)})|m\rangle\langle m| + \sum_{m \neq l}^M \beta_{ml}^{(n)}|m\rangle\langle l| \tag{9}$$

In equation (9), $\varepsilon$ is defined as the vibrational transition frequency (or site energy) of the $m$th amide-I mode ($m$=1 to $M$) in the $n$th polypeptide. The normal distribution (Gaussian distribution with the standard deviation $\sigma$) is very useful to describe the site energy fluctuations $\{\xi_m^{(n)}\}$ in the fashion of "white noise" (where $n$ denotes sampling size). The ensemble properties can be obtained by averaging over $N$ molecules. However, special distributions can also be employed to account for correlated energy fluctuations in the fashion of "color noise". The pair-wise coupling $\beta_{ml}^{(n)}$ can be computed using various coupling schemes described above. Standard bond lengths and angles can be generated easily for peptides with known coordinates of heavy atoms. Further, the diagonal disorder describes the static ensemble averaging, which is valid in the case of Bloch dynamics [55-57] where the fast and slow structural dynamics are separated in time.
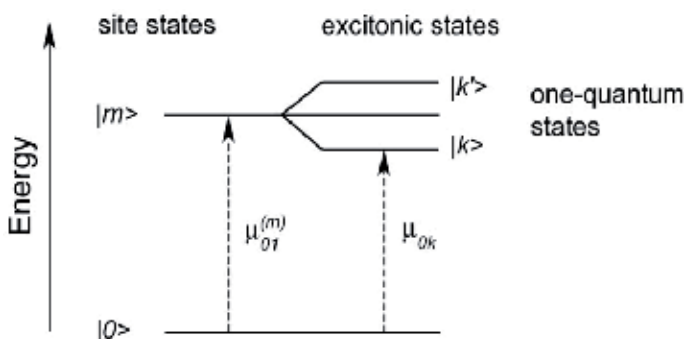


**Figure 1.** Excitonic model. A set of site states forms the one-excitonic band due to vibrational coupling. Only one-quantum states are given. Transition dipoles for both site states and excitonic states are shown.

The strength of the transition dipole of each eigenmode gives the total linear IR spectrum, as shown previously [3]:

$$S(\omega) = \left\langle \sum_{k}^{M} |\vec{\mu}_{0k}|^2 \left\{ \frac{\gamma_{k0} / \pi}{(\omega - \omega_{k0})^2 + \gamma_{k0}^2} \right\} \right\rangle \tag{10}$$

where $\vec{\mu}_{0k} = \sum_{m=1}^{M} a_{km}^{(n)} \vec{\mu}_{01}^{(m)}$, $\vec{\mu}_{01}^{(m)}$ is the local transition dipole vector of the $v = 0 \rightarrow v = 1$ transition of the $m$th amide unit in a peptide conformation and $a_{km}^{(n)}$ is the amplitude of the site $m$ in the eigenstate $k$. $\gamma_{k0}$ is the homogeneous linewidth for the $|0\rangle \rightarrow |k\rangle$ transition.

# 3. Results and discussion

### 3.1. Conformation dependent amide-I normal mode vibration in peptide oligomers

First we examine the anharmonic parameters of the amide-I mode of a model dipeptide. The molecular structure of the glycine dipeptide (Ac-Gly-NMe, or $CH_3CONHC_aH_2CONHCH_3$) is shown in Figure 2, in which backbone dihedral angles are defined to be $\phi$ ($CNC_aC$) and $\psi$ ($NC_aCN$). Here ten well-known secondary conformations are chosen, namely $\alpha_{L2}$-helix ($\phi$ = +90°, $\psi$ = -90°); $\pi$-helix (-57°, -70°); polyproline-II (PP$_{II}$, -75°, +135°); $\alpha_{L1}$-helix (+60°, +60°); C$_7$ conformation (+82°, -69°); extended structure (180°, -180°); $\alpha$-helix (-58°, -47°); 3$_{10}$-helix (-50°, -25°); anti-parallel $\beta$-sheet (-139°, +135°); and parallel $\beta$-sheet (-119°, +113°). Harmonic and anharmonic frequencies of the two amide-I modes in these dipeptides are evaluated using the density functional theory and Hartree-Fock (HF) methods. The results from the two methods are found to be highly correlated, as shown in Figure 3. Two amide-I normal modes in these dipeptides are linear combinations of the two amide-I local modes, which are dominated by the C=O stretching vibration. In the left column of Figure 3, two amide-I normal mode frequencies (harmonic picture) are shown: one is the symmetric stretching and has a relatively higher frequency (panel A) and the other is the asymmetric stretching whose frequency is lower (panel C). In order to better compare the HF frequencies (squares) and DFT frequencies (circles), the HF results are subtracted by 150 cm$^{-1}$. The results show that the calculated normal-mode harmonic frequencies at the level of Hartree-Fock theory have the same trend as those obtained at the level of the density functional theory. One can also draw the same conclusion from the anharmonic frequencies that are given in the right column of Figure 3 (panel B and D). In addition, the frequency difference between the high- and low-frequency modes in the harmonic picture (panel E) and in the anharmonic picture (panel F) are also meaningful to compare, because the frequency separation is closely related to the inter-mode coupling. Clearly the frequency separations obtained by the HF and DFT methods are also in good agreement, for both the harmonic and anharmonic cases. Further more, for the ten conforma-tions the averaged DFT anharmonic frequency of the high-frequency mode is found to be 31.7 cm$^{-1}$ lower than that of the harmonic frequency, indicating the effect of considering the
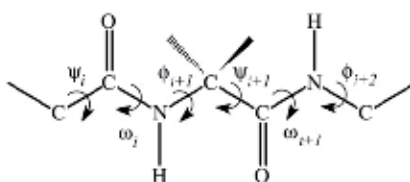
**Figure 2.** A fragment of peptide oligomer showing dihedral angles for peptide back bone and amide unit. The middle carbon is $C_\alpha$.
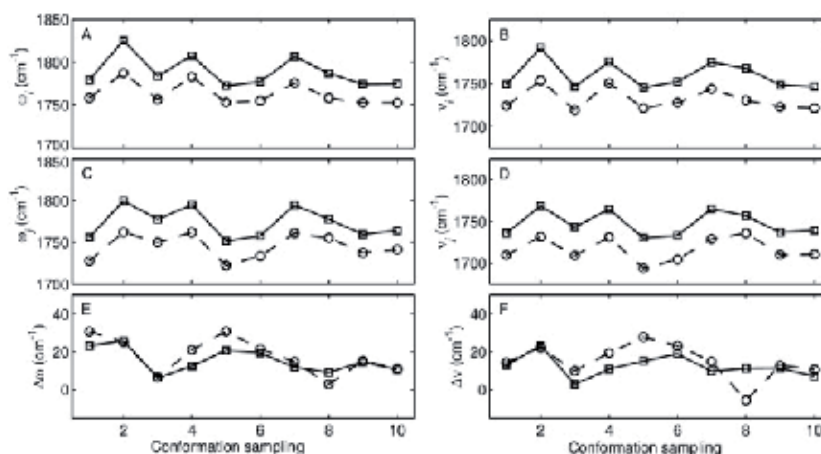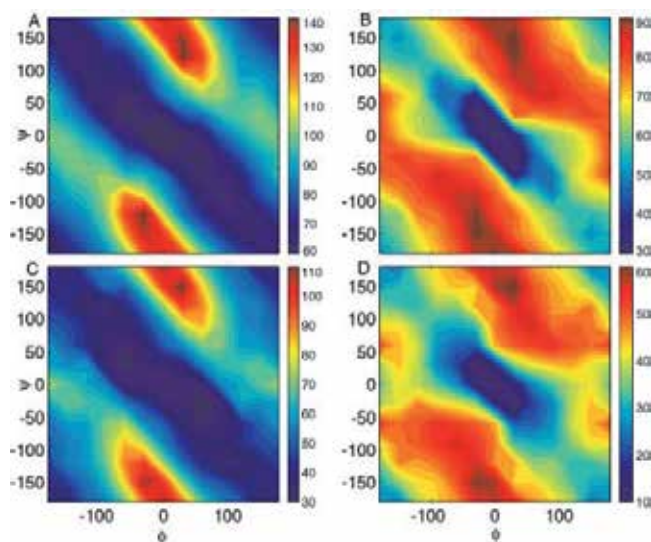


**Figure 3.** Harmonic and anharmonic frequencies and their difference (in cm$^{-1}$) of the two amide-I modes in ten representative peptide conformations obtained at the level of DFT (circle) and HF (square) for comparison. 1: $\alpha_{L2}$-helix (+90°, -90°); 2: $\pi$-helix (-57°, -70°); 3: PP$_{II}$ (-75°, +135°); 4: $\alpha_{L1}$-helix (+60°, +60°); 5: C$_7$ (+82°, -69°); 6: extended structure (+180°, -180°); 7: $\alpha$-helix (-58°, -47°); 8: 3$_{10}$-helix (-50°, -25°); 9: anti-parallel $\beta$-sheet (-139°, +135°); and 10: parallel $\beta$-sheet (-119°, +113°). Panel A: harmonic frequency for the high-frequency mode; panel B: anharmonic frequency for the high-frequency mode; panel C: harmonic frequency for the low-frequency mode; panel D: anharmonic frequency for the low-frequency mode; panel E: harmonic frequency difference; and panel F: anharmonic frequency difference. The HF results are subtracted by 150 cm$^{-1}$. Adapted from reference [30] with permission.

anharmonic potential. Similarly, the lowered value is 28.7 cm$^{-1}$ for the low-frequency mode. On the other hand, for the HF results, the anharmonic frequency drops 29.0 cm$^{-1}$ for the high-frequency mode, and 26.0 cm$^{-1}$ for the low-frequency mode. This indicates a similar anharmonic energy decrease using the two different methods. However, it is also noted that for some typical structures the frequency splitting show method-dependence, which will result in method-dependent inter-mode coupling, as discussed below. The performance of the DFT (B3LYP) and HF methods in computing the anharmonicities of the amide-I modes of peptide oligomers has been examined previously [29] and it was shown that the two methods were able to provide an optimum compromise between reliability and computer time.

Next, the full conformation space (-180° $\leq \phi \leq$ +180°, -180° $\leq \psi \leq$ +180°) for peptide backbone is explored with total 169 samplings of partially optimized structures ($\Delta\phi = \Delta\psi = 30°$). The partial optimization is performed at the HF level of theory by fixing $\phi$ and $\psi$ to desired values each

time, to sample the entire conformational space. The result is given in Figure 4. The two amide-I normal-mode frequencies (panel A and B) show significant conformation sensitivity, with different dependences on the two dihedral angles. In panel A, the harmonic high-frequency component exhibits a low-frequency region that is anti-diagonally arranged (from lower right to upper left). In panel B, the harmonic low-frequency component, however, exhibits a similarly arranged low-frequency region, but in much smaller area. The conformational dependences of the anharmonic normal-mode frequencies, which are given in panel C and D respectively, resemble those of their harmonic counterparts (panel A and B respectively). However, a detailed analysis shows subtle difference in mean value and distribution of the harmonic and anharmonic frequencies: on average the anharmonic frequency drops *ca*. 30 cm$^{-1}$ from the harmonic frequency. Further, the obtained harmonic frequencies change more dramatically along $\psi$ in the region of ($-90° \leq \phi \leq 90°$), as shown in Figure 4 (panel A and B). A similar behavior has been observed in a previous study [52]. Our results show that such a pattern still remains in the behavior of the anharmonic frequencies $\nu_i$ and $\nu_j$ in the ($\psi$, $\phi$) conformational space (panel C and D).



**Figure 4.** Conformation-dependent normal-mode frequencies (in cm$^{-1}$) for the two amide-I modes with and without anharmonic correction. (A): high-frequency harmonic component ($\omega_i$); (B): low-frequency harmonic component ($\omega_j$); (C): high-frequency anharmonic component ($\nu_i$); and (D): low-frequency anharmonic component ($\nu_j$). Frequencies are subtracted by 1900 cm$^{-1}$. Adapted from reference [30] with permission.

### 3.2. Conformation dependent amide-I local mode vibration in peptide oligomers

Local-mode frequencies can be obtained by decoupling the two amide-I normal modes in either the harmonic or anharmonic picture. The results are shown in Figure 5. In the harmonic picture, the obtained zero-order amide-I vibration frequency (denoted as $\omega_i^0$) of the NMe side (or the C-terminus side, as shown in Figure 2) is generally higher than the zero-order frequency

(denoted as $\omega_j^0$) of the Ac side (or the N-terminus side). The two harmonic local-mode frequencies also show quite different dihedral-angle dependences, which is clearly shown in A and B panels. Figure 5A depicts a relatively larger low-frequency area (anti-diagonally located) for $\omega_i^0$, with a mean value of $\tilde{\omega}_i^0$ =1943.8 cm$^{-1}$. Figure 5B shows a relatively smaller low-frequency area with a mean value of $\tilde{\omega}_j^0$ =1934.3 cm$^{-1}$. Further, the conformational dependence of the harmonic local-mode frequencies bears a strong resemblance to that of the normal-mode frequencies. This is evident by comparing Figure 5 and Figure 4. The harmonic local-mode picture shown in Figure 5 A and B is also quite similar to that reported in a previous work [58], in which B3LYP functional and 6-31+G* basis set were used.

In the anharmonic picture, the conformational dependence of the local-mode frequencies differs slightly from that in the harmonic picture. The results are shown in Figure 5, C and D panels. In panel C, the conformational dependence of the zero-order vibrational frequency $(v_i^0)$ of the amide-I unit at the C-terminus side is shown, while in panel D the conformational dependence of the zero-order vibrational frequency $(v_j^0)$ of the amide-I unit at the N-terminus side is shown. It is found that their mean values are $\tilde{v}_i^0$ = 1914.3 cm$^{-1}$ and $\tilde{v}_j^0$ = 1904.5 cm$^{-1}$ respectively, thus $\tilde{v}_i - \tilde{v}_i^0$ = 5.5 cm$^{-1}$ and $\tilde{v}_j - \tilde{v}_j^0$ = -5.1 cm$^{-1}$. This means that in the anharmonic picture, the average frequency splitting between the two amide-I modes due to coupling is 10.6 cm$^{-1}$, while in the harmonic picture the average frequency splitting is slightly larger (12.0 cm$^{-1}$). One can also estimate the average frequency splitting $(\tilde{v}_i^0 - \tilde{v}_j^0)$, which is 9.8 cm$^{-1}$, indicating the extend of local-mode non-degeneracy in the anharmonic picture.

Thus the computation results shown in Figure 5 indicate a generally non-degenerate zero-order frequency picture under both the harmonic and anharmonic approximations. Such a non-degeneracy is believed to be an intrinsic property of polypeptides. For example, in a $^{13}$C labeled β-hairpin two amide-I modes on the same peptide chain are found to have different zero-order frequencies by both 1D and 2D IR studies [59]. The non-degeneracy of the local states is believed to be due to the variation of local chemical and solvent environment of peptide amide group (-CONH-) [60]. Such a non-degenerate local-mode picture should be taken into account during empirical modeling of the 1D and 2D IR spectra of peptides and proteins. In particular, a set of zero-order transition energies can be initialized as the diagonal elements of the one-exciton Hamiltonian. Because these local-mode frequencies are backbone dihedrals (ϕ, ψ) dependent, they bear site-specific local structure characteristics and are also sensitive to solvent environment. On the other hand, the normal modes in peptides do not carry direct local-structure identities because of the mode delocalization. Under such circumstances the IR frequency and peptide structure relationship cannot be established in a straightforward way. It is for these reasons that peak assignment in conventional IR spectroscopy could be troublesome.

Further, because the amide-I local-mode frequency in the conformational space in the anharmonic picture appears to be quite similar to that in the harmonic picture one may scale the frequency from the latter to the former. This suggests a simple way to approximately obtain the anharmonic frequencies. However, care should be taken when the scaling method is
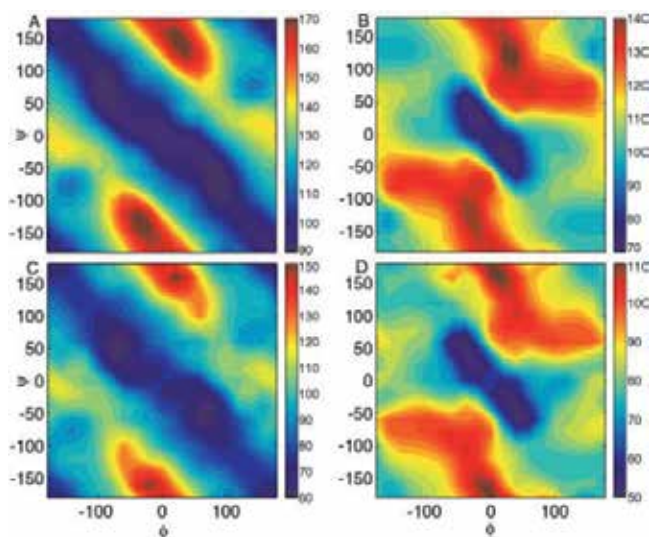
**Figure 5.** Conformation-dependent local-mode frequencies (in cm$^{-1}$) for the two amide-I modes with and without anharmonic correction. (A): high-frequency harmonic component ($\omega_i^0$); (B): low-frequency harmonic component ($\omega_j^0$); (C): high-frequency anharmonic component ($\nu_i^0$); and (D): low-frequency anharmonic component ($\nu_j^0$). Frequencies were subtracted by 1900 cm$^{-1}$. Adapted from reference [30] with permission.

utilized, because it is well known that the frequency scaling is not applicable simultaneously to all the 3$N$-6 modes in a molecule. The frequency scaling scheme would be useful only when a very limited number of modes were considered; for example, amide-I modes only in this case. Furthermore, to obtain solution-phase vibrational frequencies, solution-phase frequency models has to be established, and several of such have become available particularly for the amide-I modes [58,61,62]. In addition, for a solvated peptide, the solvation effect may be added to the scaled harmonic frequencies or to the un-scaled anharmonic frequencies so as to yield modified zero-order frequencies for spectral modeling.

### 3.3. Anharmonicity, coupling and mode delocalization

In this work the diagonal anharmonicity is defined as the decrease of the energy gap between the first excited state and its overtone state ($n$ = 1 and $n$ = 2 where $n$ is the vibrational quantum number) with respect to that of the ground state and first excited state ($n$ = 0 and $n$ = 1). The diagonal anharmonicity, inter-mode coupling, and mode delocalization are very important anharmonic parameters. The conformational dependence of these parameters is examined and the results are given in Table 1 for several dipeptides in which two units are either covalently bonded or hydrogen bonded.

We first discuss the anharmonicity of a single vibrator case. In an isolated peptide unit, for example, *trans*-NMA, the amide-I mode is highly localized, the diagonal anharmonicity is found to be 18.0 cm$^{-1}$ by computation. The diagonal anharmonicity begins to change and exhibits conformational sensitivity in a two-vibrator case. For example in alanine dipeptide

with the $\alpha$-helical conformation (–58°, –47°) the anharmonicities of both amide-I modes are smaller than that in the isolated amide unit, whereas in the conformation (–75°, +135°) and both anharmonicities are comparable with the value in the isolated amide unit. In AcProNMe the anharmonicity decreases for the C=O hydrogen-bonded amide-I mode. In hydrogen-bonded *trans*-NMA dimer, for the free and C=O hydrogen-bonded amide-I modes, the two diagonal anharmonicities decrease even more. Experimentally, an anharmonicity of 16.0 cm$^{-1}$ was reported for NMA [63], and smaller values were reported for two spatially connected amide units in different conformations, for example, 9-11 cm$^{-1}$ in the $\alpha$-helix [64] and 13±2 cm$^{-1}$ in the amino-end amide of AcProNH$_2$ [65]. Also, relatively large value (*ca.*16.0 cm$^{-1}$) was found for two amide units in an alanine dipeptide with a negligible coupling constant [53]. Thus the calculated values correlate reasonably with the experimental results. This suggests that the diagonal anharmonicity of the amide-I mode may serve as a probe for the secondary structure of peptides, while only the off-diagonal anharmonicity was believed to be useful previously for structural determination because of its link to the pair-wise coupling of two vibrators.

As shown in equation (4), the wave function mixing angle is determined by the coupling and transition energy gap of two local modes. Large mixing angle means large mode delocalization. The results of the mixing angle and inter-mode coupling for several dipeptides are listed in Table 1. For alanine dipeptide in the $\alpha$-helical conformation ($\phi$, = –58°, $\psi$ = –47°), the mixing angle between two local states is $\xi$ = 31.8°, while the inter-mode coupling is 4.9 cm$^{-1}$ in the anharmonic picture (or 6.0 cm$^{-1}$ in the harmonic picture). Thus somewhat different coupling is expected when using the anharmonic frequency scheme rather than the harmonic case, even though the latter approach has been very popular previously [3,38,66]. For the dipeptide with dihedral angles of (–75°, +135°), the mixing angle is $\xi \approx 0.1°$, and the coupling is very small (between –0.01 and –0.08 cm$^{-1}$) regardless of which frequency scheme is used. For the dipeptide with dihedral angles of (–50°, –25°), the mixing angle is $\xi$ = 69.5° and the inter-mode coupling is 6.0 cm$^{-1}$ in the anharmonic picture (but –1.0 cm$^{-1}$ in the harmonic picture). For AcProNMe, the mixing angle is $\xi$ = 8.9° and the coupling is *ca.* –8.2 cm$^{-1}$ using either frequency scheme. In the case of the *trans*-NMA dimer, the mixing angle between two local states is $\xi$ = 24.2°, while the inter-mode coupling is –3.1 cm$^{-1}$ in the anharmonic picture or –5.0 cm$^{-1}$ in the harmonic picture. Further, from the results shown in Table 1, one sees that generally the larger the diagonal anharmonicity, the smaller the mixing angle. The correlation between the anharmonicity and mode delocalization has been noted previously in the case of the C=O stretching modes of acetic acid dimer [67].

The term $|\tan2\xi|$ is a very sensitive measure of the vibrational delocalization. However, from equation (4) one obtains $|\tan2\xi| = |\beta_{ij}/(v_i^0 - v_j^0)|$, suggesting that highly delocalized states may not be strongly coupled. This is because, $|\tan2\xi|$ is determined by the ratio of the coupling and frequency separation. Thus for the case of a significant coupling but a much larger energy separation, one could still have $|\tan2\xi| \ll 1$, i.e., localized but still strongly coupled states. Two typical examples are shown in Table 1. For alanine dipeptide in the $\alpha$-helical conformation, the two amide-I modes are both significantly delocalized ($|\tan2\xi| = 1.0$) and coupled ($\beta_{ij}$ = 4.9 cm$^{-1}$). For the remaindering dipeptides, the amide-I modes are largely

localized (with small $|\tan 2\xi|$), but the strength of coupling varies. In particular, proline dipeptide AcProNMe shows a significant coupling ($\beta_{ij}$ = -8.2 cm$^{-1}$), but the two states are pretty much localized, which is mainly because of the presence of two largely separated transition frequencies.

Further, the degree of mode delocalization can be characterized by using the potential energy distribution that describes the relative contributions of various displacement coordinates to the total change in potential energy during the vibration. Here we examine the mode delocalization in gas-phase and in explicit solvent environment. We carry out computations at the harmonic level for alanine dipeptide systems in either $\alpha$-helical or $\beta$-sheet conformation, with four water molecules included in each case. The results are given below (Figure 6 and Table 2). Similar short peptide systems were examined previously to study the hydration effect of peptides [68]. The solution-phase local-mode frequencies are found to red shift from those in the gas-phase because the two amide units are both H-bonded with solvent molecules (Table 2). However, it is clear the frequency separations between the high-frequency mode and low-frequency mode for ADP in gas and in solution phases are quite similar. So it is expected that the decoupled local mode frequency separations are similar too. In other words, solvent effect on frequency separation (and mode localization caused by that) is not significantly affected by the first hydration layer in this case.

| ith and jth amide-I modes | alanine dipeptide | | | proline dipeptide | NMA dimer |
|---|---|---|---|---|---|
| $(\phi, \psi)$ | (−58, −47) | (−75, +135) | (−50, −25) | (−83, +71) | |
| $\nu_i^0$ | 1734.2 | 1714.0 | 1734.8 | 1711.4 | 1704.2 |
| $\nu_j^0$ | 1729.3 | 1675.0 | 1748.7 | 1660.5 | 1698.6 |
| $\Delta_{ii}$ | 11.5 | 21.3 | 14.9 | 19.9 | 8.7 |
| $\Delta_{jj}$ | 11.7 | 19.3 | 21.9 | 17.3 | 13.3 |
| $\beta_{ij}$ | 4.9 | −0.1 | 6.0 | −8.2 | −3.1 |
| $\xi$ | 31.8 | 0.1 | 69.5 | 8.9 | 24.2 |
| $\left| \beta_{ij} / \left( \nu_i^0 - \nu_j^0 \right) \right|$ | 1.0 | 2.5×10$^{-3}$ | 0.4 | 0.2 | 0.6 |

**Table 1.** Anharmonic local-mode frequency ($\nu$, in cm$^{-1}$), anharmonicity ($\Delta$, in cm$^{-1}$), coupling ($\beta$, in cm$^{-1}$), and wave function mixing angle ($\xi$, in degree) for two nearest neighboring amide units in various dihedral angles ($\phi$ and $\psi$, in degree). The diagonal anharmonicity is obtained from the *ab initio* calculations. Adapted from reference [29] with permission

One sees that the PED values of the two modes decrease similarly (with a few percent variation). This is found to be the case for both conformations. Here the decreased PED indicates more mode delocalization, reaching over water bending modes through hydrogen-bonding interactions. This hydration picture is reasonable for short peptides because one can hardly have one amide unit hydrogen-bonded with solvent and another not, in a solvated short

peptide. This suggests that given a homogeneous solvent environment, the amide-I mode-delocalization in short peptide would probably change similarly for each amide unit. Note that for longer peptides containing different side chains and forming intramolecular hydrogen-bonds, it might be true that only some of the amide-I frequencies would be red-shifted due to hydrogen-bonding interaction, but certainly this is a case-dependent story.

| mode | α-helix | | | | β-sheet | | | |
| | gas phase | | solution phase | | gas phase | | solution phase | |
| | $\omega_i$ | PED | $\omega_i$ | PED | $\omega_i$ | PED | $\omega_i$ | PED |
| --- | --- | --- | --- | --- | --- | --- | --- | --- |
| a | 1771.1 | 0.57 | 1733.7 | 0.53 | 1749.4 | 0.56 | 1716.3 | 0.36 |
| b | 1758.0 | 0.58 | 1721.7 | 0.46 | 1733.3 | 0.60 | 1694.0 | 0.41 |

**Table 2.** Computed harmonic frequency and PED for the amide-I modes in ADP- $(H_2O)_4$ in the α-helix and β-sheet conformations at the level of B3LYP/6-31+G*.
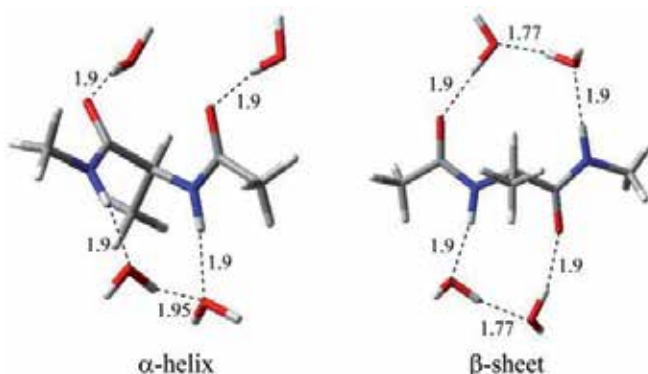


**Figure 6.** Optimized ADP- $(H_2O)_4$ systems in the α-helix (left) and β-sheet (right) conformations at the level of B3LYP/6-31+G*. Distance is in Å.

### 3.4. Simulated 1D IR spectra of peptides

The simulated 1D IR spectra of two typical turn conformations (Table 3) employing the vibrational exciton model in the frequency domain are shown in Figure 7. More details can be found in a recent work [3]. Discernable conformational-dependent spectral features are seen in simulated 1D IR spectra of these peptide structures. The spectral features include absorption peak positions and line width profiles. For the γ–turn, two amide-I local modes are coupled

and transition intensities are not equal. For the β–turn, three coupled local transitions form excitonic band structure (normal modes) that differs from that of the γ–turn. In Figure 7, stick spectrum are also given in each panel. Inhomogeneous distribution of the transition energies are clearly shown in each case [69]. Further, because of transition intensity transfer, a direct result of vibrational coupling, the computed 1D IR spectra show patterns that significantly different from the local-mode picture with three independent bands.

| species | dihedral angles [a] | | | | | | | hydrogen-bonding ring |
|---|---|---|---|---|---|---|---|---|
| γ–turn | $\omega_1$ | $\phi_2$ | $\psi_2$ | $\omega_2$ | | | | |
| classic | +172.6 | 74.9 | -75.0 | −170.8 | | | | $C_7$ |
| β–turn | $\omega_1$ | $\phi_2$ | $\psi_2$ | $\omega_2$ | $\phi_3$ | $\psi_3$ | $\omega_3$ | |
| type I | +175.3 | −60.0 | −30.0 | −177.1 | −90.0 | +0.0 | −171.2 | $C_{10}$ |

[a]. Defined in Figure 2.

**Table 3.** Glycine-based peptide oligomers in turn conformations: Ac–Gly$_n$–NMe ($n$ = 1 for the γ–turn and $n$ = 2 for the β–turn).
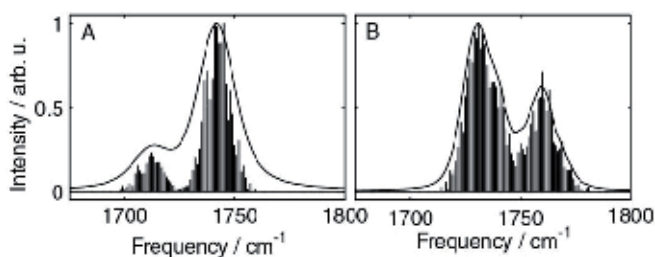


**Figure 7.** Simulated 1D IR of selected peptide fragments in (A) the classic γ-turn and (B) the type-I β-turn. Sticks indicate ensemble sampling.

## 4. Conclusions

This chapter discusses the methods and application of anharmonic vibration parameters for the purpose of connecting the secondary structure of proteins and peptides to their IR spectra. Using the amide-I mode in particular, the usefulness of the methods is clearly demonstrated. The performance of the DFT and HF theories in predicting the anharmonic frequencies are compared and the conformational dependence of the obtained parameters are examined. The methods to compute vibrational coupling are also reviewed and examples are discussed. The coupled nature of the amide-I band for typical secondary structures is analyzed using the potential energy distribution function, and the local-mode properties (frequency and coupling) are discussed. Since the solvent effect on these parameters is unavoidable, as has shown for PED analysis, solvent molecules must be taken into account in assessing the vibrational

properties of solute. Polarizable continuum method [70] for solvent model can be used for such purposes. In addition, site-dependent dynamical interactions between peptide and water molecules in the hydration shells needs to be examined by molecular dynamics simulations employing proper molecular mechanical force fields, so that the statistical distributions and correlations of the transition frequencies can be computed. This can be done by carrying our instantaneous normal mode analysis, for example. Time-dependent vibrational couplings can also be computed based on the molecular dynamics trajectories. Nevertheless, simultaneous assessment of vibrational parameters of multiple vibrational modes shall prove useful in understanding the characteristics of linear and nonlinear infrared spectra of both static and equilibrium dynamical structures of proteins, peptides and other biomolecules [71].

## Acknowledgements

## Author details

Jianping Wang[*]

Address all correspondence to: jwang@iccas.ac.cn

Institute of Chemistry, the Chinese Academy of Sciences, Beijing National Laboratory for Molecular Sciences, Beijing, P. R. China.

## References

[1] Mantsch HH, Chapman D. Infrared spectroscopy of biomolecules, Wiley-Liss, New York, 1996.

[2] Barth A, Zscherp C. What vibrations tell us about proteins. Quarterly Reviews of Bio‐physics 2002;35:369-430.

[3] Wang J, Hochstrasser RM. Characteristics of the two-dimensional infrared spectro‐scopy of helices from approximate simulations and analytic models. Chemical Phys‐ics 2004;297:195-219.

[4]   Miyazawa T. Perturbation treatment of the characteristic vibrations of polypeptide chains in various configurations. The Journal of Chemical Physics 1960;32:1647-52.

[5]   Miyazawa T, Blout ER. The infrared spectra of polypeptides in various conformations: amide I and II bands. Journal of the American Chemical Society 1961;83:712-19.

[6]   Chirgadze YN, Nevskaya NA. Infrared spectra and resonance interaction of amide-I vibration of the antiparallel-chain pleated sheet. Biopolymers 1976;15:607-25.

[7]   Mukherjee S, Chowdhury P, Gai F. Effect of dehydration on the aggregation kinetics of two amyloid peptides. The Journal of Physical Chemistry B 2008;113:531-35.

[8]   Cerf E, Sarroukh R, Tamamizu-Kato S, Breydo L, Derclaye S, Dufrêne YF, Narayanaswami V, Goormaghtigh E, Ruysschaert JM, Raussens V. Antiparallel β-sheet: a signature structure of the oligomeric amyloid β-peptide. Biochemical Journal 2009;421:415-23.

[9]   Goormaghtigh E, Cabiaux V, Ruysschaert JM. Determination of soluble and membrane protein structure by Fourier transform infrared spectroscopy. I. Assignments and model compounds. Subcellular Biochemistry 1994;23:329-62.

[10]  Watson TM, Hirst JD. Density functional theory vibrational frequencies of amides and amide dimers. The Journal of Physical Chemistry A 2002;106:7858-67.

[11]  Merrick JP, Moran D, Radom L. An evaluation of harmonic vibrational frequency scale factors. The Journal of Physical Chemistry A 2007;111:11683-700.

[12]  Cowan ML, Bruner BD, Huse N, Dwyer JR, Chugh B, Nibbering ETJ, Elsaesser T, Miller RJD. Ultrafast memory loss and energy redistribution in the hydrogen bond network of liquid H2O. Nature 2005;434:199-202.

[13]  Asbury JB, Steinel T, Stromberg C, Corcelli SA, Lawrence CP, Skinner JL, Fayer MD. Water dynamics: vibrational echo correlation spectroscopy and comparison to molecular dynamics simulations. The Journal of Physical Chemistry A 2004;108:1107-19.

[14]  Lee K-K, Park K-H, Park S, Jeon S-J, Cho M. Polarization-angle-scanning 2D IR spectroscopy of coupled anharmonic oscillators: A polarization null angle method. The Journal of Physical Chemistry B 2011;115:5456-64.

[15]  King JT, Kubarych KJ. Site-specific coupling of hydration water and protein flexibility studied in solution with ultrafast 2D-IR spectroscopy. Journal of the American Chemical Society 2012;134:18705-12.

[16]  Li D, Yang F, Han C, Zhao J, Wang J. Correlated high-frequency molecular motions in neat liquid probed with ultrafast overtone two-dimensional infrared spectroscopy. The Journal of Physical Chemistry Letters 2012;3:3665-70.

[17]  Yu P, Yang F, Zhao J, Wang J. Hydration dynamics of cyanoferrate anions examined by ultrafast infrared spectroscopy. The Journal of Physical Chemistry B 2014;118:3104-14.

[18] Hochstrasser RM. Two-dimensional spectroscopy at infrared and optical frequencies. Proceedings of the National Academy of Sciences of the United States of America 2007;104:14190-96.

[19] Maekawa H, Ballano G, Toniolo C, Ge N-H. Linear and two-dimensional infrared spectroscopic study of the amide I and II modes in fully extended peptide chains. The Journal of Physical Chemistry B 2010;115:5168-82.

[20] Middleton CT, Marek P, Cao P, Chiu C-c, Singh S, Woys AM, de Pablo JJ, Raleigh DP, Zanni MT. Two-dimensional infrared spectroscopy reveals the complex behaviour of an amyloid fibril inhibitor. Nature Chemistry 2012;4:355-60.

[21] Costard R, Heisler I, A., Elsaesser T. Structural dynamics of hydrated phospholipid surfaces probed by ultrafast 2D spectroscopy of phosphate vibrations. The Journal of Physical Chemistry Letters 2014;5:506-11.

[22] Nielsen HH. The vibration-rotation energies of molecules. Reviews of Modern Physics 1951;23:90-136.

[23] Califano S: Vibrational states, John Wiley and Sons, London, New York, Sydney, Toronto, 1976.

[24] Barone V. Anharmonic vibrational properties by a fully automated second-order perturbative approach. The Journal of Chemical Physics 2005;122:014108/1-08/10.

[25] Barone V. Accurate vibrational spectra of large molecules by density functional computations beyond the harmonic approximation: The case of azabenzenes. The Journal of Physical Chemistry A 2004;108:4146-50.

[26] Zhao J, Wang J. Chain-length and mode-delocalization dependent amide-I anharmonicity in peptide oligomers. The Journal of Chemical Physics 2012;136:214112.

[27] Wang J. Conformational dependence of anharmonic NH stretch vibration in peptides. Chemical Physics Letters 2009;467:375-80.

[28] Zheng ML, Zheng DC, Wang J. Non-native side chain IR probe in peptides: Ab initio computation and 1D and 2D IR spectral simulation. The Journal of Physical Chemistry B 2010;114:2327-36.

[29] Wang J, Hochstrasser RM. Anharmonicity of Amide Modes. The Journal of Physical Chemistry B 2006;110:3798-807.

[30] Wang J. Conformational dependence of anharmonic vibrations in peptides: amide-I modes in model dipeptide. The Journal of Physical Chemistry B 2008;112:4790-800.

[31] Cheam TC, Krimm S. Transition dipole interaction in polypeptides: ab initio calculation of transition dipole parameters. Chemical Physics Letters 1984;107:613-16.

[32] Krimm S, Bandekar J. Vibrational spectroscopy and conformation of peptides, polypeptides, and proteins. Advances in Protein Chemistry 1986;38:181-364.

[33] Hamm P, Lim M, DeGrado WF, Hochstrasser RM. The two-dimensional IR nonlinear spectroscopy of a cyclic penta-peptide in relation to its three-dimensional structure. Proceedings of the National Academy of Sciences of the United States of America 1999;96:2036-41.

[34] Moran A, Mukamel S. The origin of vibrational mode couplings in various secondary structural motifs of polypeptides. Proceedings of the National Academy of Sciences of the United States of America 2004;101:506-10.

[35] Hamm P, Hochstrasser RM, in M.D. Fayer (Ed.), Ultrafast Infrared and Raman Spectroscopy. Marcel Dekker Inc., New York, 2001, p. 273-347.

[36] Dybal J, Cheam TC, Krimm S. Carbonyl stretch mode splitting in the formic acid dimer: electrostatic models of the intermonomer interaction. Journal of Molecular Structure 1987;159:183-94.

[37] Torii H, Tasumi M. Infrared intensitites of vibrational modes of an -a-helical polypeptide: calculations based on the equilibrium charge/charge flux (ECCF) model. Journal of Molecular Structure 1993;300:171-79.

[38] Hamm P, Woutersen S. Coupling of the amide I modes of the glycine dipeptide. Bulletin of the Chemical Society of Japan 2002;75:985-88.

[39] Qian W, Krimm S. Origin of the C=O stretch mode splitting in the formic acid dimer. The Journal of Physical Chemistry 1996;100:14602-08.

[40] Yokoyama I, Miwa Y, Machida K. Extended molecular mechanics calculations of thermodynamic quantities, structures, vibrational frequencies, and infrared absorption intensities of formic acid monomer and dimer. Journal of the American Chemical Society 1991;113:6458-64.

[41] Yokoyama I, Miwa Y, Machida K. Simulation of Raman spectra of formic acid monomer and dimer in the gaseous state by an extended molecular mechanics method. The Journal of Physical Chemistry 1991;95:9740-46.

[42] Besler BH, Merz KMJ, Kollman PA. Atomic charges derived from semiempirical methods. Journal of Computational Chemistry 1990;11:431-39.

[43] Chirlian LE, Francl MM. Atomic charges derived from electrostatic potentials: A detailed study. Journal of Computational Chemistry 1987;8:894-905.

[44] Breneman CM, Wiberg KB. Determining atom-centered monopoles from molecular electrostatic potentials. The need for high sampling density in formamide conformational analysis. Journal of Computational Chemistry 1990;11:361-73.

[45] Reed AE, Weinstock RB, Weinhold F. Natural population analysis. The Journal of Chemical Physics 1985;83:735-46.

[46] Bradbury EM, Elliott A. The infrared spectrum of crystalline N-methylacetamide. Spectrochimica Acta 1963;19:995-1012.

[47] Torii H, Tasumi M. Model calculations on the amide-I infrared bands of globular proteins. The Journal of Chemical Physics 1992;96:3379-87.

[48] Dwivedi AM, Krimm S. Vibrational analysis of peptides, polypeptides, and proteins. X. Poly(glycine I) and its isotopic derivatives. Macromolecules 1982;15:177-85.

[49] Rey-Lafon M, Forel MT, Garrigou-Lagrange C. Study of normal modes of cis- and trans-amide groups using force fields of d-valarolactam and N-methylacetamide. Spectrochimica Acta, Part A 1973;29:471-86.

[50] Torii H, Tasumi M. Ab initio molecular orbital study of the amide I vibrational interactions between the peptide groups in di- and tripeptides and considerations of the conformation of the extended helix. Journal of Raman Spectroscopy 1998;29:81-86.

[51] la Cour Jansen T, Dijkstra AG, Watson TM, Hirst JD, Knoester J. Modeling the amide I bands of small peptides. The Journal of Chemical Physics 2006;125:044312/1.

[52] Gorbunov RD, Kosov DS, Stock G. Ab initio-based exciton model of amide I vibrations in peptides: Definition, conformational dependence, and transferability. The Journal of Chemical Physics 2005;122:224904-12.

[53] Kim YS, Wang J, Hochstrasser RM. Two-dimensional infrared spectroscopy of the alanine dipeptide in aqueous solution. The Journal of Physical Chemistry B 2005;109:7511-21.

[54] Jamróz MH. Vibrational energy distribution analysis VEDA 4, Warsaw, 2004.

[55] Mukamel S: Principles of nonlinear optical spectroscopy, Oxford University Press, 1995.

[56] Cho M: Two-dimensional optical spectroscopy, CRC Press, Boca Raton, London, New York, 2009.

[57] Hamm P, Zanni M: Concept and methods of 2D infrared spectroscopy, Cambridge University Press, Cambridge, New York, Melbourne, Madrid, Cape Town, Singapore, Sao Paulo, Delhi, Tokyo, Mexico City, 2011.

[58] Jansen TL, Knoester J. A transferable electrostatic map for solvation effects on amide I vibrations and its application to linear and two-dimensional spectroscopy. The Journal of Chemical Physics 2006;124:044502/1-02/11.

[59] Wang J, Chen J, Hochstrasser RM. Local structure of β-hairpin Isotopomers by FTIR, 2D IR, and ab initio theory. The Journal of Physical Chemistry B 2006;110:7545-55.

[60] Wang J, Zhuang W, Mukamel S, Hochstrasser RM. Two-dimensional infrared spectroscopy as a probe of the solvent electrostatic field for a twelve residue peptide. The Journal of Physical Chemistry B 2008;112:5930-37.

[61] Schmidt JR, Corcelli SA, Skinner JL. Ultrafast vibrational spectroscopy of water and aqueous N-methylacetamide: comparison of different electronic structure/molecular dynamics approaches. The Journal of Chemical Physics 2004;121:8887-96.

[62] Hayashi T, Zhuang W, Mukamel S. Electrostatic DFT map for the complete vibrational amide band of NMA. The Journal of Physical Chemistry A 2005;109:9747-59.

[63] Hamm P, Lim M, Hochstrasser RM. Structure of the amide I band of peptides measured by femtosecond nonlinear-infrared spectroscopy. The Journal of Physical Chemistry B 1998;102:6123-38.

[64] Fang C, Wang J, Kim YS, Charnley AK, Barber-Armstrong W, Smith AB, III, Decatur SM, Hochstrasser RM. Two-dimensional infrared spectroscopy of isotopomers of an alanine rich alpha-helix. The Journal of Physical Chemistry B 2004;108:10415-27.

[65] Rubtsov IV, Hochstrasser RM. Vibrational dynamics, mode coupling and structure constraints for acetylproline-NH2. The Journal of Physical Chemistry B 2002;106:9165-71.

[66] Ham S, Cha S, Choi J-H, Cho M. Amide I modes of tripeptides: Hessian matrix reconstruction and isotope effects The Journal of Chemical Physics 2003;119:1451-61.

[67] Lim M, Hochstrasser RM. Unusual vibrational dynamics of the acetic acid dimer. The Journal of Chemical Physics 2001;115:7629-43.

[68] Bohr HG, Frimand K, Jalkanen KJ, Nieminen RM, Suhai S. Neural-network analysis of the vibrational spectra of N-acetyl L-alanyl N8-methyl amide conformational states. Physical Review E 2001;64:021905-1.

[69] Wang J. Assessment of the amide-I local modes in gamma- and beta-turns of peptides, Physical Chemistry and Chemical Physics 2009;11:5310-5322.

[70] Cances E, Mennucci B, Tomasi J. A new integral equation formalism for the polarizable continuum model: Theoretical background and applications to isotropic and anisotropic dielectrics. The Journal of Chemical Physics 1997;107:3032-41.

[71] Wang J. Ab initio-based all-mode two-dimensional infrared spectroscopy of a sugar molecule. The Journal of Physical Chemistry B 2007;111:9193-96.

# Probing Brain Oxygenation
# with Near Infrared Spectroscopy (NIRS) —
# The Role of Carbon Dioxide
# and Blood Pressure

Alexander Gersten

Additional information is available at the end of the chapter

## 1. Introduction

The Near Infrared spectroscopy (NIRS) is a technique, which allows measuring the oxygenation of the brain tissue [22, 1, 6, 9, 37, 52, 58, 63].

The problem is to penetrate the brain with a light, which can cross the skin and skull and be absorbed mostly by the hemoglobin ($HbO_2$) and the deoxyhemoglobin (Hb). The ratio of the oxygenated hemoglobin ($HbO_2$) to the total hemoglobin ($tHb=HbO_2+Hb$) is the regional oxygen saturation rSO2. It appears that the most suitable light is in the 650-1000 nm range of the near infrared light. In this range, there exists another absorber cytochrome oxidase (CtOx), but as its concentration is quite small, it is often neglected [60]. Instruments that take into account the CtOx use 3 different wavelengths, otherwise 2 wavelengths are used.

There is a continuous improvement in the instrumentation. Three types are in use: continuous wave (CW) mostly used, time resolved and intensity modulated [9]. An improved resolution is obtained using the spatially resolved spectroscopy (SRS), in which multi-distance sensors are used. Another distinction can be made. Photometers, are the simplest, they use CW light, single-distance and one sensor. The oximeters use multi-distance (SRS) techniques with CW and usually two sensors [15, 9, 58]. Multi-channel CW imaging systems generating images of a larger area started to be used [15, 52].

We have done measurements with two instruments: the INVOS Cerebral Oximeter of Somanetics (www.somanetics.com; Thavasothy et al., 2002), and the hemoencephalograph (HEG) photometer of Hershel [66]. The results are presented in the following sections.

## 2. Theoretical considerations

The theoretical considerations are based on the modified Beer-Lambert law [22],

$$A = \left[ a_1 \cdot c_1 + a_2 \cdot c_2 + ... + a_n \cdot c_n \right] \cdot d \cdot DPF + G, \tag{1}$$

where $A$ is the attenuation coefficient, measured in optical densities (OD),

$$A = log_{10} \left[ I_0 / I \right] \tag{2}$$

$I_0$ is the incident light intensity and I the intensity of the light collected by the sensor after returning from the brain.

It is a generalization of Beer-Lambert Law, in which the attenuation $A$ of an incident light is proportional to the concentration $c$ of the compound in the solution and the optical pathlength $d$:

$$A = log_{10} \left[ I_0 / I \right] = a \cdot c \cdot d, \tag{3}$$

a is the specific extinction coefficient of the absorbing compound (measured in 1/micromolar per cm), c is the concentration of the absorbing compound in the solution (measured in micromolar), $d$ is the distance in cm that the light covers in the medium, $a \bullet c$ is the absorption coefficient of the medium. For different absorbing compounds, the absorbing coefficient is the sum of the contributions,

$$A = log_{10} \left( I_0 / I \right) = \left[ a_1 \cdot c_1 + a_2 \cdot c_2 ... + a_n \cdot c_n \right] d. \tag{4}$$

The Beer-Lambert law should be modified to include a term $G$ that describes the scattering attenuation and a multiplying factor due to scattering, the differential pathlength factor (DPF), which multiplies the length d. All these corrections appear in the modified Beer-Lambert law as given in Eq. (1).In Fig.1 the specific extinction coefficients of hemoglobin (HbO$_2$), the deoxyhemoglobin (Hb) and cytochrome oxidase (CtOx) are displayed.
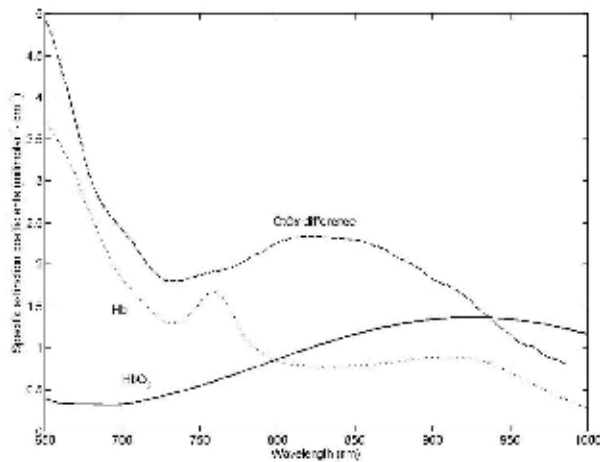
**Figure 1.** The specific extinction coefficients of HbO$_2$, Hb, and the difference absorption spectrum between the oxidized and reduced forms of CtOx, the data are from [7].

It appears that DPF depends on the human age. According to [7]:

$$DPF_{780} = 5.13 + \left(0.07Y\right)^{0.81},$$

(5)

where DPF$_{780}$ is the PDF at 780 nm and $Y$ is the age of the subject in years.

## 3. Oxygen utilization

For a more complete description of oxygen utilization see [22]. Here we will only mention [22] that "a typical oxygen carrying capacity of the blood is 19.4 ml of O$_2$ per dl of blood with 19.1 ml O$_2$/dl carried by hemoglobin and only 0.3 ml O$_2$/dl dissolved in plasma [7]. A typical averaged value for adult cerebral blood flow (CBF) is 47.7 ml/100 ml/min (Frackowiak et al., 1980) corresponding to total oxygen delivery of 9.25 ml O2/100 ml/min. [7]. Typical oxygen consumption of the adult brain is 4.2 ml O$_2$/100 ml/min (Frackowiak et al., 1980). CBF, cerebral blood volume (CBV) and cerebral oxygen extraction (COE) are significantly greater in grey matter compared to white matter in normal human adults (Lammertsma et al., 1983; cope, 1991). Only part of the arterial oxygen that arrives in the brain is absorbed and utilized. The fraction that is utilized, known as the oxygen extraction fraction (OEF), is defined as

$$OEF = \left(SaO_2 - SvO_2\right)/SaO_2,$$

(6)

where SaO$_2$ and SvO$_2$ are the arterial and venous oxygen saturations respectively."

In a well-done experiment, the EOF, measured in normal control subjects, was 0.41±0.03 [11]. Assuming $SaO_2$ equal to 0.95 (an average adult value) the $SvO_2$ will be, using Eq. (6), equal to 0.56±0.03. In the brain tissue, the absorption of the hemoglobin is mostly venous. A 75% venous contribution, leads in the frontal region to $rSO_2$ of about 66±3%, which is observed in experiments.

## 4. The INVOS oximeter

The Somanetics INVOS Cerebral Oximeter (ICO) uses two wavelengths, 730 and 810 nm and measures $rSO_2$ of the brain in the area under the sensor, which is attached to the forehead. The spatially resolved spectroscopy (SRS) method is applied by using in the sensor two source-detector distances: 3 cm from the source and 4 cm from the source, which penetrates deeper into the brain. The SRS method leaves a signal originating predominantly in the brain cortex.

Oximeter provides a "predominately cerebral" measurement where over 85 percent of the signal, on average, is exclusively from the brain" (www.somanetics.com).

## 5. The HEG

The Toomim's hemoencephalograph (HEG) uses two wavelengths, 660 and 850 nm is a single-distance CW spectrophotometer. The distance between the source and receiver is 3 cm. The HEG measures the intensity ratios of the 660 nm light to 850 nm light. The HEG does not measure $rSO_2$, but is an important tool in the biofeedback research. The HEG is a very sensitive device. The source-detector is 3 cm, while the Somanetics INVOS Cerebral the oximeter has two distances 3 and 4 cm. Therefore, the INVOS Oximeter penetrates deeper into the brain and is more stable and less influenced by biofeedback.

A normalization of the HEG readings was done using measurements of 154 adult attendees at a professional society meeting, which is not directly related to rSO2. We have shown (Gersten et. al. 2011a) that one can relate the readings of the HEG to $rSO_2$ and even calibrate it separately for each individual. An improved derivation is given below.

## 6. Evaluating the $rSO_2$ from ratios of intensities

The regional hemoglobin saturation ($rSO_2$) is defined as

$$rSO_2 = 100C_{HbO2}/\left(C_{HbO2} + C_{Hb}\right)\%,\qquad(7)$$

which is the percentage of the total hemoglobin that is oxygenated. Above $C_{Hb}$ and $C_{HbO2}$ are the concentrations of deoxyhemoglobin and oxyhemoglobin respectively. The modified Beer-Lambert law, Eq. (4), for a definite wavelength $\lambda$ is,

$$A(\lambda) = log_{10}\left(I_0(\lambda)/I(\lambda)\right) = \left[a_1(\lambda)\cdot c_1 + a_2(\lambda)\cdot c_2 + \ldots + a_n(\lambda)\cdot c_n\right]\cdot d\cdot DPF + G. \tag{8}$$

It will be more convenient to work with natural logarithms $ln$;

$A(\lambda) = log_{10}(I_0(\lambda)/I(\lambda)) = -ln(I(\lambda)/I_0(\lambda))/00(10),$

Let us define the ratio of the relative intensities with wavelengths $\lambda_1$ and $\lambda_2$ as,

$R(\lambda_1, \lambda_2) = (I(\lambda_1)/I_0(\lambda_1))/ (I(\lambda_2)/I_0(\lambda_2)),$
$ln(R_{1,2}) = ln(R(\lambda_1, \lambda_2)) = ln(10) \times (A(\lambda_2) - A(\lambda_1)),$

The scattering component G is generally unknown and is highly dependent on the measurement geometry making it difficult to obtain absolute value of attenuation as a function of chromophore concentrations. However, under the assumption that G does not change during the measurement period, it is possible to determine changes in attenuation. Under this assumption, using Eq. (8), G is cancelled out in $A(\lambda_2)-A(\lambda_1)$, and we obtain,

$$ln(R_{1,2}) = ln(10)[(aHb((\lambda_2)) - a_{Hb}(\lambda_1))C_{Hb} + (a_{Hb\,O2}(\lambda_2) - a_{Hb\,O2}(\lambda_1))C_{Hb\,O2}]d\cdot DPF. \tag{9}$$

Let us introduce the constant D:

$$D = ln(10)d\cdot DPF, \tag{10}$$

Then

$$ln(R_{1,2}) = [(a_{Hb}(\lambda_2) - a_{Hb}(\lambda_1))(C_{Hb} + C_{Hb\,O2}) + (a_{Hb\,O2}(\lambda_2) - a_{Hb}(\lambda_2) - a_{Hb\,O2}(\lambda_1) + a_{Hb}(\lambda_1))C_{Hb\,O2}]D = $$
$$(C_{Hb} + C_{Hb\,O2})[100(a_{Hb}(\lambda_2) - a_{Hb}(\lambda_1)) + (a_{Hb\,O2}(\lambda_2) - a_{Hb}(\lambda_2) - a_{Hb\,O2}(\lambda_1) + a_{Hb}(\lambda_1))rSO_2]D/100. \tag{11}$$

Let us introduce the following constants:

$$C_{Tot} = C_{Hb} + C_{Hb\,O2} \quad \text{the total hemoglobin,} \tag{12}$$

$$H(\lambda_1,\lambda_2)= 100(a_{Hb}(\lambda_2)-a_{Hb}(\lambda_1)), \tag{13}$$

$$K(\lambda_1,\lambda_2)=a_{Hb\,O2}(\lambda_2)- a_{Hb}(\lambda_2)-a_{Hb\,O2}(\lambda_1)+ a_{Hb}(\lambda_1), \tag{14}$$

$$M= C_{Tot} \cdot D/100, \tag{15}$$

Then,

$$ln(R_{1,2})=M\cdot(H(\lambda_1,\lambda_2)+ K(\lambda_1,\lambda_2)\cdot rSO_2). \tag{16}$$

Above, the constant M is not known. One can determine it in two ways, by introducing a third wavelength, or by calibrating with other device. If third wavelength is added one obtains,

$$ln(R_{1,2})/ln(R_{1,3})=(H(\lambda_1,\lambda_2)+ K(\lambda_1,\lambda_2)\cdot rSO_2)/(H(\lambda_1,\lambda_3)+ K(\lambda_1,\lambda_3)\cdot rSO_2), \tag{17}$$

from which $rSO_2$ can be evaluated. If one would like to calibrate M using other device, one can calibrate M only with respect to a standard total hemoglobin $C_0$,

$$M=(C_{Tot}/C_0) \times(C_0\times D/100)==(C_{Tot}/C_0) \times M_0, \tag{18}$$

Where $C_{Tot}$ can be determined from a blood test.

## 7. Peculiarities of brain's blood flow: Role of carbon dioxide

Breathing may have dramatic effects on the brain blood flow. This was already known long time ago to Chinese, Indians and Tibetans. We will develop simple mathematical models which allow a quantitative description of cerebral blood flow. In recent years considerable progress was made in utilizing measurements of the regional cerebral blood flow (rCBF) in order to study brain functioning [44, 2, 8]. It seems however that the physical and mathematical aspects of the global cerebral blood flow (CBF), or average rCBF, were not sufficiently explored. Our

main interest is the use of physical principles [35], physical and mathematical reasoning as well as means to describe the main features of CBF in a simple way.

The human brain consists of about 2% of the adult body weight, but consumes (at rest) about 15% of the cardiac output (CO) and about 20% of the body's oxygen demand [61, 25]. Glucose is the main source of cellular energy through its oxidation [61]. The cerebral glucose utilization is almost directly proportional to the CBF, [29; 33]. The CBF can be influenced by abnormal glucose levels, is increased during hypoglycemia [36] and decreased during hyperglycemia [10]. Normal mean CBF is approximately 50-55 ml/100g/min, but declines with age (above the age of about 30), in a rate of approximately 58.5-0.24×age ml/100g/min [50, 27], see also [69], for other details).

The cardiac output can be increased many times (up to about tenfold) during very heavy exercise or work. Only part of the cardiac output increase can be accommodated by the brain blood vessels because of autoregulatory mechanisms and because of the vessels limited capacitance, which is influenced by their elasticity, limited space of the cranium and the presence of the cerebrospinal fluid (CSF).

Autoregulatory mechanisms exist, which maintain the CBF approximately constant for cerebral perfusion pressure (CPP) over an approximate range of 60-160 mm Hg [29,[3] 67]. Outside this autoregulatory range the CBF may decrease (CPP<60 mm Hg) as in the case of hypotonia [61] or increase (CPP>160 mm Hg) as in the case of high hypertension [25]. Again, the above statements are valid only for normal functioning. For some abnormal functioning the autoregulatory mechanisms may break down, for example if $PaCO_2$> 70 mm Hg [29, 30].

The CBF is also influenced by the value of cerebral tissue $PaO_2$, whose normal range is about 100 mmHg. Only below approximately 40-50 mmHg there will be a very strong increase of CBF [25], mobilizing the organism to prevent suffocation. The main parameter influencing the CBF is the arterial $PaCO_2$. About 70% increase (or even less) in arterial $PaCO_2$ may double the blood flow (normal value of $PaCO_2$ is about 40 mmHg.) [61, 25].

The CBF is very sensitive to $PaCO_2$and it is our aim to demonstrate with a simple physical model that important information about CBF capacitance can be obtained by considering only the dependence of CBF on $PaCO_2$. Slowing down the breathing rate, without enhancing the airflow [20, 18, 19], or holding the breath, can increase $PaCO_2$. It is plausible that this is one of the essences of yoga pranayama [4, 39, 40, 46], and of Tibetan six yogas of Naropa [13, 51]. It seems that biofeedback training of breathing [20], or methods advocated in yoga, may become important for treating health problems.

In Sec. 8 We have developed a simple physical model, and have derived a simple four parameter formula, relating the CBF to $PaCO_2$. With this model experimental data sets of rhesus monkeys and rats were well fitted. In Sec.9 exact formulae were found, which allow to transform the fits of one animal to the fits of another one. The merit of this transformation is that it allows to use rats data as monkeys data (and vice versa) simply by rescaling the $PaCO_2$ and the CBF data.

## 8. A mathematical model of CBF as a function of arterial $CO_2$

Inspection of experimental data, especially the more accurate ones on animals, like those done with rhesus monkeys [55], or with rats [59] led us to conclude that the CBF (which will be denoted later as B) is limited between two values. We interpreted this as follows: the upper limit $B_{max}$ corresponds to maximal dilation of the arterioles and the lower (non-negative) limit $B_{min}$ to the maximal constriction of the vessels. Reivich has fitted his data with a logistic model curve [55], which has two asymptotes

$$B(p) = \left( 20.9 + \frac{92.8}{1 + 10570 \exp[-5.251 \ \ \log_{10}(p/1mmHg)]} \right) ml/100g/\min, \qquad (19)$$

where p= $PaCO_2$ in mmHg. Instead of the variable $B$ (the CBF) we will use the normalized to unity quantity $z$ defined as

$$z = \frac{B - B_{min}}{B_{max} - B_{min}}. \qquad (20)$$

The dependence of the CBF on $PaCO_2$ will be described with the dimensionless variable $x=\log(p/p_1)$, where $p=PaCO_2$ in mmHg and $p_1$ is a fixed value of $PaCO_2$, which may be taken to be $p_1$=1mmHg. The variable $p$ is physical only for $p≥0$, in order to avoid formulae which may be valid for $p<0$ the variable $x=\log(p/p_1)$, valid for $p≥0$ was introduced. We can incorporate the above requirements and use the following assumptions:

$$\frac{dB}{dx} = AF(z) = AF\left( \frac{B - B_{min}}{B_{max} - B_{min}} \right), \qquad F(1/2) = 1,$$

$$0 \le z \le 1, \ \ 0 \le B_{min} \le B \le B_{max}, \qquad (21)$$

where A is a constant (reactivity), and $F(z)$ is a function which depends on CBF only. We will add the following boundary conditions on $F(z)$:

$$F(0) = F(1) = F'(0) = F'(1) = 0, \qquad (22)$$

where $F'(z)=dF(z)/dz$. The condition F(0)=0 corresponds to the requirement that the constriction is maximal at $B=B_{min}$, F(1)=0 correspond to maximal dilation for $B=B_{max}$. Another physical boundary constraint can be formulated for the derivatives $F'(z)$ as follows: $F'(0)=F'(1)=0,$

which means that the approach to the limits is smooth. We will assume that the constricting and dilating forces are the same; mathematically this condition can be expressed in the following manner,

$$F(\frac{1}{2}+z)=F(\frac{1}{2}-z), \quad or \quad F(z)=F(1-z). \tag{23}$$

There are many solutions, which satisfy the requirements Eqs. (21-23). We found the following ones:

$$F(z)=4^{n}z^{n}(1-z)^{n}, \quad and \quad F(z)=\sin^{n}(\pi z), \quad n\geq 2. \tag{24}$$

We will choose

$$F(z)=\sin^{2}(\pi z), \tag{25}$$

which will also enable us to integrate analytically Eq. (21) and to obtain a rather simple result to visualize. We will be able to utilize it for rescaling rats data to rhesus monkeys data and eventually to human data. This path will also enable us to translate rats data to monkey and eventually human data. From Eq.(20):

$$dB=(B_{max}-B_{min})dz, \tag{26}$$

Eqs. (21) and (25) can be converted to

$$\frac{dz}{\sin^{2}(\pi z)}=\frac{Adx}{(B_{max}-B_{min})}. \tag{27}$$

One can easily check that

$$\int\frac{dz}{\sin^{2}(\pi z)}=-\frac{1}{\pi}ctg(\pi z)+C, \tag{28}$$

where C is an arbitrary constant. From Eq. (28) we obtain,

$$\int_{z_1}^{z_2} \frac{dz'}{\sin^2(\pi z')} = -\frac{1}{\pi} ctg(\pi z_2) + \frac{1}{\pi} ctg(\pi z_1) = \frac{1}{\pi} \frac{\sin\pi(z_2 - z_1)}{\sin\pi z_2 \sin\pi z_1}. \tag{29}$$

Integrating Eq. (27), using Eq. (28), we obtain

$$\int_{z_r}^{z} \frac{dz'}{\sin^2(\pi z')} = -\frac{1}{\pi} ctg(\pi z) + \frac{1}{\pi} ctg(\pi z_r) = \int_{x_r}^{x} \frac{A dx}{\Delta B} = \frac{A(x - x_r)}{\Delta B} \tag{30}$$

were $\Delta B = B_{max} - B_{min}$. From Eq.(30) we obtain,

$$z = \frac{1}{\pi} arcctg\left( ctg(\pi z_r) - \pi \frac{A(x - x_r)}{\Delta B} \right) \tag{31}$$

From Eq. (31) and the relation: $arcctg(\pi z) + arctg(\pi z) = \frac{\pi}{2}$, we get:

$$z = \frac{1}{2} - \frac{1}{\pi} arctg\left( ctg(\pi z_r) - \pi \frac{A(x - x_r)}{\Delta B} \right) \tag{32}$$

Eq. (32) describes the dependence of CBF (z in Eq. (32)) on $p$ in terms of 5 parameters: $z_r$, $x_r$, $A$, $B_{min}$, $B_{max}$. The number of parameters can be further reduced to four.

## 8.1. The four parameter formula

A simple way to eliminate $z_r$ from Eq. (32) is to choose $z_r = 0.5$ (the value half way between the extremes) then $ctg(\pi z_r) = 0$. Eq. (32) will have the simple form,

$$z = \frac{1}{2} + \frac{1}{\pi} arctg\left( \pi \frac{A(x - x_r)}{\Delta B} \right) \tag{33}$$

and after substituting $z = (B - B_{min}) / \Delta B$,

$$B = B_0 + \frac{\Delta B}{\pi} arctg\left( \pi \frac{A(x - x_0)}{\Delta B} \right), \tag{34}$$

and after substituting $x = \log(p/p_1)$, the four parameter formula is

$$B(p) = B_0 + \frac{\Delta B}{\pi} \, arctg\left( \pi \, \frac{A \ln(p/p_0)}{\Delta B} \right), \tag{35}$$

where,

$$B_0 = B(z_r = \tfrac{1}{2}) = \tfrac{1}{2}(B_{max} + B_{min}); \quad \left(\frac{dB}{dx}\right)_{B = B_0}$$
$$= A, \quad x_0 = x(z_r = \tfrac{1}{2}), \quad p_0 = p(z_r = \tfrac{1}{2}). \tag{36}$$

## 8.2. Experimental data with rhesus monkeys and rats

To our knowledge the experimental data of Reivich [55] are the only published data which tabulate CBF and $PaCO_2$ for individual animals. This will enable us to check our model and find individual variations. The fit results are given in table 1. and displayed in Fig. 1. It should be noted that for monkey's No. 2 and 3 the data were insufficient to determine all the parameters. In Fig. 1, the dotted lines were obtain ned using the all monkeys parameters. This model seems to describe the main features of the data.

| Monkey No. | $B_{min}$ ml/100g/min | $B_{max}$ ml/100g/min | $p_0$ mmHg | A ml/100g/min |
|:---:|:---:|:---:|:---:|:---:|
| 1 | 44.7±5.2 | 95.2±4.8 | 61.0±2.1 | 147.7±76.6 |
| 2 | | not enough data | | |
| 3 | | not enough data | | |
| 4 | 17.6±2.6 | 125.4±3.3 | 91.4±5.0 | 82.2 ±12.2 |
| 5 | 14.7±2.5 | 123.1±2.8 | 54.6±2.0 | 95.6±11.9 |
| 6 | 9.2±3.1 | 121.1±3.0 | 70.6±4.7 | 48.2±5.6 |
| 7 | 18.3±1.3 | 86.9±2.0 | 43.9±1.7 | 84.7±8.8 |
| 8 | 27.3±2.7 | 142.2±3.7 | 82.7±1.3 | 416±145 |
| all monkeys | 13.6±2.5 | 122.5±2.7 | 60.3±1.9 | 79.3±8.2 |
| rats | 89.0±10.4 | 512.4±18.1 | 38.0±1.1 | 581.7±91.0 |
| all men | 23.3±1.9 | 165.9±3.9 | 53.2±0.7 | 251.5±18.1 |

**Table 1.** The fit of Eq. (36) to experimental data of individual monkeys [55], all off the monkeys and rats [59].
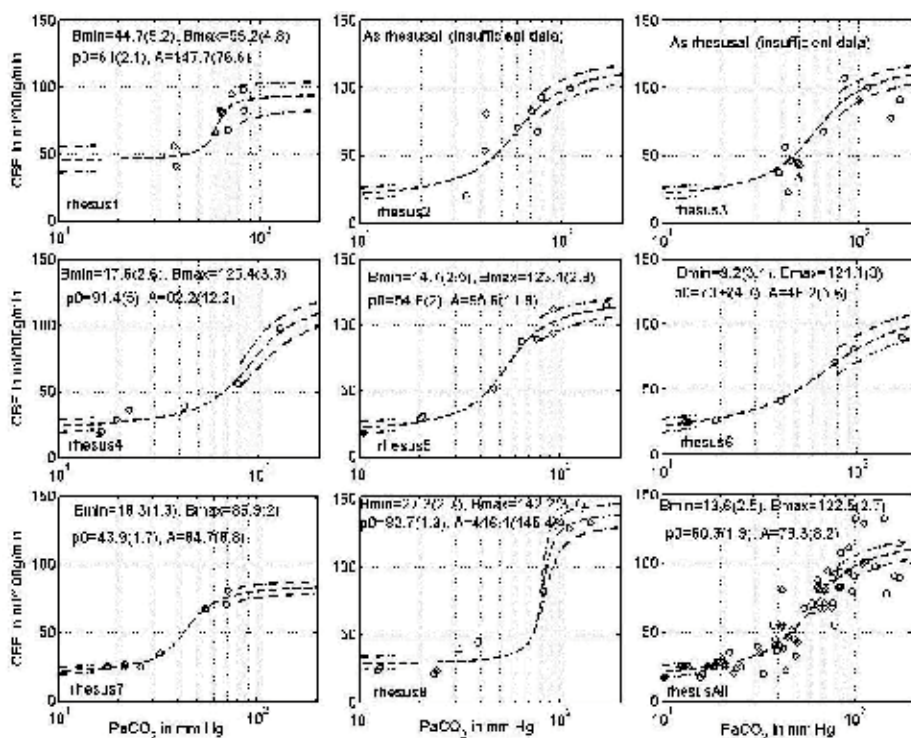
**Figure 2.** The fits to the experimental data of [55] with parameters given in Table 1. The dotted line is the rescaling of the monkeys best fit according to Eqs. (44) and (45).
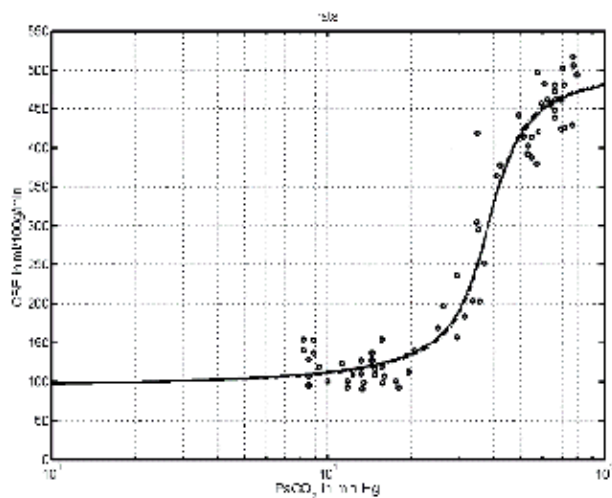


**Figure 3.** The dependence of CBF of rats on the partial tension of $CO_2$. The continuous curve is the best fit to Eq. (36) for the data of [59]. The parameters are given in Table 1.

## 9. Rescaling the data

In this section, we will transform rat data to serve as monkey data and vice versa. We will utilize Eq. (21), and use the upper index R to denote rats and upper index M to denote monkeys. Let us consider two separate fits (e.g. for all monkeys and for rats):

$$B^R(p^R) = B_0^R + \frac{\Delta B^R}{\pi} arctg\left( \pi \frac{A^R \ln(p^R / p^R{}_0)}{\Delta B^R} \right), \tag{37}$$

$$B^M(p^M) = B_0^M + \frac{\Delta B^M}{\pi} arctg\left( \pi \frac{A^M \ln(p^M / p_0^M)}{\Delta B^M} \right). \tag{38}$$

Let us assume the possibility that the curve (37) is converted to curve (38) and vice versa. We will show that it is possible to do this by rescaling the variables p (PaCO2) and B (CBF). Instead of demanding that Eq.(37) be equal to Eq. (38) we will require the equivalent conditions,

$$\pi \frac{A^R \ln(p^R / p^R{}_0)}{\Delta B^R} = \pi \frac{A^M \ln(p^M / p^M{}_0)}{\Delta B^M}, \tag{39}$$

$$\frac{B^R(p^R) - B^R{}_0}{B^M(p^M) - B^M{}_0} = \frac{\Delta B^R}{\Delta B^M}. \tag{40}$$

Equation (39) transforms the p coordinates, and Eq.(40) transforms the B variables. Thus, for example, if we would like to transfer the monkey data to rat data we will rewrite Eq. (40) and Eq. (41) as follows,

$$p^R = p_0^R \exp\left( \frac{\Delta B^R A^M \ln(p^M / p_0^M)}{\Delta B^M A^R} \right), \tag{41}$$

$$B^R(p^R) = \frac{\Delta B^R}{\Delta B^M}\left( B^M(p^M) - B_0^M \right) + B_0^R. \tag{42}$$

Eq. (41) transforms the $p^M$ coordinates (using the parameters of Table 1.) into $p^R$ coordinates and Eq.(42) transforms the CBF $B^M$ data into $B^R$ data. The transition of the rat's data to monkey's data is achieved via the equations

$$p^M = p_0^M \exp\left( \frac{\Delta B^M A^R \ln(p^R / p_0^R)}{\Delta B^R A^M} \right), \qquad (43)$$

$$B^M(p^M) = \frac{\Delta B^M}{\Delta B^R}\left( B^R(p^R) - B_0^R \right) + B_0^M. \qquad (44)$$

In Fig. 3. The data of the rhesus monkeys (circles) with the fit of all monkeys (the line as in Fig. 1.) are supplemented with the rat data (stars) according to Eqs. (43) and (44).
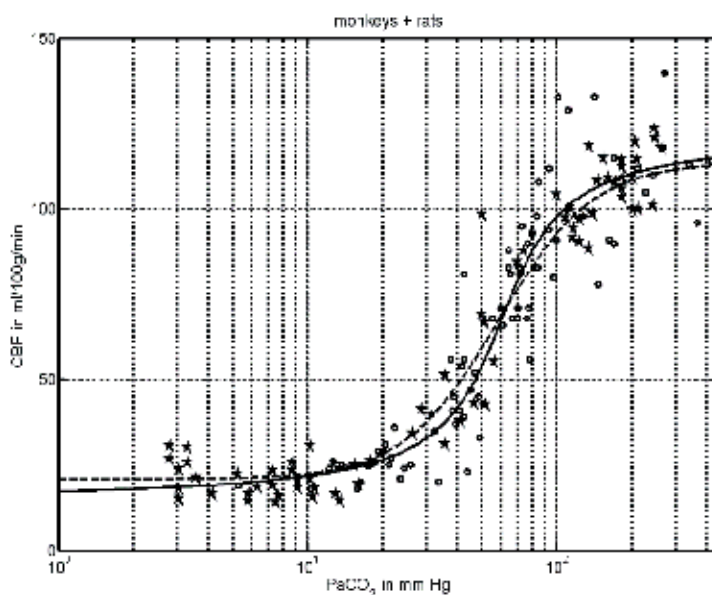


**Figure 4.** The data of the rhesus monkeys (circles) with the fit of all monkeys Eq.(46) (solid line) and Eq. (19) (dashed line) supplemented with the rat data (stars) according to Eqs. (43) and (44).

## 10. Human data

For obvious reasons there are no experimental data on individual humans available in a very wide range of $PaCO_2$. The measurements on animals usually ended with weighing their brains and calibrating the results for 100g of brain tissue. Recently restrictions were imposed on experiments in which animals are killed. In recent years, the emphasis was placed on getting regional CBF (rCBF) measurements rather than global CBF. As a result, the extended animal measurements are rather old.

Our fit to human data, based on (Reivich 1964, Ketty and Schmidt 1948 and Raichle et all 1970) is given in Fig. 4, with parameters of Table 1 (all men). In [55] it was observed that the human data (in a narrow interval of PaCO2), which existing in that time, were within the experimental errors very close to the rhesus monkey data. One can see it in Fig. 4 (circles, the data of [55]. Therefore the fit of [55], Eq. (19) of the rhesus monkey data was and is still being used as the relation between $PaCO_2$ and CBF of humans.
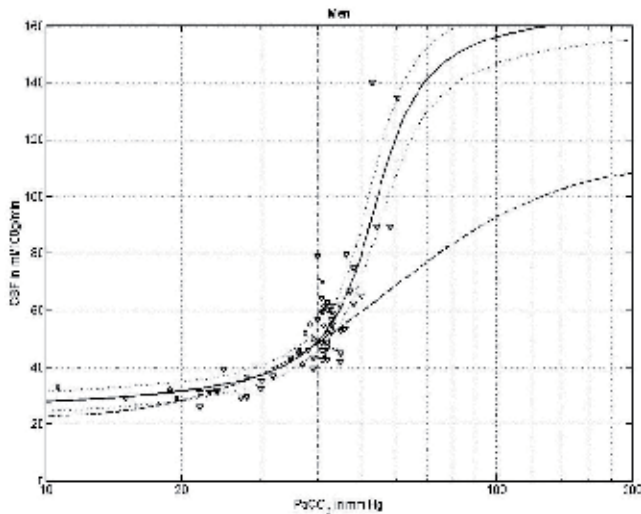


**Figure 5.** Human CBF data [55], circles), [42], triangles) and [53], hexagons). The dashed line of the fit of Eq. (19) represents the rhesus monkey data. The dotted lines deviate from the solid line, given by Eq. (46), by shifting all parameters by two error bars.
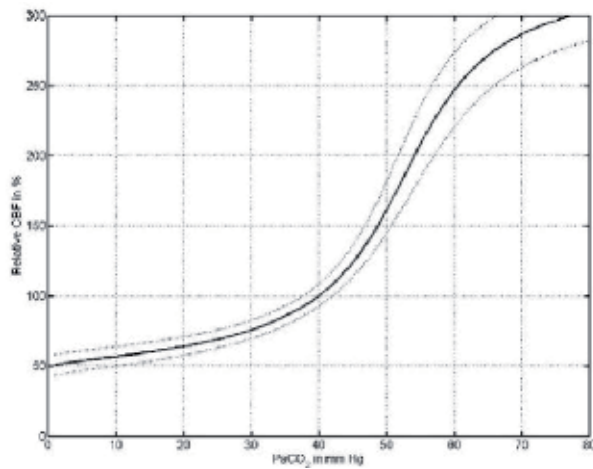


**Figure 6.** Relative changes of human CBF with respect to its values at $PaCO_2$=40 mm Hg.

Our fit to the rhesus monkey data (from Table 1.) is,

$$B(p) = 68.0 + 34.7\,arctg\left(2.29\ln(p\,/\,60.3mmHg)\right)ml\,/\,100g\,/\,\min \qquad (45)$$

The fits of Eqs. (10.1) and (10.2) are quite similar and are depicted in Fig. 3. They may serve as a first estimate of human CBF below $PaCO_2$=45 mm Hg. Eq. (10.1) represents the human data in some medical textbooks and publications without mentioning that it is a fit of Rhesus monkeys (for example: [25]. Our fit to human data

$$B(p) = 94.6 + 45.4\;arctg\left(5.54\ln(p\,/\,53.2mmHg)\right)ml\,/\,100g\,/\,\min \qquad (46)$$

deviates from that of the Rhesus monkeys in the hypercapnia region ($PaCO_2$ above 45 mm Hg). More accurate human data in this region are needed to confirm our fit. Changes in $PaCO_2$ induce dramatic changes in CBF. This can be seen in Fig. 5, where relative changes of CBF are given. One can see that changing $PaCO_2$ from normal (40 mm Hg) by 10 mm Hg can change CBF by about 25%-55%.

## 11. Experimental detection of oxygen waveforms

In (Gersten et al., 2009) we have presented simultaneous measurements of EtCO2 (by capnometer, closely related to PaCO2) and rSO2 (with the INVOS Oximeter of Somanetics model 5100B) during intensive breathing exercises.

The fastest recording rate of the 5100B oximeter was 12. This time is much longer than the average period, of about 4 seconds, of normal respiration. In order to detect oxygenation periodicity we had to study respiration periods of about 36 seconds or larger (i.e. 3 data points or more for each breathing period). This is still a rather small amount of data points per respiration period. We have compensated for this small number by using a cubic spline interpolation of the data points, adding new interpolation points through this method. The cubic spline interpolation is a very effective method of smooth interpolation. We found six people well acquainted with yoga pranayama, who could easily perform breathing exercises with periods around 36 seconds. All of them performed the following routine which lasted for 15 minutes. They were asked to breathe in the following way: to inhale for 4 units of time (UOT), to hold the breath for 16 UOT and to exhale for 8 UOT, this we denote as the 4:16:8 (pranayama) routine. The unit of time (UOT) is about 1 second. The yoga practitioners develop an internal feeling of UOT which they employ in their practices. They learn to feel their pulse or they learn to count in a constant pace. Often they practice with eyes closed. In order not to distract or induce additional stress we preferred not to supply an external uniform UOT. The primary concern for this research was to have a constant periodicity and in this case the

practitioners have succeeded to maintain it. The data were analyzed with spectral analysis which took into account non-stationary developments, which were subtracted from $rSO_2$ and BVI data. Sharp picks corresponding to the breathing periodicity were found in the spectral analysis of $EtCO_2$ (the amount of $CO_2$ during expiration), the overlapping of the periodicities is shown in Fig. 7 (subfigures 2a, 2b, 2c, 2d, 2e, 2f) and Table 2.



(a)

(b)

(c)

(d)

(e)

(f)
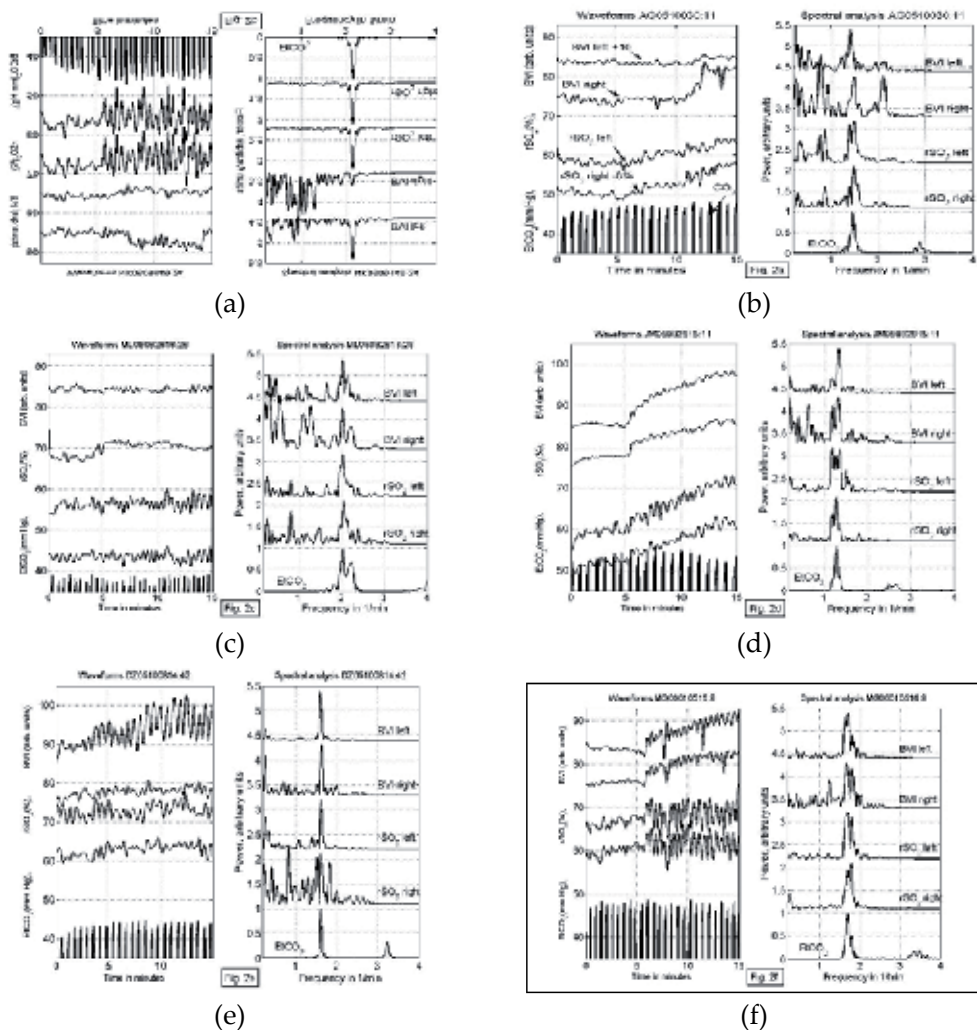
**Figure 7.** subfigures 2a-2f). On the perpendicular axis are the readings of the capnometer, $rSO_2$ right sensor (subtracted with 8%), $rSO_2$ left sensor, BVI right sensor, BVI left sensor (increased by 10). On the right hand side the corresponding spectral analyses of the waveforms are given, from [22].

|     | PaCO$_2$ | rSO$_2$ right | rSO$_2$ left | BVI right | BVI left |
|-----|----------|---------------|--------------|-----------|----------|
| **AG** | 1.47 (1.42-1.51) | 1.49 (1.45-1.53) | 1.48 (1.45-1.54) | 1.49 (1.42-1.53) | 1.42 (1.38-1.47) |
| **NK** | 2.15 (2.12-2.18) | 2.14 (2.12-2.17) | 2.14 (2.12-2.17) | ------------------ | 2.14 (2.11-2.17) |
| **ML** | 2.03 (1.98-2.07) | 2.05 (2.01-2.15) | 2.03 (1.95-2.08) | 2.03 (1.99-2.07) | 2.03 (2.00-2.06) |
| **JM** | 1.30 (1.26-1.34) | 1.30 (1.26-1.33) | 1.30 (1.17-1.40) | 1.33 (1.29-1.37) | 1.35 (1.31-1.38) |
| **DZ** | 1.62 (1.59-1.65) | 1.62 (1.59-1.67) | 1.62 (1.60-1.65) | 1.63 (1.61-1.67) | 1.61 (1.57-1.65) |
| **DG** | 1.70 (1.65-1.73) | 1.79 (1.65-1.82) | 1.70 (1.62-1.82) | 1.66 (1.62-1.89) | 1.71 (1.61-1.74) |

**Table 2.** The position of the dominant frequencies (in units of 1/minute) of Fig. 7 in the spectral analysis, in parenthesis the extension of the half width is given, from [22]

## 12. Simple exercises

Significant increase of PaCO$_2$ (and of total CBF) can be achieved with untrained people using very simple breathing procedures. The reason for that is the dependence of PaCO$_2$ on ventilation [68],

$$PaCO_2 = K \, (\dot{V}_{CO_2} / \dot{V}_A), K = 863 \text{ mm Hg,} \tag{47}$$

where $\dot{V}_{CO_2}$ is the metabolic CO$_2$ production and $\dot{V}_A$ is the alveolar ventilation.

In [22] we have described the influence on the brain oxygenation of simple exercises performed by 18 students for the first time. The exercises, each lasting for 5 minutes, were:

1. Simple breathing exercises. It was possible to increase the PaCO$_2$ by either breathing slowly or by holding the breath.

2. Simple arithmetic counting, concentrating on a mental problem changes brain's oxygenation locally [5].

3. Biofeedback, as observed by Hershel [66]

In [23] we calibrated the HEG readings using the rSO$_2$ readings of the INVOS oximeter of Somanetics. We found,

$$x_1/x_2 = ln(y_1/32.08) / ln(y_2/32.08), x \equiv rSO_2, y \equiv \text{HEG readings.} \tag{48}$$

Simultaneous measurements were taken using HEG and a capnometer. Eighteen students participated in the experiment in which HEG and $CO_2$ data were recorded for 5 intervals of baseline, simple breathing exercises, simple arithmetic tasks and biofeedback. The results show that almost all participants could increase their brain oxygenation or CBF, but in each case it was strongly dependent on one of the three methods used. We can conclude that it is possible to substantially increase local oxygenation or global CBF using one of the three methods described above, but the preferred method is highly individual. The protocol of this research was approved by the IRB of Hunter College of the City University of New York.

The participants were 18 participants from the introductory course to psychology (PSY 100) in Hunter College of the City University of New York. All participants had to sign an informed consent. At least two experimenters were present during each experiment. The confidentiality of the participants was protected. Illustrative examples from [22] are given below.
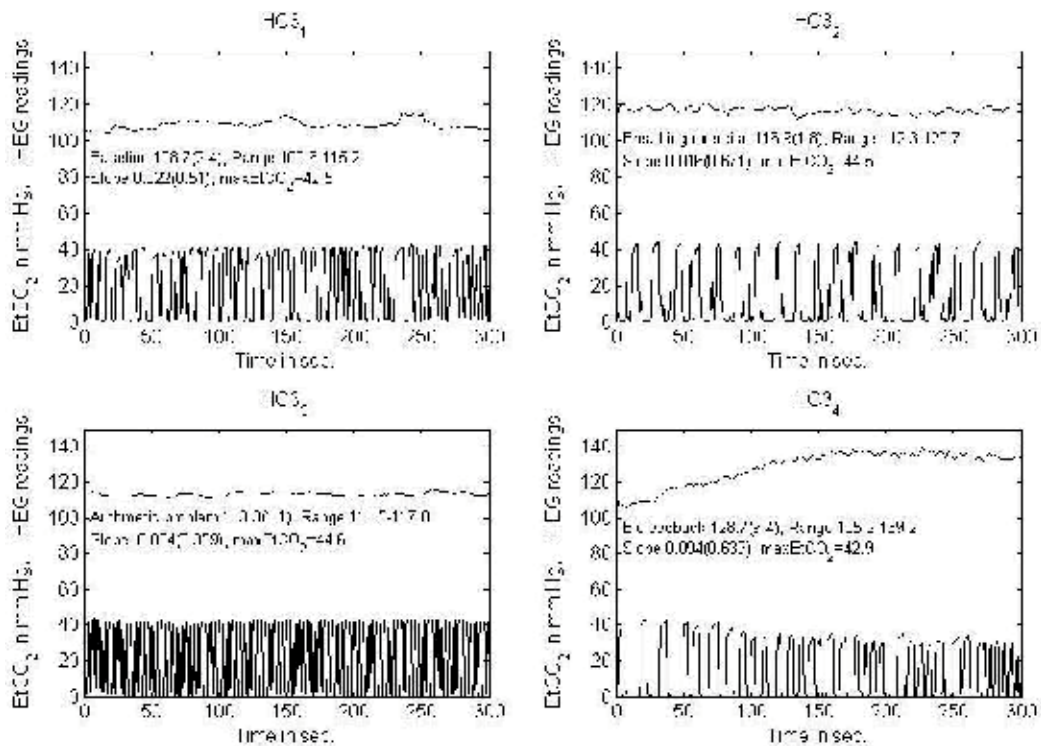


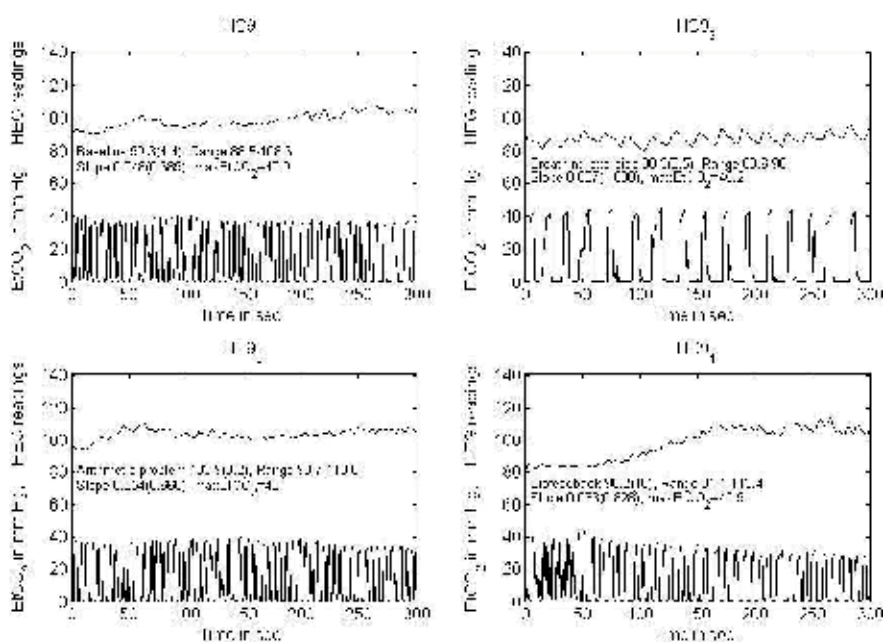**Figure 8.** The HEG and the capnometer readings of participant No. 3. SD in parenthesis [22].

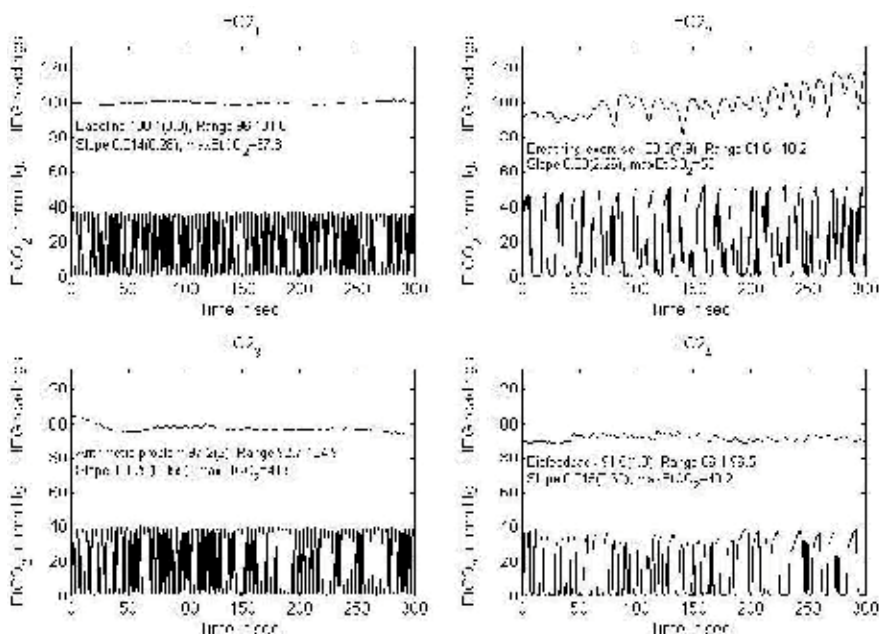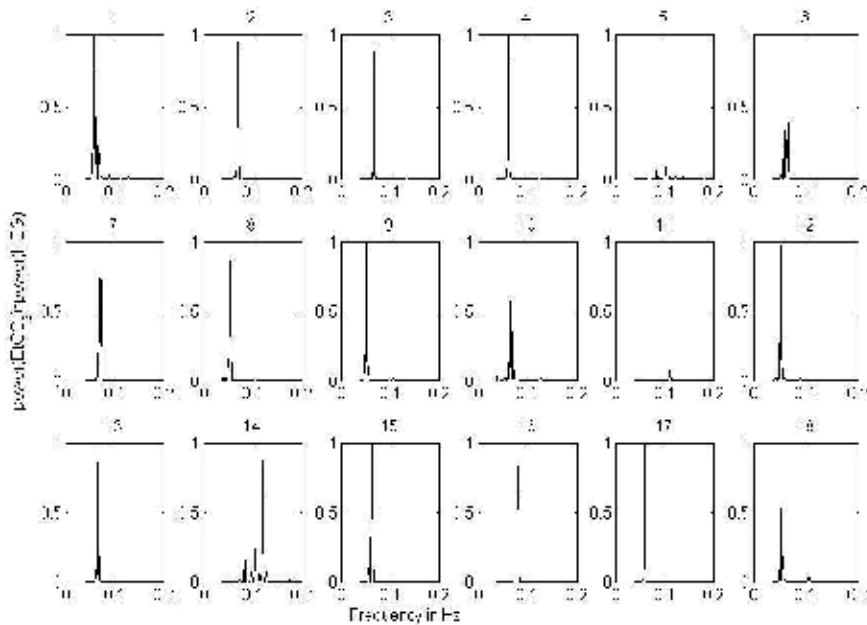**Figure 9.** The HEG and the capnometer readings of participant No. 9. SD in parenthesis [22].



**Figure 10.** The HEG and the capnometer readings of participant No. 2. SD in parenthesis [22].

In most cases the HEG and the $CO_2$ waveforms had the same periodicity, which is well depicted in Fig. 11.



**Figure 11.** The correlation between the power spectra of the $EtCO_2$ periodic pattern and the corresponding HEG periodic pattern is depicted by their multiplication. The power spectra are normalized to unity. Maximal correlation is achieved when the multiplication is equal to one [22].

Below, in Table 3, one can observe the remarkable increase of PaCO2 with very simple breathing exercises. One should remember that this was a first attempt, without previous training.

| N | Baseline | Breath. Ex. | Arith. Prob. | Biofeedback | % increase |
|---|---|---|---|---|---|
| 1 | 37.5 | 46.9 | 39.4 | 34.5 | 25.2 |
| 2 | 36.6 | 44.9 | 39.2 | 34.4 | 22.8 |
| 3 | 40.1 | 40.7 | 42.1 | 34.0 | 1.5 |
| 4 | 35.4 | 38.4 | 38.0 | 32.0 | 8.3 |
| 5 | 37.5 | 36.7 | 38.5 | 39.1 | -2.0 |
| 6 | 36.9 | 39.6 | 35.6 | 36.3 | 7.4 |
| 7 | 31.4 | 39.8 | 38.3 | 38.3 | 27.0 |
| 8 | 37.5 | 46.2 | 40.2 | 38.5 | 23.2 |
| 9 | 37.5 | 41.9 | 35.5 | 34.6 | 11.7 |

| N | Baseline | Breath. Ex. | Arith. Prob. | Biofeedback | % increase |
|---|---|---|---|---|---|
| 10 | 33.3 | 38.8 | 36.4 | 36.4 | 16.5 |
| 11 | 37.1 | 39.6 | 37.5 | 38.6 | 6.5 |
| 12 | 40.0 | 43.7 | 40.3 | 40.6 | 9.1 |
| 13 | 38.2 | 45.9 | 39.3 | 38.7 | 20.1 |
| 14 | 33.3 | 34.1 | 35.9 | 36.3 | 2.4 |
| 15 | 38.2 | 45.7 | 42.3 | 40.6 | 19.8 |
| 16 | 28.6 | 33.9 | 28.9 | 28.8 | 18.4 |
| 17 | 40.3 | 43.3 | 41.2 | 39.0 | 7.6 |
| 18 | 35.4 | 42.6 | 40.6 | 37.9 | 20.3 |
| mean(SD) | 36 (3) | 41.3(4.0) | 38.3(3.2) | 36.6(3.1) | 13.7(8.8) |

**Table 3.** Mean values of $EtCO_2$ in mm Hg. Last column is the increase in % due to breathing exercises compared to baseline.

## 13. Autoregulation

The autoregulation of cerebral blood flow (CBF), or the independence of CBF on changes of mean arterial blood pressure (MABP) in a wide range of MABP (the so called "plateau"), is considered to be a well established fact. But looking carefully at the existing experimental data we could not find even one publication which gives a proper experimental support for the existence of the plateau of the autoregulation.

The first publication, seemingly proving autoregulation in humans, was that of [48]. However, the data at different points on the plateau were taken from different people [48], Reivich 1969). As individual differences are quite important, the above procedure is not accurate and may serve as an indication only. [30] has done experiments with 12 dogs, measuring CBF for a wide range of MABP. However, he presented and discussed results taken together on 8 normocapnic animals and 4 hypercapnic ones. Fortunately, he tabulated the experimental data for each dog separately. Harper's data are the only published data, which describe for each animal separately the dependence of the CBF on MABP in a wide range of MABP. We shall use extensively Harper's data and analyze their content.

[49] have done measurements of CBF on baboons for a wide range of MABP. Unfortunately the data were analyzed collectively i.e. on several baboons simultaneously. Individual baboons were not tabulated. Averaged data are supporting autoregulation. As one can see from this introduction, there is no firm experimental basis for autoregulation. In the following sections, we shall propose simple models that go beyond autoregulation but contain its main elements. For more recent reviews of the experimental and theoretical situation, the reader is encouraged to consult the reviews of [3, 24, 62, 67] and the references therein. The book of [26] has complementary material and references.

### 13.1. A generalization of the simple model of autoregulation

The oversimplified classical picture of autoregulation is depicted in Fig. 12. In this picture for MABP's in the range of 60-130 mm Hg there is no change in the CBF. This range may change somewhat for the cases of hypertension and hypotension. The plateau is shifted to the right in the case of hypertension, and to the left in the case of hypotension. Let us explain the picture in Fig. 12 in terms of a simple control feedback model. Without any feedback the CBF is expected to be proportional to the MABP

$$CBF(MABP) = S \cdot MABP, \tag{49}$$

where S is a constant describing the sloap of the to the flow in units of ml/min/100g/mmHg. In order to get the plateau the line of Eq.(13.1), the CBF should be diminished from the values of Eq.1 by a contribution, which is different for various MABP's. In a feedback control model this subtracted quantity is -F(MABP) CBF, where F(MABP) is a feedback (gain) function depending on MABP. Eq.(13.) should be now replaced with

$$CBF(MABP) = S \cdot MABP - F(MABP) \cdot CBF(MABP). \tag{50}$$
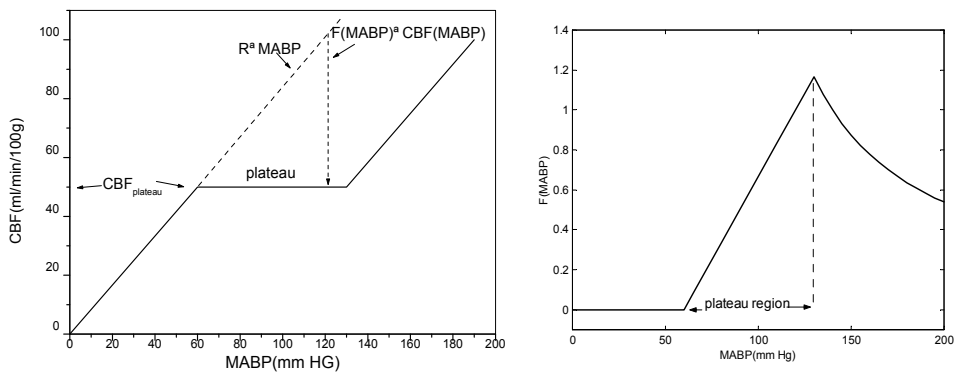


**Figure 12.** The classical picture of autoregulation. For MABP's in the range of 60-130 mm Hg there is no change in the CBF. The feedback function F of Eq.(53) as a function of MABP. In the plateau region it is linear.

By bringing the second l.h.s. term of Eq.(50) to the left we obtain

CBF(MABP) + F(MABP) · CBF(MABP)= (1+ F(MABP)) · CBF(MABP)= S · MABP

and after dividing both sides by 1+ F(MABP) we finally obtain

$$CBF(MABP) = \frac{S \cdot MABP}{1 + F(MABP)}. \tag{51}$$

Eq.(47) can also be written in the following form

$$F(MABP) = \frac{S \cdot MABP}{CBF(MABP)} - 1. \tag{52}$$

In many instances the constant S may be determined relatively well from experiments in which CBF is measured at different MABP's. In these cases Eq.(52) is very advantageous, as it allows to determine F(MABP) directly from the experiments. We shall extensively employ this procedure analyzing [30] experiments.

In order to get the continuous line and the plateau of Fig.12, the feedback function F(MABP) has to have the following form

$$F(MABP) = \begin{cases} 0, & for \quad 0 \leq MABP \leq 60 mmHg \\ \dfrac{R \cdot MABP}{CBF_{plateau}} - 1, & for \quad 60 mmHg \leq MABP \leq 130 mmHg, \\ \dfrac{MABP}{MABP - 70 mmHg} - 1, & for \quad MABP \geq 130 mmHg \end{cases} \tag{53}$$

where $CBF_{plateau}$ is the value of CBF on the plateau (here 50 ml/min/100g, as an example). It should be stated that the behavior of the CBF above 130 mm Hg is only a guess and is uncertain. We see a sharp raising of the CBF in the data of [49], but we do not se this raising in the data of Harper. For reasons of symmetry we have assumed the same slope above MABP of 130 mm Hg as below 60 mmHg. That is the reason why we have pointed out in Fig.12 that the models above MABP equal to 130 mm Hg are uncertain. The dependence of F, as given by Eq.(53) on MABP is depicted in Fig.12. One should note that in the plateau region the dependence on MABP is linear and thus very simple. We shall generalize this model by allowing linear dependence of F on MABP, but with different strengths. Above MABP of 130 mm Hg one may see in Fig.12 the breakdown of the linearly growing biofeedback contribution, but one should remember that our knowledge of what is going on in this region is quite uncertain.

The autoregulation as being depicted in Fig.12 is an over idealized picture. We know that very strong deviations from this picture exists in the case of hypercapnia, for which there is almost no feedback suppression as well as autoregulation. We shall consider such effects by changing the feedback of Eq. (50) by

$$CBF(MABP) = R \cdot MABP - c \cdot F(MABP) \cdot CBF(MABP), \tag{54}$$

i.e. we have changed the overall strength of the feedback by multiplying the feedback function by a constant which we denote as c. Eq.(53) is obtained with c=1, i.e. there is no change. In Fig.

13 we consider the three cases: c=1, c=0.1, 1.3. The c=0.1 case represents a strong suppression of the feedback, as we shall see later on this is typical for hypercapnia.

The case of c=1.3 represents an increase in feedback. As a consequence the CBF is supressed and is decreasing in the plateau region with the increase of MABP. We shall find such a behavior in some of the dogs of [30]. To our best knowledge this a new effect not described in the literature. We suspect, extrapolating from hypercapnia (for which c<<1), through normo-capnia (for which autoregulation is assumed, i.e. c~1) to hypocapnia, that in the last case c>1.
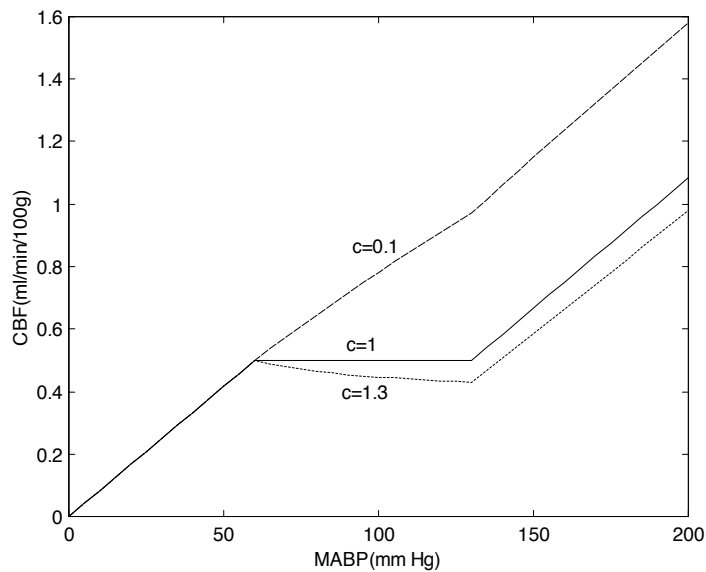


**Figure 13.** The change in CBF as a result of the change in the feedback strength. The constant c is a multiplication factor which multiplies the feedback function F(MABP).

### 13.2. Harper's experiments with dogs

[30] performed an experiment with 12 dogs in which he measured CBF while changing MABP in a wide range. His paper contains tables of the experimental data for each dog separately. To our best knowledge, these are the only published data of individual animals for which CBF was measured in a wide range of MABP. As we shall see later on, the parameters describing CBF in terms of MABP differ to great extent between the animals. Therefore, by trying to make a better statistics incorrect conclusions may be derived. For example, Harper in his paper claims: "Over a fairly wide range of blood pressure (from 90 to 180 mm Hg) the blood flow remained relatively constant, despite a varying blood pressure. This phenomenon will hereafter be referred to as 'autoregulation'." For some averaging procedures, this may look so, but as we shall analyze each dog separately, we shall notice rather large deviations. In our analysis we shall use the simple model of autoregulation Eq.(53) modified by Eq.(54). In the

data of the dogs, we do not see the sharp raise of CBF at larger MABP's; therefore we shall use the following model of the feedback function

$$F(MABP) = \begin{cases} 0, & for \quad 0 \leq MABP \leq MABP_1 \\ c \cdot \left( \dfrac{R \cdot MABP}{CBF(MABP_1)} - 1 \right), & for \quad MABP_1 \leq MABP, \end{cases} \tag{55}$$

where the constant c was introduced to indicate the change with respect to the ideal autoregulation, i.e. the case where the CBF do not change with MABP in the plateau region. For ideal autoregulation c=1. The above model of the feedback assumes that the feedback function remains linear; the difference with the ideal autoregulation is only in the strength of the feedback.

The model has three parameters R, $MABP_1$, c. One of them is the threshold arterial mean blood pressure $MABP_1$ below which there is no feedback. Below $MABP_1$ the CBF depends only on the slope parameter R, CBF=R MABP. At the transition point $MABP_1$

$$CBF(MABP_1) = R \cdot MABP_1. \tag{56}$$

Substituting Eq.(56) into Eq.(55) we obtain

$$F(MABP) = \begin{cases} 0, & for \quad 0 \leq MABP \leq MABP_1 \\ c \cdot \left( \dfrac{MABP}{MABP_1} - 1 \right) & for \quad MABP \geq MABP_1 \end{cases}' \tag{57}$$

while CBF is obtained through Eq.(54).

The parameters were determined in the following way. First the parameter R was determined from the line starting from zero and tangential to the experimental points (not intersecting the lines connecting experimental points). Next, using Eq.(52) the experimental values of F(MABP) were determined from the value of R and experimental values of CBF(MABP). The feedback function was obtained by fiting the experimental data with Eq.(57), a linear fit. The parameters so determined for all the 12 dogs separatly are given in table 1. To the table were also added the avarage values of $PaCO_2$ for each dog. For dogs B9-B12, which were in hypercapnia, there was practically no autoregulation, and the CBF data could be fitted with strait lines.

One should note that in Table 4 the values of the parameter c are far away from the value c=1, which correspond to the ideal autoregulation. One should also note the two cases (Dogs B6 and B7) for which c>1, which differ from previous cases in that their CBF may go down with increasing MABP

Table 4.The parameters of fitting the CBF equations.

Above, we have analyzed the data obtained by [30] in 12 Dogs, in which CBF was measured over a wide range of MABP. This is, to our knowledge, the only publication in which the data for each individual animal were tabulated. Contrary to the belief that these data support the picture of classical autoregulation, i.e. that CBF is almost constant in the plateau region, we found a somewhat different picture. The analysis of the data for each animal separately indicates that large deviations from the classical autoregulation may exist. We were able to interpret these data by a simple model that is based on the following assumptions: 1) up to a threshold level of MABP, denoted as *MABP1*, CBF is directly proportional to MABP (as in a rigid pipe). Above *MABP1* up to a level of MABP2, at which breakthrough occurs, there is a regulated suppression of CBF which can be explained by a negative feedback on CBF. This feedback is well described by a linear function of MABP (see Eq.(57) with a slope proportional to the parameter $\beta$ which may vary considerably among different individuals. The classical autoregulation model with a plateau between *MABP1* and *MABP2* is a particular case of this model with $\beta=1$. This model describes quite well the results obtained in dogs (Harper 1966) for which, as seen in Fig. 14, the individual feedback slope parameter varied to great extent, indicating the importance of using data obtained in individuals rather than the averaged data obtained for different individuals. Blood pressure medications are prescribed with the assumption of ideal autoregulation. Many side effects of these medications may result from disturbing the CBF.
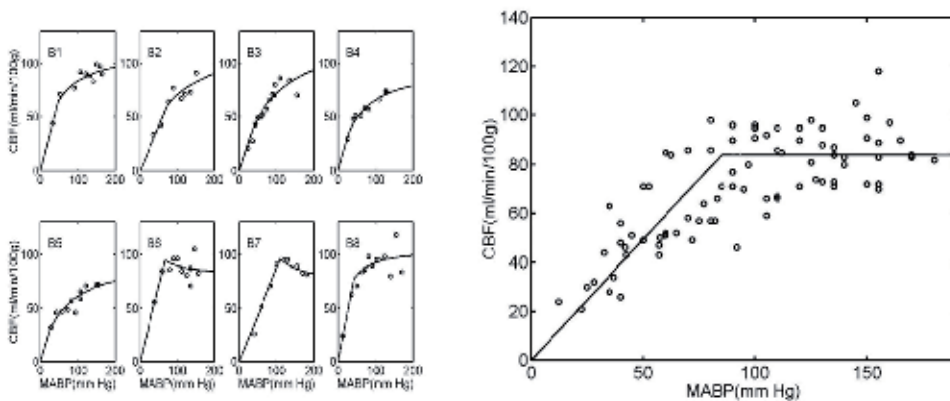


**Figure 14.** On the left individual expose a large deviation from ideal autoregulation. On the right all data do not exclude an ideal autoregulation.

## 14. Conclusions

Probing brain oxygenation is an important subject in medicine, physiology, psychology and education. Although the near infrared spectroscopy (NIRS) is not as powerful as MRI or fMRI, it is more available, less expensive, easier to handle, non-invasive and can be done in quite

different circumstances, like in different positions or motion. In our experiments, we have used INVOS Cerebral Oximeter (ICO) and the spectrophotometer HEG described in Secs 4 and 5.

Breathing affects to great extent the brain physiology. Arterial partial pressure of carbon dioxide ($PaCO_2$) is among the major factors controlling the cerebral blood flow (CBF). The results can change dramatically even within a range of 50% from normal. The effect of $PaCO_2$ is peculiar in being almost independent of autoregulatory CBF mechanisms and allows exploring the full range of the CBF. In Sec. 8 a simple model and a simple formula (Eq. (35)), describing the dependence of the CBF on $PaCO_2$ was derived. Our model gives good quantitative predictions. Moreover, it allows imitating human data using animal data. With the results of our model, it is possible to devise breathing exercises and procedures which aim is to improve brains blood circulation.

The correlation between the $CO_2$ levels and the regional oxygen saturation ($rSO_2$) were studied in an experiment using very slow breathing patterns with the INVOS Cerebral Oximeter (ICO), with an important result of a definite periodic correlation between respiration, oxygenation and blood volume changes. The results shown in Sec. 11 are quite impressive. The deficiency of using the ICO was its very low sampling rate $1/12$ Hz. For experimentation, we had to use subjects proficient in Yoga breathing.

The HEG had the advantage of a higher sampling rate of 1 Hz. With the HEG we could conduct experiments with untrained normal subjects. Our experiments with 18 student subjects is described in Sec. 12. Our three methods used in simple exercises can be used on the general population, are non-invasive, without the use of pharmaceuticals and have no side effects. They differ from each other in that the breathing affects mostly the global blood flow, arithmetic problem solving and biofeedback affects the regional blood flow (in our case the Fp1 region). Both our theoretical and experimental work differs from other studies due the specific instrumentation and our experimental procedure. Most of the results came close to our expectation.

We concluded that breathing can be used effectively to control CBF by the ventilatory control of end tidal $CO_2$. This research may have implications for complementary diagnosis and treatment of conditions involving regional cerebral metabolism such as cerebral vascular ischemia, seizures disorders, stroke, Alzheimer's disease, and more. Following that thought could lead us to improved cognitive function through a higher supply of oxygen to specific regions of the brain. We foresee future more detailed investigations to be made in the area of the effect of $CO_2$ on specific regions of the brain. This would be of great interest because a higher $CO_2$ supply results in a higher blood flow and thus to more oxygen and better overall brain function, specifically cognitive function.

As far as autoregulation is concerned, the individual data show a large deviation from the plateau model of autoregulation. Based on individual differences, a statistics based model may lead to incorrect administration of medications, which may influence strongly the cerebral blood flow and probably the blood flow to other organs. This may be the primary reason for side effects. Here experimentation with NIRS oximeters can be of great help for understanding how to treat individuals.

## Author details

Alexander Gersten[*]

Department of Physics, Ben-Gurion University of the Negev, Beer-Sheva, Israel

## References

[1] Alfano RR, Demos SG, Gayen SK.(1997). Advances in optical imaging of biomedical media. *Ann N Y Accad. Sci.* vol. 820, pp. 248-70

[2] Angerson WJ, Sheldon CD, Barbenel JC, Fisher AC and Gaylor JDS (Eds.) (1989). *Blood Flow in the Brain*, Clarendon Press, Oxford.

[3] Aslid, R., K. F. Lindegard, W. Sorteberg and H. Nornes. (1989) Cerebral Autoregulation Dynamics in Humans. Stroke, 45-52, 20, and references therein.

[4] Bernard T (1960) *Hatha Yoga*, Arrow Books, London.

[5] Chance B., Zhuang Z., UnAh Chu, Alter C., and Lipton L. (1993), "Cognition activated low frequency modulation of light absorption in human brain," *Proc. Natl. Acad. Sci. USA*, Vol.90, pp.3770-3774.

[6] Chance B. (1998). Near infrared images using continuous, phase-modulated, and pulsed light with quantitation of blood and blood oxygenation. *Ann N Y Accad Sci*; 838: 29-45

[7] Cope M. (1991). The application of near infrared spectroscopy to noninvasive monitoring of cerebral oxygenation in the newborn infant. *Ph.D. thesis,* University College, London

[8] Costa DC and Ell PJ (1991) *Brain Blood Flow in Neurology and Psychiatry*, Churchill Livingstone, Edinburgh.

[9] Delpy DT, Cope M. (1997). Quantification in tissue near-infrared spectroscopy. *Philosophical Transactions of the Royal Society of London, Series B- Biological Sciences.* 352(1354): 649-659

[10] Duckrow RB (1995) Decreased cerebral blood flow during acute hyperglycemia. *Brain Res.* 703(1-2): 145-150

[11] Derdeyn C.P. et al. (2002). Variability of cerebral blood volume and oxygen extraction: stages of haemodynamic impairment revisited. *Brain*, Vol. 125, pp. 595-607

[12] Elwell C.E. et al. (1996),"Influence of Respiration and Changes in Expiratory Pressure on Cerebral Haemoglobin Concentration Measured by Near Infrared Spectroscopy. *J. Cereb. Blood Flow Metab.* Vol. 16, pp. 353-357

[13]   Evans-Wentz WY (1958) *Tibetan Yoga and Secret Doctrines*, Oxford University, London

[14]   Feihl F. and Perret C. (1994). Permissive Hypercapnia, How Permissive Should We Be?, *American Journal of Respiratory and Critical Care Medicine Vol.* 150, pp. 1722-1737.

[15]   Ferrari M, Mottola L, Quaresima V. (2004). Principles, Techniques, and Limitations of Near Infrared Spectroscopy. *Can J Appl Physiol*; Vol. 29(4), pp. 463-487

[16]   Fox SI (1999), *Human Anatomy*, McGraw-Hill, Boston

[17]   Frackowiak RSJ, Lenzi GL, Jones T, Heather JD. (1980). Quantitative measurement of regional cerebral blood flow and oxygen metabolism in man using 15O and positron emission tomography: theory, procedure, and normal values. *J Comput Assist Tomogr*, Vol. 4, pp. 727-736

[18]   Fried R (1987), *The Hyperventilation Syndrome*, Johns Hopkins Univ. Press; Baltimore

[19]   Fried R., (1990) *The Breath Connection,* Plenum Press, New York.

[20]   Fried, R. and Grimaldi, J. (1993) *The Psychology and Physiology of Breathing,* Plenum, New York,

[21]   Fujishima, M, Scheinberg, P, Busto, R & Reinmuth, 0M (1971). The relation between cerebral oxygen consumption and cerebral vascular reactivity to carbon dioxide.*Stroke 2,* 251-257.

[22]   Gersten A., et al., (2012)"Probing brain oxygenation waveforms with near infrared spectroscopy (NIRS)", *Infrared Spectroscopy – Life and Biomedical Sciences*, Theophile Theophanides, Editor, Intech, Chapter 8 and references therein.

[23]   Gersten A et al. (2009), Probing brain oxygenation with near infrared spectroscopy, *NeuroQuantology*, Vol 7, Issue 2, pp. 258-266.

[24]   Gotoh, F. and K. Tanaka. Regulation of cerebral blood flow. Chapter 3 of Handbook of Clinical Neurology. Vol. 53, 1988, Adams,R. D. et al.(Eds.), Elsevier, Amsterdam 1988 and references therein.

[25]   Guyton AC (1991) *Textbook of Medical Physiology,* W.B. Saunders, New York 1991

[26]   Hademenos, J. H. and T. F. Massoud. The Physics of Cerebrovascular Diseases. Springer, New York 1998.

[27]   Hagstadius S and Risberg J (1983) The effects of normal aging on the rCBF during resting and functional activation. *RCBF Bulletin*, 6, 116-120,

[28]   Hale T. (1999) *Breathing free,* Hodder & Stoughton, London

[29]   Harper A.M. (1989). Measurement of Cerebral Blood Flow – Basic Physiological Principles. In (Angerson et al., 1988) pp. 1-10.

[30] Harper A.M. (1966), Autoregulation of cerebral blood flow: influence of the arterial blood pressure on the blood flow through the cerebral cortex. J. Neurol. Neurosurg. Psychiat., 398-403, 29 1966.

[31] Harper AM, Deshmukh VD, Rowan J0, Jennett WB. (1972). The influence of sympathetic nervous activity on cerebral blood flow. *Arch. Neurol., 27*:1-6.

[32] Harper AM, Glass HI (1965) Effect of alterations in the arterial carbon dioxide tension on the blood flow through the cerebral cortex at normal and low arterial blood pressures. *Journal of Neurology, Neurosurgery and Psychiatry, 28*: 449-452.

[33] Harper AM and McCulloch J (1985) Cerebral blood flow and cerebrovascular disease, in Swash M and Kennard C (Eds.): *Scientific Basis of Clinical Neurology*, Churchill Living-stone, Edinburgh, pp. 518-32.

[34] Herlhoz K et al. (1987) Regional cerebral blood flow in man at rest and during exercise. J. Neurol. 234:9.

[35] Hobbie RK (1988) *Intermediate Physics for Medicine and Biology*, 2d ed., Wiley, New York NY

[36] Horinaka N et al. (1997) Examination of potential mechanisms in the enhancement of cerebral blood flow by hypoglycemia and pharmacological doses of deoxyglucose. *J. Cereb. Blood Flow Metab.* 17(1): 54-63.

[37] Hoshi Y. (2003). Functional near-infrared optical imaging: utility and limitations in human brain mapping. *Psychophysiology*, Vol. 40, pp. 511-520

[38] Imray C.H.E.et al. (2000), "Cerebral Oxygenation at high altitude and the response to carbon dioxide, hyperventilation and oxygen", *Clinical Science* 98, 159-164

[39] Iyengar BKS (1981) *Light on Pranayama,* Allen & Unwin, London.

[40] Joshi KS (1983) *Yogic Pranayama*, Orient, New Delhi.

[41] Kety, SS, & Schmidt, CF (1946). The effects of active and passive hyperventilation on cerebral blood flow, cerebral oxygen consumption, cardiac output, and blood pressure of normal young men. *Journal of Clinical Investigation, 15*, 107-119.

[42] Kety S.S., & Schmidt C.F. (1948). Effects of arterial tensions of carbon dioxide and oxygen on cerebral blood flow and cerebral oxygen consumption of normal young men. *Journal of Clinical Investigation, Vol. 27*, pp. 484-492.

[43] Kissack, C.M., Garr1, R.R., Wardle, S.P., Weindling, A.M. (2005). Cerebral fractional oxygen extraction is inversely correlated with oxygen delivery in the sick, newborn, preterm infant. *J Cereb Blood Flow & Metab*, Vol. 25. pp. 545–553

[44] Knezevic S, Maximilian VA, Mubrin Z, Prohovnik I, Wade J (Eds.) (1988) *Handbook of Regional Cerebral Blood Flow,* Lawrence Erlbaum Associates, London.

[45]  Kuvalayananda, Swami (1933) Oxygen absorption and carbon dioxide elimination in Pranayama *Yoga Mimamsa*, 4, 267-289.

[46]  Kuvalayannda, Swami (1983) *Pranayama*, Kaivalyadama, Lonavla, India.

[47]  Lammertsma, A.A. et al. (1990). Cerebral Blood flow, blood volume and oxygen utilization: Normal values and the effect of age. *Brain*, Vol. 113. pp. 27-47

[48]  Lassen, N. A. Cerebral blood flow and oxygen consumption in man. Physiol. Rev. 39: 183-238, 1959.

[49]  MacKenzie, E. T. et al. (1979) Effects of Increasing Arterial Pressure on Cerebral Blood Flow in the Baboon: Influence of the sympathetic Nervous System. Pfluegers Arch. 378, 189-195,

[50]  Maximilian VA and Brawanski A (1988) Functional and Vascular Challenge Procedures During Noninvasive rCBF Measurements, (in Knezevic et al., 1988) pp 79-121.

[51]  Mullin G.H. (1996). *Tsongkhapa's Six Yogas of Naropa*, Snow Lion, Ithaca NY

[52]  Obrig H., Villringer A. (2003). Beyond the visible - imaging the human brain with light. *J. Cereb. Blood Flow & Metab.*, Vol. 23, pp. 1-18

[53]  Raichle, M.E., Posner, J.B. and Plum F. (1970), Cerebral Blood Flow During and After Hyperventilation, *Arch. Neurol.* 23, 394- 403.

[54]  Raj D, Anderson AW and Gore JC, (2001), "Respiratory effects in human functional magnetic resonance imaging due to bulk susceptibility changes', *Physics in Medicine and Biology*, Vol. 46, pp. 3331-3340.

[55]  Reivich, M. (1964). Arterial $PC0_2$ and cerebral hemodynamics. *American Journal of Physiology, 206,* 25-35.

[56]  Reivich, M. Regulation of the Cerebral Circulation. In: *Clinical Neurosurgery*, Vol. 16, Chapter XIX.

[57]  Riggs, D.S. (1970) *Control Theory and Physiological Feedback Mechanisms*, Williams & Wilkins, Baltimore.

[58]  Rolfe, P. (2000). In Vivo Near-Infrared Spectroscopy. *Ann. Rev. Biomed. Eng.* Vol. 02, pp. 715-54

[59]  Sage JI, Van Uitert RL and Duffy TE (1981) Simultaneous measurement of cerebral blood flow and unidirectional movement of substances across the blood-brain barrier: theory, method, and application to leucine. J. Neurochem. 36: 1731-1738

[60]  Sato, N., Hagihara, B., Kamada, T., Abe, H. (1976) *Anal Biochem*, Vol. 74. Pp. 105-117

[61]  Sokoloff, L. (1989). Circulation and Energy Metabolism of the Brain, In: Siegel GJ (ed.), *Basic Neurochemistry*, fourth ed., Raven Press, New York NY

[62] Sokoloff, L. (1996), Circulation in the Central Nervous System. In: *Comprehensive Human Physiology, Vol. 1, Greger, R. and U. Windhorst (Eds.)*. Chapter 28, p. 561, and references therein.

[63] Strangman G., Boas D.A., Smton J.P. (2002). Non-invasive neuroimaging using near-infrared light. *Biol Psychiatry*. 52. pp. 679-693

[64] Suzuki S., Takasaki S., Ozaki T., Kobayashi Y. (1999). A tissue oxygenation monitor using NIR spatially resolved spectroscopy. *Proc SPIE*; Vol. 3597. Pp. 582-592

[65] Thavasothy et al. (2002), "A comparison of cerebral oxygenation as measured by the NIRO 300 and the INVOS 5100 Near-Infrared Spectrophotometers". *Anesthesia*, 57, 999-1006

[66] Toomim H. et al. (2004), "Intentional Increase of Cerebral Blood Oxygenation Using Hemoencelography (HEG): An Efficient Brain Exercise Therapy", *Journal of Neurotherapy* 8(3), pp 5-21 and In: Tinius T. (Ed.) *New Developments in Blood Flow Hemoencephalography*, Haworth Medical Press, pp 5-21.

[67] Ursino, M. (1991) Mechanisms of Cerebral Blood Flow Regulation. Critical Reviews in Biomedical Engineering 255-288, 18, and references therein.

[68] West, J.B. (1992) *Pulmonary Pathophysiology – the essentials*, 4th Ed., Williams & Wilkins, Baltimore.

[69] Yamamoto M, Meyer JS, Sakai F, Yamaguchi F. (1980). Aging and cerebral vasodilator response to hypercarbia. *Archives of Neurology, 37,* 489-496.

# High Resolution Infrared Spectroscopy of Phonons in the II-VI Alloys — The Temperature Dependencies Study

E.M. Sheregii

Additional information is available at the end of the chapter

http://dx.doi.org/10.5772/59050

## 1. Introduction

The cubic II-VI systems HgTe, CdTe and ZnTe are extremely interesting technologically materials with many applications such as infrared as well as quantum electronics devices [21, 29, 5, 44; 26]. The phonon frequencies of these alloys belong to the far-infrared region and investigation of their phonon spectra was one of more important problem in the infrared spectroscopy during 70-th years. The temperature dependence of the phonon HgTe-mode frequencies in binary HgTe, ternary HgCdTe (MCT) and HgZnTe (MZT) materials has been the subject of an intense debate in the last three decades [16, 14, 2,1, 29, 4; Kozyrev et al., 1996; 31, 12, 35, 28], due to contradictory results regarding in particular the abnormal temperature shift of the HgTe-like TO-phonon frequency. The latter is opposite to the normal phonon frequency temperature shift of many alkali compounds as well as most of semiconductors. In fact, the HgTe-like TO-phonon frequency increases when temperature increases while the normal temperature shift associated with a crystal lattice expansion, has to be opposite: the frequency decreases when temperature is raised.

The different behaviour has been qualitatively explained by an electron-phonon (*e-p*) interaction contribution in work of [29] as the *e-p*-interaction would produce positive frequency shifts as the temperature is raised whose magnitude would exceed the negative shifts due to anharmonicity. However, the claiming that the *e-p*-coupling in the temperature shift of the optical phonon modes has a significant role should be better and quantitatively verified.

The *e-p* interaction is the main mechanism of charge carriers scattering in semiconductor crystals and low-dimensional structures together with impurities and defects. Particularly, the scattering on long wave longitudinal optical (LO($\Gamma$)) phonons have an universal character because the latter generates a macroscopic polarized pole, and electrons experience very

effective interaction. Several resonance effects also occur such as the pinning of magneto-optical inter-band transitions observed in InSb by Johnson and Larsen (Johnson & Larsen, 1966). They affect the energy spectrum of electrons via the interaction with LO(Γ)-phonons. Effects produced by the direct polarized e-p-interaction, i.e., phonons affect the electron energy spectrum, are described in few review articles and books [22, 13]. In addition, the role of effects due to a direct non-linear polarized e-p-interaction has been shown in [32, 33].

On the other hand, reverse effects, i.e., how light electrons affect the phonon spectrum are much less known. Recently, we have shown [35] that the singularity in an electron energy spectrum induces a discontinuity in the phonon frequency temperature dependence of the $Hg_{1-x}Cd_xTe$ alloys. That means the appearance of an unexpected effect of strong resonance influence on oscillations of heavy atoms by the electron subsystem. In our short communication [36] we called this effect as returnable e-p interaction. It was shown that even though the returnable e-p-coupling has a non-polarized character, yet a deformation mechanism takes place [35, 36, 19]. It is necessary to note that singularity in the electron spectrum that induced the resonance returnable *e-p* interaction, is point of total zero of energy gap ($E_g \equiv \Gamma_6 - \Gamma_8 = 0$) well known in the $Hg_{1-x}Cd_xTe$ alloys (Dornhaus & Nimtz, 1985) and called later as a Dirac point.

It is then important to test the occurrence of this or similar effects in other semiconductor compounds. Moreover, it seems that the abnormal temperature dependence of the HgTe-like phonon modes can be solved in this framework, because the presence of a returnable e-p interaction could explain the positive temperature shift of the optical phonon frequencies. On the other hand, the positive temperature shift of the phonon frequency is characteristic for the HgTe-like modes in different Hg-based alloys such as the abovementioned HgCdTe, the HgCdSe [40, 39] and the HgZnTe as shown in the sequel. Data suggest that a spin-orbit relativistic contribution, larger for heavy atoms, play an important role in this phenomenon because of its effect on the chemical bond [42,17, 30].

The aim of this contribution is to generalize experimental data on the temperature dependence of the TO-phonon modes in the $Hg_{1-x}Cd_xTe$ and $Hg_{1-x}Zn_xTe$ alloys of different compositions and analyze the influence of the resonance returnable e-p-interaction in case when the temperatures are close to singular Dirac point ($E_g \equiv \Gamma_6 - \Gamma_8 = 0$) and far from this point for alloys where the Dirac point exists. Such analyses should be performed on a background of obligatory anharmonic contribution caused by the temperature extension of the crystal lattice. That analyses should be distributed on the alloy compositions where the Dirac point exists not, also.

The rich experimental reflectivity data in the far IR region of MCT and MZT alloys that were collected during 2002-2006 years for different compositions and in a wide temperature range using a synchrotron radiation source [34, 27, Cebulski et al., 2008; 35, 36, 28] allow unique opportunity for such investigation.

## 2. Experiment

In order to investigate the temperature behaviour of the phonon modes for HgZnTe and HgCdTe alloys, several optical reflectivity measurements were performed in the far-IR region

at the DAΦNE-light laboratory at Laboratori Nazionale di Frascati (Italy) using a synchrotron radiation source (details on the experimental set-up are available in work(Cestelli Guidi et al., 2005)). A BRUKER Equinox 55 FT-IR interferometer modified to collect spectra in vacuum, was used. As IR sources both the synchrotron radiation from the DAΦNE storage ring and a mercury lamp were used. Measurements were performed from 20 to 300 K and in the wave-number range 50-600 cm⁻¹. In order to provide the spectral resolution of 1 cm⁻¹ (2 cm⁻¹ in some cases), we typically collected 200 scans within 600 s of acquisition time with a bolometer cooled to 4.2 K. The reflectivity was measured using as a reference a gold film evaporated onto the surface of the investigated samples. This method enabled us to measure the reflectivity coefficient $R(\omega, T)$ with an accuracy of 0.2%. The

$Hg_{1-x}$ Cdx Te crystals were grown at the Institute of Physics of the Polish Academy of Sciences in Warsaw (Poland) while the $Hg_{1-x}$ $Zn_x$ Te ones at the CNRS-Groupe dEtude de la Matire Condense (Meudon, France). The reflectivity curves $R(\omega, T)$ for $Hg_{0.90}Zn_{0.10}Te$ in the frequency range from 80 cm⁻¹ to 220 cm⁻¹ and in the temperature range 30-300 K are shown in Fig. 1.

Data show that the main phonon band consists of two subbands: a HgTe-like band in the range 118-135 cm⁻¹ and a ZnTe-like band in the range of 160-180 cm⁻¹. Both of them are characterized by a fine structure. A non-monotonic temperature dependence of the reflectivity maxima can be also recognized. Similar $R(\omega, T)$ curves are showed in Fig.2 for the $Hg_{0.763}Zn_{0.237}Te$. The maxima on reflectivity curves in Fig. 2 are shifted with increase of temperature towards lower phonon frequencies monotonically.

To recognize the real frequency positions of a phonon mode, it is however necessary to calculate for each obtained experimental curve $R(\omega, T)$ the imaginary part of the dielectric function $Im[(\omega, T)]$ as function of frequency and temperature. That ones were calculated from the reflectivity spectra shown in Fig. 1 and 2 by means of the Kramers-Kronig (KK) procedure. This procedure is described in details in the work of [6]; was applied to experimental results presented in several papers, for example [35, 28, 25]. An estimated uncertainty of 1.5% takes place at calculation the $Im[(\omega, T)]$ curves for all experimental data. The $Im[(\omega, T)]$ curves at different temperatures are shown in Fig. 3 a,b for the $Hg_{0.90}$ $Zn_{0.10}$ Te sample as well as in Fig. 4 a,b for the $Hg_{0.763}$ $Zn_{0.237}$ Te sample. In Fig. 3 the $Im[(\omega, T)]$-curves are presented separately for HgTe-band (Fig. 3a) and for ZnTe-band (Fig.3b).

It is necessary to underline here that the maximum of the HgTe-like sub-band (Fig. 3a) shifts towards higher frequencies when the temperature increases from 30 K to 80 K while at temperature higher than 85 K the maximum shifts to lower frequencies. A non-monotonic temperature dependence of the ZnTe-like sub-band (Fig. 3b) with maximum frequency position near 85 K is also observed.

The frequency positions of HgTe-like and ZnTe-like sub-band maxima determined from the $Im[(\omega, T)]$ curves at different temperatures in the range 30-300 K are shown for the sample $Hg_{0.90}$ $Zn_{0.10}$ Te in Fig. 5a and 5b, respectively.
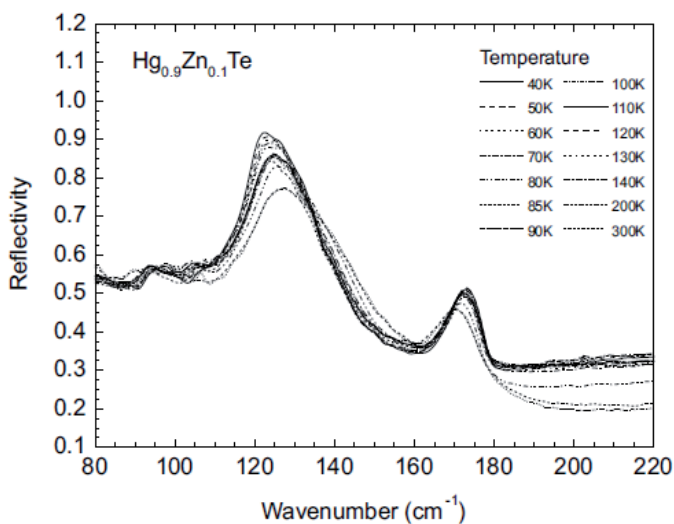
**Figure 1.** Reflectivity $R(\omega, T)$ for Hg0.90 Zn0.10 Te in the frequency region from 80 cm−1 to 220 cm −1 and in the temperature interval 30 K-300 K
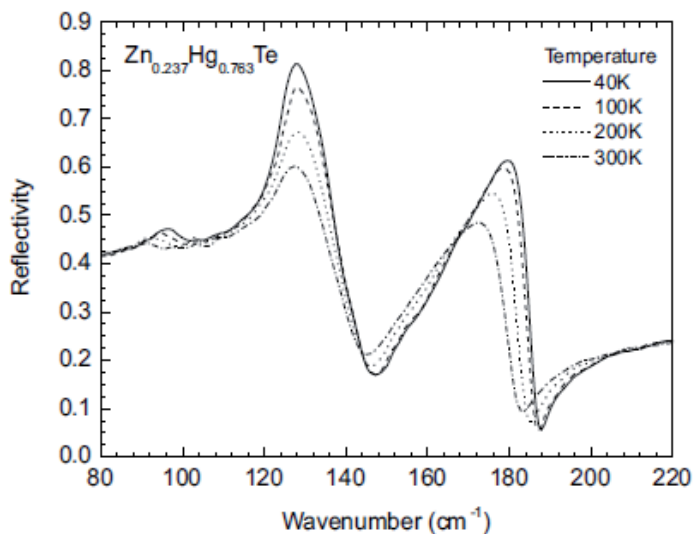


**Figure 2.** Reflectivity $R(\omega, T)$ for Hg0.237 Zn0.763 Te in the frequency region from 80 cm−1 to 220 cm −1 and in the temperature interval 40 K-300 K

The KK-transformation was also performed for the $R(\omega, T)$ curves shown in Fig.2 (the $Hg_{0.763}$ $Zn_{0.237}$ Te sample). The Im[$(\omega, T)$] curves at different temperatures for this sample are shown

in Fig. 4, while the positions of the $Im[(\omega, T)]$-maxima are shown in Fig.6 a,b for the HgTe-like mode and the ZnTe-like mode, respectively.

Analogous investigations of the temperature dependence of the phonon frequencies for different modes were performed for another semiconductor alloy contained the mercury as one of component, namely: HgCdTe. The results were published earlier: [35, Sheregii et al. (2010), 28]. The measured curves of $R(\omega,T)$ for $Hg_{0.885} Cd_{0.115}$ Te in the frequency region from 80 cm$^{-1}$ to 170 cm$^{-1}$ and the temperature interval 40 K – 300 K are shown in Fig. 7. From Fig. 7 it is clearly seen, that the main phonon band consists of two subbands: a HgTe-like band in the range of 118-13 cm$^{-1}$ and a CdTe-like band in the range of 140-160 cm$^{-1}$ both characterized by a fine structure well known for the alloy phonon spectra [43, Kozyrev and Vodopynov 1996, 25]. A non-monotonic dependencies of the reflectivity maxima are seen too. The $Im[\varepsilon(\omega,T)]$ curves calculated from the reflectivity spectra are showed in Fig. 8 a,b. We have also to underline here that maximum of the HgTe-like sub-band is shifted towards higher frequencies when the temperature increases from 170 K to 240 K while for temperature higher than 240 K the maximum is shifted to lower frequencies. The similar temperature behaviour demonstrates the CdTe-like sub-band maximum.

The Verleur-Barker model [43] with five structural cells together with the statistical approach developed recently [26] is applied to the $Hg_{1-x} Zn_x$ Te solid solutions. According to this model each of the two sub-bands: HgTe-like and ZnTe-like in the case of the $Hg_{1-x} Zn_x$ Te alloys, consists of not more the four modes due to the oscillations of the Hg-Te or Zn-Te dipole pairs in each of the five tetrahedra $T_n$, where n is the number of Zn-atoms in the cell. Therefore, the maximum of each sub-bands can be associated to one of these four modes depending on the composition of alloy. In the case of the $Hg_{0.90} Zn_{0.10}$ Te alloy we combine the $T_0$-mode with the HgTe-like sub-band and the $T_1$-mode with the ZnTe-like mode, similarly to the $Hg_{0.85} Cd_{0.15}$ Te alloy. Regarding the Hg0.763 Zn0.237 Te alloy the maximum of the HgTe-like sub-band is attributed to the $T_1$-mode, while the maxi-mum of the ZnTe-like subband, to the $T_2$-mode. A comparison of the temperature dependence of the TO-mode frequencies showed in Fig.3 and 6 point out a monotonic behaviour of the curves of the $Hg_{0.763}Zn_{0.237}$Te sample (Fig.6 a,b), while discontinuities occur in the curves of the semimetallic composition $Hg_{0.9} Zn_{0.1}$ Te (Fig.4 and 5) with a positive temperature shift of the HgTe-like mode frequency and a negative temperature shift, for both compositions, of the ZnTe-like mode. In the sample $Hg_{0.763} Zn_{0.237}$ Te a similar temperature dependence of the HgTe-like and ZnTe-like TO-modes as in the sample $Hg_{0.80} Cd_{0.20}$ Te are observed the HgTe-like and CdTe-like TO-modes as shown in Fig. 10 a and b, respectively. For the sample $Hg_{0.763} Zn_{0.237}$ Te, the frequency of the HgTe-like mode is practically independent of the temperature.

In Fig. 9 are shown the frequency positions of the HgTe-like and CdTe-like sub-band maxima on the $Im[\varepsilon(\omega,T)]$ curves for sample $Hg_{0.885}Cd_{0.115}$Te. It is seen from Fig. 9 that discontinuity is taken place precisely at 245 K for both HgTe-and CdTe modes. General-ly, for CdTe-mode is observed negative temperature shift of the phonon frequency, while for HgTe-mode is positive one.
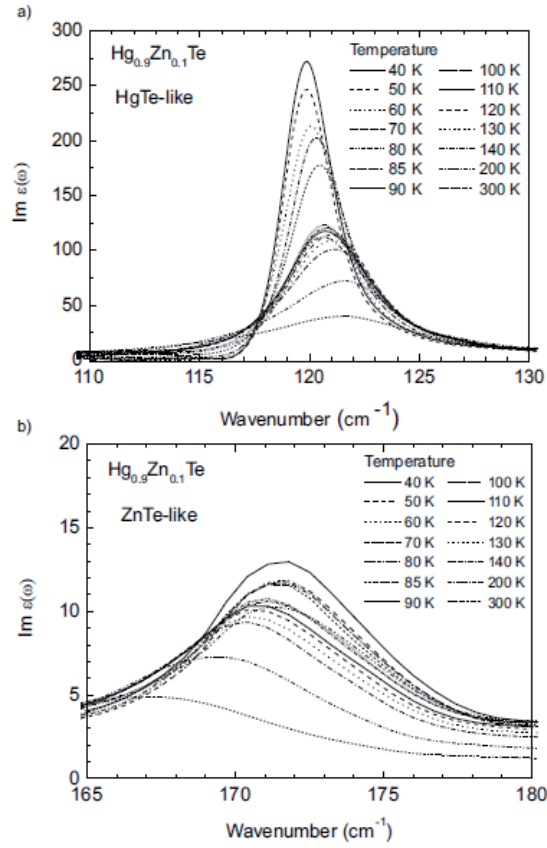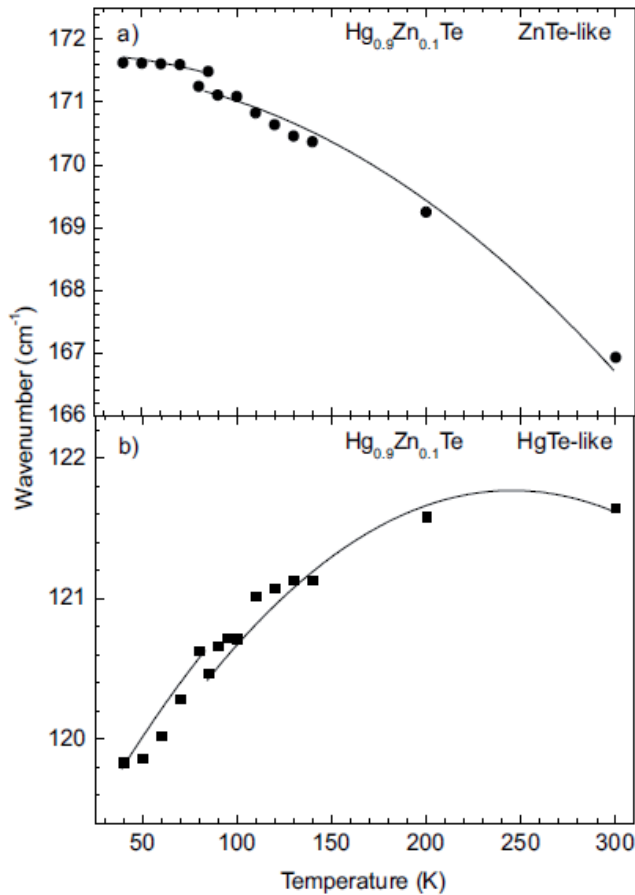
**Figure 3.** The Im[(ω, T)] curves of the $Hg_{0.90} Zn_{0.10}$ Te obtained from the reflectivity curves of Fig.1: a) the Im[(ω, T)] curves for the HgTe-like mode; b) the Im[(ω, T)] curves for the ZnTe-like mode.
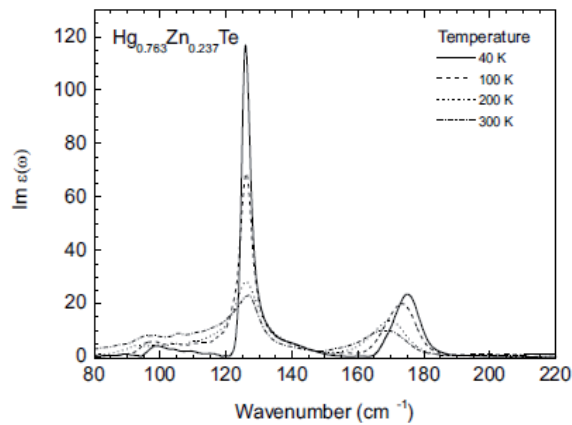


**Figure 4.** The Im[ε(ω, T)] curves of the Hg0.763 Zn0.237 Te obtained from the reflectivity curves of Fig.2.
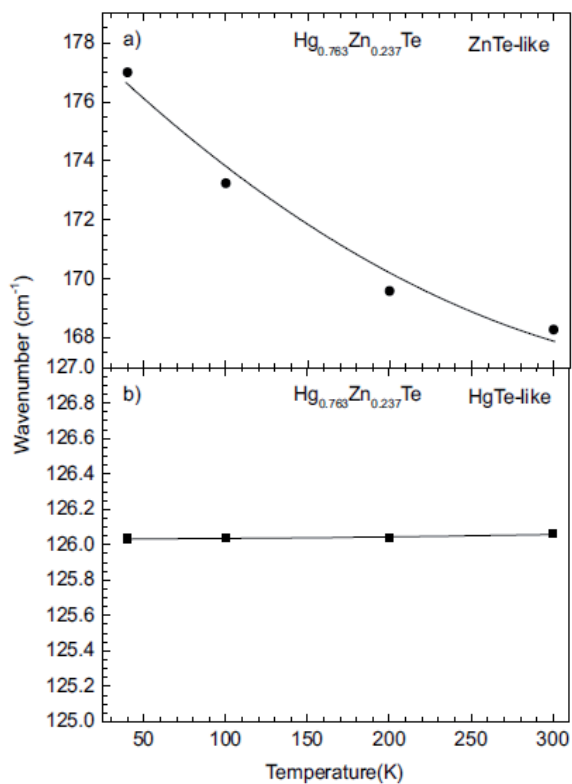
**Figure 5.** The frequency positions of ZnTe-like a) and HgTe-like b) sub-band maxima on the Im[(ω, T)] curves for the Hg0.90 Zn0.10 Te at different temperatures in the range 30 300 K.

It is interesting to compare the temperature dependences of the phonon modes for another alloy of HgCdTe. As was shown in Fig. 6b for the sample $Hg_{0.763} Zn_{0.237}$ Te, the frequency of the HgTe-like mode is practically independent of the temperature. Similar behaviour takes place for CdTe-mode in alloy $Hg_{0.80}Cd_{0.20}$Te as it is seen in Fig. 10 where are shown the temperature dependences for the phonon mode frequencies for this alloy.

So, it is possible to generalise the obtain experimental results on temperature behaviour of the phonon spectra for four alloys contained the mercury – $Hg_{1-x} Zn_x$ Te and $Hg_{1-x} Cd_x$ Te. If composition x is near the value where the particularity in energy structure takes place, namely the Dirac point ($E_g \equiv \Gamma_6 - \Gamma_8 = 0$), for example in the case of the $Hg_{1-x} Cd_x$ Te alloys that is x=0.1 – 0.17 and in the case of the $Hg_{1-x} Zn_x$ Te alloys it is x=0.06 – 0.11, then positive temperature shift is observed for the HgTe-modes with discontinuity the temperature where the Dirac point takes place.

**Figure 6.** The positions of the Im[(ω, T)]-maxima for the Hg0.763 Zn0.237 Te sample a) the ZnTe-like mode and b) the HgTe-like mode.
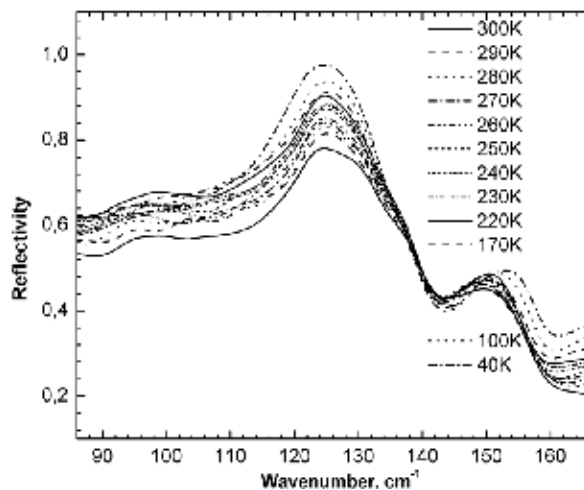


**Figure 7.** Reflectivity $R(\omega, T)$ for Hg0.885 Cd 0.115 Te in the frequency region from 80 cm−1 to 220 cm −1 and in the temperature interval 40 K-300 K

(a)



(b)
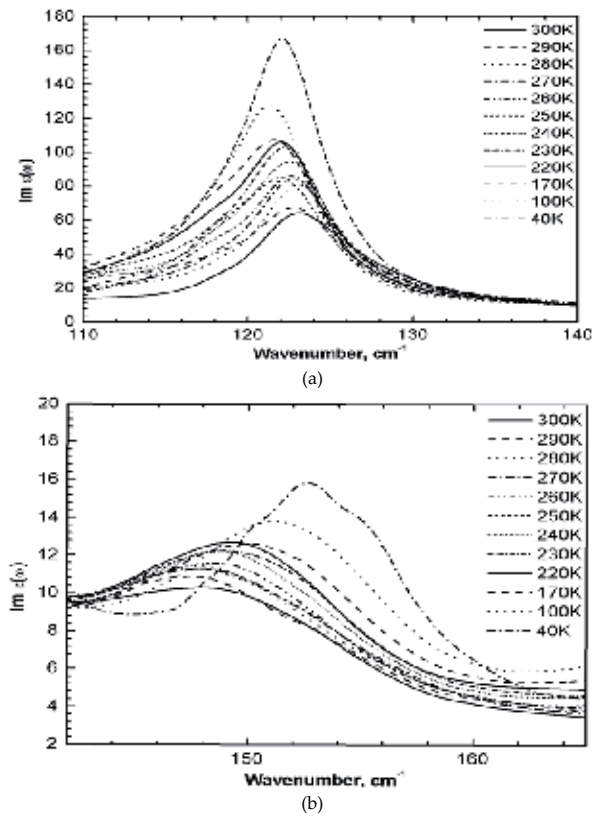
**Figure 8.** Reflectivity $R(\omega, T)$ for Hg0.*885* Cd *0.115* Te in the frequency region from 80 cm−1 to 220 cm −1 and in the temperature interval 40 K-300 K
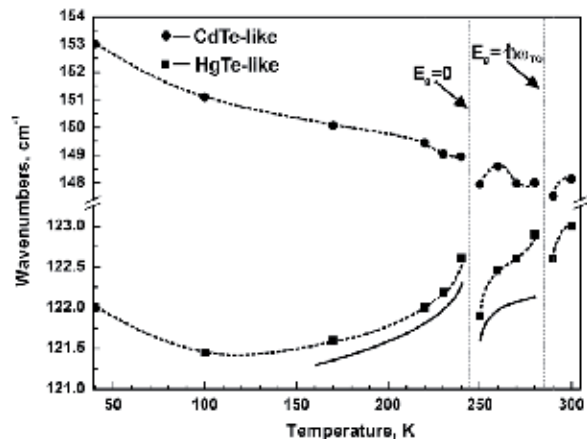


**Figure 9.** Reflectivity $R(\omega, T)$ for Hg0.*885* Cd *0.115* Te in the frequency region from 80 cm−1 to 220 cm −1 and in the temperature interval 40 K-300 K
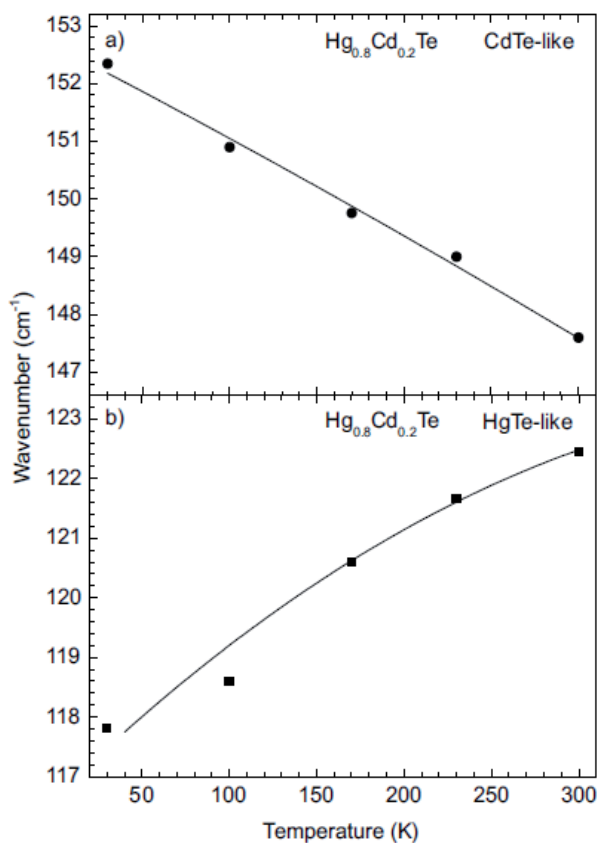
**Figure 10.** The positions of the Im[(ω, T)]-maxima for the $Hg_{0.80} Cd_{0.20}$ Te sample a) the CdTe-like mode and b) the HgTe-like mode.

| Alloys | mode | A (cm⁻¹) | B (cm⁻¹) | C (cm⁻¹) |
|---|---|---|---|---|
| $Hg_{0.85}Cd_{0.15}Te$ | HgTe-like | 121.8 | -3.7 | 1.9 |
| | CdTe-like | 152.0 | -2.3 | -0.4 |
| $Hg_{0.80}Cd_{0.20}Te$ | HgTe-like | 118.0 | 4 | -0.6 |
| | CdTe-like | 152.4 | -2 | -0.4 |
| $Hg_{0.90}Zn_{0.10}Te$ | HgTe-like | 119.2 | 3.6 | -1.04 |
| | ZnTe-like | 171.2 | -0.26 | -1.87 |
| $Hg_{0.763}Zn_{0.237}Te$ | HgTe-like | 126.03 | 0.001 | 0.005 |
| | ZnTe-like | 177.0 | -10 | 2 |

**Table 1.** Parameters of alloys necessary to calculate the anharmonic contribution to the phonon frequency change

| Alloy | W (eV) | $\Xi_{CV}$ (meV) | A (Å) | $E_F$ (meV) |
|---|---|---|---|---|
| $Hg_{0.85}Cd_{0.15}Te$ | 8 | 5 | 6.49 | 6 |
| $Hg_{0.80}Cd_{0.20}Te$ | 8 | 5 | 6.49 | 1 |
| $Hg_{0.90}Zn_{0.10}Te$ | 7 | 3 | 6.63 | 6 |
| $Hg_{0.763}Zn_{0.237}Te$ | 7 | 3 | 6.65 | 1 |

**Table 2.** Parameters of alloys necessary to calculate the e-p contribution to the phonon frequency change

In the case of compositions apart from that areas where Dirac point cold be presence (for x>0.17 for $Hg_{1-x}Cd_xTe$ alloys as well as for x>0.11 for the $Hg_{1-x}Zn_xTe$ alloys) an ambivalence behaviour for the temperature dependences of the HgTe-modes is observed – could be or strong positive temperature shift or complete independency on the temperature takes place.

## 3. Discussion

### 3.1. Basic theory

In view of the most general assumptions, it is possible to start from the following equation for the temperature shift of the $TO_i$-phonon mode frequencies $\nu_{T\,Oi}$ [18]:

$$\Delta \nu_{TO_i}(T) = \left(\frac{\partial \nu}{\partial T}\right)_P dT + \left(\frac{\partial \nu}{\partial T}\right)_V dT \tag{1}$$

The first term in Eq. (1) corresponds to the crystal expansion and to an anharmonic contribution to the harmonic crystal potential. This anharmonic term has been analyzed in detail by different authors in the last decades. The theory developed by Maradudin and Fein (Maradudin & Fein, 1962) as well as by [14] is based on the classical anharmonic oscillator. The potential energy is:

$$V(x) = cx^2 - gx^3 - fx^4 \tag{2}$$

where, the cubic term $gx^3$ gives a thermal expansion but no change in the frequency at the first order. The quartic term $fx^4$ and the cubic term to the second order $(gx^2)^2$ may induce a change in the frequency of the modes. The role of these terms was estimated [10] by assuming for Si atoms a covalent interatomic bond within the Morse potential:

$$V(r) = D[(e^{-a(r-r_0)} - 1)^2 - 1] \tag{3}$$

where the constants D, a and r0 are determined, respectively, by bonding energy, stiffness of bond and interatomic spacing. Using the Morse potential to determine the coe ▪ cients of the Taylor series expansion of the potential, [14] find that the quartic term is positive, i.e., it increases with the frequency, but accounts for only 3/5 respect to the cubic term to the second order that is negative. The result is then a net decrease in the frequency.

In the quantum-mechanical approach each power of x correspond to a creation or an annihilation operator for a phonon, and the frequency shift of the optical mode is calculated as the self-energy of the mode [24]. Using this technique [10] performed detailed numerical calculations for the diamond structure using eigenvectors and eigenfrequencies of the harmonic model deduced by fitting the parameters of the dispersion curves obtained by inelastic neutron scattering data. The appropriate anharmonic interaction was determined by fitting experimental thermal expansion data. Later, Ipatova I.P. et al. (Ipatova et al., 1967) working on ionic crystals and Schall M. et. al. (Schall et al., 2001) in the CdTe and ZnTe semiconductors applied this theory to explain the temperature dependence of the dielectric function in the far IR frequency range.

The second term in equation (1) is due to the e-p interaction and it is interesting to underline that an analogue expression takes place for the temperature dependence of the energy gap in semiconductors (Yu & Cardona, 1996) where two contributions also occur: the anharmonic one and that induced by the e-p interaction.

### 3.1.1. Anharmonic contribution

An expression was derived by Ipatova I.P. et al. [16] for the temperature dependence of the phonon mode frequency $\nu_{TO}$ or the damping of an oscillator $\gamma_{TO}$ in the quartic anharmonic force constant approximation:

$$Y(T) = A + B\left(\frac{T}{\Theta}\right) + C\left(\frac{T}{\Theta}\right)^2$$ (4)

where Y(T) is one of the measured quantities $\nu_{TO}$ or $\gamma_{TO}$, $\Theta$ is the characteristic temperature of the phonon subsystem $\Theta = h\nu_{TO}/k_B$ ($k_B$ is the Boltzmann constant), A, B, C are the parameters obtained by fitting and for the CdTe phonon frequency (Ref. 12): A=4.361 THz (or 150 cm$^{-1}$), B=-0.0298 THz (or-1.00 cm$^{-1}$), C=-0.0348 THz (or-1.16 cm$^{-1}$). The same parameters for the ZnTe are: 5.409 THz (or 190 cm$^{-1}$),-0.0457 THz (or-1.52 cm$^{-1}$) and-0.0341 THz (or-1.37 cm$^{-1}$), respectively. In this case, it is clear that A is the frequency $\nu_{TO}(0)$ of the TO-phonon mode at T=0 and the first term in the equation (1) can be rewritten as:

$$\Delta\nu_{TO}^I(T) = B\left(\frac{T}{\Theta}\right) + C\left(\frac{T}{\Theta}\right)^2$$ (5)

Because A and B are usually negative parameters, equation (5) always points out a frequency decrease, i.e., a softening of the phonon frequency on increasing the temperature. This behaviour has been observed in many ionic crystals and wide-gap semiconductors.

### 3.1.2. The e-p interaction contribution

As mentioned in the Introduction, the returnable e-p interaction could be responsible for the abnormal temperature dependence of the phonon frequency in both HgCdTe as well as HgZnTe. This kind of e-p interaction induces a discontinuity in the temperature dependence of the phonon frequencies in the resonant case, i.e., Dirac points. Actually, it is possible to assume that far from a Dirac point the returnable e-p interaction may overcome the anharmonic contribution and reverse the sign of the phonon frequency temperature dependence associated with the lattice dilatation.

As shown in [19], the preferred mechanism explaining the influence of the electronic structure of the crystal on its phonon spectrum is a deformation potential that mediates the interaction of electrons with the transverse optical phonons (TO-phonons). The TO-phonons are clearly recognized in optical reflectivity experiments, therefore the deformation potential is responsible for the interaction of electrons with TO-phonons. We are interested only in the terms of the deformation potential matrix that correspond to the energy region between the valence and the conduction band. Therefore, the self-energy of the TO-phonons with a small wave-vector q is given by the formula [19, 35]:

$$\omega_{TO}^{*2} = \omega_{TO}^2 - \int dE F(E) \left\{ \frac{1}{E + E_g + \hbar\omega_{TO}} + \frac{1}{E + E_g - \hbar\omega_{TO}} \right\} \tag{6}$$

where $E_g$ is the energy gap and

$$F(E) = \frac{2}{2\pi^3} \int \frac{\omega_{TO}}{\hbar} \left( V_{cv}(k,q)^2 \cdot \delta\left(E - E_c(k+q) - E_v(k)\right) dk \right) \tag{7}$$

$V_{cv}$ (k, q) does not depend on the wave vector of the long-wave optical phonons (q 0); thus, $E_c$ (k+q) − $E_v$ (k)=$E_g$.

We can identify two kinds of singularities in Eq. (6): the first is obtained when Eg is equal to, and the second occurs when Eg equals zero. In the second case, if the temperature increases, the $E_g$ (T) dependence approaches zero from the negative side of the energy gap (the in-version band-structure). On the other hand, decreasing the temperature, the $E_g$ (T) dependence approaches zero from the positive side of the energy gap (normal band structure), hence, a discontinuity in $\omega_{TO}$ (T) may occur also at $E_g$ (T)=0.

In order to describe the e-p contribution to the phonon frequency temperature dependence we may use an equation derived from Eq. (6) to determine the frequency change:

$$\omega_{TO}^{*2} = \omega_{TO}^2 \pm \frac{4\Xi_{CV}^2}{Ma^2 W} \ln \frac{W}{2E_F + |E_g|} \tag{8}$$

where $\Xi(k, q)$ is the optical deformation potential, $E_F$ is the Fermi energy measured from the band edge, W is the sum of the conduction and the valence bands width, $a$ is the lattice constant and $E_g \equiv \Gamma_6 - \Gamma_8$ is the energy gap between the $\Gamma_6$ band, which is the conductive band in a normal semiconductor and the $\Gamma_8$ band, which is usually the top of the valence band. After a simple trans-formation from Eq. (8) we can obtain an expression for $\Delta v^{II}$ (T), the phonon frequency change associated to the returnable e-p interaction:

$$\Delta v^{II}(T) = \pm 2 \frac{\Xi_{CV}}{a} \sqrt{\frac{1}{MW} \ln \frac{W}{2E_F + (E_g)}} \tag{9}$$

Looking at $\Delta v^{II}$ (T) we may recognize the sign of this contribution through the corresponding sign of the deformation potential $\Xi(k, q)$ : the sign is "-" when the energy gap ($E_g \equiv \Gamma_6 - \Gamma_8$) is positive (usually $E_g > 0$, in a normal semiconductor the deformation potential is negative) or the sign is "+" when $E_g < 0$ (that takes place before a Dirac point). Therefore, before the resonance case ($E_g \equiv \Gamma_6 - \Gamma_8 = 0$) when $E_g < 0$, $\Xi(k, q) > 0$ and the contribution of the returnable e-p interaction to the temperature change of the phonon frequency has a reversed sign with respect to the anharmonic contribution which is always negative. At some temperature a full reverse sign of the frequency could occur, i.e., when the phonon contribution overcomes the anharmonic one, on increasing the temperature also the frequency starts increasing. It enables us to explain the abnormal temperature dependence of the optical phonon frequency.

A different scenario occurs after the resonance: the sign is-for the phonon contribution to the temperature change of the phonon frequency when $\Xi(k, q) < 0$. The phonon frequency suddenly decreases and a discontinuity takes place at the Dirac point. However, on increasing the temperature the $E_g \equiv \Gamma_6 - \Gamma_8$ also increases, and the negative phonon contribution to the temperature change of the phonon frequency is reduced that implies a decrease of the negative change of this frequency. Therefore, the magnitude of the phonon frequency increases with the temperature after the Dirac point only if the phonon contribution overcomes the anharmonic one, a condition occurring not far from the resonance. As a consequence, the abnormal temperature dependence of the optical phonon frequency may occur also after the resonance.

### 3.1.3. Full temperature shift of the TO-phonon frequency

According to the above, the full temperature shift of the TO-phonon frequency in the semiconductor crystals is $\Delta v(T) = \Delta v^I(T) + \Delta v^{II}(T)$ (T) and the temperature dependence of the TO-phonon mode $v_{TO}$ (T) can be written as:

$$\nu(T) \equiv \nu_{TO}(0) + \Delta\nu_{TO}(T) = \nu_{TO}(0) + B\left(\frac{T}{\Theta}\right) + C\left(\frac{T}{\Theta}\right)^2 + 2\frac{\Xi_{CV}}{a}\sqrt{\frac{1}{MW}\ln\frac{W}{2E_F + (E_g)}} \qquad (10)$$

From the comparisons of Eqns (5), (9) and (10) the anharmonic contribution exhibits for all crystals a monotonic function vs. temperature and, because the B and C constants are usually negative, the phonon frequency decreases (Ipatova et al., 1967; Schall et al., 2001). Actually, the e-p contribution depends dramatically on the temperature because $E_g(T)$ crosses through a point where $E_g=0$. In this point a singularity occurs and, because the e-p contribution is huge, a discontinuity in the temperature dependence of the phonon mode frequency is observed for $Hg_{0.89}Cd_{0.11}Te$ at 245 K (Sheregii et al., 2009). When $E_g < 0$, the $\Delta\nu^{II}(T)$ is positive and leads to the hardening of the phonon mode with increase of temperature. However, this contribution quickly reduces decreasing the temperature. Indeed, when temperature decrease the value of $|E_g|$ increases and $\Delta\nu^{II}(T)$ becomes smaller than $\Delta\nu^{I}(T)$ what means a softening of the phonon mode at low temperatures. In the semiconductor case at $(E_g > 0)$, the $\Delta\nu^{II}(T)$ is negative and $|\Delta\nu^{II}(T)| > |\Delta\nu^{I}(T)|$ is fulfilled, because at $E_g \sim 0$ the e-p contribution is large. However, the increase of $|E_g|$ when temperature increase, leads to a decrease of the total negative change of the phonon frequency that implies a positive temperature shift of the magnitude of the phonon mode frequency already observed in the $Hg_{1-x}Cd_xTe$ as well as in another mercury contained alloys. So, it seems to be possible to explain this positive temperature shift of the phonon frequency by the e-p contribution Nevertheless, concerning the role of the returnable e-p coupling, it is necessary to carry out a reliable experimental test of the above theoretical assumptions on the temperature dependence of the phonon mode frequency.

In what follows, we will present the analysis of the experimental data which are described above. Data allow to answer if the returnable e-p coupling contribution is enough to explain the abnormal temperature dependence of the HgTe-like mode frequency in both MCT and MZT alloys.

### 3.2. Analyses and Interpretation of experimental results

#### 3.2.1. Alloy $Hg_{0.85}Cd_{0.15}Te$

The analysis of the observed temperature dependence of the TO-phonon modes for these semimetallic and semiconductor alloys is based on Eq. (10).

In order to calculate the *e-p* contribution to the temperature shift according to Eqns.(9,10) we need to know the temperature dependence of the energy gap $E_g(T)$. An empirical formula for $E_g(x,T)$ is presented in (Sheregii et al., 2009) derived for the $Hg_{1-x}Cd_xTe$ alloy. According this empirical formula the Dirac point $(E_g \equiv \Gamma_6 - \Gamma_8 = 0)$ takes place for sample $Hg_{0.85}Cd_{0.15}Te$ at temperature 245 K. In Table 1 values of other important parameters are presented such as the optical deformation potential $\Xi(k, T)$, the Fermi energy $E_F$, the sum of the conduction, and the valence bands width as well as the lattice constant *a* for the HgCdTe and HgZnTe alloys. The *A*, *B* and *C* parameters for the anharmonic contribution for each sample are listed in Table 2.
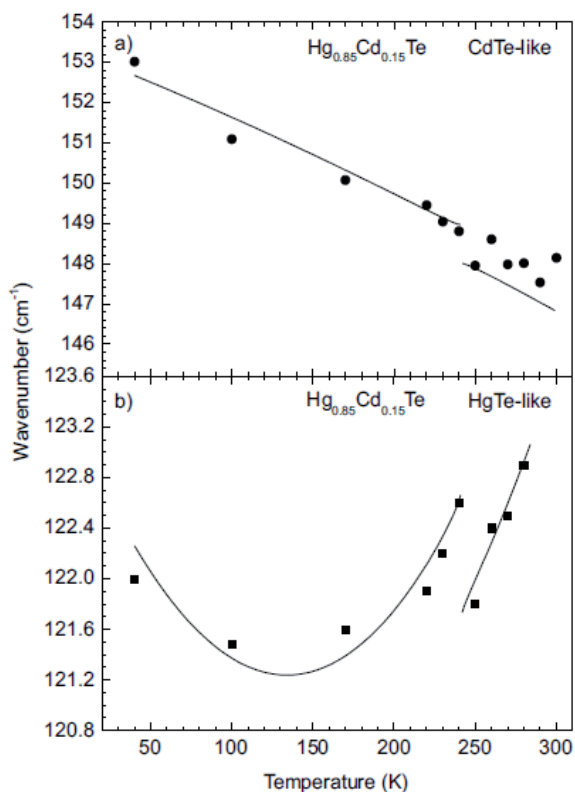
**Figure 11.** The CdTe-like (a) and HgTe-like (b) TO-mode positions in the frequency scale at different temperatures for the sample $Hg_{0.85}Cd_{0.15}Te$ – the same experimental pointa as in Fig. 9; solid curves are calculated according the Eqn. 10.

Result of the *e-p* contribution calculation according Eqn. (9) is shown by solid curve in Fig. 9. The discontinuity at 245 K is displayed by theoretical curve in narrow region of temperature very impressible and agree with experimental dependences very well. However, we need to confirm that Eq. (10) satisfactorily describes the experimentally observed temperature dependence of both HgTe-like and CdTe-like mode frequencies in wide temperature region together with the discontinuity observed at 245 K. Anharmonic and e-p terms in Eq. (10) match the experimental dependence of HgTe-mode in the whole temperature range from 40 K to 300 K for this sample as it is shown in Fig. 11b. The anharmonic contribution dominates at low temperature from 40 K to 120 K and the temperature shift of the HgTe-like $T_0$-mode is negative. After the minimum at 121 K, the *e-p*-contribution overcomes the anharmonic one, and the HgTe-like $T_0$-mode frequency start increasing up to resonance at 245 K. At the resonance (Dirac point) the *e-p*-contribution change sign and the phonon frequency suddenly decreases: the discontinuity takes place and the following increase of the temperature leads to a decrease of the negative *e-p*-contribution that induces the increase of the phonon frequency up to room temperature. It is important to note that theoretical curve in Fig. 11b is calculated with a positive value of the constant C. In the case of the CdTe-like mode (see Fig. 11a) both B and C

parameters are negative similarly to the CdTe-binary but the linear constant B is slightly larger than nonlinear while C is slightly smaller compared to the binary one. On the contrary, in the case of the HgTe-like mode it is impossible to have a satisfactorily theoretical agreement with experimental curves using negative values of both B and C constants. As a consequence, we take positive sign for the C constant what implies that *the thermal expansion can lead to an ambivalent effect in the frequency temperature dependence of the HgTe-like mode*.

### 3.2.2. Alloy $Hg_{0.80}Cd_{0.20}Te$

In the case of the $Hg_{0.80} Cd_{0.20}$ Te-alloy the singularity in the second term of Eq. (10) is very far (formally should exist at temperature closed to absolute zero) and the effect of the returnable e-p interaction is negligible. That is shown in Fig. 10b where we show experimental data and theoretical curves of the HgTe-like mode. Here the solid curve is calculated with the *e-p* term while the dotted one without it. Parameters are listed in Tables 1 and 2. A good fit of the experimental data was obtained with B > 0. It is clear from their behaviour that the phonon frequency of the HgTe-like mode strongly increases with the temperature, almost linearly, so that B must be large and positive.

The CdTe-like mode frequency has an opposite behavior vs. temperature with respect to the HgTe-like one: the frequency strongly decreases vs. temperature. It is a classical behavior where the anharmonic contribution dominates in the phonon frequency. The parameters B and C are close to that of the sample $Hg_{0.85} Cd_{0.15}$Te and also of the binary CdTe.

### 3.2.3. Alloy $Hg_{0.90}Zn_{0.10}Te$

To calculate according to Eqns. (9, 10) the *e-p* contribution to the temperature shift of the temperature dependence of the energy gap $Eg(T)$ of the $Hg_{1-x} Zn_x$ Te, it is necessary to write an empirical formula $Eg (x,T)$ similar to that of the $Hg_{1-x} Cd_x$ Te (Talwar, 2010):

$$E_g\left(x,T\right) = -0.302 + 2.731x + 3.2410 - 2x - 0.629x2 + 0.533x3 + 5.310 - 4(0.76x0.5 - 1.29x)T \qquad (11)$$

From the above *equation* calculated for the $Hg_{0.9} Zn_{0.1}$ Te and shown in Fig. 12, the zero-gap state should take place at 85 K.

Really, at this temperature 85 K a discontinuity of the temperature dependences of the HgTe-like and ZnTe-like modes is observed (see Fig. 5a and 5b). These discontinuities are smaller than in the $Hg_{0.85} Cd_{0.15}$ Te sample. In the case of the HgTe-like mode for the sample $Hg_{0.9} Zn_{0.1}$ Te (Fig. 5a), Eq. (10) describes quite well the experimental behavior with the discontinuity at 85 K but with a value *B=3.6* which is positive that points out a strong increase of the phonon frequency with the temperature. So, the returnable *e-p*-interaction contribution in the second term in Eq. 10 describes the discontinuity in the phonon frequency temperature dependence but on top of a general increase of the frequency. A third factor, connected with the expansion but included not in Eqn. (10) openly, should cause this increase. The ZnTe-like mode temper-
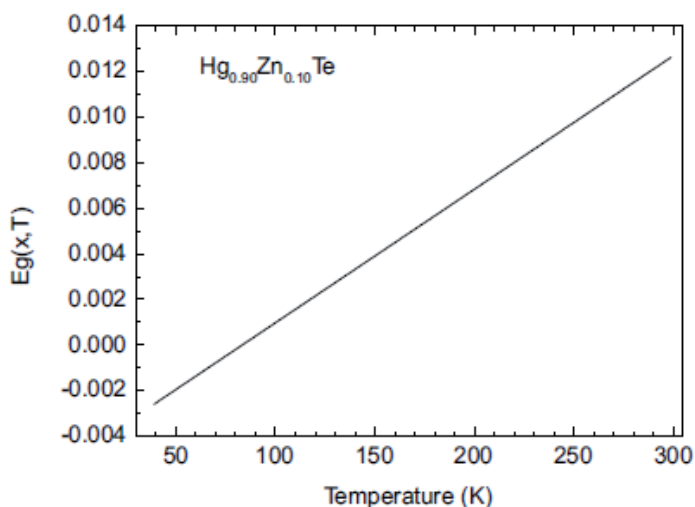
**Figure 12.** Temperature dependence of the energy gap ($E_g \equiv \Gamma_6 - \Gamma_8$) for the Hg0.9 Zn0.1 Te alloy calculated according to the Eq.11 (see text).

ature behavior (Fig. 5b) can be interpreted by Eq.10 with the anharmonic constants $B=-0.26$ and $C=-1.87$ with a discontinuity always at 85 K.

### 3.2.4. Alloy $Hg_{0.237}Zn_{0.763}Te$

The sample $Hg_{0.763}$ $Zn_{0.237}$ Te is characterized by the HgTe-like phonon frequency practically independent of the temperature as showed in Fig. 6b, and constants B and C close to zero. The *e-p* contribution is then negligible similarly to the $Hg_{0.80}$ $Cd_{0.20}$ Te. Therefore, the two contributions are compensated in this system: one due to the anharmonicity that induces a negative frequency shift while the second, an unknown yet, induces positive temperature shift but the latter one is connected with thermal expansion too.

The temperature dependence of the ZnTe-like mode frequency in the case of the $Hg_{0.763}$ $Zn_{0.237}$ Te alloy points out a maximal negative shift among all the alloys we investigated: $B=-10$ while $C=2$ is positive. The latter is due to the character of the mode frequency temperature dependence we observed. This character is different from the temperature dependence of the same mode for the $Hg_{0.90}$ $Zn_{0.10}$ Te (Fig. 5a and 5b) as well as the CdTe-like TO-phonon frequency temperature dependence of both HgCdTe samples (Fig. 9 and 10a). In the binary ZnTe the temperature dependence of the ZnTe mode frequency is significantly smaller [14].

### 3.2.5. The relativistic contribution to vibrational effects

From the above data the positive temperature shift is characteristic in different alloys only of the HgTe-like modes. It means that contribution of Hg-atoms to the chemical bonds mainly affects the abnormal temperature dependence of the HgTe-like phonon frequencies. It is then

useful to consider the peculiarities of the chemical bonds in the case of the II-VI compounds with Hg.

Using a simple chemical picture of these compounds, Hg atoms contribute to bonds with two s electrons while Te atoms with two s and four p electrons. In comparison with Ca, Sr, and Ba chalcogenides, the ionicity of Hg chalcogenides is reduced. The Hg-d-electrons are partially delocalized, and, therefore, the effective nuclear charge, experienced by the valence electrons, increases. This generates a more tightly bound of Hg valence s electrons and, hence, a less ionic and more covalent bond. In this respect, Hg-atoms in the II-VI compounds are similar to the isoelectronic Cd and Zn in the same semiconductors. However, the d-shell delocalization is stronger in Hg than in Cd or Zn and, in fact, enough strong to pull the s level below the chalcogen p level10. As a con-sequence, an inverted band structure is obtained. The role of d-electrons in II-VI compounds is discussed in more detail by Wei and Zunger, [42], while the contribution of the spin-orbit interaction to chemical bonds and electronic structure is consid-ered in [12]. This contribution increases with the number of atoms, and it is larger for Hg atoms with respect to Cd and Zn ones. In HgTe, the $\Gamma_8$ band is higher in energy than the $\Gamma_6$ one, whereas the situation is reversed in CdTe and ZnTe. Actually, this is because the energy difference between the $\Gamma_8$ and $\Gamma_6$ levels is determined by three factors: i) the chalcogen p-spin-orbit splitting, ii) the Hg-d-spin-orbit splitting and iii) the coupling strength among these states – so-called pd-coupling. For the p states, the $\Gamma_8$ symmetry is higher in energy than the $\Gamma_7$, whereas for d-states the situation is reversed. Thus, if the p-spin-orbit coupling with the Hg-d-spin-orbit split states becomes reasonably small as in CdTe (ZnTe), the order of the Hg-d-spin-orbit split states drives the sequence order of $\Gamma_8$ and $\Gamma_6$ levels. Alternatively, if due to large pd-coupling the d character dominates in these bands, the $\Gamma_8$ level may also end up higher than the $\Gamma_6$ level.

However, how the difference between CdTe (ZnTe) and HgTe electronic structures translates into a temperature dependence of the phonon frequency? As it was underlined in the Subsec-tion 3.1, a similar equation to Eq.(1) takes place for the temperature dependence of the energy gap in semiconductors where two contributions, the anharmonic one and that associated to e-p interaction, interplay with each other. It is interesting to note that the energy gap of HgCdTe and HgZnTe alloys have the same positive shift (Dornhaus & Nimtz, 1985) as the HgTe-like modes frequencies, actually opposite to the temperature shift observed for the energy gap of both CdTe and ZnTe [41, 23]. This difference in the $E_g(T)$ dependences for binary CdTe(ZnTe) and ternary HgCd(Zn)Te is due to the Hg-d-spin-orbit split states and, probably, is translated into the $\nu_{TO}(T)$ also due to a large pd-coupling of the chemical bonds. Although, the temper-ature dependence of the expansion coe ˙ cients in CdTe(ZnTe) and HgTe are similar (Bagot, 1993), the role of the lattice expansion on the $\nu_{TO}(T)$ dependences is different, similarly to the $E_g(T)$. It is possible to claim that the role of the quartic term in the potential of the Eq.(2) (see Subsection 3.1) is different for a Hg-Te bond compared to Cd-Te and Zn-Te ones because of the Hg-d-spin-orbit split states: overcomes others terms and positive temperature shift of the phonon frequency takes place.

## 4. Conclusion

It was performed an extensive experimental investigation of the temperature dependence of the phonon mode frequencies for Hg-based semiconductor alloys of II-VI compounds using the synchrotron radiation as a source in the far-infrared region. In the case of the $Hg_{0.9}Zn_{0.1}Te$ alloy we found a discontinuity of the temperature dependence of HgTe-like T0-mode and ZnTe-like $T_1$-mode similarly to the $Hg_{0.85}Cd_{0.15}Te$ alloy firstly found five years ago by [35]. A theoretical expression (Eqn. (10) in subsection 3.1) for the temperature shift of the phonon mode frequency has been derived including an anharmonic contribution as well as a term of a returnable electron-phonon interaction. It was shown that this expression including both abovementioned contributions satisfactorily describes the temperature shift of $Hg_{0.85}Cd_{0.15}Te$ and $Hg_{0.90}Zn_{0.10}Te$ alloys containing a Dirac point ($E_g \equiv \Gamma_6 - \Gamma_8 = 0$) if one of the two constants B and C describing the anharmonic shift of the HgTe-like mode, is positive. Moreover, in the case of the semiconductor alloys $Hg_{0.80}Cd_{0.20}Te$ and $Hg_{0.763}Zn_{0.237}Te$ the role of the returnable *e-p* contribution is negligible but a positive temperature shift for the HgTe-like modes takes place. The result cannot be explained as summing an *e-p* interaction as pointed out by (Rath et al., 1995).

The difference between the temperature behaviour of HgTe-like modes and CdTe-or ZnTe-like ones can be explained by the Hg-d-spin-orbit split contribution to the chemical bond. This contribution is responsible of the positive temperature shift of the energy gap of ternary HgCdTe and HgZnTe alloys with a narrow gap because the relativistic contribution to chemical bonds is also at the origin of the abnormal temperature shift of electron states in Hg-based semiconductors – inverse band structure. Similar effect is reasonably expected that the Hg-d-spin-orbit split contribution leads to an abnormal temperature shift of the HgTe-like phonon mode frequency.

## Acknowledgements

## Author details

E.M. Sheregii

University of Rzeszow, Centre for Microelectronics and Nanotechnology, Poland

# References

[1] Amirtharaj P.M.,. Dhart N.K, Baars J. & Seelewind H., (1990) Investigation of phonons in HgCdTe using Raman scattering and far-infrared reflectivity, *Semicond. Sci. Technol.* Vol. 5, No. 3S (March 1990), pp. S68-S72, 0268-1242

[2] Baars J. & Sorgers F., (1972), Reststrahlen spectra of HgTe and CdHg1-Te, *Solid State Commun*. Vol. 10, No. 9 (1 May 1972) pp. 875–878, 0038-1098

[3] Bagot D. & Granger R., (1993), Thermal Expansion Coefficient and Bond Strength in Hg1−xCdxTe and Hg1−xZnxTe, *Phys. Status Solidi (b)*, Vol. 177, No2 (1 June 1993), pp. 295–308, 1521-3951

[4] Biao Li.,.Chu J.H, Ye H.J., Guo S.P., Jiang W. & Tang D.Y., (1996), Direct observation of vibrational modes in Hg1−x Cd x Te, *Appl. Phys. Lett.*, Vol. 68, No 23 (03 June 1996), pp.3272-3275, 0003-6951

[5] Brune C., Liu C.X., Novik E.G., Hankiewicz E.M., Buhmann H., Chen Y.L., Qi X.L., Shen Z. X., Zhang S. C., & Molenkamp L.W., (2011) Quantum Hall Effect from the Topological Surface States of Strained Bulk HgTe, *Phys. Rev. Lett.*, Vol. 106, No12 (25 March 2011), pp. 126803-1-4, 1079-7114

[6] Cebulski J., Wo´zny M., & Sheregii E. M., (2013) Reinterpretation of the phonon spectra of the GaAsP alloys, *Phys. Status Solidi* B, Vol. 250, No 8 (August 2013), pp. 1614–1623, 1521-3951

[7] Cestelli Guidi M., Piccinini M., Marcelli A., Nucara A., Calvani P.& Burattini E., (2005), Optical performances of SINBAD, the Synchrotron INfrared Beamline At DAΦNE

[8] *Journal of the Optical Society of America A*, Vol. 22, No 12 (December 2005), pp. 2810-2817, 1084-7529

[9] Cohen M. L. & Chelikowsky J.R., (1989) Electronic Structure and Optical Properties of Semiconductors, in: *Springer Series in Solid-State Science*, *vol. 75*, pp. 1-264, Springer Verlag, 0-387-51391-4, Berlin-Heidelberg

[10] Cowley R.A., (1965) Raman scattering from crystals of the diamond structure, *J. Phys. (Paris)*, Vol. 26, No 11 (November 1965), pp 659-667,

[11] Dornhaus R. & Nimtz G., (1983) The Properties and Applications of HgCdTe Alloys, p.159-2 in: *Springer Tracts in Modern Physics*, *vol. 98,* pp. 1-121, Springer-Verlag, 978-3540120919, Berlin

[12] Delin A. & Kluner T., (2002) Excitation spectra and ground-state properties from density-functional theory for the inverted band-structure systems β-HgS, HgSe, and HgTe, *Phys. Rev. B,* Vol. 66, No 14 (29 July), pp. 035117-1-8, 1550-235X

[13] Gantmacher B. & Levinson Y., (1984) *Carrier scattering in metals and semiconductors (rus.)*, Nauka, 1704060000-063, Moskva

[14] Hart T., Aggarwal R.L. & Lax B., (1970) Temperature Dependence of Raman Scattering in Silicon, *Phys. Rev. B* Vol.1, No 2 (15 January 1970), pp. 638-642, 1550-235X

[15] Ingale A., Bansal M.L. & Roy A.P., (1989) Resonance Raman scattering in HgTe: TO-phonon and forbidden-LO-phonon cross section near the E1 gap, *Phys. Rev. B* Vol. 40, No 18 (15 December 1989), pp. 12353-12358, 1550-235X

[16] Ipatova I.P., Maradudin A.A. & Wallis R.F., (1967) Temperature Dependence of the Width of the Fundamental Lattice-Vibration Absorpion Peak in Ionic Crystals. II. Approximate Numerical Results, *Phys. Rev.* Vol. 155, No 3 (15 March 1967), pp. 882-889, 1550-235X E.J. Johnson E. & Larsen D. M., (1966) Polaron Induced Anomalies in the Interband Magnetoabsorption of InSb, *Phys. Rev. Lett.*, Vol. 16,No7 (11April 1966), pp. 655-669, 1079-7114

[17] de Jong W. A., Visscher L., & Nieuwpoort W. C., *J.* (1997) Relativistic and correlated calculations on the ground, excited, and ionized states of iodine, *The Journal of Chem. Phys.* Vol. 107, No21 (01 December 1997) 9046-9052, 0021-9606

[18] Yu P. & Cardona M., (2010) Fundamentals of Semiconductors: Physics and Materials Properties, 4 Edition, Springer, 978-3-642-00710-1, Heidelberg

[19] Kawamura H., Katayama S., Takano S. & Hotta S., (1974) Dielectric constant and Soft mode in Pb1-xSnxTe, *Solid State Comm*. Vol. 14, No 3 (1 Februar 1974), pp. 259-261, 0038-1098

[20] Kozyrev S.P., L.K. Vodopyanov & R.Triboulet, (1998) Structural analysis of the semiconductor-semimetal alloy Cd 1-x Hg x Te by infrared lattice-vibration spectroscopy, *Phys. Rev. B,* Vol. 58, No 3 (15 July 1998), pp. 1374-1384, 1550-235X

[21] M.Konig, S. Wiedmann, C. Brne, A. Roth, H. Buhmann, L.W. Molenkamp, X. L. Qi & S. C. Zhang, (2007) Quantum Spin Hall Insulator State in HgTe Quantum Wells, *Science*, Vol. 318, No 5851 (20 September 2007), pp. 766-770, 1095-9203

[22] Levinson Y.M. & Rashba E.I., (1973), Electron-phonon and exciton-phonon bound states, *Rep. Progr. Phys.* Vol. 36, No12 (December 1973), pp.1499-1524, 1361-6633

[23] Madelung O., (1996), *Semiconductor Basic Data, 2nd revised Edition*, Springer-Verlag, 3-540-60883-4, Berlin, Heidelberg

[24] Maradudin A.A. & Fein A.E., (1962) Scattering of Neutrons by an Anharmonic Crystal, *Phys. Rev.*, Vol. 128, No12 (15 December 1962), pp. 2589-2596, 1550-235X

[25] M. Marchewka, M. Wozny, J. Polit, V. Robouch, A.Kisiel, A. Marcelli & E.M. Sheregii, (2014), The stochastic model for ternary and quaternary alloys: Application of the Bernoulli relation to the phonon spectra of mixed crystals, *J. Appl. Phys.*, Vol. 115, No 1 (January 2014) pp. 113903-1-15, 0021-8979

[26] Orlita M., Basko D. M., Zholudev M. S.,Teppe F., Knap W., Gavrilenko V. I., Mikhai-lov N. N., Dvoretskii S. A., Neuebauer P., Faugeras C., Barra A-L., Martinez G. & M. Potemski, (2014) Observation of three-dimensional massless Kane fermions in a zinc-blende crystal, *Nature Physics*, Vol. 10, No.3 (March 2014), pp. 233-238, 1745-2473

[27] Polit J., Sheregii E.M, Cebulski J., Robouch B., Marcelli A., Castelli Guidi M., Piccinini M., Kisiel A., Burattini E. & Mycielski A., (2006), Phonon and Vibrational spectra of hydrogenated CdTe, *J. Appl. Phys.*, Vol. 100, No. 1 (July 2006), 013521-1-12, 0021-8979

[28] Polit J., E.M. Sheregii, J. Cebulski, A. Marcelli, B. Robouch, A. Kisiel & A. Mycielski, (2010) Additional and canonical phonon modes in Hg 1−x Cd x Te(0.06≤x≤0.7), *Phys. Rev. B*, Vol.82, No 14 (30 July 2010), pp. 014306-1-12, 1550-235X

[29] Rath S., Jain K.P., Abbi S.C., Julien C. & Balkanski M., (1995) Composition and tem-perature-induced effects on the phonon spectra of narrow-band-gap Hg 1-x Cdx Te, *Phys. Rev. B*, Vol. 52, No 24 (15 December 1995), pp. 17172-17178, 1550-235X

[30] Raptis S. G., Papadopoulos M. G., & Sadlej A. J., (1999) The correlation, relativistic, and vibrational contributions to the dipole moments, polarizabilities, and first and second hyperpolarizabilities of ZnS, CdS, and HgS, *J. Chem. Phys.*, Vol. 111, No. 17 (November 1999), pp. 7904 – 7915, 0021-9606

[31] Schall M., Walther M. & Jepsen P. Uhd, (2001) Fundamental and second-order pho-non processes in CdTe and ZnTe, *Phys. Rev. B*, Vol. 64, No. 15 (3 August 2001), pp. 094301-1-8, 1550-235X

[32] Sheregii E. M. & Ugrin Yu. O. (1992), CdxHg1-xTe phonon-spectra research by means of magnetophonon resonance, *Sol. State Comm.*, Vol.83, No12 (September 1992), pp. 1043-1046, 0038-1098

[33] Sheregii E.M., (1992) Role of Two-Phonon Transitions in Resonance Effects in Semi-conductors, Europhys. Lett., Vol. 18, No. 4 (21 Februar 1992), pp. 325-329, 1286-4854

[34] Sheregii E.M., j.Polit, J. Cebulski, A. Marcelli, M. Castelli Guidi, B. Robouch, P. Calva-ni, M. Piccini, A. Kisiel, I. V. Ivanov-Omskii, (2006), First interpretation of phonon spectra of quaternary solid solutions using fine structure far-IR reflectivity by syn-chrotron radiation, *Infrared Physics & Technology*, Vol. 49, No. 1-2 (September 2006), pp. 13-18, 1350-4495

[35] Sheregii E.M., Cebulski J., Marcelli A. & Piccinini M., (2009) Temperature Depend-ence Discontinuity of the Phonon Mode Frequencies Caused by a Zero-Gap State in HgCdTe Alloys, *Phys. Rev. Lett.*,Vol. 102, No 2 (30 January 2009), pp. 045504-1 – 4, 1079-7114

[36] Sheregii E. M., J. Cebulski, A. Marcelli, M. Piccinini, (2011), Returnable Electron-Pho-non Interaction in the II-VI Compound Alloys, *China J. Phys.*, Vol. 47, No. 1 (February 2011) pp. 214-220,

[37] Sheregii E.M., (2012) High Resolution Far Infrared Spectra of the Semiconductor Al-loys Obtained Using the Synchrotron Radiation as Source, In: *Infrared Spectroscopy-*

*Materials Science, Engineering and Technology*, Prof. Theophanides Theophile (Ed.), pp. 467-492, INTECH, 978-953-51-0537-4, Rijeka

[38]  Sher A., Chen A.B., Spicer W.E. and Shih C.K., (1985), Effects influencing the structural integrity of semiconductors and their alloys, *J. Vac. Sci. Technol*. A Vol. 3, No.1 (January 1985), pp.105-111, 0734-2101

[39]  Szuszkiewicz W., Dynowska E., Grecka J., Witkowska B., Jouanne M., Morhange J.F., Julien C., Hennion B., (1999) Peculiarities of the Lattice Dynamics of Cubic Mercury Chalcogenides *Phys. Stat. Sol. (b)*, Vol. 215, No. 1 (September 1999), pp. 93-98, 1521-3951

[40]  Talwar D.N. & Vandevyver M., (1984) On the anomalous phonon mode behavior in HgSe *J. Appl. Phys.* Vol. 56, No. 9 (September 1984), pp. 2541-2550, 0021-8979

[41]  Talwar D. N., Tzuen-Rong Yang, Zhe Chuan Feng, & Becla P., (2011), Infrared reflectance and transmission spectra in II-VI alloys and superlattices, *Phys. Rev. B,* Vol. 84, No. 21 (8 November), pp. 174203-1-7, 1550-235X

[42]  Wei S.H. and Zunger, (1988), Role of metal d states in II-VI semiconductors, *Phys. Rev. B* Vol. 37, No. 10, pp. 8958-8965, 1550-235X

[43]  Verleur H.W. & Barker A.S., (1966), Infrared Lattice Vibrations in GaAsxP1-x Alloys, *Phys. Rev.* Vol. 149, No. 2 (16 September 1966), pp. 715 – 729, 1550-235X

[44]  Zholudev M., Teppe F., Orlita M., Consejo C., Torres J., Dyakonova N., Czapkiewicz M., Wrobel J., Grabecki G., Mikhailov N., Dvor)etskii S., Ikonnikov A., Spirin K., Aleshkin V., Gavrilenko V., & Knap W., (2012) Magnetospectroscopy of two-dimensional HgTe-based topological insulators around the critical thickness, *Phys. Rev. B,* Vol. 86, No. 22 (16 November 2012), pp. 205420-1-12

# Medical Applications of Infrared Spectroscopy

# An FT-IR Spectroscopic Study of Metastatic Cancerous Bones

J. Anastassopoulou, M. Kyriakidou, S. Kyriazis, T.H. Kormas, A.F. Mavrogenis, V. Dritsa, P. Kolovou and T. Theophanides

Additional information is available at the end of the chapter

## 1. Introduction

Breast cancer is the most frequently diagnosed cancer in women aged 40 to 65 years, with more than 464,000 new cases (13.5% of all cancer cases) per year in Europe [1,2]. Approximately 5% of breast cancer patients have advanced (metastatic) disease at diagnosis. Despite important progress in adjuvant and neoadjuvant therapies, up to 90% of cancer deaths are due to complications arising from metastatic dissemination of the disease [3,4].For patients with established metastatic disease, therapy is usually for palliation.

Metastasis is a complex process, entailing tumor cells acquiring a set of features that allow them to develop new foci of the disease. Its exact mechanism remains unclear. Metastasis has been described as the migration of tumor cells from the primary tumor, followed by intravasation, survival, extravasation of the circulatory system, and progressive colonization of a distant site [5-7]. In a second definition, tumor cell genomic instability occurs that enables invasion and distant organ colonization [8].In another definition, metastasis is described in terms of seed and soil [9]. Tumor cells (seeds) spread widely through the body, but grow only in supportive locations (congenial soil). Thus the various microenvironments (soils) of metastases contribute to the observed heterogeneity [9].

The most common sites of breast cancer metastases are the bones, brain, adrenal glands and other parts of the body [10,11]. Metastatic bone disease alters the mechanical properties of the involved bones, produces painful osteolysis, microfractures, and eventually complete fractures.The extent to which metastases are site specific and the transformation of healthy cells into cancer cells also remain poorly understood. A hallmark of breast cancer metastasis is the redundancy of pathways that mediate the process or its component steps, and theabound of promoting genes[3]. Some pathways contribute to bone metastasis, while other pathways have

been reported to mediate lung and liver metastasis. Advanced next-generation sequencing techniques have also been used to interrogate whole cancer genomes at the single-nucleotide level and have distinguished between mutations in breast cancer metastases [12,13]. However, one metastasis may be distinct from another within the same patient accurate prediction of the molecular profile of metastatic disease by profiling the primary tumor is not feasible. In this setting, novel detection techniques are necessary [14].

Fourier transform infrared spectroscopy is a physicochemical, non-destructive, sensitive and reproducible method which provides important information about changes in the molecular structure of the bone due to the disease [15-29]. The advantage of the method is that it needs small amounts of the sample (only few micrograms) and we could study the sample without any preparation, such as coloring or demineralization as it is done in histopathology, since the spectra are based on individual chemical characteristics of the bone. Another important advantage of the infrared spectroscopy is that the method does not require any preparation of the sample, such as coloring or decalcification, as in methods like histopathology, where the samples are decalcified and labeled with color and are analyzed only the changes in the organic phase of the tissues.In infrared spectroscopy, the spectrum is the sum of all the frequencies of the components present and provides information on all components simultaneously [15-21].

Here within it is presented the influence of cancer on the molecular structure of the constituents of the bone (Hydroxyapatite, Collagen and Protein) and the characterization of the spectral differences between healthy and cancerous bones, in order to have a better insight of the process of the disease.

## 2. Materials and methods

### 2.1. Sample preparation

Although breast cancer metastases to skeleton bones are frequent sites of first distant relapse,however the bone samples are not easy to be obtained. Six bone sections from breast metastatic cancer patients (39 and 65 years), who suffered from breast cancer and underwent a reconstruction with an osteoarticular allograft, were used for the present study. Small amount of fresh bones (cancellous or/compact), were immersed successively in hydrogen peroxide solution ($H_2O_2$) and in acetone, according to a modification method [15-17, 20,30]. Hydrogen peroxide and acetone processing is known to reduce the fat tissue and blood chromophores of fresh bone, but it does not remove the organic components completely.

### 2.2. Sample analysis

#### 2.2.1. Infrared spectroscopy

The conformational and molecular changes of healthy and cancerous bones were recorded using a Nicolet 6700 thermoscientific Transform Infrared (FT-IR) spectrometer, which was connected to an attenuated total reflection (ATR) accessory. This technique is convenient in

this case for the cancerous bones since it is almost impossible to powderize these tissues.Moreover, impregnated with PMMA bone appears less suited, because when remove the plastic there is dangerous to loose important components.

Each absorption spectrum of the samples was consisted of 120 co-added spectra at a resolution of 4 cm$^{-1}$ and all spectra were obtained in the same way in absorption mode in the spectral region 4000-400 cm$^{-1}$.The interpretation of the spectra was done by analyzing the spectra and comparing the spectral data between cancerous and healthy tissues in order to follow and show the characteristic pattern of the disease. Data analysis was performed with the OMNIC 7.3 software.

### 2.2.2. Scanning electron microscope

Scanning electron microscopy (SEM) is also a non-destructive method, which allows the investigation of the surfaces of cancerous bone tissues, without any decalcification, coloring or coating. Under these conditions, there is not any change in chemical bonds between mineral and organic phase of the sample.

The distribution of the morphology of samples and bone mineral content were obtained using the (SEM) equipped with a microanalyzer probe EDX (Electron Dispersive X-rays analysis) from Fei Co, Eindhoven, The Netherlands

### 2.2.3. X-Ray diffraction

X-Ray diffraction, XRD, was used to identify the crystal structure of hydroxyl apatite and the presence of other calcium phosphate salts, which were produced with the progress of the cancer metastasis and development.

Powdered bone diffraction patterns were recorded using a Siemens D-500 X-Ray diffractometer based on an automatic adjustment and analysis system. The diffraction interval was of 2θ 5-80° and scan rate of 0.030°/s.

# 3. Results and discussion

## 3.1. Infrared spectroscopic analysis

In the treatment of breast cancer, the occurrence and growth of distant metastases is the major cause of morbidity and mortality. Long distant metastasis of breast cancer to bones induces micro-fractures changing the patients' quality of life. To understand the mechanism of the cancer cell dispersive and damaging effects which are induced to bone structure is of high interest in order to study the disease. Figure 1 shows the FT-IR spectra of a) healthy radius bones and b) of cancerous bones from a woman (59 years old) with a primary breast cancer.
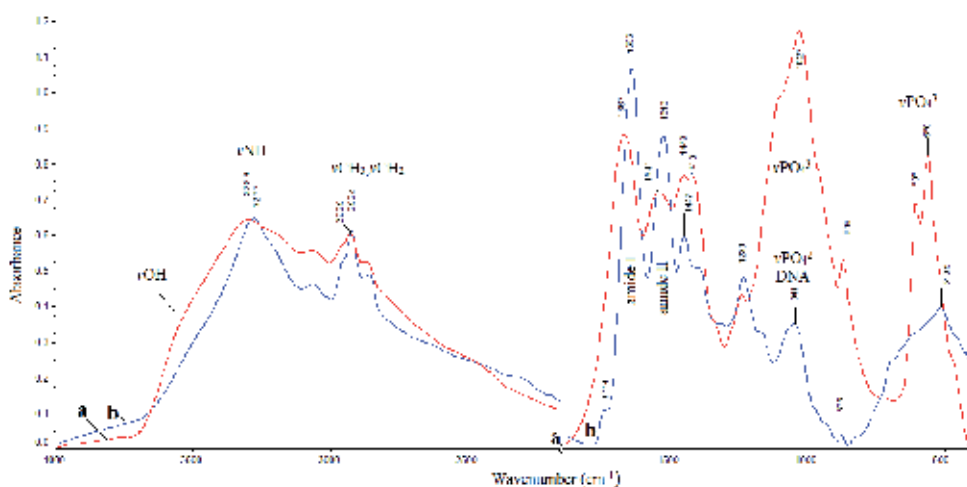
**Figure 1.** FT-IR spectra of a) healthy bone and b) cancerous bone from a 59 years woman with metastatic bone cancer from breast cancer the original site

Comparison of the two spectra showed considerable changes in the whole spectral range of 3600-400 cm⁻¹. The intensity of the shoulder band near 3550 cm⁻¹ for healthy bones was reduced or disappeared in all cancerous bones. Deconvolution of this band showed that it was double with maxima at 3515 cm⁻¹ and 3400 cm⁻¹, which are dominated by the absorption of stretching vibration of $v$OH functional groups of water and hydroxyapatite, respectively [15-17, 19,20]. The intensities of these bands are sensitive at the demineralization of the bones due to disease cancer and they can show the progress of osteolysis. The broad band in the region 3300-3000 cm⁻¹is made up from the two bands at 3209 cm⁻¹ and 3187cm⁻¹, assigned to NH vibrations [15-30]. In cancerous bone spectra the band at 3209cm⁻¹ shifted to higher wavenumbers at 3277 cm⁻¹ and the 3187 cm⁻¹ was reduced in intensity, but it was not shifted. It seems that in cancerous bones the binding of proteins changed in structure and they did not give neither inter-nor intra-molecular hydrogen bonding of the NH hydrogen bonding leading to the result that decalcification takes place and finally the disease changes the secondary molecular structure of the proteins.

The absorption bands of the symmetric and asymmetric stretching vibrations of methyl ($v_{as}CH_3$ and $v_sCH_3$) groups were found at 2965 cm⁻¹ and 2880 cm⁻¹ and of methylene ($v_{as}CH_2$and $v_sCH_2$) were near 2926 cm⁻¹ and 2854 cm⁻¹, respectively [15-31]. These bands did not shift but their intensities increased for cancerous bones. These changes indicated that the environment of lipids, phospholipids and proteins has changed and that the permeability and fluidity of the membranes have increased, due to the damage induced by the disease and demineralization [15-30].

Interesting was the appearance of a new band in the spectra of cancerous bones at about 1745 cm⁻¹, which was assigned to $v$C=O carbonyl stretching vibration of ester carbonyl groups (RO-C=O) and was attributed to formation of aldehydes [31,32]. It is known that aldehydes are recognized as native "cancer markers" [33]. This carbonyl band was also proposed to charac-

terize the apoptotic cells [34]. This particular band indicates that lipid peroxidation was one of the pathways during the process of metastasis of bone cancer and could be used as "marker band" for the progression of the disease.This fact leads also to the hypothesis that the immune-like systemis a contribution to the development of metastasis, in agreement with literature data [34].

Considerable changes were also observed in the region 1700-1500 cm$^{-1}$. This region is known to be characteristic of proteins and is sensitive in order to evaluate the secondary structure of proteins and to distinguish that collagen exists as $\alpha$-helix [15-17,30-32]. A shift to lower frequencies of the absorption band of Amide I of proteins from about 1650 cm$^{-1}$ in healthy bones to 1630 cm$^{-1}$ in cancerous bones was observed. This shift to lower frequencies suggests that the proteins changed their secondary structure from $\alpha$-helix to random coil due to cancer processing. These results were confirmed also from SEM analysis.

Figure 2 shows the morphology of the cancerous bone. One can see that the bone is rich in fibrils, concerning the damage of collagenous and non-collagenous proteins, as well as the demineralization of the bone. The proteins changed their native structure as shown from the arrows on the points of damaged proteins (Fig. 2C). Image J analysis gives the relative intensity of the pixels which correspond to electron density of the proteins (Fig. D & E). The curves show the analyzed regions at the misfolding points.
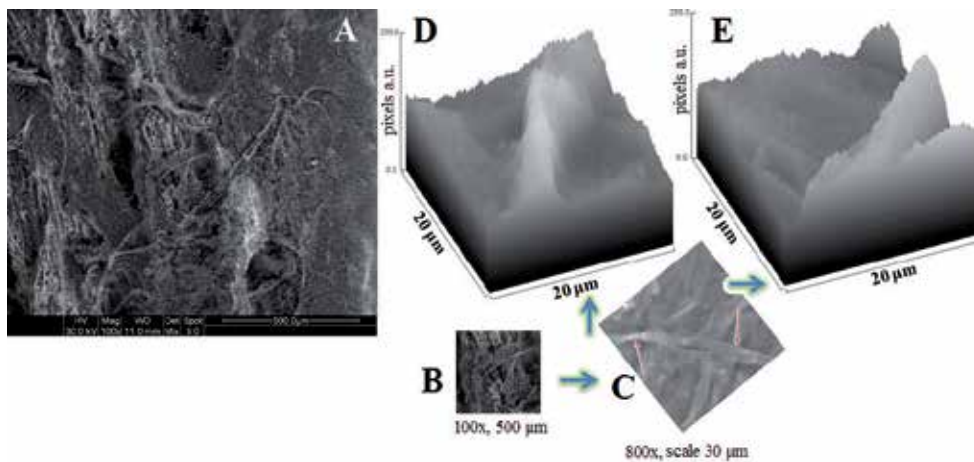


**Figure 2.** SEM morphology of metastatic breast cancerous bone (scale 500 μm, Mag. 100x). B Selected region rich in proteins, C: Higher magnitude 800x (scale 50 μm), which shows the misfolding of proteins. D & E ImageJ analysis of the folding regions

The Amide II band at 1555 cm$^{-1}$, which is consisted from δNH in-plane and $v$CN stretching vibrations, is very sensitive to environmental changes. It was found that the intensity of this band decreases and in almost all patients and sifts to lower wavenumbers.The ratio of the bands of [Amide I$_{1650}$]/[Amide II$_{1550}$] decreases with increasing the grade of cancer and it was found in the patients healthy bones to be equal to 1.11,whereas in the cancer it was 1.3. Although the differences are very small they are significant and it was found also in breast

cancer and colon cancer [18;21].These changes represent the "structural change and abnormality" of proteins, induced from cancer disease, which decrease the probability of remineralization of the bones and thus increases the fragility of the bones.

Figure 1 clearly shows the absorption band at 1418 cm$^{-1}$, which is assigned to stretching vibration of carbonate anions ($v$CO$_3^{2-}$) of hydroxyapatite containing carbonate ions. Thisband is also reduced in intensity confirming the substitution of phosphate anions with carbonates in hydroxyapatite following the total demineralization of cancerous bones [17,20].

The band at about 1040 cm$^{-1}$ refers to stretching vibrations of $v$C-O coupled with the bending vibration of $\delta$C-OH groups of glycogenic bonds [36,37]. We found that the intensity of this band increases in the spectra of cancerous bones. The $v$OH absorption bands are sensitive upon isotopic substitution (deuteration), concerning the substitution of hydrogen atoms with deuterium in the C-OH groups of glucose (spectra not shown here). The increasing amount of glycogenic materials inhibits the mineralization of the bones [38]. From the conformational protein folding changes in combination with the increase glycogenic bonds (starch) it is suggested the production of amyloid-like proteins [39]. The formation of fibrils is also well shown in SEM morphology (Figure 2).

Furthermore, the spectra show characteristic differences between healthy and cancerous bone in the regions 1200-900 cm$^{-1}$and 600-500 cm$^{-1}$, where the phosphate groups ($v_3$PO$_4^{3-}$) of hydroxyapatite absorb. The characteristic bands of $v_3$PO$_4^{3-}$and $v_4$PO$_4^{3-}$in cancerous bones have been dramatically decreased due to cancer, proving that osteolysis of the bones is taking place. These findings show that in cancerous bone a progressive mineral deficiency occurs in agreement with clinical and histological analyses indicating that the bone destruction is mediated by the osteoclasts [40]. Moreover, in the fingerprint region of the cancerous spectra between 1200-900 cm$^{-1}$ are coupled also the bands which are assigned to phosphodiester C-O-PO$_2^-$of DNA [23-25,41-43]. These bands were not observed in normal bone tissue, maybe they were masked because of high concentration of hydroxyapatite.

## 3.2. FT-IR spectra after removal of organic components

To understand further the mechanisms of osteolysis of bone from metastatic cancer the boneswere washed using organic solvents to eliminate the organic mass of the bones. Figure 3 shows the spectra of the bone before (spectrum a) and after elimination of dissolved organic components (spectrum b).

Comparison of the two spectra shows that after treatment with hexane all the organic components with low molecular weight have been dissolved and disappeared from the sample and are not shown in their spectra. It is interesting to note that the bands in the region 1100-900 cm$^{-1}$ and 700-500 cm$^{-1}$, where the bands of hydroxyapatite absorb, the bands of $v$PO$_4^{3-}$have almost disappeared after treatment with hexane. From these findings it was suggested that the bands haveresulted from other phosphate proteins, which also have phosphate groups with hydroxyapatite or fragments of phospholipids. However, these bands do not show that there is present biological hydroxyapatite. In addition, XRD analysis revealed that cancerous bones were not consisted from biological hydroxyapatite, but there was apatite rich in organic phase.
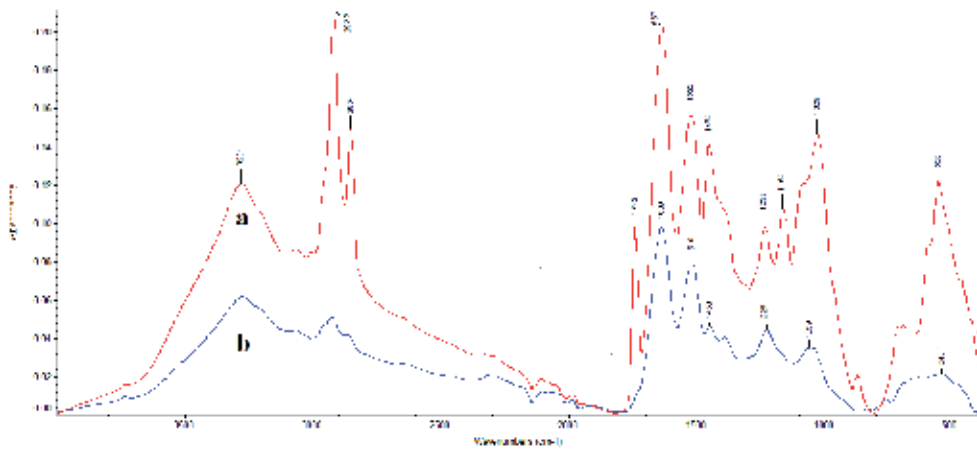
**Figure 3.** FT-IR spectra of cancerous bone tissues in the region 4000-400 cm$^{-1}$; a: without any preparation, b: after elimi-
nation of the organic components of the bone. The arrow shows free calcium phosphate.

The size of the crystals at $2\theta=25,85°$ was found to be 15 nm much smaller than the normal bone's
hydroxyapatite which is 20-25 nm [44].

The SEM analysis of cancerous bones before treatment with hexane is given in Figure 4A. The
relative element concentration of the white spot and of the dark region, are shown in the Figure.
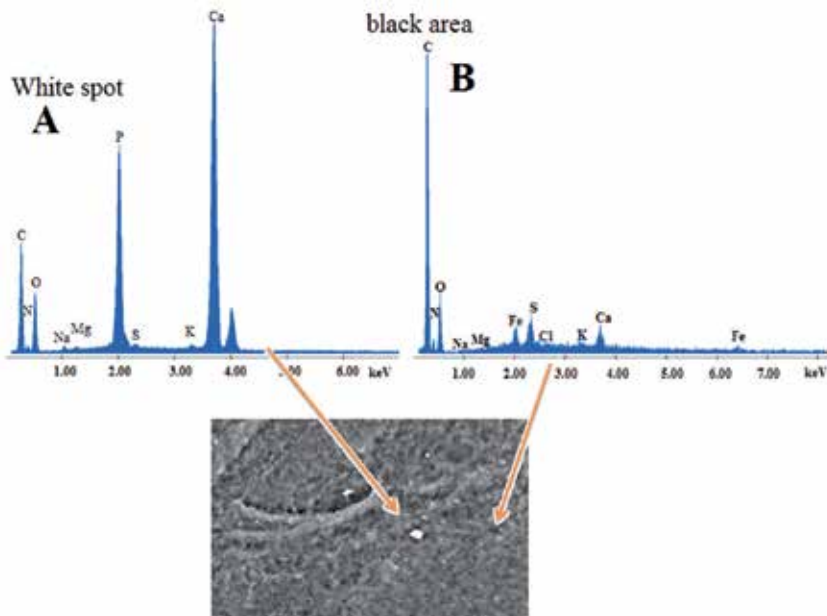


**Figure 4.** SEM-EDXmorphology and composition of metastatic breast cancerous bone before treatment: A; on white
spot and B; on black area. Scale 100 μm, Mag 400x

From EDX chemical analysis it was found that the extent area of the bone was poor in calcium and only the spread white spots were rich in minerals. By washing the bone with hexane the morphology of the surface changed (Figure 5). Figure 5 gives the SEM morphology of the bone after washing it with hexane. Figure 5Agives the relative concentration of the chemical elements of the white spots. It is obvious that the concentration of calcium of white spot is significantly reduced. The same picture was found for the extent area of the sample, where the calcium has almost disappeared (Figure 5B).
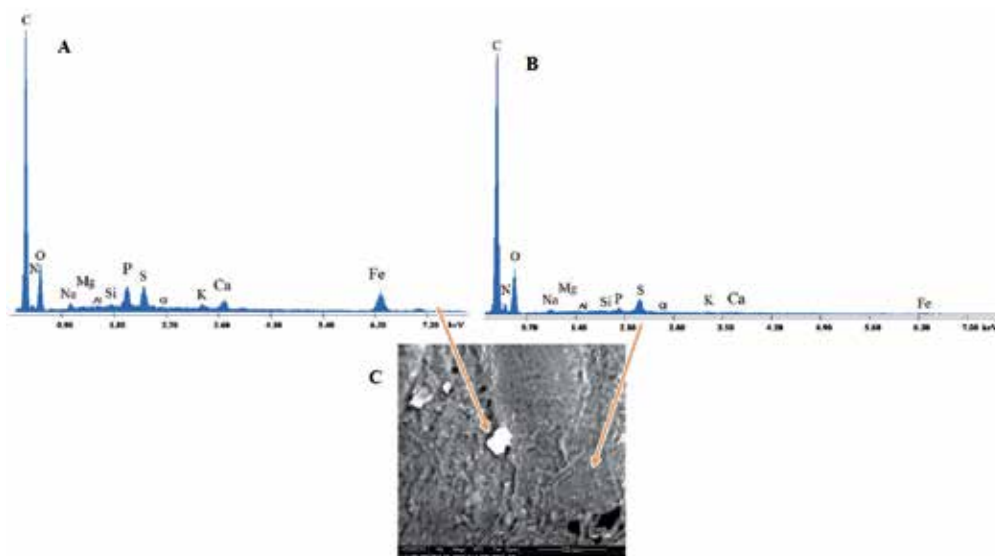


**Figure 5.** SEM-EDX results, composition of metastatic breast cancerous bone after treatment A; on white spot and B; on balk area and C SEM morphology of the tissue. Scale 100 µm, Mag 400x

These SEM results are in agreement with infrared spectroscopic results, which suggest that the mineral phase maybe a mixture of calcium salts of phosphate together with calcium carbonate, but not a biological hydroxyapatite. It was found from XRD analysis at $2\theta=25,85°$ that the crystal of hydroxya showed also that the size of the hydroxyapatite crystals is 15 nm. This size is smaller than in healthy bones, which in adults was found 20-25 nm [44, 45].

## 4. Conclusions

The results obtained here using FT-IR spectroscopy and SEM analysis have shown that cancerous bone from metastatic breast cancer leads to considerable changes in bone density, especially in the structure of biological apatite that decreases dramatically or even it is destroyed due to osteolysis.Proteins change their secondary structure from $\alpha$-helix to random coil and aldehydes are produced during cancer metabolism.The intensity of the aldehyde band indicates the magnitude of the damage caused by the cancer. Furthermore, It is also noticed

that the proportion of inorganic mass is reduced in comparison to the organic matrix upon cancer invasion of the bones.

Furthermore, FT-IR spectroscopy can provide more information than histopathology, since it does not need any decalcification for analysis. From a clinical point of view, major disadvantages of bone decalcification are the laborious procedure that proceeds only slowly with incubation times up to several weeks depending on the extent of mineralization, the frequent loss of immune-reactivity, and the acid hydrolysis of DNA. In addition, excessive decalcification may lead to negative or non-diagnostic biopsy of the bone specimen (Rey, 1991). In this case, FT-IR spectroscopy is a rapid technique and it provides much more information compared to histology for a fast diagnosis of bone tumors.

## Author details

J. Anastassopoulou[1*], M. Kyriakidou[1], S. Kyriazis[1], T.H. Kormas[2], A.F. Mavrogenis[3], V. Dritsa[1], P. Kolovou[1] and T. Theophanides[1]

*Address all correspondence to: ianastas@central.ntua.gr

1 National Technical University of Athens, Chemical Engineering Department, Radiation Chemistry & Biospectroscopy, Athens, Greece

2 Anticancer Hospital "AgiosSavvas", Orthopaedic Department, Athens, Greece

3 First Department of Orthopaedics, Athens University Medical School, ATTIKON University Hospital, Athens, Greece

## References

[1] Malvezzi M, Bertuccio M, Levi P, LaVecchia F, Negri E. European cancer mortality predictions for the year 2013. Annals of Oncology 2013; 24(3): 1–9.

[2] Ferlay J, Steliarova-Foucher E, Lortet-Tieulent J, Rosso S, Coebergh JWW, Comber H, Forman D, Bray F. Cancer incidence and mortality patterns in Europe: Estimates for 40 countries in 2012. European Journal of Cancer 201; 49: 1374– 1403.

[3] Nguyen DX, Bos PD, Massagué J. Metastasis: from dissemination to organ-specific colonization. Nat Rev Cancer 2009; 9: 274-284.

[4] Delea T, Langer C, McKiernan J, Liss M, Edelsberg J, Brandman J, Raut M,Oster G. The cost of treatment of skeletal-related events in patients with bone metastases from lung cancer. Oncology 2004; 67: 390-396.

[5]    Steeg PS. Tumor metastasis mechanistic insights and clinical challenges. Nat Med 2006; 12: 895-904.

[6]    Welch DR. Do we need to redefine a cancer metastasis and staging definitions? Breast Disease 2006; 26: 3-12.

[7]    Comen E, Norton L, Massagué J. Clinical implications of cancer self-seeding. Nature Reviews Clinical Oncology 2011; 8: 369-377.

[8]    Klein CA. Parallel progression of primary tumours and metastases. Nat Rev Cancer 2009; 9:302-312.

[9]    Paget S. The distribution of secondary growths in cancer of the breast. Cancer Metastasis Rev 1989;8:98-101.

[10]   Shuker DEG. The Cancer Clock. In: Missailidis S.(ed), J Wiley & Sons, Ltd., 2007. p. 3-24.

[11]   Lu C, Onn A,Vaporciyan AA, Chang JY, Glisson BS, Wistuba II, Rothand JA, Herbst RS.Cancer Medicine. In: Hong WK, Bast RC, Hait WN, Kufe DW, Pollock RE, Weichselbaum RR, Holland JF, Frei E.(eds). Holland-FreiPeople's Medical Publishing House-USA: Shelton, CT, 2008. p999-1043.

[12]   Shah SP, Morin RD, Khattra J, Prentice L, Pugh T, Burleigh A, Delaney A, Gelmon K, Guliany R, Senz J, Steidl C, Holt RA, Jones S, Sun M, Leung G, Moore R, Severson T, Taylor GA, Teschendorff AE, Tse K,Turashvili G, Varhol R, Warren RL, Watson P, Zhao Y, Caldas C, Huntsman D, Hirst M, Marra MA, Aparicio S. Mutational evolution in a lobular breast tumour profiled at single nucleotide resolution. Nature 2009; 461:809-813.

[13]   Ding L, Ellis MJ, Li S, Larson DE, Chen K, Wallis JW. Genome remodelling in a basal-like breast cancer metastasis and xenograft. Nature 2010; 464: 999-1005.

[14]   Marino N, Woditschka S, Reed LT, Nakayama J, Mayer M, Wetzel MP, Steeg PS. Breast cancer metastasis: issues for the personalization of its prevention and treatment. American Journal of Pathology 2013; 183(4):1084-95.

[15]   Petra M, Anastassopoulou J, Theologis T, Theophanides T. Synchrotron micro-FT-IR spectroscopic evaluation of normal paediatric human bone. Journal of Molecular Structure 2005; 733: 101-110.

[16]   Kolovou P, Anastassopoulou J. Synchrotron FT-IR spectroscopy of human bones.The effect of aging. In : V. Tsakanov and H. Wiedemann (eds), Brilliant Light in Life and Material Sciences. Springer; 2007. p. 267-272

[17]   Anastasssopoulou J, Kolovou P,Papagelopoulos P, Theophanides T. In:heophanides T.(ed). Infrared Spectroscopy/Book 2, Intech Publications.2012. p259-271

[18]   Anastassopoulou J, Boukaki E, Arapantoni P, Valavanis C, Konstadoudakis S, Conti C, Ferraris P, Giorgini G, Sabbatini, S, Tosi G. In: Tsakanov V. and Wiedemann H(eds), Brilliant Light in Life and Material Sciences, Springer, 2008. p. 273-278.

[19] Anastassopoulou J, Kolovou P, Mavrogenis A. Bone and Cancer. A synchrotron micro-infrared study. Metal Ions in Biology and Medicine 2008; 10: 210-213.

[20] Anastassopoulou J, Kyriakidou M, Mavrogenis AE, Papagelopoulos PJ, Theophanides T. Demineralization of bones due to breast cancer metastasis: an Infrared study. Metal Ions in Biology and Medicine 2011;11:123-126.

[21] Conti C, Ferraris P, Giorgini E, Rubini C, Sabbatini S, Tosi G, Anastassopoulou J, Arapantoni P, Boukaki E, Theophanides T, Valavanis C. FT-IR Microimaging Spectroscopy:Discrimination between healthy and neoplastic human colon tissues. Journal of Molecular Structure 2008; 881: 46-51.

[22] Theophanides T, Angiboust JP, Manfait M. In: Twardowski H.(ed.) Spectroscopic and Structural Studies of Biomaterials I: Proteins. Wilmslow: Sigma Press; 1988.

[23] Theophanides T. Infrared and Raman Spectra of Biological Molecules. NATO Advanced Study Institute, Dodrecht: D. Reidel Publishing Co; 1978.

[24] Theophanides T. Fourier Transform Infrared Spectroscopy. D. Reidel Publishing Co. Dodrecht; 1984.

[25] Theophanides T, Rizzarelli E. Chemistry and Properties of Biomolecular Systems, Topics in Molecular Organisation and Engineering, Kluwer Academic Publishers, Dodrecht, The Netherlands,1991.

[26] Theophanides T, Anastassopoulou J, Fotopoulos N. Fifth International Conference on the Spectroscopy of Biological Molecules, Kluwer Academic Publishers, Dodrecht,.The Netherlands;1997.

[27] Theophanides T. Infrared Spectroscopy-Life and Biomedical Sciences. Vol.I InTech, open science; 2012.

[28] Theophanides T. Infrared Spectroscopy Materials Science, Engineering and Technology Vol. II, In Tech open science;2012.

[29] Dritsa V. FT-IR spectroscopy in medicine. In: Theophanides T. (ed). Infrared Spectroscopy-Life and Biomedical Sciences, intech publishers;2012.

[30] Dritsa V, Pissaridi K, Koutoulakis E, Mamarelis I, Kotoulas C, Anastassopoulou J. An Infrared spectroscopic study of aortic valve. A possible mechanism of calcification and the role of magnesium salts. In Vivo 2014; 84: 91-98.

[31] Anastassopoulou J, TheophanidesT. Raman studies of model vesicle systems. Journal of Applied Spectroscopy 1990; 44:523-525.

[32] Mamarelis I, Pissaridi K, Dritsa V, Kotileas P, Tsiligiris V, Anastassopoulou J. Oxidative Stress and Atherogenesis. An FT-IR Spectroscopic Study. In Vivo 2010; 24: 883-888.

[33] Ginestier C, Hur MH, Charafe-Jauffret E, Monville F, Dutcher J, Brown M, Jacquemier J, Viens P, Kleer CG, Liu S, Schott A, Hayes D, Birnbaum D, Wicha MS, Dontu G.

ALDH1 is a marker of normal and malignant human mammary stem cells and a predictor of poor clinical outcome.Cell Stem 2007; 1: 555–567.

[34]   Umegaki K, Sugisawa A, Shin SJ, Yamada K, Sano M. Different onsets on oxidative damage to DN and lipids in bone marrow and liver in rats given total body irradiation. Free Radical Biol. Med. 2001; 31: 1066-1074.

[35]   Nusblat LM, Dovas A, Cox D. The non-redundant role of N-WASP in podosome-mediated matrix degradation in macrophages. Eur. J. Cell Biology 2011; 90: 205-212.

[36]   Yano K, Ohoshima S, Shimizu Y, Moriguchi T, Katayamac H. Evaluation of glycogen level in human lung carcinoma tissues by an infrared spectroscopic method. Cancer Letters 1996; 110: 29-34.

[37]   Theophanides T. Fourier Transform Infrared Spectra of Calf Thymus DNA and its Reactions with Anticancer Drug cis-platin. Applied Spectroscopy, 1981;35: 461-465.

[38]   Buckwalter J, Einhorn M, Cooper R, Recker R. Bone Biology. Journal of Bone Joint Surgery 1995; 77-A: 1256-1283.

[39]   Anastassopoulou J, Kyriakidou M, Kyriazis S, Dritsa V, Kormas Th. Protein folding and cancer. Anticancer Research 2014; *in press*

[40]   Guise TA. Molecular Mechanisms of Osteolytic Bone Metastases. Cancer 2000; 88: 2892-2898.

[41]   Tajmir-Riahi HA, Theophanides T. An FT-IR Study of DNA and RNA Conformational Transitions at Low Temperatures. Journal of Biomolecular Structure and Dynamics 1985; 3: 537-542.

[42]   Theophanides T, Tajmir-Riahi HA. Flexibility of DNA and RNA upon binding to different Metal Cations. An Investigation of the B to A to Z Conformational Transition by Fourier Transform Infrared Spectroscopy. Journal of Biomolecular Structure and Dynamics 1985; 2: 995-1004.

[43]   Anastassopoulou J, Theophanides T. Aquation of metal ions and infrared and Raman spectra of metal complexes and their interaction with DNA components, in insights into vibrational spectroscopy of nucleic acids and their complexes. In:Muntean CM, Bratu I. (eds)2009;p 47-66.

[44]   Meneghini C, Dalconi MCh,Nuzzo S, Mobilio S,Wenk RH. Rietveld Refinement on X-Ray Diffraction Patterns of BioapatiteinHuman Fetal Bones, Biophysical J. 2003;84: 2021–2029.

[45]   Petra M. Infrared ans micro-infrared spectroscopic studies of bones. Comparison between pathological and artificial bones, PhD Thesis, 2003. in Greek

# Enamel Structure on Children with Down Syndrome — An FT-IR Spectrosocpic Study

V. Dritsa, D. Sgouros, K. Pissaridi, P. Bochlogyros,
M. Kyriakidou and V. Mamareli

Additional information is available at the end of the chapter

## 1. Introduction

Dental enamel and dentin comprise natural hydroxyapatite (HAP), including inorganic and organic compounds, define the quality and tolerance of these tissues. Enamel is the hardest tissue and differs significantly from dentin in organic and inorganic composition and structural organization. Enamel is composed of long and narrow crystals of carbonated hydroxyapatite, which are packed into parallel arrays. The organization of hydroxyapatite crystals during enamel formation regulates on the extracellular matrix proteins such as amelogenin,proteinases, enamelins, ameloblastins and amelotin [1, 2]. Despite the low abundance of these proteins, they play essential roles in controlling the nucleation, growth, and organization of hydroxyapatite crystals. Specifically, enamelin is phosphorylated enamel, specific glycoprotein, which may function as nucleation sites and substantially promote the apatite crystal growth [3]. Dentin is mainly composed of hydroxyapatite, an organic matrix rich in type I collagen and fluid which is similar to plasma. Due to its high organic and lower crystallinity, dentin is more porous and acid soluble tissue [4].

The development of dental diseases is attributed to the interaction of enamel with the oral environment, saliva and microorganisms. Enamel due to its highly mineralized structure is prone to microbial attack and can be dissolved and solubilized by acidic agents. Microbial adhesion to tooth surfaces, specifically enamel salivary pellicle is a general prerequisite for initiation of plaque formation. Microbial multiplication is the dominant feature in the build-up of dental plaque [5]. Plaque is a biofilm of densely packed bacteria, which regulates the exchange of nutrients and products of metabolism and demineralization between saliva and tooth surface. The pattern of bacterial colonization is dependent on the surface structure and topographic features of the tooth [6, 7]. Among the factors that affect plaque mineralization

and calculus formation, calcium plays an important role. Calcium is involved in the stabilization of the lipopolysaccharide (LPS) that constitutes the major component of the surface of gram-negative bacteria [8].

Due to the early stage of tooth formation, tooth morphology is related to genetic factors. Individuals with hereditary disorders such as Down syndrome (DS) have remarkably small teeth. The antero-posterior shortened palate, microdontia of permanent dentition, while some primary teeth are larger, altered crown morphology and shape, taurodontism and hypodontia spacing, agenesis, hypoplasia and hypocalcification are some common dental characteristics associated with DS [9-11]. Many studies have described that hypoplasia of enamel results in a reduced amount of enamel matrix and a decreased opacity of enamel layer, in patients with Down syndrome [9].

FT-IR spectroscopy has proven to be a fundamental and valuable technique in biology and medicine due to its high sensitivity to detecting changes in the functional groups belonging to tissue components such as lipids, proteins and nucleic acids [12]. It has been successfully applied in the study of various human tissues such as mineralized tissue, breast cancer, colon cancer, arteries, cartilage [13-17].

In this work, we analyze the structural and chemical characteristics of enamel as well as the appearance of bacteria in extracted teeth from children with dental abnormalities. Fourier transform infrared (FT-IR) spectroscopy and Scanning Electron Microscopy (SEM) were used for the determination of the structural changes in teeth. Teeth of children with no adverse medical history were used as a control group. Supragingival calculus was taken from both groups and was analyzed by spectroscopic analysis in order to investigate the influence of disease on the presence of bacteria.

## 2. Materials and methods

### 2.1. Teeth preparation

Ten teeth extracted from children (6-14 years) with Down syndrome were used in this study. Five teeth of children with no adverse medical history and five teeth from adults were used as a control group (Scheme 1).



**Sheme 1.** The extracted teeth were divided in four sections.

All extractions were done for orthodontic or periodontal reasons. After extraction, the teeth were rinsed with distilled water to remove blood remnants. Each tooth was carefully split into two with a low speed diamond saw. The enamel was separated using a hand–guided dental saw. The milled teeth powdered for used for FT-IR analysis.

### 2.2. FT-IR spectra

The FT-IR spectra were obtained with a Nicolet 6700 Thermoscientific spectrometer, connected to an attenuated total reflection, ATR, accessory. For each region a series of spectra were recorded and every spectrum consisted of 120 co-added spectra at a resolution of 4 cm$^{-1}$ and the OMNIC 7.1 software was used for data analysis. All the spectra for each patient and region were obtained in the same way.

### 2.3. Scanning Electron Microcopy — SEM

Analysis of teeth morphology was performed by Scanning Electron Microcopy–SEM using a Fei Co at an accelerating potential 25 kV. Qualitative elemental data analysis of the samples was determined by EDX (Energy-dispersive X-ray spectroscopy).

## 3. Results and discussion

### 3.1. FT-IR spectroscopy

Figure 1 shows the comparison of the representative FT-IR spectra of enamel in healthy and DS patients. The spectra provide distinct features for the determination of the chemical composition and structure of the teeth.
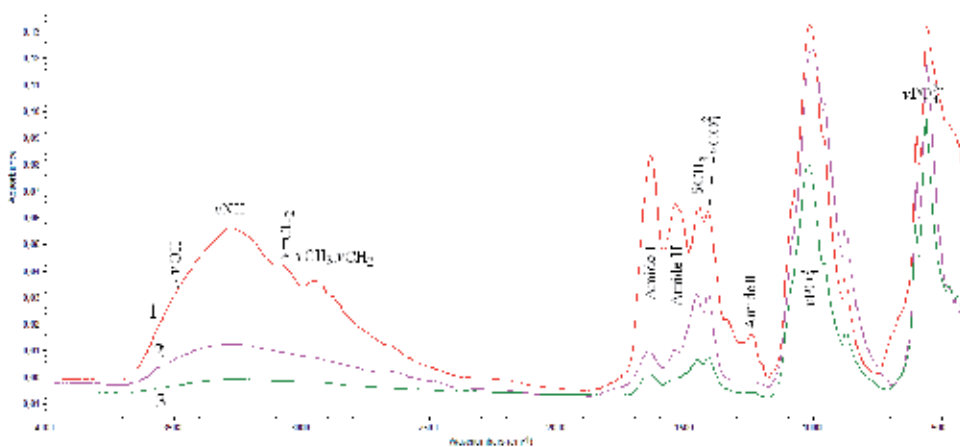


**Figure 1.** FT-IR absorption spectra of enamel obtained from healthy (1), DS (2) and adult (3) in the region 4000-400 cm$^{-1}$.

In the region 4000-2500 cm$^{-1}$, enamel of DS patient showed a broad band at 3397 cm$^{-1}$, which is attributed to stretching vibration of hydroxyl group ($v$OH) of hydroxyapatite and crystalline water. In normal enamel, the absorption band at 3301 cm$^{-1}$ shows a red shift compared to that of DS spectra, concerning that this band is assigned to hydroxyl group $v$OH-of hydroxyapatite. A second band was also determined at 3290 cm$^{-1}$ due to the adsorption of the stretching vibration $v$NH group of Amide I. The band at 3070 cm$^{-1}$ is assigned to the olefinic or aromatic stretching vibration of $v$CH group of aminoacids of collagenous proteins [18-20]. In the region 3000-2800 cm$^{-1}$, the bands of antisymmetric and symmetric stretching vibrations of methyl ($v$CH$_3$) and methylene ($v$CH$_2$) groups of enamelin and teeth proteins were indicated[12,20]. In normal enamel the absorption band at 3301 cm$^{-1}$shows a red shift compared to that of DS spectra, concerning that this band is assigned to hydroxyl group $v$OH-of hydroxyapatite. A less intense band was observed in adult enamel improving the lower concentration of organic phase in accordance with literature data [13, 16, 21].

In the region 1800-400 cm$^{-1}$ of the infrared spectra of enamel the observed absorption bands at 1651 cm$^{-1}$are dominated to Amide I group of proteins. In DS patients' spectra enamel indicated an intense band, which reveals that the mineralization of enamel has not been properly formed, recognized as an"*imperfect osteogenesis*" due to collagen defects [9]. Despite the fact that the level of collagen proteins is not rich, a low band was also indicated in the case of the control group, resulting that collagen is one of the basic components of enamel [1, 4]. The amide II absorption band was shown at 1544 cm$^{-1}$and had the highest absorbance in DS enamel. It is the second band of the peptide bond, and it arises mainly from the NH in-plane bending and the –CN stretching vibration[12-21]. The Amide II band in enamel confirms that its organic substrate consists of collagen proteins. The analysis of the spectra by Fourier self-deconvolution was used to enhance resolution in the region 1800-1500 cm$^{-1}$ (Fig.2).
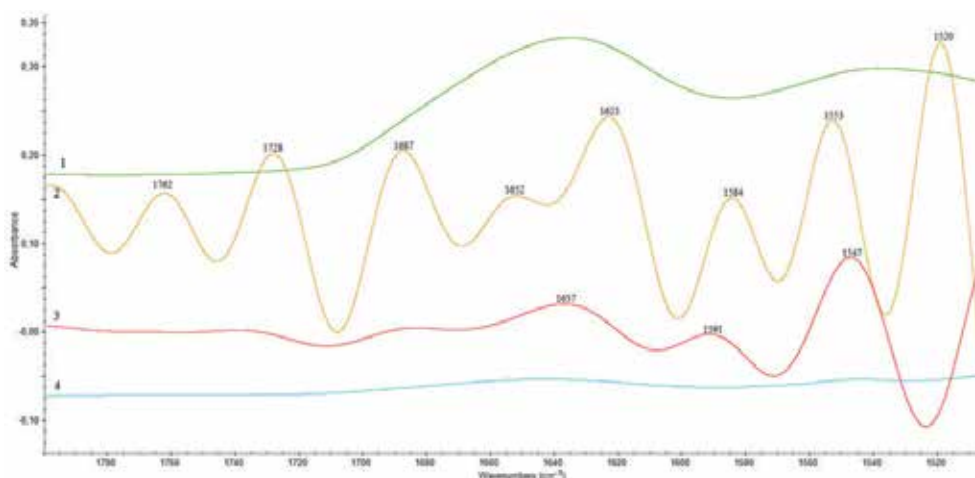


**Figure 2.** FT-IR spectra and deconvolution analysis in the region 1800-1500 cm$^{-1}$1)DS enamel2) Deconvolution analysis of DS enamel 3) Deconvolution analysis of healthy enamel 4) Healthy enamel.

Deconvolution of DS enamel revealed a number of absorptions in the amide bands. The band at 1762 cm$^{-1}$ is attributed to stretching vibration ofcarboxyl groups(-COO$^{-}$). The shift of this band is related to the Ca$^{2+}$binding to COO$^{-}$groups [1].

The band at 1728 cm$^{-1}$ is due to the stretching vibration of the carbonyl group-C=O of enamelin collagenous proteins [3]. The broad band in the region 1700–1600 cm$^{-1}$ is Amide I band, constituted from the bands at 1687 cm$^{-1}$, 1652 cm$^{-1}$ and 1623 cm$^{-1}$. The amide I band at 1652 cm$^{-1}$ is indicative of $\alpha$-helical structure, although part of the absorption at this frequency also corresponds to random coil structure at 1623 cm$^{-1}$ and antiparallel $\beta$-sheet at 1687 cm$^{-1}$ [3, 15]. The decreased intensity of the characteristic band of $\alpha$-helix structures in combination with the increased of those of $\beta$–sheet and carboxyl group band suggested that the high concentration of calcium leads to conformational changes of enamelin.

The band at 1584 cm$^{-1}$ is assigned to asymmetric stretching vibration of carboxyl groups ($v$COO$^{-}$) of proteins. The characteristic absorption band of Amide II due to the stretching vibrations C-N and bending vibration $\delta$N-H was detected at about 1553 cm$^{-1}$.The band at 1520 cm$^{-1}$ is related to the vibration of the tyrosine side chains [22].

Due to the high absorption of amide bands, DS enamel is accompanied by a high content of organic matrix and decrease in mineralization which leads to deficient enamel formation (hypominerilization) [22]. On the contrary the deconvolution analysis of healthy enamel revealed three bands at lower frequencies 1637 cm$^{-1}$, 1591 cm$^{-1}$ and 1547 cm$^{-1}$, which are assigned to the vibrations of Amide I, carboxyl groups ($v$COO$^{-}$) and Amide II of proteins, respectively. These spectral results are in agreement with the fact that enamel is characterized by a low abundance of proteins [1-4].

The band at 1463 cm$^{-1}$corresponds to the bending vibration of $\delta$CH$_2$group which are overlapped from the absorption bands of carbonate group $v_3$CO$_3^{2-}$of hydroxyapatite. The band at 1408 cm$^{-1}$in DS enamel and 1414 cm$^{-1}$for control enamel correspond to the stretching vibration of COO$^{-}$and $v_3$CO$_3^{2-}$ions. DS enamel showed an intense band at 1243 cm$^{-1}$, which matched the spectra pattern of Amide III (in plane N-H bending and C-N stretching vibrations) [23]. No relative band was observed for healthy enamel.

The phosphate ion, PO$_4^{3-}$, is the principal molecular species giving rise to the HA absorbance in the region 900-1200 cm$^{-1}$ (Fig. 3).

The bands at 1030 cm$^{-1}$in control enamel and 1014 cm$^{-1}$ in DS enamel are assigned to the antisymmetric stretching mode of phosphate ions $v_{3as}$PO$_4^{3-}$of hydroxyapatite group PO [16, 20, 24]. The band shift to lower wavenumbers is an indicator of the smaller crystals in Down syndrome patients. Furthermore, the shoulder band which is shown in the spectra of healthy enamel at 1085 cm$^{-1}$ is attributed to antisymmetric stretching vibration of hydroxyapatite $v_3$PO$_4^{3-}$group. This band in DS enamel spectra showed a red shift at 1099 cm$^{-1}$ concerning less mature enamel, due to the molecular structure and development of mineral environment, the crystallinity and crystal size [25]. The shoulder bands at 966 cm$^{-1}$ and 960 cm$^{-1}$ for DS enamel and control enamel, respectively, are assigned to the antisymmetric stretching $v_1$PO$_4^{3-}$vibration [3, 16, 21].
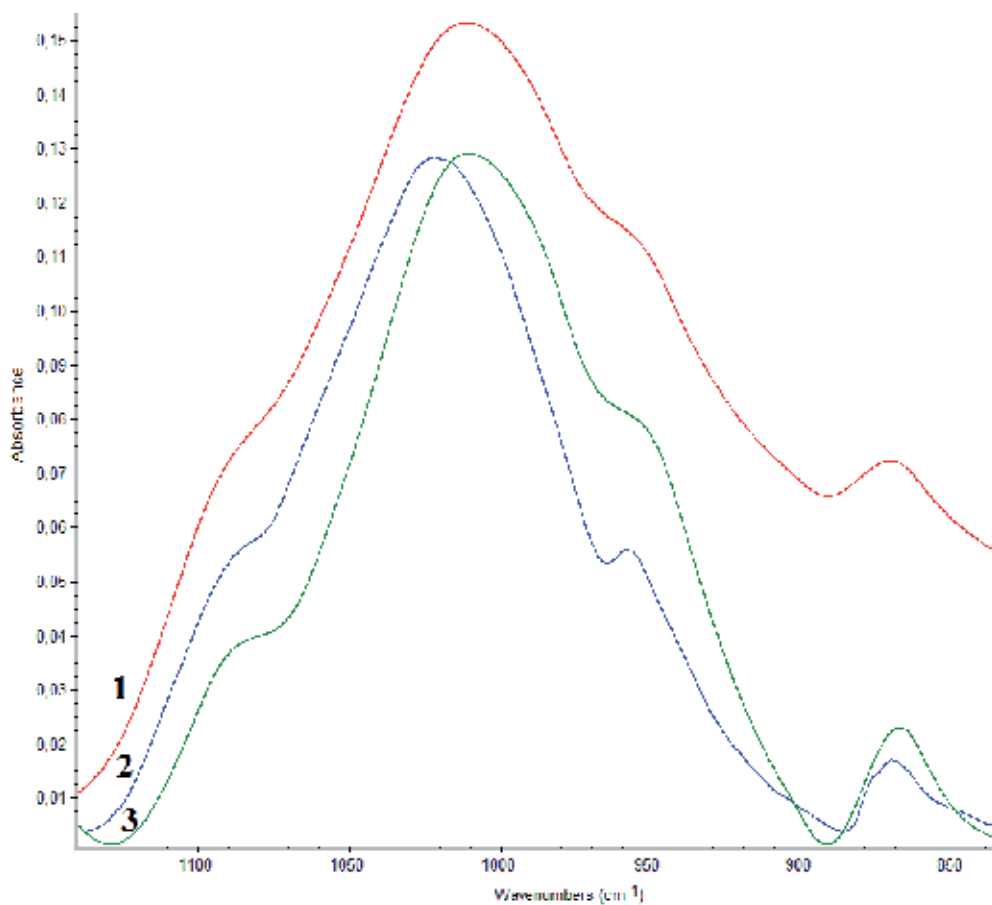
**Figure 3.** FT-IR absorption spectra of enamel obtained from; (1) DS (2) adult and (3) control children in the region 1200-800 cm$^{-1}$.

The absorption band at about 874 cm$^{-1}$ present at three samples is attributed to the stretching vibration of carbonate ions $v_2CO_3^{2-}$. These data lead to the result that calcium carbonates exists in type B and have replaced phosphate ions $vPO_4^{3-}$in hydroxyapatite [17]. The following bands, at 604 and 567 cm$^{-1}$in enamel are due to the bending vibration of phosphate ions $v_4PO_4^{3-}$(O–P–O) [13, 17]. The spectra data confirmed that enamel consists mainly from inorganic compounds due to the low intensity of the amide bands of proteins in the region 1650-1240 cm$^{-1}$.

To the contrary, DS enamel contains organic compounds, as it is shown from the presence of the amide bands of collagen proteins. In the primary teeth, the presence of carbonate ions of calcium is more intense in comparison with the older teeth as it was demonstrated by the bands at 1455 cm$^{-1}$ and 874 cm$^{-1}$. Finally, DS hydroxyapatite crystals are smaller in size in comparison those of health enamel and the crystallization has changed from biological to amorphous or mineral hydroxyapatite [13, 24, 25].

### 3.2. SEM analysis

SEM–EDX has been widely used to evaluate the morphology and elemental content of dental enamel. Significant differences were revealed between SEM images in the control enamel and DS enamel. Surface SEM images of enamel are shown in figure 5. The normal enamel indicated an ordered appearance with hydroxyapatite crystals forming rods and interrod enamel (Fig 4A &B) [28].
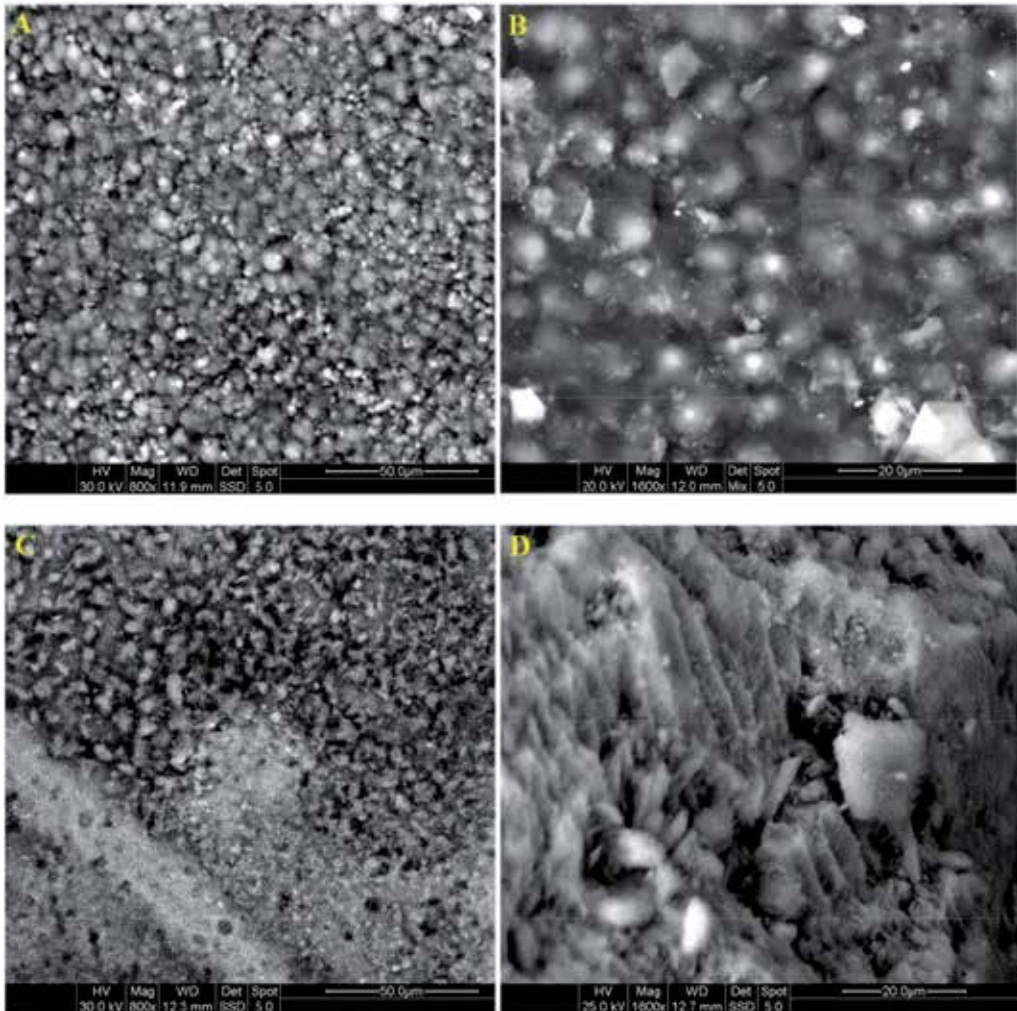


**Figure 4.** SEM imaging of surface enamel. A) Outer enamel layer in control children (800x magnification) B)Normal enamel typically displayedand well-organized crystallites (1600x magnification) C) Outer enamel layerin DS children (800x magnification) D)DS Enamel demonstrated area of amorphous material (1600x magnification).

In contrast, DS enamel was disorganized, the crystals were irregularly orientated and difficult to distinguish (Fig. 4C). At higher magnification, DS enamel has irregularly shaped porous

and prismatic structure. There were also observed white mineralized zones in enamel surface due the transformation of hydroxyapatite from biological to mineral structure.

This was also confirmed from the FT-IR spectra due to the increase of Amide III and $\delta CH_2$ bands. Amorphous material that did not demonstrate any crystallite was observed in the DS teeth but not in any of the control teeth examined (Fig.4D).

EDX analysis was used to determine the elemental components in enamel tissues. Apart from Ca and P which are the main components of hydroxyapatite, Na, Mg and Cl were also indicated in the analysis. Carbon and oxygen comes from the organic matrix and carbonate ions. The ratio of Ca/ P ranged from 1.91 to 2.04 in normal enamel and 1.77 to 1.96 in DS enamel. The lower concentration of Ca is due to the greater content of organic material in DS enamel [28]. The presence of Mg has been shown to be selectively acquired in the transitional stage. The selective uptake of magnesium reaches a maximum at the beginning of maturation due to association with enamel proteins. Crystal development includes a reduction in magnesium, carbonate and fluoride [22, 28]. DS enamel indicated high concentration of magnesium, which is related to high protein concentrations, resulting from insufficient mineralization. EDX analysis showed that the content of Mg varied from 0.4 to 0.55% in control enamel and 1.18 to 1.47% for DS enamel. Finally, DS enamel was altered both quantitatively and qualitatively, suggesting that protein dysfunction may result in enamel abnormalities in its structure and composition.
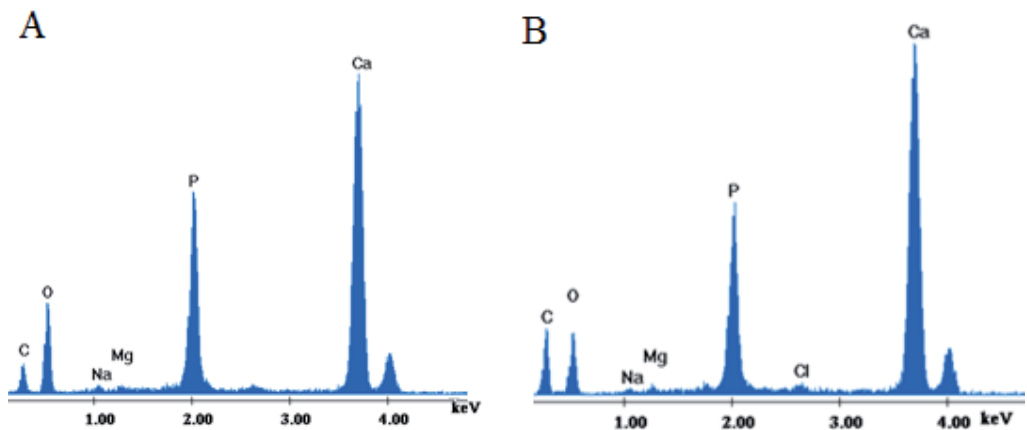


**Figure 5.** EDX analysis of healthy (A) and DS (B) enamel in an area surface

SEM observations were made on supragingival calculus, which is a product of calcification of dental plaque. In DS teeth, attached calculus formed a homogenous surface with calcified deposits. The calculus crystals were packed together with minimum porosity (Fig.6). In control teeth, supragingival calculus revealed a higher level of porosity with empty spaces due to the presence of microorganisms during the calcification process (Fig.6). Rod–like microorganisms could be identified in the calcified surfaces [29].
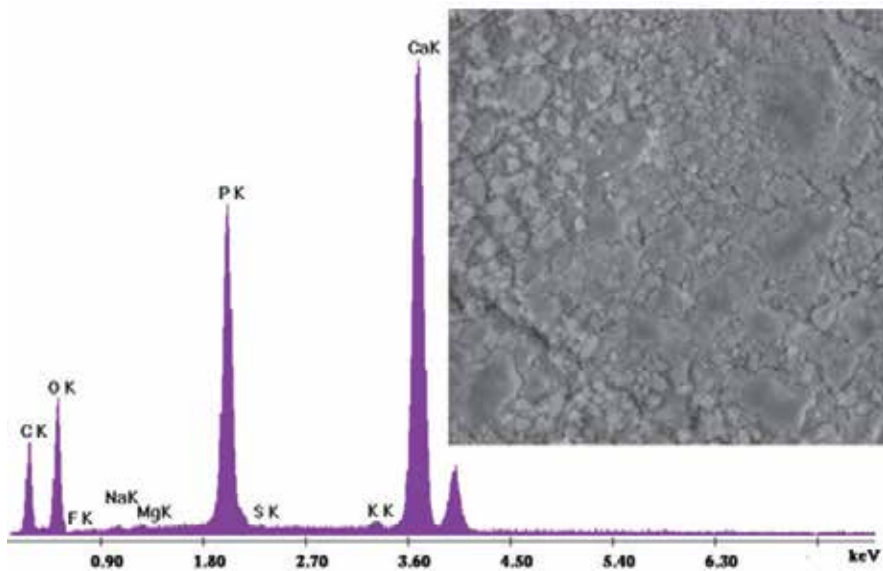
**Figure 6.** SEM imaging of DS enamel, region rich in mineral deposits (scale 300 μm) and their EDAX analysis of the area.
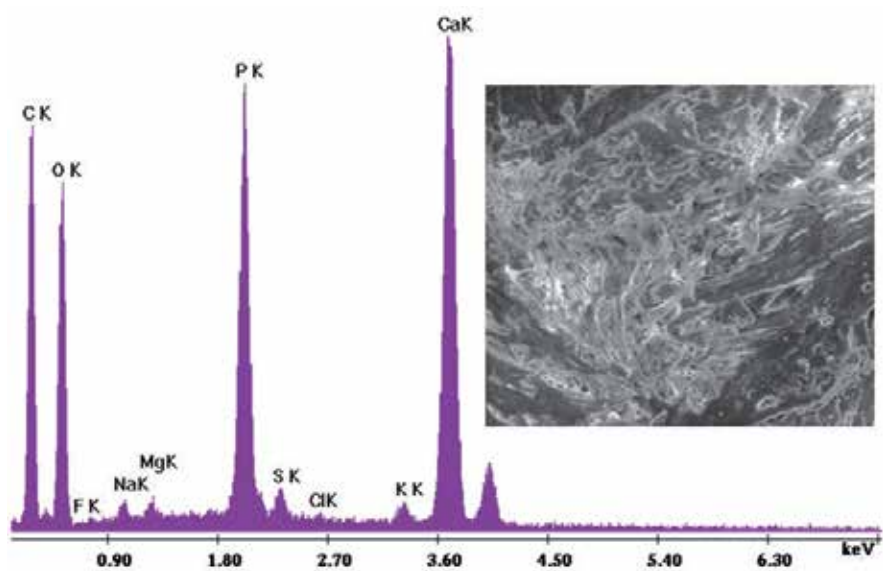


**Figure 7.** SEM imaging of control enamel, region rich in rod-like microorganisms (scale 300 μm) and their EDAX analysis of the area.

The presence of microorganisms in control teeth was also confirmed by EDX analysis. Apart from the main constituents of plaque such as Ca, P, C, O, high concentration of sulphur in

healthy patients was detected in contrast with Down syndrome patients. The presence of sulfur is characteristic feature of bacteria, which contain in their amino acids sulfur groups, leading to a diverse community of microorganisms found on the tooth surface of healthy patients [7, 30, 31].

It is suggested that the alterations in the structure of enamel of patients with Down syndrome may influence the attachment of oral bacteria in order to colonize and form biofilm due to high calcium concentration [32].

## 4. Conclusions

The investigation of enamel structure in children with Down Syndrome (DS) was carried out using Fourier Transform Infrared Spectroscopy (FT-IR) and Scanning Electron Microscopy (SEM) in combination with EDX. FT-IR spectroscopy allowed the analysis at the molecular level leading to the correlation of mineral content and organic matrix with enamel structure. High concentration of organic compounds was indicated in enamel from DS children teeth due to the lower degree of calcification. On the contrary, the low absorbance of amide bands in healthy children's enamel confirmed the lower composition of organic compounds. DS hydroxyapatite crystals were smaller in size to the health enamel crystals, while the molecular structure changed from biological to amorphous or mineral one, as it was demonstrated by SEM analysis. Supragingival calculus showed significant differences in morphology between the healthy and Down syndrome patients, as well as differences in elemental composition. In healthy patients, high concentration of sulphur was detected in contrast with Down syndrome patients. On the tooth surface of healthy patients, the presence of bacteria was detected. Further evaluation of dental samples from different groups of patients is required in order to identify the structural and composition variations of enamel and the mechanism of these abnormal features.

## Author details

V. Dritsa[1*], D. Sgouros[1], K. Pissaridi[2], P. Bochlogyros[1], M. Kyriakidou[1] and V. Mamareli[3]

*Address all correspondence to: vdritsa@central.ntua.gr

1 National Technical University of Athens, Chemical Engineering Department, Radiation Chemistry &Biospectroscopy, Zografou Campus, Athens, Greece

2 University of Patras, Department of Chemistry, Food Chemistry and Technology, Greece

3 University of Patras, School of Medicine, Greece

# References

[1] Moradian-Oldak J. Amelogenins: assembly, processing and control of crystal mor-phology. Matrix Biology 2001; 20: 293-305.

[2] Margolis HC, Beniash E, Fowler CE. Role of macromolecular assembly of enamel ma-trix proteins in enamel formation. Journal of Dental Research 2006; 85: 775-793.

[3] Fan D, Lakshminarayanan R, Moradian-Oldak J. The 32 kDa enamelin undergoes conformational transitions upon calcium binding. Journal of Molecular Structure 2008; 163: 109-115.

[4] Marshall GW, Marhsall SJ, Kinney JH, Balooch M. The dentin substrate: structure and properties related to bonding. Journal of Dentistry 1997; 25: 441-458.

[5] Scheie A. Advances in Dental Research 1994; 8: 246-253.

[6] Nyvad B, Fejerskov O. Structure of Dental Plaque and the Plaque-Enamel Interface in Human Experimental Caries. Caries Research 1989; 23: 151-158.

[7] Marsh P D. Dental plaque: biological significance of a biofilm and community life-style. Journal of Clinical Periodontology 2005: 3: 7-15.

[8] Rose RK, Turner SJ, Dibidin GH. Effect of pH and calcium concentration on calcium diffusion in streptococcal model-plaque biofilms. Archives of Oral Biology 1997; 42:795-800.

[9] Shapiro BL. Prenatal dental anomalies in mongolism: comments on the basis and im-plications of variability. Annals of the New York Academy of Science 2006; 171: 562-577.

[10] Zilberman U, Patricia S, Kupietzky A, Mass E. The effect of hereditary disorders on tooth components: a radiographic morphometric study of two syndromes. Archives of Oral Biology 2004:49: 621-629

[11] Desai SS. Down syndrome: A review of the literature. Oral Surgery, Oral Medicine, *Oral Pathology Oral Radiology and Endod*ology 1997;84: 279-285

[12] Theophanides T. Infrared and Raman Spectra of Biological Molecules. NATO Ad-vanced Study Institute, D. Reidel Publishing Co, Dodrecht;1978.

[13] Kolovou P, Anastassopoulou J. Brilliant Light in Life and Material Sciences. In: Tsa-kanov V, Wiedemann H (ed.) New York: Springer; 2007. p 267-272.

[14] Anastassopoulou J, Boukaki E, Conti C, Ferraris P, Giorgini E, Rubini C, Sabbatini S, Theophanides T, Tosi G. Microimaging FT-IR spectroscopy on pathological breast tissues.Vibrational Spectroscopy 2009; 51: 270-275.

[15] Conti C, Ferraris P, Giorgini E, Rubini C, Sabbatini S, Tosi G, Anastassopoulou J, Arapantoni P, Boukaki E, Theophanides T, Valavanis C. FT-IR Microimaging Spec-

troscopy:Discrimination between healthy and neoplastic human colon tissues. Journal of Molecular Structure 2008; 881: 46-51.

[16] Dritsa V. FT-IR spectroscopy in medicine. In Theophanides T. (ed.). Infrared Spectroscopy-Life and Biomedical Sciences.Croatia:Intech; 2012. p271-288.

[17] Petra M, Anastassopoulou J, Theologis T, Theophanides T. Synchrotron micro-FT-IR spectroscopic evaluation of normal paediatric human bone, Journal of Molecular Structure 2005;. 78: 101-110.

[18] Nyquist RA, Kagel RO. Infrared spectra of inorganic compounds. New York: Academic Press; 1971.

[19] Bellamy LJ. The Infrared Spectra of Complex Molecules. New York: Wiley;1958.

[20] Theophanides T. Fourier transform infrared spectroscopy. Dordrecht: D. Reidel Publishing Co; 1984.

[21] Petra M, J. Anastassopoulou J, Dovas A, Yfantis D, T. Aging of human bones. An infrared study. In: Centano JA. (ed), Metal Ions in Biology and Medicine, 2000. p736-

[22] Mamarelis I, Pissaridi K, Dritsa V, Kotileas P, Tsiligiris V, Anastassopoulou J. Oxidative Stress and Atherogenesis. An FT-IR Spectroscopic Study. In Vivo 2010; 24: 883-888.

[23] Theophanides T, Angiboust JP, Manfait M. In: Twardowski H.(ed.) Spectroscopic and Structural Studies of Biomaterials I: Proteins., Wilmslow: Sigma Press; 1988.

[24] Gadaleta SJ, Paschalis EP, Betts F, Mendelsohn R, Boskey AL. New Infrared Spectra Structure Correlations in the Amorphous Calcium Phosphate to Hydroxyapatite Conversion. Calcified Tissue International 1996; 38: 9-16.

[25] Bohic S, Heymann D, Pouezat JA, Gauther O, Dalcusi G. Transmission FT-IR microspectroscopy of mineral phases in calcified tissues. C R Acad. Paris 1998; 321: 865-876.

[26] Robinson C, Kirkham J, Brookes J, Bonass WA, Shore RC. Chemistry of Enamel Development. International Journal of Developmental Biology,1995; 39: 145-152.

[27] Mahoney EK, Rohanizadeh R, Ismail FSM, Kilpatrick NM, Swain MV. Mechanical properties and and microstructure of hypomineralised enamel of permanent teeth. *Biomaterials* 25, 5091 (2004).

[28] Wright JT, Robinson C, Shore R. Characterization of the enamel ultrastructure and mineral content in hypoplastic amelogenesis imperfecta. Oral Surgery, Oral Medicine and Oral Pathology 1991; 72: 594-601.

[29] Lustmann J, Lewin-Epstein J, Shteyer A. Scanning electron microscopy of dental calculus. Calcified Tissue Research 1976; 21(1): 47-55.

[30] Zee KY, Samaranayke LP, Attstrom R. Scanning electron microscopy of microbial colonization of 'rapid' and 'slow' dental-plaque formers in vivo. Archives of Oral Biology 1997;42: 735-742.

[31] He B, Huang S, Zhang C, Jing J, Hao Y, Xiao L, Zhou X. Mineral densities and elemental content in different layers of healthy human enamel with varying teeth age. Archives of Oral Biology 2011; 56: 997-1004.

[32] Theodorakopoulou O, Anastassopoulou J. Influence of traditional mathematics and mechanics on modern science and technology. In : Sih GC, Spyropoulos CP (ed), Eptalofos, SA, 2004. p.453-462.

# Macromolecules and Food Quality

# Evaluation of Crosslinking Reaction in Adhesive Based Styrene-Butadiene Elastomers Using Infrared Spectroscopy

Beatriz Adriana Salazar Cruz, Ana María Mendoza Martínez,
Alejandro Esquivel de la Garza, Sergio Moctezuma Espiricueto and
José Luis Rivera Armenta

Additional information is available at the end of the chapter

http://dx.doi.org/10.5772/58911

## 1. Introduction

An adhesive is a material that is applied to the surfaces of articles to join them permanently by an adhesive bonding process, and is capable of forming bond to each of the two parts and only a small quantity is required compare to weight of final materials [1]. Since antiquity, the use of adhesives has been very important for humanity, Greeks and Egyptians were the first to use glue to bond surfaces.

Adhesion refers to a complicated set of inter-connected phenomena that is not easy to understand, and by means several semi-empirical tests try to be predicted the strength of an isolated adhesive joint or the strength of a more complex structure, such a laminate, of a fiber-reinforcer of particle-filled composite [2].

Adhesives are classified according with common characteristics to facilitate their understanding and use, although no one classification is universally recognized. Classifications include source, function, chemical composition, physical form and application. Within the most used adhesive are natural or synthetic rubber-based materials, usually due its good properties.

Based solvent technology in adhesive is one of the most used for wood industry, mainly Polychloroprene, which has high temperature resistance and good paste strength. However, for halogenated compounds generated and for marketing strategy, this material is intended to be replaced by Styrene-Butadiene rubber (SBR) and Styrene-Butadiene-Styrene (SBS) copolymers, and Styrene-butadiene-Ethylene-Styrene (SEBS).

The formulation of Pressure-sensitive adhesives (PSA) consists of elastomers, tackifiers, and various additives have been widely used as tapes in stationery and for electric and medical purposes. Elastomers are widely used, however and additional crosslinking is needed to increase cohesive strength. The use of polydiene-based triblock copolymers (for instance, SBS, SIS) have increase due to higher cohesive strength resulting from the physical network of polystyrene (PS) blocks [3].

PSA is aggressive and permanently tacky, adheres without the need of more than finger or hand pressure, requires no activation by water, solvent or heat, exerts a strong holding force and has sufficient cohesiveness and elasticity that it can be removed from smooth surface without leaving a residue [2].

Styrene-butadiene (S-B) copolymers appeared in 1947, as an option as a raw material for adhesives. Block styrene-butadiene copolymers have applications as: shoe soles, impact modifiers, asphalt modifiers, adhesives and sealants. SB copolymers used in adhesives are A-B-A type, where A is styrenic block and B represents elastomeric block, which can be insatured, as SIS and polybutadiene (SBS), or satured as ethylene butylene, which promote stickiness and ability to wet the adhesive, further allowing viscosity variations which can be strengthened by adhesive resins of low molecular weight. Polystyrene block shows a good adhesion to wood, but not to plastics, except itself. For bonding polystyrene, a low-molecular weight styrene polymer with peroxide catalyst is used. Resistance to high temperature is limited, Copolymers of SBR, are much less brittle and more valuable as adhesives [1].

In general, a synthetic adhesive consists of: a synthetic based resin (homopolymer, copolymer or blend of polymers); one or more secondary resins and auxiliar polymers to improve adhesive characteristics; additives (plasticizer, hardener, antioxidants and bactericide); fillers and pigments, and solvent for blend substances.

Adhesive resins are generally, rosinas and derivatives, terpene and modified terpene, aliphatic, cicloaliphatic and aromatic; the addition of resins on depends of compatibility with polymeric base that affects final adhesive properties [4]. To achieve this bond there are two procedures, one involving crosslinking mechanisms (vulcanization) and the other using an unvulcanized adhesive. Usually, both procedures are used, adding in the adhesive formulation promoting additives of adhesion and vulcanization, and in some cases, applying an external adhesive onto the substrates to be bonded.

The resins are used in thermoplastic rubbers to carry out one or more functions. Resins are low molecular weight materials, compatible or partially compatible with copolymers, show a higher Tg than polymer o copolymer, and help to improve wetting kinetic. The adhesive resins allow the adhesive to enter more closely contact with substrate which results in an increase in bond strength.

Solvent-based adhesives, also called, pressure sensitive adhesives (PSA), are adhesives that bonding when pressure is applied to bond adhesive between two substrates. There are two type failures in PSA: adhesive and cohesive failure, adhesive failure occurs in interphase between adhesive and substrate and cohesive failure occurs in the adhesive. Used materials for PSA process must have:

- Viscous properties that promote the flow

- Must be able to dissipate energy by adhesion

- Must have a partially elastic behavior

The PSA formulation includes solvents, the selection of adequate solvent allows a more effective bonding of polymers having low intermolecular forces. The solubility parameters theory developed by Hildebrand and Scott [5, 6, 7, 8, 9], contributed to development of these parameters, specially focused on the concept to formulation of solvent-based coatings. The solubility parameters cannot be measured directly due polymers are not volatile. That can be calculated by small molar attractions constants, but generally are inferred to maximum solubility or it swelling power [1]. In other words, PSA must been viscoelastic, the materials that constituting PSA adhesive listed in decreasing order of volume and increasing cost: natural rubber, SBS copolymers, functionalized polymers, neoprenes, nitrile-butadiene copolymers (NBR), thermoplastic elastomers, polyacrylates, polyvynil acrylates and silicones.

The crosslinking (vulcanization or curing) is a bond that links one polymer chain to another by means covalent or ionic bonds, creating a three-dimensional network structures. The term crosslinking is often used in synthetic polymers, it refers to the use of crosslinks to promote a difference in the polymers' physical properties, as flexibility that decreases, the hardness that increases and the melting point that increases as well.

The sulfur was the first crosslinker to be discovered and together with activators and accelerators is still by far the most frequently used curing system [10]. The crosslinking is used in several technologies of commercial and scientific interest to control and enhance the properties of the resulting polymer system or interphase, such as thermosets and coatings, and can be initiated by heat, pressure, change in pH or radiation [11].

Organic peroxides are compounds of the general structure. RO-OR'. The relatively weak oxygen-oxygen bond breaks easily leading to the formation of two oxygen centered radicals: RO, and initiates the free radical processes. The use of peroxide as crosslinking agent of rubber dates from 1914, when Ostromislensk crosslinked for first time natural rubber with benzoil peroxide. However, use of peroxides had not the success because it led to formation of vulcanized with resistance to traction and to curing lower than crosslinked materials with sulfur. The introduction of Polyethylene in 30's increased the use of free radical donors as crosslinking agents. Afterwards, in 1950, was discovered that di-t-butyl peroxide allowed to obtain better quality vulcanized than benzoil peroxide, but had the disadvantage of high volatility. Shortly after, was discovered that dicumyl peroxide (DCP) shows a good combination of physical and chemical properties.

In absence of other additives, vulcanization with peroxides consists exclusively in creation of a carbon-carbon bond between polymer chains. The polymer crosslinking reaction with peroxide carries out in 3 steps, first one homolytic rupture, formation of cumyloxi radical and the third one gives as product dimehtyl bencyl alcohol (DMBA), or acetophenone plus a methyl radical. This crosslinking reaction is rather complex, because of numerous side reactions that

compete with crosslinking mechanism. Main side reactions are: addition of radical to double bond, cleavage reaction of polymer radical, radical transference and oxygenation.

Thermal decomposition of peroxide is a first order reaction that only depends of temperature and time. Although in general peroxides decompose in radicals, its stability varies considerably. Some peroxides are instable at room temperature, while others show no evidence of decomposition when heated at 100°C for several hours. In general, all peroxides used in rubber vulcanization are stable by at least reached temperatures during preparation compound. Peroxide stability is determinate by chemical groups bonded to oxygen atoms of peroxide.

After DCP homolytic rupture, radical fragments can suffer rearrangements that change its initial identity. This response can decrease radical efficiency. Cumiloxy radical can experiment beta cleavage to form acetophenone and methyl radical (figure 1).
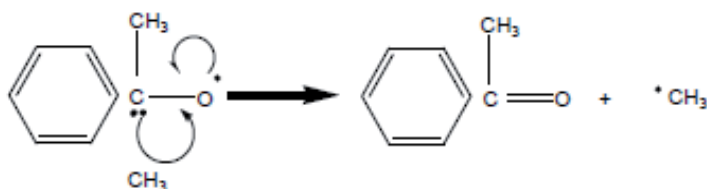


**Figure 1.** β-cleavage of cumiloxy radical to form acetophenone.

Some reports have use IR for evaluation of grafting surface and evaluation of curing reaction in adhesives reporting that is a useful tool for that kind of studies [12, 13]. Also is possible with IR to identify decreasing of peaks attributed to double bonding in polybutadiene backbone when crosslinking process is carry out [14].In this case, radical energy does not reduce significatively, then peroxide eficiency is not alterated, with advantage that methyl radical is not esterically hindranced as initial cumiloxy radical and can participate more effectively in reactions where esteric limitations or diffusion are a limitation. Formed radical from peroxide decomposition react with hydrogen atoms found in the surrounding. Figure 2 shows heterolytic decomposition of DCP where peroxide radicals are obtained.

Peroxide radicals can react potentially by addition to double bonging or by allylic hydrogen abstraction. Double bondings can act as reaction points. In general, results indicate both mechanisms can be carry out in insatured elastomer vulcanization, prevailing hydrogen abstraction.

Infrared (IR) is one of oldest technique useful for surface analysis, and to probe the surface compositions of polymers that have been surface-modified by an etching process or by deposition of a film. IR has numerous characteristics that make it useful in adhesion science, mainly because is sensitive to functional groups and provides information about curing reactions of adhesives and about other chemical reactions that are relevant in adhesion [2].
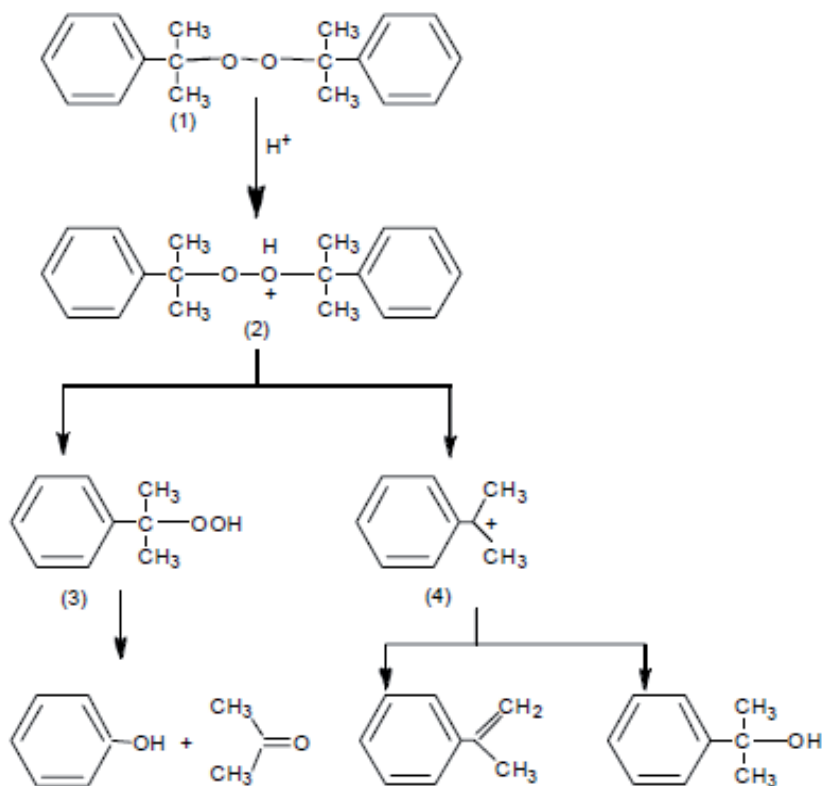
**Figure 2.** Heterolytic decomposition of DCP.

Although it is important to understand the crosslinking process, there is a few literature on the subject, so in this work a study of the crosslinking reaction in pressure sensitive adhesives (PSA) based styrene-butadiene copolymer (SBS) using as crosslinking agent dicumyl peroxide (DCP) was carried out, using infrared spectroscopy to evaluate crosslinking reaction and possible side reactions, and progress of crosslinking reaction according with preparation. Effect of DCP, crosslinking time, total styrene content in elastomer, molecular weight of elastomer and resin type in adhesive formulation were evaluated variables in crosslinking process. Also effect of crosslinking on mechanical properties of adhesive was evaluated.

## 2. Methodology

### 2.1. Materials

Adhesives formulations based solvent, also called pressure sensitive adhesives (PSA), consist of elastomer, resin, crosslinking agent and solvents. In this case two block copolymers styrene-butadiene-styrene (SBS) were used: (E1) 33% and (E2) 31% styrene content, linear structure,

provided by Dynasol Elastomers S.A. de C.V. plant Altamira; two resins were used, one compatible to polybutadiene segment (ester, R1) and other one compatible to polystyrene segment (styrenated R2), as crosslinking agent dicumyl peroxide (DCP) was used, which was provided by Retilox Co.; and a mix of solvent consisting of toluene, acetone and n-hexane (all ACS grade), which were selected according with compatibility of all adhesive components.

| Components | Amount (phr) |
|---|---|
| Polymer (SBS) | 100 |
| Resin | 40 |
| Dicumyl peroxide | 3.5 - 0.81 |
| Toluene | 150 |
| Hexane | 150 |
| Acetone | 150 |

**Table 1.** Formulation amount used for Adhesive preparation

## 2.2. Adhesives preparation

Adhesives preparation consists in mixed all components in a glass reactor using a mechanic stirrer at high shear rate. The addition sequence was established according to several experimentations, based on solubility, dispersion, color, viscosity and mixing time. First, elastomer in corresponding amount was added at low shear rate (500 rpm), after that, shear rate was increased until 1500 rpm and then resin was added, finally DCP (3 concentration levels, 0.81 phr [1], 2.19 phr [2], 3.6 phr [3] and 0 phr) was added until complete dispersion was reached. Final mixture was poured in glass container closed and storage in room conditions. Table 1 show amounts used according with Roebeson [15] and Bohwmoick [16]. Table 2 show the codes used for adhesives formulations prepared.

| Resins | R1 | | R2 | |
|---|---|---|---|---|
| Polymer | E1 | E2 | E1 | E2 |
| | 0 | 0 | 0 | 0 |
| DCP | 1 | 1 | 1 | 1 |
| (phr) | 2 | 2 | 2 | 2 |
| | 3 | 3 | 3 | 3 |

**Table 2.** Codes for adhesive formulations. For instance formulation E1-R1 2 means Elastomer with 33% styrene content, ester resin and 2.19 phr DCP concentration.

Adhesive films were prepared pouring specific amount of adhesive mixture in a manufactured container with siliconated paper, and were evaporating until complete solvent remotion, at room conditions. The films were cured in convection oven at 180°C for 90 minutes.

### 2.3. Infrared spectroscopy

IR analysis was carried out to evaluate crosslinking reaction, by means monitoring typical functional groups of this kind of reaction. IR spectra were recorded with a Perkin Elmer Spectrum 100 model spectrophotometer, using for analysis the Attenuated Total Reflactance (ATR) technique, with a diamond/KRS-5 plate, using 12 scans and resolution of 4 $cm^{-1}$, in a wavenumber range from 4000-400 $cm^{-1}$.

### 2.4. Fracture mechanical test

The necessity of fracture analysis in adhesives applied in wood, helps to estimate internal forces (cohesion) and interphase forces of adhesive line. Adhesive mixtures were impregnated in pine wood substrates of 4*1*0.064 in dimensions. Specimens were conditioning at 50±2% relative humidity and 23±1°C temperature until equilibrium. Substrates surface was cleaned with acetone to remove any residue. Measurements were carried out according with ASTM D1002. Impregnation process consists in the addition of adhesive on two wood specimens trying to maintain a constant thickness of adhesive film. Contact area was 1 $in^2$ and two wood specimens were pressed and allowed to cure for 24, 48 and 72 hrs at room temperature and constant DCP concentration. The method consists in a 0.2 mm thickness, a 10 KN load and 0.5 in/min displacement. It was necessary 5 repetitions of each specimen.

## 3. Results and discussion

### 3.1. Monitoring crosslinking reaction by means IR

There are different variables that play an important role during the crosslinking reaction, between the most important are: crosslinking agent concentration, reaction time, resin type, temperature. By means IR it is possible identify functional groups associated to crosslinking reaction so useful information about the process can be obtained.

Figure 3 shows IR spectra of adhesive mixture E1-R1with DCP high concentration at different times. From the spectra 3 important regions draw attention due are associated to crosslinking reaction: 3400, 1724 and 724 $cm^{-1}$. It is possible identify signals at 966, 911 and 721$cm^{-1}$ attributed to out-of-plane bendings of $\gamma$(=CH) trans, $\omega$(=CH2) vynil and $\gamma$(=CH) cis groups respectively, present in polybutadiene domains Those peaks decrease with time which is associate to crosslinking that occurs in double bonding. In the other hand, typical signals from polystyrene domains (1601, 1492, 1450, 699 and 540 $cm^{-1}$), remain without significative changes [17, 18]. That is indicative that crosslinking reaction carries out preferably in double bonds of polybutadiene domains.
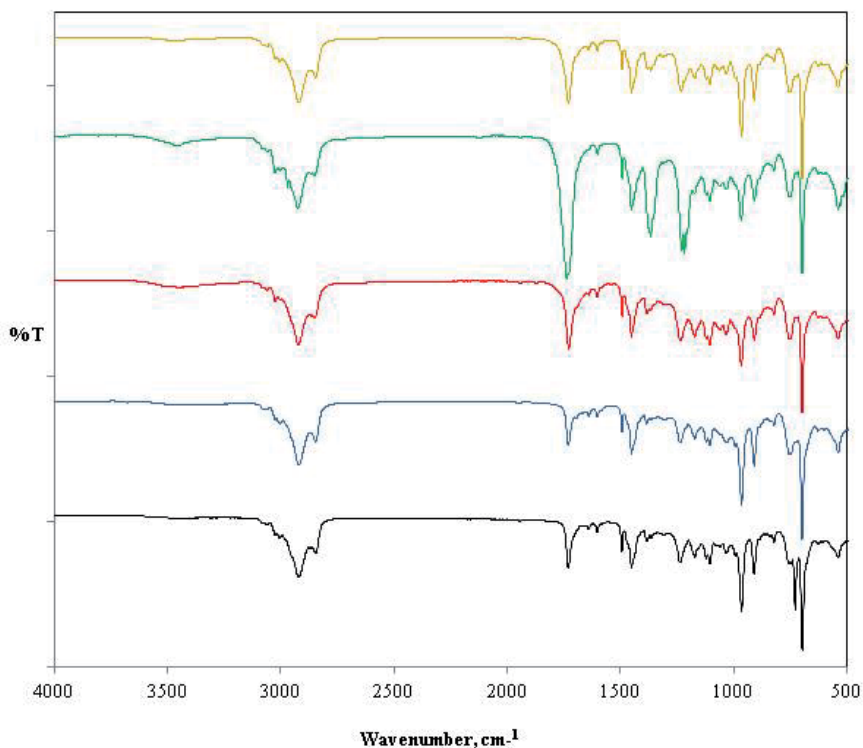
**Figure 3.** IR spectra of E1-R1-3 adhesive mixture at different times @170°C, o min (black), 30 min (blue), 60 min (red), 90 min (green), 120 min (yellow).

Crosslinking reaction consist in first step DCP homolytic rupture, after hydrogen abstract from polymer chain, and then bonding of two polymer chain forming a three dimensional structure. In DCP rupture, the cumyloxi radical can stabilize forming $\alpha,\alpha$, dimethyl bencyl alcohol or acetophenone.

Curing effect in adhesive E1-R1 with DCP was monitored by means IR spectroscopy. Figure 4 shows main regions in IR spectra for adhesive: 3400 cm$^{-1}$ for $\alpha,\alpha$, dimethyl bencyl alcohol, 1725 cm$^{-1}$ for acetophenone and 724 cm$^{-1}$=C-H cis, at 0, 30, 60, 90 and 120 min. It is evident decreasing in intensity according with time for signals attributed to double bonding of elastomer (720 cm$^{-1}$) due these groups participate in crosslinking reaction. In the other hand, an increasing of signals assigned to carbonyl and hydroxyl groups confirm abstraction reaction and beta cleavage reaction in crosslinking with peroxides. As consequence methyl radical is obtained, which present the advantage that is less esterical hindrance compared with Cumyloxi radical. Wu et al [17], Ellul et al [19] report the same behavior and that polystyrene characteristic peaks (1601, 1492, 1450, 699 and 540 cm$^{-1}$) remain with not significative change.
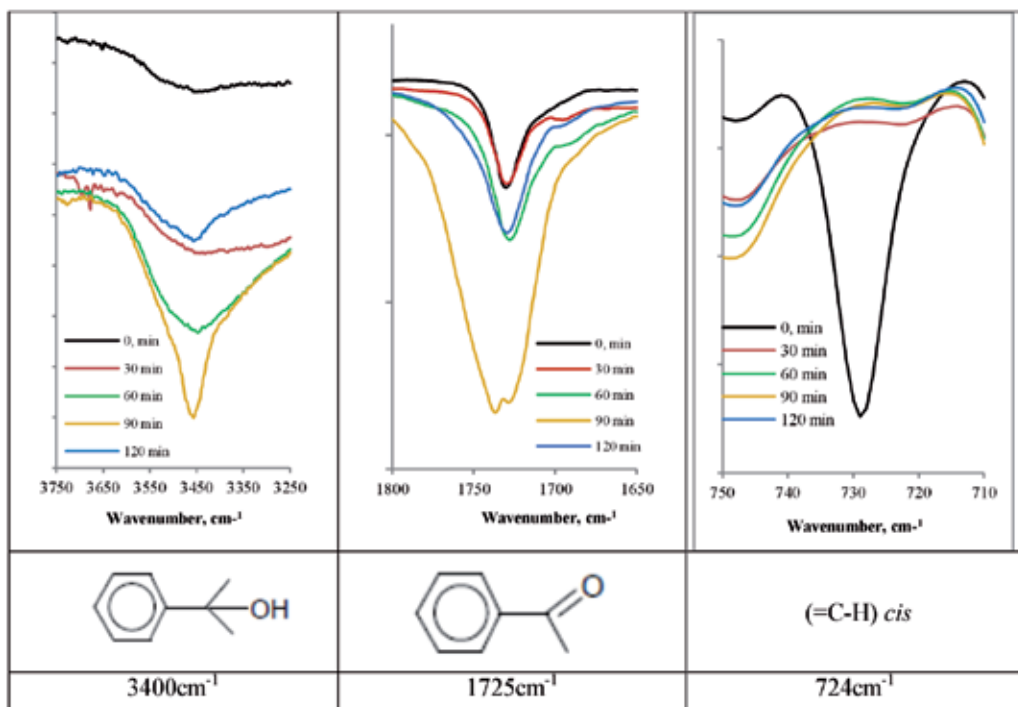
**Figure 4.** IR spectra for main peaks in adhesive E1-R1 formulation at different times.

The same analysis was carried out for adhesive formulations E1-R2, E2-R1 and E2-R2, with different DCP content, and a similar behavior was observed for these 3 peaks at 3400, 1725 and 724 cm$^{-1}$.

DCP concentration on crosslinking reaction was evaluated in figure 5. The presence of side reactions can be identified when thermal decomposition is carry out. The 3 main signals plus peaks at 866 and 1452 cm$^{-1}$, attributed to out of plane bending of $\gamma$(=C-H) cis, were monitored to evaluate crosslinking effect. It is observed that adhesive with high DCP concentration show increasing on peaks at 3400, 1725 and 725 cm$^{-1}$ compared with adhesive with low DCP concentration, which was expected due high DCP concentration may cause crosslinking reaction between SBS chains because an important requirement for this reaction to be success-ful is that the amount of free radicals is high enough to be able to abstract the active hydrogens on the polymer. Evidence of side reactions was not found. Wu et al [17] reports that a high peroxide concentration in adhesive formulation causes the free radical concentration in the system increase and because there are lots of double-bonds in the SBS macromolecule structure, excessive peroxide may cause crosslinking reaction between SBS molecule chains. Dlezniski [20] reports a high DCP concentration increase the possibility of side reactions that compete with crosslinking reaction and then decrease crosslinking points in polymer back-bone.
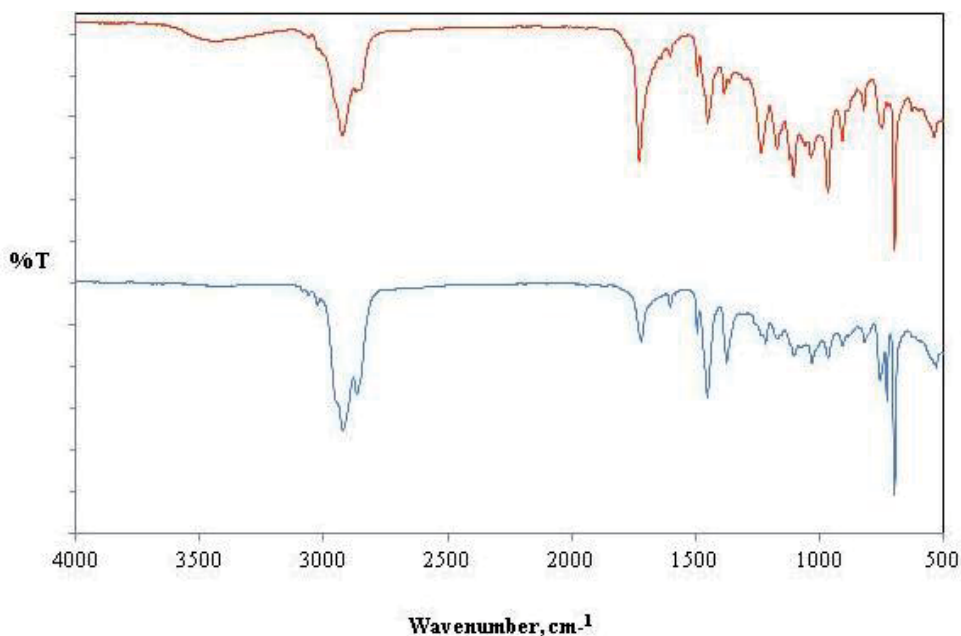
**Figure 5.** IR spectra of E2-R1-1 (blue) and E2-R1-3 (red), at 90 min @ 170°C.

In order to determinate how the resin nature affect the crosslinking reaction, two resins were studied. Main functional groups of two resins are listed: R1 (ester resin) present peaks under 3000 cm$^{-1}$, 1755 cm$^{-1}$, due insaturations and ester group, which make it compatible with polybutadiene block in SBS backbone, helping to curing process with DCP; and R2 (styrene resin) present an assignation at 2945 attributed to methylene group, overtones in 2000-1750 cm$^{-1}$ attributed to aromatic group, which contribute to compatibility with polystyrene block in SBS.

Figure 6 shows IR spectra of E2-R1-3 and E2-R2-3 where is evaluated effect of resin in cross-linking process for. It can observe that due polarity R1 generates a high electronic density that helps to crosslinking process in adhesive mixture, in spectrum is observed in range from 1500 to 100 cm$^{-1}$ where the presence of some peaks and complexity are indicative of crosslinking effect. In the other hand, the crosslinking effect it is observed in peaks at 1725 and 3450 cm$^{-1}$ from carbonyl and carboxyl groups respectively. The resin nature is important according with functional groups and type of reaction that can be carry out.

Styrene content in the elastomer becomes important because certain functional groups present in resin having affinity with the vinyl bonds and it is of interest to determine the effects that has styrene content in crosslinking reaction. E1 has 33% and E2 31% of total styrene content, respectively, both elastomers generate similar structures but styrene content can produces steric hindrance of Polystyrene block. Signal at 1725 and 3400 cm$^{-1}$ are related with crosslinking, also peaks in 1500-1000 cm$^{-1}$ region indicate gel formation which is associated with a reticulated structure.
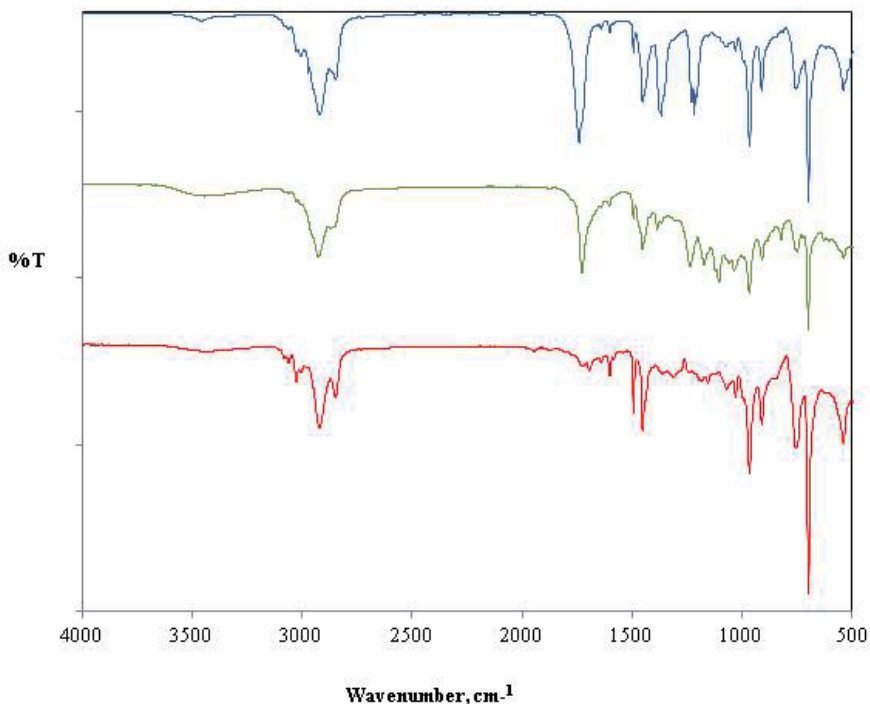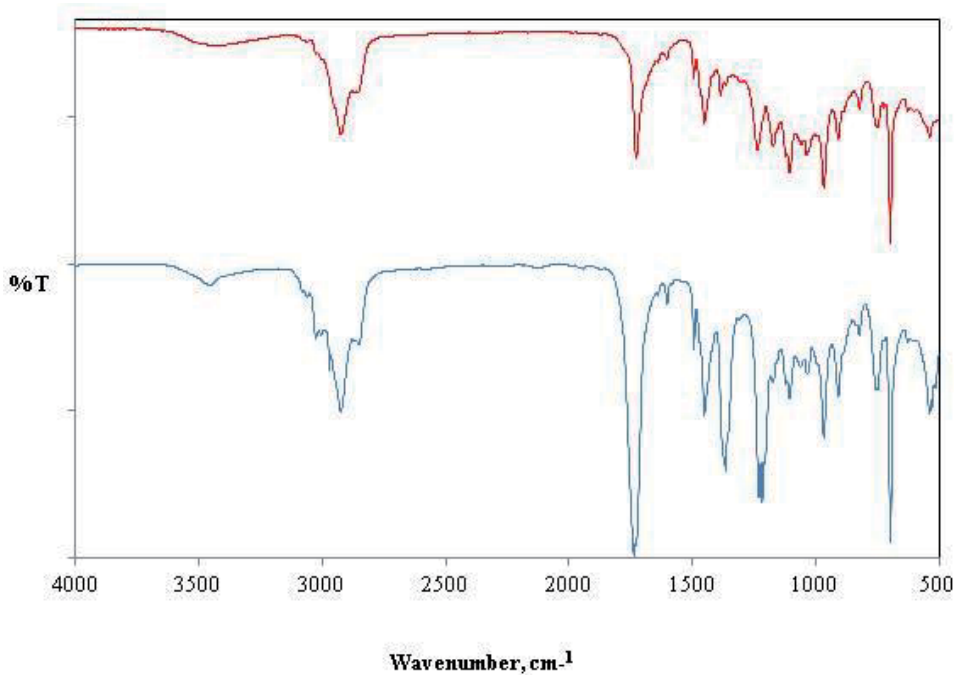
**Figure 6.** IR spectra of adhesive mixtures E2-R1 (green), E2-R2 (blue) and without resin (red) @170°C.

The formation of macrophase-separated resin domains and the tack strength of the adhesive are significantly changed by the presence of the microphase structure when either the mid or end block domains are saturated. Considering the near-surface morphology of the block copolymer, the chain connectivity in block copolymer imposes limitations on the degrees of freedom of molecules, avoiding the crosslinking reaction [21].

Also resin type and molecular weight were evaluated. Resin R1 was identified compatibility to PB segment and R2 was compatible to PS segment. Due the polarity a high electronic density is present in region 1500-100 cm$^{-1}$, where several signals are attributed to crosslinking effect. Resin R2, signal at 1725cm$^{-1}$ and 3450 cm$^{-1}$ corresponding to carbonyl and carboxyl groups are related to crosslinking effect.

About effect of molecular weight, figure 7 shows spectra or E1-R1-3 and E2-R1-3 adhesive mixtures, E1 has higher molecular weight than E2. The main differences are identified in: 3400, 1725, and 1400 cm$^{-1}$, peaks associated to hydroxyl groups, carbonyl groups which are from thermal decomposition of DCP, and to double bond respectively. High molecular weight can causes steric hindrance to generated radicals from DCP decomposition by thermal effect generate abstraction process of unsaturated segments in SBS backbone, then minimizing crosslinking between polymeric radicals. However, crosslinking is carrying out, because some peaks are identified in range from 1500 to 1000 cm$^{-1}$ that indicates crosslinking of C-C bonds.

**Figure 7.** IR spectra of E1-R1-3 (blue) and E2-R1-3 (red) adhesive mixtures @170°C.

For a deep analysis of DCP decomposition, thermal analysis was carried out, in inert atmosphere of nitrogen, with a heating ramp of 10°C/min from 40 to 600°C. Figure 8 a and b show TGA thermogram where it can observe DCP decomposition start at 145°C and elastomers around 380°C, it is important to be sure elastomers do not experiment thermal degradation at temperatures where DCP decompose (150-200°C). Derivative curves show that the maximum temperature is in 446°C and DCP at 161°C, thus can be sure that any exothermic process observed under 200°C implies activation of peroxide to form radicals to crosslinking.
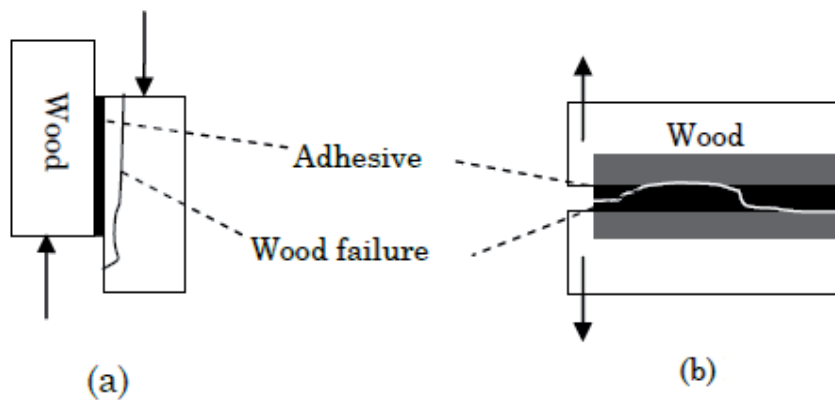
### 3.2. Fracture mechanical test

The necessity of a fracture analysis to evaluate adhesive applied in wood, help to estimate internal forces (cohesive area) and interphase forces of adhesive line. Figure 9 shows type of forces when an adhesive is applied in wood. For this test some criteria were established:

- Superposition that in adherent region shear stress is constant.

- Wood specimens were from pine wood and the same batch.

- The substrates were conditioned for a week.

- The substrate surface was cleaned with acetone to eliminate any residual dust or grease.
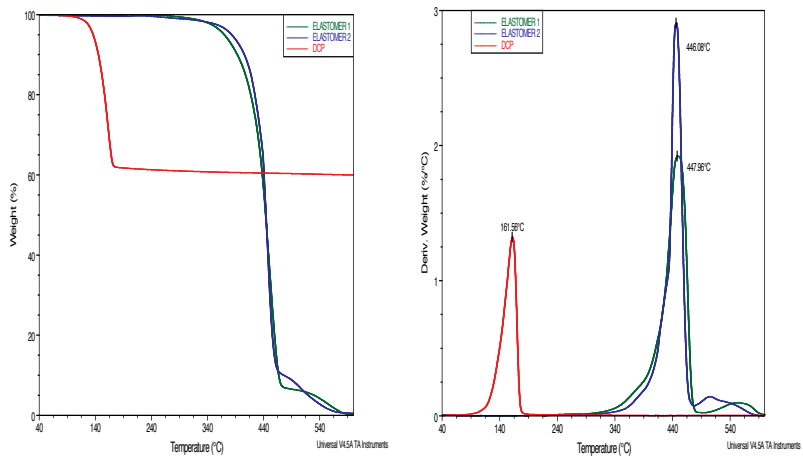
**Figure 8.** Loss weight (left) and weight derivative (right) from TGA thermogram of E1, E2 and DCP.



**Figure 9.** Analysis of tension force (a) and fracture analysis (b) in adhesives on wood substrate.

In table 3 is showed the type of failures that occur in different adhesives after mechanical test. Adhesives that include R1 in its formulation present cohesive failure (adhesive thickness) after mechanical test, while adhesives including R2 in formulation show adhesive failure (substrate interphase), increasing the percentage with time; this behavior is assumed to polarity on R1 that stimulate substrate affinity with adhesive.

In the other hand, an increase of DCP concentration causes a considerable diminishing of the maximum load for adhesive mixtures with R1 and R2, which is indicative that crosslinking reaction is not favored with increasing peroxide radicals. An explanation of this behavior is the competition between side reactions and crosslinking reaction which causes a decrease in crosslink points. Dlezneski [20] reports similar behavior when peroxides are used for crosslink

styrene-butadiene based elastomers. However, Marzocca et al [22] found that an increment of DCP content in cured polybutadiene reflects in a high crosslinking density in materials. Here the difference is use of resins in formulation and presence of polystyrene domains in polymer structure justifying that behavior.

| Time, (h). | 0 | 24 | 48 | 72 |
|---|---|---|---|---|
| E1-R1-1 |  |  |  |  |
| failure | Cohesive | Cohesive | cohesive | cohesive |
| E1-R2-1 |  |  |  |  |
| failure | Cohesive | Adhesive 60% | Adhesive 70% | Adhesive 90% |

**Table 3.** Failure type present in adhesive after single lap shear test in adhesives E1-R1-1 and E1-R2-1.

It is important to detail stickiness in prepared adhesives is higher for adhesive with R1 respect to adhesives with R2, this adhesiveness increase, attributed to a more compatible behavior on wood surface, which also explains the failure type in adhesives with R2 (cohesive). In the other hand, R2 is more compatible to polystyrene block, shows less adhesiveness with substrate, so that cause the interphase failure (adhesive).

The DCP was added to adhesive mixture and cured at 170°C for 120 min. Effect of DCP concentration on adhesives mixtures prepared with R1 and R2 are shown in figure 11 (R1) and 12 (R2). It is evident that adhesives prepared with E2 show higher maximum load compared with adhesives with E1, this behavior is attributed to lower styrene content in E2 generates less steric hindrance in curing process. The selective compatibility of the R1 with polystyrene domains over polybutadiene is important for controlling the ordered structures of SBS-resin blends [21].

According with results, lower DCP content in adhesive mixtures present better mechanical response for E1 and E2, due supports higher stress. Adhesive mixture with E2 present higher maximum load than E1 adhesives, attributed to the less steric hindrance caused by the styrene domains that favoring crosslinking.
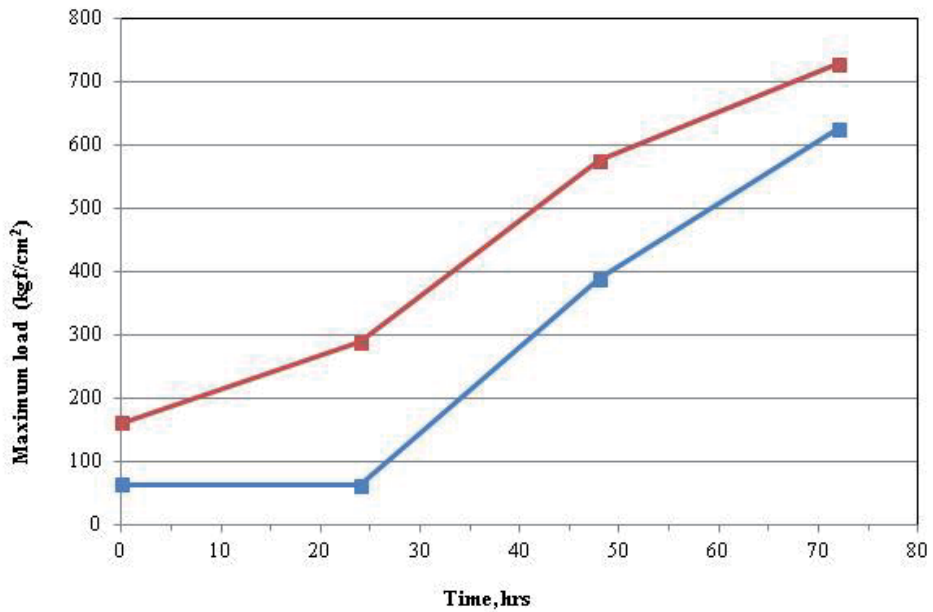
**Figure 10.** Effect of the time for adhesives mixtures E1-R1 (blue) and E2-R1 (red) without DCP on maximum load.
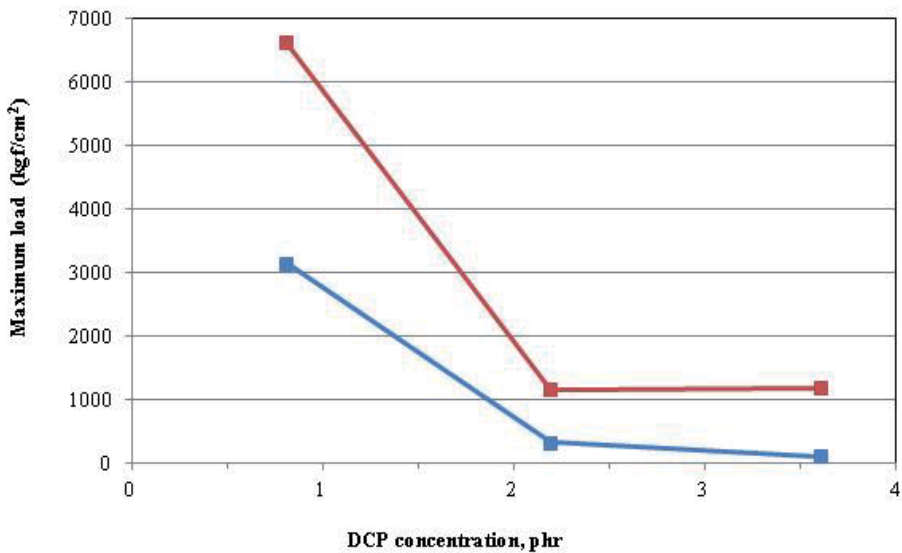


**Figure 11.** Effect of DCP concentration on maximum load for E1-R1(blue) and E2-R1 (red) adhesive mixture cured @170°C.

The effects discused are because every component in adhesive mixture play an importan role in crosslinking procees and each of components in the formulation tend to develop of adhesive or cohesive properties to the adhesive, so it is importante to achieve an optimal combination of resin, polymer, addtivies and solvents used in the preparation of adhesive materials. The success of an adhesive depends on reaching an ideal balance of adhesive and cohesive forces, any imbalance of these cause a failure in the adhesive performance.
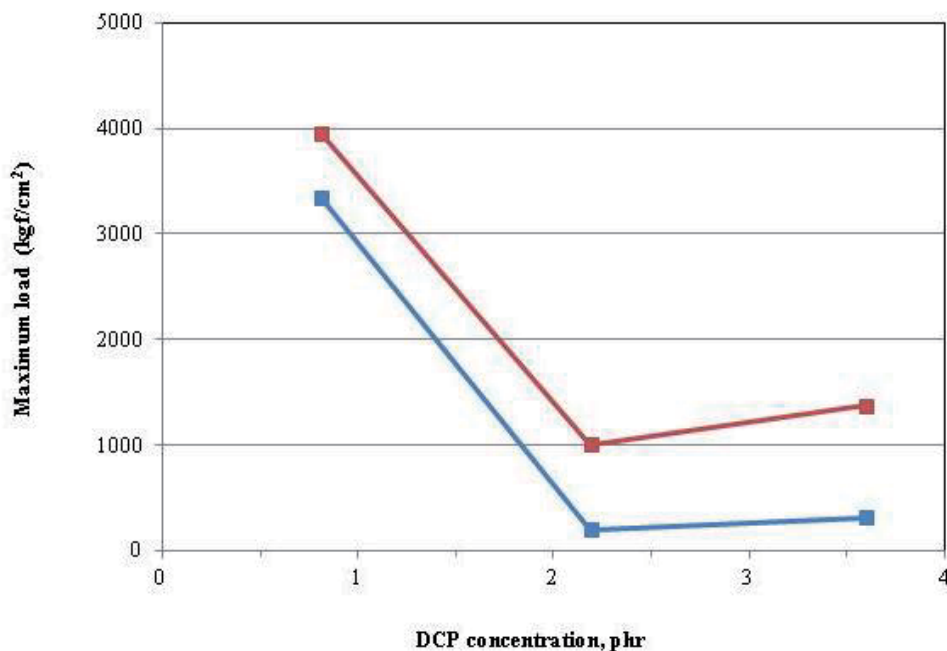


**Figure 12.** Effect of DCP concentration on maximum load for E1-R2 and E2-R2 adhesive mixture cured @170°C.

## 4. Concluding remarks

From presented results in this research it can be concluded that is possible use infrared spectroscopy to evaluate crosslinking reaction in adhesives based polystyrene-butadiene using as crosslinking agent dicumyl peroxide. It was possible identify effect of diverse variables in crosslinking process, such as crosslinking time, crosslinking agent content, styrene content in elastomer, resin type, molecular weight of elastomer.

By means IR was possible probe that peroxide radical can react in double bonding region of elastomers, mainly by alylic radical abstraction, which can be identified for decreasing of signals at 966, 724 and 911 cm$^{-1}$ attributed to out-of-plane deformation $\gamma$(=CH) trans, $\gamma$(=CH) cis and $\omega$(=CH2) of vynil groups respectively, and the increasing of peaks at 1724 and 3450 cm$^{-1}$ from carbonyl and hydroxil groups.

Ester resin (R1) was more effective to crosslink reaction because its groups show partial afinity and compatibility with polystyrene domains and polybutadiene domains, compared with R2 that only is compatible with polybutadiene block; so styrene content is also an important parameter for a good adhesive formulation if ester resin is used.

It was found that DCP lower content produces better mechanical properties than higher contents, because there is a competition among crosslinking reaction and side reactions during curing process.

## Acknowledgements

## Author details

Beatriz Adriana Salazar Cruz[1], Ana María Mendoza Martínez[1],
Alejandro Esquivel de la Garza[2], Sergio Moctezuma Espiricueto[2] and
José Luis Rivera Armenta[1*]

*Address all correspondence to: jlriveraarmenta@itcm.edu.mx

1 Instituto Tecnológico de Ciudad Madero, División de Estudios de Posgrado e Investigación, J. Rosas y J. Urueta S/n, col. Los Mangos, Ciudad Madero, Tamaulipas, México

2 Departamento de Asistencia Técnica y Desarrollo, Dynasol Elastomeros, S.A. de C.V. Carretera Tampico-Mante, Col. Santa Amalia, Altamira, Tamaulipas, México

## References

[1] Ebnesajjad, S., Adhesives Technology Handbook. 2nd Ed. Norwich NY USA; William Andrew. 2008.

[2] Chaudhury, M., Pocius, A.V. Adhesion Science and Engineering, vol. 2 Surfaces, Chemistry & Applications. Amsterdam, The Neetherlands. Elsevier. 2002.

[3] Kim, J.K. Kim, W.H. Lee, D.H. Adhesion properties of UV crosslinked polystyrene-block-polybutaidne-block-polystyrene copolymer and tackifier mixture. Polymer 2002; 43 5005-5010.

[4]   Skeist, I. Handbook of adhesive. 3rd Ed. New York, NY, United States of America; Chapman & Hall. 1990.

[5]   Hildebrand, J.H. Scott R.L. The solubility of nonelectrolytes. 3rd. Ed. New York, NY, United States of America; Reinhold. 1950.

[6]   Burrel, H. Solubility Parameters for Film Formers. Official Digest 1955: 27 (369) 726-740.

[7]   Hansen, C.M. The three dimensional solubility parameter-Key to paint component affinities: II and II, Dyes, emulsifiers, mutual solubility and compatibilities and pigment. Journal of Paint Technology 1967; 39, 505.

[8]   Hansen, C.M. Beerbower, A. Kirk-Othmer Encyclopedia of chemical technology, Supplementary. 2nd Ed. New York, NY, United States of America; A. Standen. 1971.

[9]   Crowley, J.D. Teague, G.S. low, J.W. A three dimensional approach to solubility. Journal of Paint Technology 1966; 38 269-280.

[10]  Stevens, M.P. Polymer Chemistry. An Introduction. 3rd Ed. New York NY. United States of America; Oxford University Press, 1999.

[11]  Zielinska, AJ. Cross-linking and modification of saturated elastomers using functionalized azides, PhD thesis. University of Twente. 2011.

[12]  Navarro-Bañon, M.V. Pastor-Blas, M.M. Martín-Martínez, J.M. Elimination of the reactivation process in the adhesion of chlorinated SBS rubber with polychloroprene adhesives. Express Polymer letters; 2007 1(4) 236-244.

[13]  Santos, R.P. de Oliveira Junior, M.S. da Costa Mattos, E. Faria Diniz, M. Lazzarini Dutra, R.C. Study by FT-IR techinique and adhesive properties of vulcanized EPDM modified with plasma. Journal of Aerospace Technology and Management; 2013 5(1) 65-74.

[14]  Loan, I.D. Mechanism of peroxide vulcanization of elastomers. Rubber Chemistry and Technology. 1967 40 149-176.

[15]  Robeson, L.M. Applications of polymer blends: emphasis in recent advances. Polymer Engineering Science; 1984 24(8) 587-597.

[16]  Bhowmick, A.K. Stephens, H.L.Handbook of elastomers. New developments and Technology. 1st Ed., New York, NY, United States of America. Marcel Dekker Inc. 1988.

[17]  Wu, G. Jiang, Y. Ye, L. A novel UV-crosslinked pressure-sensitive adhesive based on photoinitiator-grafted SBS. International Journal of Adhesion and Adhesive. 2010 30 (1) 43-46.

[18] Tyczkowski, J. Krawczyk-Klys, I. Kuberski, S. Makowski, P. Chemical nature of adhesion: Plasma modified styrene–butadieneelastomer and polyurethane adhesive joints. European Polymer Journal 2010 46 (4) 767–773.

[19] Ellul, D. Tsou, A.H. Hu, W. Crosslink densities and phase morphologies in thermoplastic vulcanizates. Polymer 2004 45 (10) 3351–3358.

[20] Dlezneski, P.R. Peroxide vulcanization of Elastomers. Rubber Chemistry Technology; 2001 74(3) 451-492.

[21] Yang, H. Sa, U. Kang, M. Ryu, H.S. Ryu, C.Y. Cho, K. Near-surface morphology effect on tack behavior of poly(styrene-b-butadiene-b-styrene) triblock copolymer/rosin films; Polymer 2006, Polymer 47 (11) 3889-3895.

[22] Marzocca, A.J. Rodriguez Garraza, A.L. Sorichetti, P.A. Matteo, C.L. Mosca, H.O. About the cure kinetics and dielectric relaxation spectroscopy in compounds of polybutadiene (BR) with dicumyl peroxide. Anales AFA 2011 23 75-79.

# Application of Near-infrared Spectroscopy for Assessing Meat Quality and Safety

Yankun Peng and Wenxiu Wang

Additional information is available at the end of the chapter

## 1. Introduction

Meat and meat products are important sources for human to obtain protein, vitamins and minerals, and has become an essential ingredient in the diet greatly prized by the consumer [1]. According to the analysis based on the Food and Agricultural Organization of the United Nations (FAO) Food Balance Sheet data, there has been a significant increase in global meat consumption over time (as is shown in Table 1). Aggregate meat consumption increased by almost 60% between 1990 and 2009, from 175,665 billion to 278,863 billion. It indicates that the meat and meat products occupy a large proportion in people's food items.

|  | 1990 | 2009 | %change |
|---|---|---|---|
| **Bovine Meat** | 54065 | 63835 | 18.1 |
| **Mutton and Goat Meat** | 9100 | 12763 | 40.2 |
| **Pig meat** | 68692 | 105503 | 53.6 |
| **Poultry Meat** | 40173 | 90664 | 125.7 |
| **Others** | 3634 | 6098 | 67.8 |
| **Aggregate** | 175665 | 278863 | 58.7 |

**Table 1.** Global Meat Consumption, 1990-2009, 'billion'

With the continuous development of living standards and the relative change of dietary structure, consumers' rising and persistent demand for safe meat and better quality of meat is emphasized. The meat industry is no exception to this expectation. Superior quality of these products is always demanded by consumers and is considered as a key factor for success in today's highly competitive market [2]. The characteristics of raw meat are easily affected by a

great many factors, such as breed, sex, age, pre-slaughter and some post-mortern factors including transporting, storing time, temperature condition, et al. The changes muscles may undergo during these periods can influence many characteristics such as color, tenderness, flavor, and juiciness [3]. Hence, it's of great importance to obtain reliable information about raw meat., In the production of meat products, meat quality is also an important manufacturing requirement, because consumers are susceptible to any forms of contamination that may occur during the manufacturing processes. The great variability in raw meat often leads to highly variable products being marketed without a controlled level of quality, which imposes great pressure on the food manufacturing industry to guarantee the quality of meat [4]. Hence, quality assurance and control are among the main tasks in production and processing of meat and meat products.

On the other hand, meat and meat products are also potential vehicles of hazards to human health. Types of hazards that may be present in meat products include chemicals (causing acute or long-term toxicity), biological agents (pathogenic bacteria, viruses), as well as physical objects (may cause injury) [5]. Biological hazards are of most concern. Their occurrence in meat and meat products is unavoidable because contaminants are present in and on the animals and in their environment. Raw meat and not fully heated (canned) or fermented/dried meat products are highly perishable, which makes them prone to quick spoilage due to microbial presence and growth. In addition, we should also pay attention to the authenticity of meat and meat products as adulteration occurred frequently in recent years and had been the limiting factor which would restrict the healthy and rapid development of meat industry. Some people may replace high value meat with low cost meat or offal or add some improper additive into meat products. The determination and detection of adulteration are indispensable as there are some people who do not accept specific meat for religious reasons. In order to guarantee the legitimate rights and interests of consumers, to eliminate adulteration is necessary...

In conclusion, to realize these needs mentioned above and to fulfil consumers' satisfaction, it is very important to provide meat and meat products that can better meet the customers' needs and market requirements. Therefore, it is a crucial element within the meat industry to accurately assess meat and guarantee the quality and safety. Different techniques such as sensory analysis, chemical procedures and instrumental methods have been employed to provide information about meat quality [6]. Sensory analysis is often implemented by professional staff. This method has been widely used in many food research fields. However, it is subjective, labourious, time-consuming and inconsistent. Chemical procedures and instrumental methods have been used in detecting quality attributes for a long time, which are more convenient, precise and effective than sensory analysis [7]. For chemical methods, the long-time standard for protein analysis is the Kjeldahl method and the method of choice for fat analyses is a solvent-based method for measuring the total fat content in meat. In terms of instrumental methods, pH is traditionally measured by pH meter by inserting it into the muscle directly after incision of the muscle, and colorimeters are commonly utilized for meat color evaluation.

However, most of the above-mentioned techniques are destructive, tedious, time consuming and require lengthy sample preparation. Therefore, these traditional methods have limited

applicability and are not suitable for fast analysis and early detection of quality attributes in industrial and commercial processing. In contrast to conventional methods, many novel and automatic technologies based on mechanical, optical, dielectrics, X-rays, spectroscopy, and nuclear magnetic resonance have emerged for detecting these quality and safety attributes. The Table 2 compared several methods. Among them, spectroscopy technique included near infrared spectroscopy (NIR), mid-infrared spectroscopy (MIR), far infrared spectroscopy (FIR) and Raman spectroscopy has been considered as one of the most promising technique [8].

| Methods | Advantages | Disadvantage |
|---|---|---|
| Ultrasound technique | Rapid, Non-destructive, Non-polluting, High sensitivity | Easily affected by operators, measurement sites as well as the ultrasonic frequency, Only detecting chemical compositions for some specific parts |
| CT scanning | Non-invasive, Providing detailed images | Expensive, Longer evaluation time, Limited range of application |
| Computer vision | Providing spatial information, Higher accuracy than manual inspection, Able to detect external attributes, Suitable for on-line detection | Limited multi-constituent information, Unable to detect internal attributes |
| Spectroscopy technique | Simple, Providing spectral information, Able to detect internal attributes | Limited sensitivity to minor components and complicated analysis |

**Table 2.** Non-destructive techniques for meat quality and safety determination

Infrared spectroscopy is the electromagnetic radiation waves between the visible light (Vis) and middle infrared (MIR). In general, the absorptions observed in the near infrared region are overtones or combinations of the fundamental stretching bands which are usually due to C-H, N-H or O-H stretching [9]. Table 3 summarizes the bands commonly observed for organic molecules in the near infrared region. Feature information of organic molecules in a sample could be obtained after scanning the sample.

| Wavelength (nm) | Assignment |
|---|---|
| 2200-2450 | Combination C-H stretching |
| 2000-2200 | Combination N-H stretching, Combination O-H stretching |
| 1650-1800 | First overtone C-H stretching |
| 1400-1500 | First overtone N-H stretching, First overtone O-H stretching |
| 1300-1420 | Combination C-H stretching |
| 1100-1225 | Second overtone C-H stretching |
| 950-1100 | Second overtone N-H stretching, Second overtone O-H stretching |
| 850-950 | Third overtone C-H stretching |
| 775-850 | Third overtone N-H stretching |

**Table 3.** Common near infrared bands of organic compounds

NIR spectroscopy has a great potential for the estimation of quality and safety attributes in meat and meat products in recent years, and has been considered as one of the effective and progressive techniques [10].. It's a potential analytical tool for sensitive and fast analysis with simplicity in sample preparation allowing a simultaneous assessment of numerous meat properties [11]. NIR has shown enormous potential to predict quality attributes, such as protein, fat, moisture, ash, myoglobin, pH value, water-holding capacity (WHC), color, marbling, tenderness and safety attributes (freshness, total bacterial count, adulteration) [12]. The existing researches indicated that NIR has been successfully applied to the quantitative determination of such attributes in meat with high accuracy and the coefficients of determination (R) of some indicators were up to 0.90 between predicted and reference values. In general, the whole process of prediction was carried out as what is shown in Fig.1.
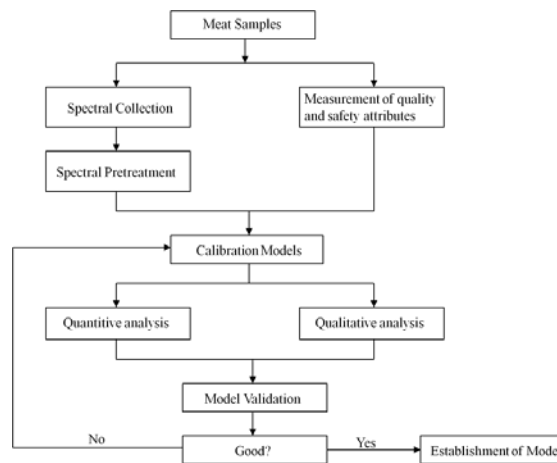


**Figure 1.** The whole process of prediction

## 2. Quality Attributes

A number of attributes are related to the quality of meat and meat products, for example, water content, fat [13], protein, ash [14], myohemoglobin, pH, tenderness, WHC, color, and marbling. The constituents are intrinsic reasons that affect meat quality [15]. Among them, water content, pH value, tenderness, WHC and color are especially important [16]. As water content is the reflectance the freshness of meat and is technologically and financially important for food-processing industry. Especially in recent years, the emergence of water injection in meat has made the fresh pork water content test become particularly important [17]. The pH value of fresh meat which may have influence on other meat properties, such as color, water-holding capacity and shelf-life, serves an important function in grading meat [18]. WHC is defined as the ability of muscle to retain water or resist water loss during postmortem storage. It is of great significance for commercial value and consumer acceptance. The quality of fresh meat

depends to a large extent on WHC. Because it has a great influence on the appearance of fresh meat during retail and might affect the sensory properties of cooked meat. Color influences the acceptability of meat and meat products and plays a major role in the purchase decision. Consumers often use meat color variations as an indicator of freshness and wholesomeness. Tenderness is also an important attribute influencing consumer opinion about the eating quality of fresh meat [19].

The following are some examples about the application of NIR to predict the water content, pH value, WHC and tenderness, respectively.

## 2.1. Water Content

Zhang. *et al* [20] collected a total of 57 samples from 31 fresh loins from three different slaughtering houses in 3 days. Each sample was vacuum-packed with serial number. All samples were stored at 4°C in a special cold storage box and transported to the nondestructive detection laboratory immediately. After removing the fat and connective tissue from the sample, all of the fresh pork samples were chopped to approximate dimensions of 8 cm×5 cm×3 cm for further analysis in laboratory. And samples were packaged again into the corresponding original vacuum bag and stored at 4°C in the refrigerator for retaining freshness. Then reflectance [21] spectrum was captured by the VIS/NIR spectra system (as is shown in Fig. 2) which consisted of an AvaSepc-USB double channel VIS/NIR spectrometer (the wavelength range is from 200 nm to 1750 nm), the matched spectrum acquisition software, light source with two halogen lamps and voltage-stabilized source, Y type fiber, optical probe, a PC, platform and white ceramic standard plate. The original spectrogram was shown in Fig.4. Standard values of water content were measured immediately after VIS/NIR spectrum data were collected according to GB-5009.3-2010. The original spectrum and statistics data of pork water content were shown in Fig. 3 and Table 4, respectively.
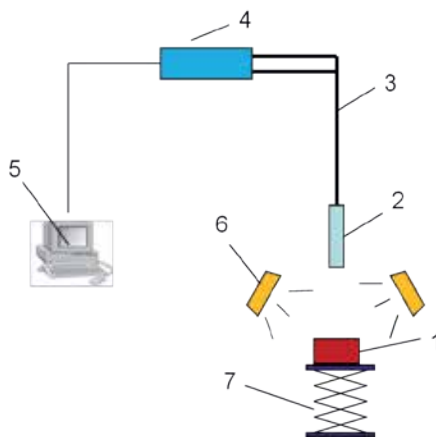


**Figure 2.** VIS/NIR; spectral system 1. Sample 2. Optical Probe 3. Fiber 4. Spectrometer 5. PC 6. Light Source 7. Platform
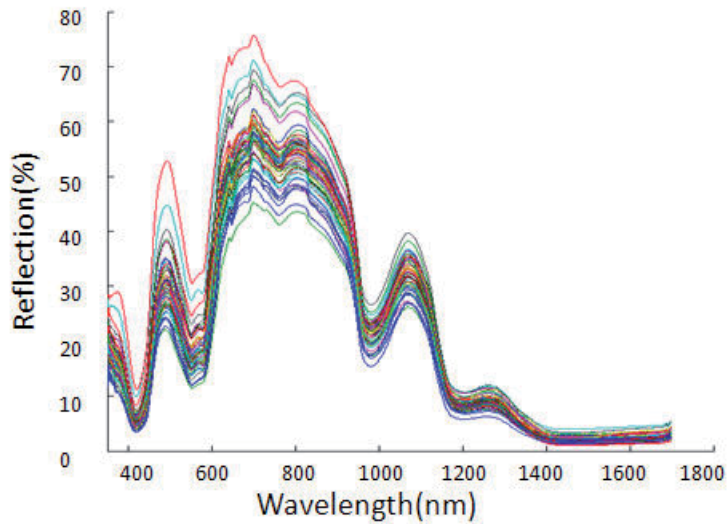
**Figure 3.** Original spectrum

| Samples sets | Water content range | Average value | Variance |
|---|---|---|---|
| Correction set | 73.05-78.08 | 75.52 | 1.44 |
| Validation set | 73.75-77.69 | 75.54 | 1.22 |
| Total samples | 73.05-78.08 | 75.53 | 1.38 |

**Table 4.** The Statistics data of pork water content

Then spectral data were analyzed using MATLAB7.6 statistical software package. Firstly, total 57 samples were randomly divided into calibration and validation sets. 43 samples were placed in the calibration set used for building the model, and others were the validation set used for testing model. To overcome the influence of thickness and surface roughness of samples and to improve modeling accuracy, different kinds of pretreatment methods included Median smooth filter (M-Filter), multiple scattering correction (MSC), first order differential (FD), standard normalized variants (SNV) and combination of them were adopted. Then partial least squares regression (PLSR) and multivariate linear regression (MLR) methods were used to establish the testing models. The models were evaluated by correlation coefficient (R) and root mean square error (RMSE) of calibration set and validation set. Good models possessed higher R and lower RMSE, and differences between the calibration set and prediction set were less.

The PLSR model use full band spectrum information and results for two sets were shown in Table 5 by using different pretreatment methods. Results show that the model was better by using of M-Filter, MSC, FD and SNV. Optimal principal components number was 15, Rc and RMSEC of calibration set were 0.90 and 0.50 respectively. Rp and RMSEP were 0.81 and 0.70 for validation set respectively.

| Pretreatment method | Optimal principal components number | Rc | RMSEC | Rp | RMSEP |
|---|---|---|---|---|---|
| MSC | 10 | 0.69 | 1.23 | 0.58 | 1.11 |
| SNV | 7 | 0.64 | 0.80 | 0.62 | 0.92 |
| MSC+FD+SNV | 10 | 0.89 | 0.50 | 0.78 | 0.81 |
| FD+MSC+SNV | 15 | 0.90 | 0.50 | 0.81 | 0.70 |

**Table 5.** Results of PLSR models based on different pretreatments

In the MLR model, most significant wavebands were selected by using stepwise regression analysis and according to relative coefficient graph, MLR equations and coefficients were obtained and the results of model were shown in Table 6. The Fig. 4 represents the residual of calibration set after using M-Filter, FD and MSC pretreatment. Residuals of No.26 and 34 samples were unusual and the two samples were eliminated. Rc was higher by using M-Filter, FD and MSC compound pretreatment, and much higher R and lower RMSE were obtained after eliminating abnormal samples. Results indicated that there was big distinction of R between calibration and validation sets, which demonstrated that stability of the model was not good.

| Pretreatment method | Variables | Rc | RMSEcv | Rp | RMSEP |
|---|---|---|---|---|---|
| M-Filter+MSC | 6 | 0.63 | 1.02 | 0.58 | 1.23 |
| M-Filter+FD+MSC | 4 | 0.86 | 0.66 | 0.77 | 1.20 |
| Eliminate the abnormal samples | 5 | 0.91 | 0.50 | 0.80 | 1.07 |

**Table 6.** Results of MLR models based on different pretreatments
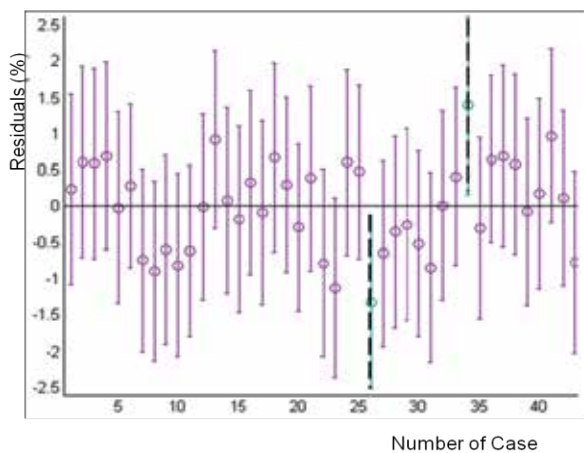


**Figure 4.** Residual plot

## 2.2. pH Value

Ma. *et al* [22] had ever applied NIR technology into prediction of pH value of beef. The sample preparation process was similar to the method mentioned above. Total 120 fresh samples were chopped to approximate dimensions of 8 cm×6 cm×2.5 cm. In order to obtain the pH value of entire shelf period, the experiment cycle was designed as 18 days. During the first 6 d, take out one sample to test every 12 h, and then take out two samples to test every 12 h for the next 12 d. The framework of detection system with visible/near infrared spectroscopy was shown in Fig. 5. The enclosed space is designed mainly to form a dark room, and exclude external light interference when testing samples.
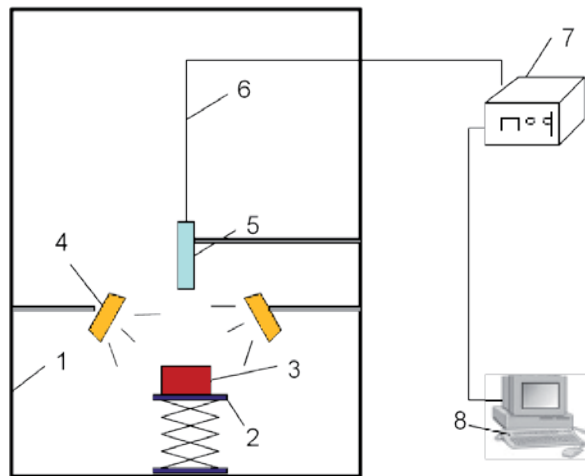


**Figure 5.** Framework of detection system with visible/near infrared spectroscopy; 1. Enclosed space 2. Platform 3. Sample 4. Light source 5. Fiber Probe 6. Fiber 7. Spectrometer 8. Computer

Once the spectral data of the samples were obtained, the pH values were determined with a pH meter. Six measurements on each sample were taken at different locations across the sample surface and averaged. Spectral data were analyzed using MATLAB7.6 statistical software package. Spectral data and pH of all samples were used for principal component analysis (PCA) and statistical analysis, respectively. Then use spectral leverage value (Leverage) and chemical absolute error (Residual) to test all the spectral anomalies or chemical value anomaly of the sample. Weed out 8 abnormal the remaining 112 samples were used for the following analysis. Total 112 samples were randomly divided into calibration and validation sets. 84 samples were placed in the calibration set used for building the model, and others were the validation set used for testing model. To eliminate the phenomenon of atlas offset or drift and high frequency noise interference, MSC and S-G smoothing were used for processing reflection spectrum of the sample data. The original spectrum and spectrum after MSC pretreatment were shown in Fig. 6 and Fig. 7. Then establish prediction model of MLR, PLSR and least square-support vector machine (LS-SVM) for prediction of pH value in beef based on full-spectrum and effective wavelengths selected by genetic algorithm (GA). GA is a

computational model based on natural selection and genetic mechanism of biological evolution and is a kind of method to search the optimal solution by simulating natural evolutionary process. It has been successfully applied to select the best feature variables in VIS/NIR spectroscopy to build a stable model, especially for PLSR (GA-PLSR) which combines the advantages of GA and PLSR.. The best model occurred when the RMSECV between the true values and predicted values was the lowest. The results were shown in Table 7.
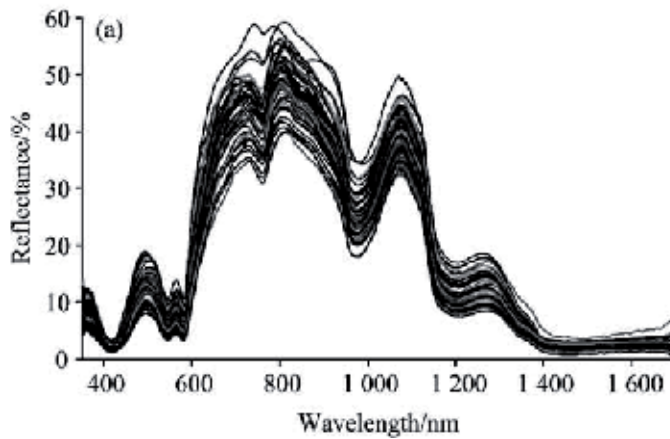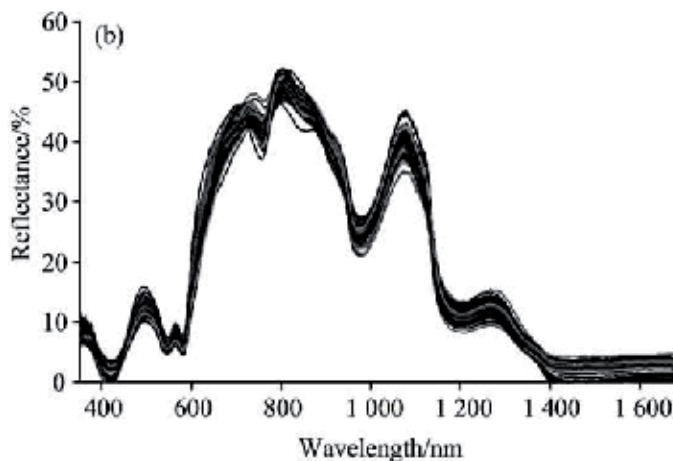


**Figure 6.** Original spectrum



**Figure 7.** Spectrum after MSC

| Pretreatment methods | MLR | | | | PLSR | | | | LS-SVM | | | |
|---|---|---|---|---|---|---|---|---|---|---|---|---|
| | Rc | SEC | Rv | SEV | Rc | SEC | Rv | SEV | Rc | SEC | Rv | SEV |
| MSC | 0.783 | 0.144 | 0.770 | 0.183 | 0.864 | 0.118 | 0.729 | 0.189 | 0.889 | 0.109 | 0.756 | 0.185 |
| MSC+SG | 0.806 | 0.137 | 0.867 | 0.150 | 0.925 | 0.088 | 0.831 | 0.155 | 0.950 | 0.075 | 0.865 | 0.142 |

**Table 7.** Prediction results of beef pH value based on different models and different pretreatment methods

As is shown, three kinds of prediction revealed better results after MSC combined with SG smoothing pretreatment. Hence adopt MSC combined with SG smoothing as the processing method below. Besides, LS-SVM model prediction accuracy was the highest, MLR prediction accuracy was the poorest. However on the whole three kinds of model prediction accuracy was not high, this mainly because useless redundancy information decreased the model prediction ability and prediction accuracy.
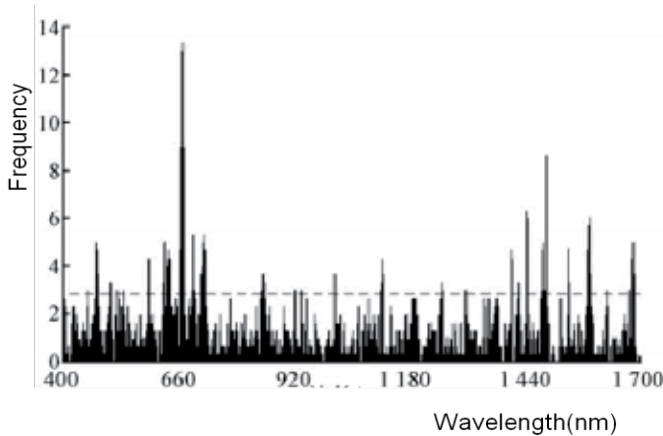


**Figure 8.** Frequencies of variables selected by GA

GA was employed for effective spectral variables selection after all band spectral variables were pretreated by MSC combined with SG smoothing. GA group size was set to 30 individuals and each individual genes variable was set to 17, mutation probability and crossover proba‐ bility was set to 1% and 50% respectively, genetic algebra was 100 generations. As the GA initial population was generated randomly, 5 times screening processes were repeated for establishment of models. The Fig. 8 showed frequencies of variables selected by GA. Effective wavelength variables whose selected frequency was higher than the horizontal dotted line in the figure was used for modeling. Table 8 showed the MLR, PLSR and LS-SVM prediction results based on the variables selected by GA. Compared with the Table7, the accuracies of three kinds of modeling had been improved, MLR model predicted results was a bit poor, PLSR and LS-SVM modeling prediction were better. The LS-SVM modeling based on effective spectrum selected by the fourth iteration selected have the best prediction results, with the correlation coefficient of calibration set and validation set of 0.950 and 0.935 respectively,

predict standard deviation was 0.074 and 0.111. The corresponding selected effective spectral variables were shown in Fig. 9. Vertical lines in the graph represent the GA selection by the wavelength of the effective variables. This study demonstrated that the LS-SVM model built by using VIS/NIR spectroscopy with GA could nondestructively and rapidly determine pH value in beef during its whole shelf-life. This research provided a basis of further developing device for nondestructive and rapid determine pH value in beef.

| Times of GA | MLR | | | | PLSR | | | | LS-SVM | | | |
|---|---|---|---|---|---|---|---|---|---|---|---|---|
| | Rc | SEC | Rv | SEV | Rc | SEC | Rv | SEV | Rc | SEC | Rv | SEV |
| 1 | 0.931 | 0.080 | 0.854 | 0.152 | 0.968 | 0.056 | 0.835 | 0.162 | 0.980 | 0.046 | 0.851 | 0.154 |
| 2 | 0.948 | 0.073 | 0.826 | 0.175 | 0.972 | 0.052 | 0.906 | 0.112 | 0.982 | 0.040 | 0.876 | 0.135 |
| 3 | 0.927 | 0.086 | 0.862 | 0.151 | 0.965 | 0.063 | 0.918 | 0.108 | 0.986 | 0.037 | 0.903 | 0.123 |
| 4 | 0.965 | 0.064 | 0.889 | 0.142 | 0.960 | 0.072 | 0.931 | 0.101 | 0.950 | 0.074 | 0.935 | 0.111 |
| 5 | 0.912 | 0.102 | 0.768 | 0.181 | 0.962 | 0.068 | 0.924 | 0.103 | 0.954 | 0.070 | 0.902 | 0.123 |

**Table 8.** Prediction results of GA-MLR, GA-PLSR, GA-LS-SVM
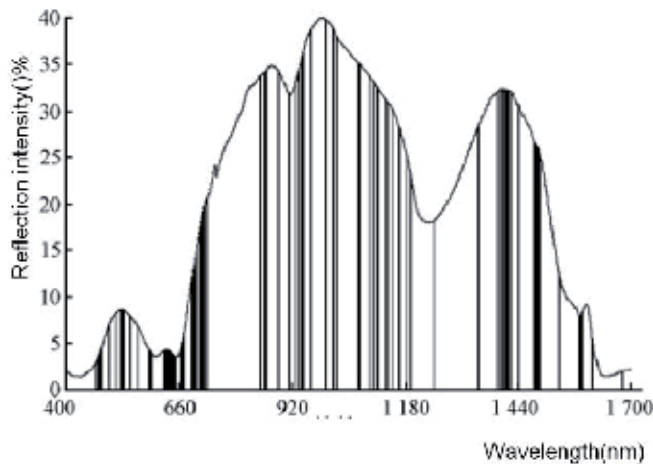


**Figure 9.** Spectra effective variables selected by GA

### 2.3. Tenderness

VIS/NIR Hyperspectral Imaging was employed by Tian *et al* [23] to prediction of beef tenderness. The hyperspectral imaging system can capture both spectral and spatial data simultaneously and process immediately in the VIS/NIR regions of the spectrum [24]. A total of 42 beef samples were collected at various retail stores and each steak was ensure to come from different animals by selecting from various retail stores. All the samples were taken from the

part of longissimus dorsi (LD) between 12 th rib and 13 th rib and then all the samples were cut into 4 cm×6 cm×2.5 cm chops. Each beef steak was first scanned by the hyperspectral imaging system. The system used in this study was a line-scan spectrograph which records a whole line of an image rather than a single pixel at a time. As shown in Fig. 10, the system consists of CCD camera along with focusing lens (12 mm), a spectrograph, a electric translation stage operated by a stepper motor and controller and a computer supported with Spectral Cube data acquisition software. In order to illuminate the sample and keep better distribution of optical intensity, two 100W halogen lamps was fixed above the sample from both sides at the height of 50 cm and at an angle of 45°.
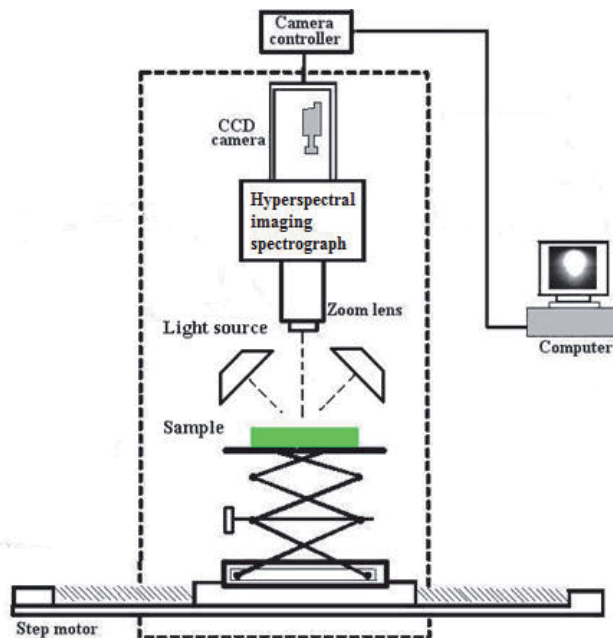


**Figure 10.** Hyperspectral imaging system

Beef sample was placed on the electric translation stage to be scanned line by line using 50 ms exposure time to build a hyperspectral line image which is then stored to composite 3D hyperspectral image. Several congruent sub-images which represent intensities with 520 wavelength bands from 380 to 1100 nm formed 3D image. The acquired hyperspectral image include both spatial and spectral information and we can get physical, geometric features and chemical information from it [25]. After that reference values of tenderness were determined. Steaks were cooked in 80°C water bath to an internal temperature of 70°C, which was moni‐tored by thermoelectric couple inserting into center of samples, avoiding fat and connective tissue. Then the samples were vacuum packaged and put in the refrigerator to store at 4°C for 12 h before removing 6-8 cores parallel to the longitudinal orientation of muscle fibers [26]. Each core was sheared perpendicular to the longitudinal orientation of the muscle fibers by a Warner-Bratzlar Shear Force (WBSF) apparatus [27]. For each sample, six cores were taken and

the mean peak WBSF value was used for data analysis. In Table 9 the relevant statistics of tenderness of beef steaks were presented.

| Quality attributes | n | Mean | Minimum | Maximum | SD | CV |
|---|---|---|---|---|---|---|
| WBSF (N) | 42 | 50.41 | 30.66 | 75.01 | 18.79 | 0.37 |

Note: n = number of samples; SD = standard deviation; CV = coefficient of variation.

**Table 9.** The reference values of WBSF values of beef steaks

Images were processed for analysis utilizing processing algorithms and analysis for identification of background from lean and fat texture parameters. The muscle lean areas were extracted from background with initial values for textural threshold which were selected from the plot of pixel intensities as shown in Fig. 11. After image segmentation, the lean muscle area was used for future texture feature and spectral information extraction. Before extraction of textural features, median filtering was used to reduce noise [28].



(a) Full mask of muscle lean          (b) Muscle lean areas of sample
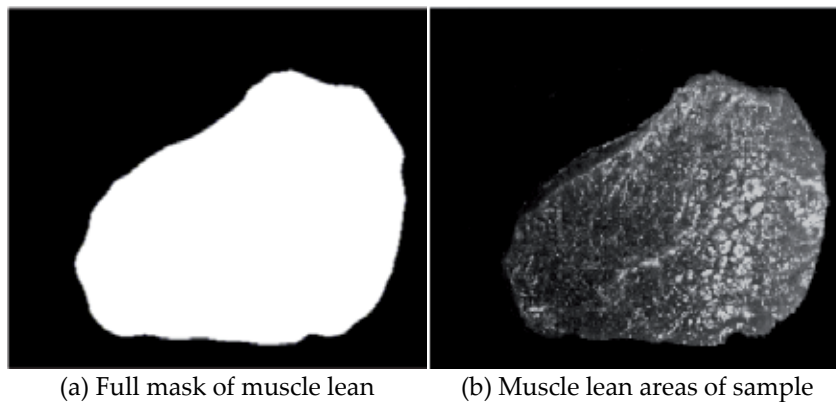
**Figure 11.** Muscle lean area of beef steak extracted from hyperspectral image

After processing, the hyperspectral image of beef samples contained only the lean part of the sample without fat, which was then used as the main region of interest (ROI) for further analysis. The average spectrum of each sample was extracted by locating the lean parts of the beef sample as the main region of interest (ROI). The extracted spectral data from all steaks were then used to construct a data matrix in which the row represents the number of samples and the column represents the number of variables. Furthermore, the reflection intensity hyperspectral data was converted to absorbance spectra by taking the base-10 logarithm of the reciprocal reflectance spectrum (log10 (1/R)) [29]. All processes of image segmentation, denoising and spectral data extraction were programmed in ENVI 4.3 and Matlab 7.6. An obvious absorbance peak within 530-580 nm and a small peak at 650 nm were presented. The

former related with oxyhaemoglobin absorption bands, and the latter with O-H third overtone or an absorption band produced by myoglobin oxidation. The samples of different tenderness presented the same spectral patterns all over the wavelength region (430-1000 nm), but there were still some differences in the magnitudes of absorbance intensities as shown in Fig. 12. The reason was because different samples from carcass were different in their major chemical composition such as fat, protein and dry matter. The tough samples had the higher absorbance intensities throughout the whole spectral region, meanwhile the tender ones had the lower absorbance (highest reflectance) compared to the mean overall average value.

For each absorbance spectrum, the first derivative was calculated to correct multiplicative scatter, baseline drifts, and to avoid the overlapping peaks. Spectra smoothing was performed on the absorbance spectra using the S-G method and moving average filter method with a span of 20 points. Fig. 13 showed the first derivative spectra of all samples. The main obvious variations bands can be identified at 450, 535 nm and 575nm. Obvious changes at 450 nm was related with Soret absorption band, attributed to traces of erythrocytes of hemoglobin, and the changes at 575 nm related with oxyhaemoglobin absorption.
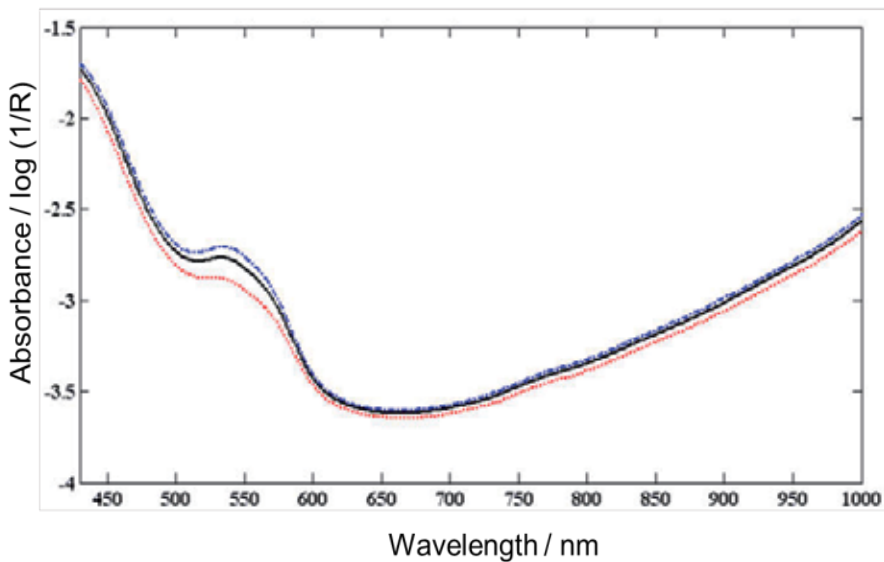


**Figure 12.** Difference in absorbance spectral profiles of beef steaks

The stepwise was performed with first derivative spectra to determine the optimal wavelengths. As shown in Table10, for tenderness, 8 wavelengths were determined as optimal wavelength to construct MLR prediction model, with coefficient of determination (Rv) of 0.88 and a root mean square error (RMSEV) of 6.49 and RPD value as 2.94 which indicated the model of meglio performance.
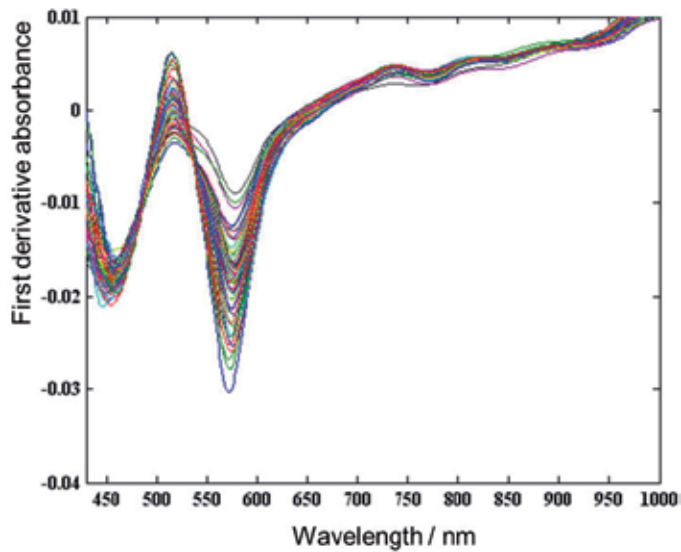
**Figure 13.** First derivative of absorbance spectral

| Quality attributes | Optimal Wavelengths | Rc | RMSEC | Rv | RMSEV | RPD |
|---|---|---|---|---|---|---|
| Tenderness | 437, 534, 549, 646, 700, 718, 776, 849 | 0.90 | 5.27N | 0.88 | 6.49N | 2.94 |

**Table 10.** MLR models based optimal wavelength of longissimus dorsi (LD)

## 3. Safety Attributes

The action of tissue enzymes, microorganisms and the degeneration of meat are the main factors which lead to meat spoilage. Meat spoilage is a dynamic and complex process which often manifest in internal changes (chemical components) and external changes (colour, texture, smell, et al). During storage, total volatile basic nitrogen (TVB-N) formed along with the changes of many substances and other basic nitrogenous compounds. TVB-N content in meat was considered as an important reference index to evaluate meat freshness. Total viable bacterial count (TVC) is one of the most important parameters during pork spoiling, by which we can have a knowledge of the degree of spoilage of meat [30]. Meats with excessive bacteria cause harm to human health, thus it is critical to guarantee the safety of meats. In addition, because of high commercial value meat industry, it has attracted the attention of adulterators for centuries. Therefore the determination and detection of adulteration are indispensable as there are some people who do not accept specific meat for religious reasons. In order to guarantee the legitimate rights and interests of consumers, to eliminate adulteration is necessary. The Fig. 14 revealed the potential authenticity problems in daily life [31].
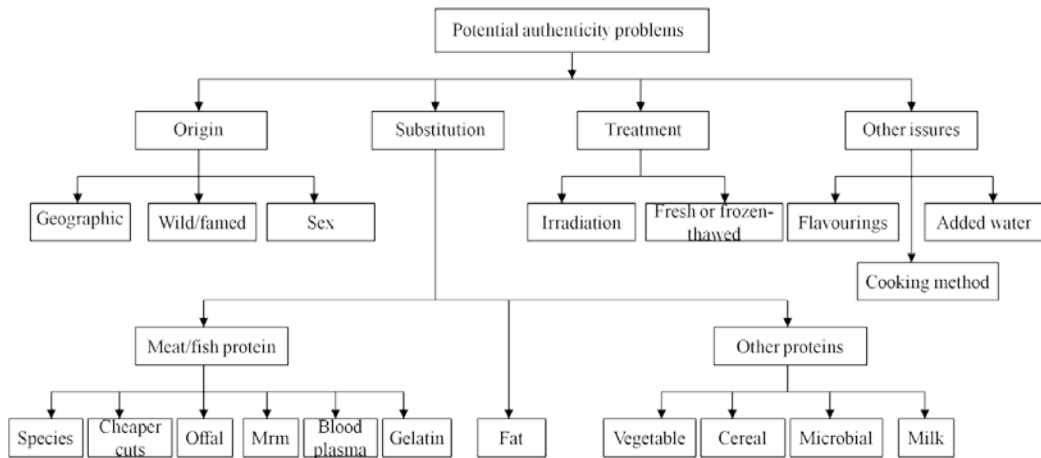
**Figure 14.** Potential authenticity problem

## 3.1. Total Volatile Basic Nitrogen (TVB-N)

Real-time and on-line detection of freshness is current industrial desire. An on-line multi-channel visible and near infrared spectral system (300-2500nm) has been developed by Zhao *et al* [32] which was progress on prediction of pork freshness. The whole system mainly included three sections: the hardware system, the software system and the model.

Among them, the hardware system mainly consisted of the visible and near infrared spectral system, signals transmission system and motion system (as is shown in Fig.15). The visible and near infrared spectral system was used for collecting spectral data. It was mainly composed of two fiber optic spectrometers (AvaSpec-2048×14 and AvaSpec-NIR256-2.5, Avantes Netherlands), fiber optic multiplexer (FOM-IR400-2×8, Avantes Netherlands), a light unit with a tungsten lamp as the light source (AvaLight-HAL, Avantes Netherlands), 7 reflection probes (FCR-7IR400-2-ME, Avantes Netherlands) and an electronic computer. The wavelengths of first fiber optic spectrometer ranged from 300 nm to 1100 nm with a spectral resolution of 0.04-20 nm, the second ranged from 1000 nm to 250 0nm with a spectral resolution of 6.0-90 nm. Various spectral data operation was completed by the spectrometers software package (Avantes AvaSoft). By using multiplexer control software (Avantes AvaFom), the switching sequence of many channels was achieved. In order to implement on-line visible and near infrared spectroscopy system [33], a secondary development was performed on the SDK platform of spectrometers software and multiplexer software.

During the actual experiment, more test points in the sample were required. Due to the need for multi-point measurement, firstly the quantity of the reflectance probe has to be determined. In multiple measurements, with increase of the number of measurements, the standard deviation of arithmetic mean decreases. To improve the accuracy of the measurement results, the number of measurements cannot be increased indefinitely. The general number of measurements is 5-10 times. There are six fibers in the outer ring of the probe
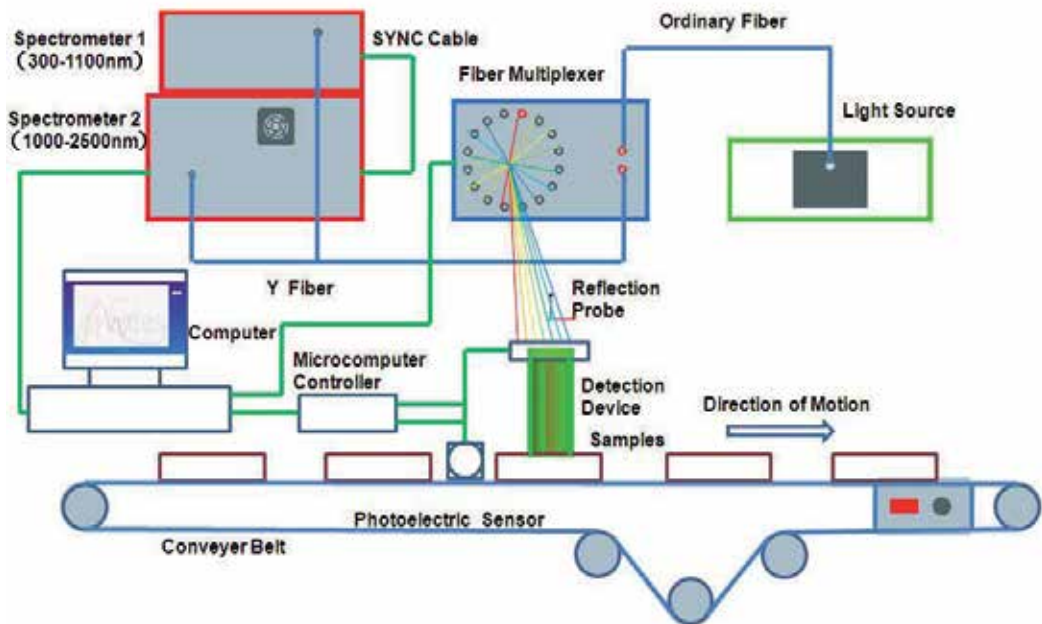
**Figure 15.** Real-time visible and near infrared multi-channel spectral system

and once fiber in the inner ring. From the arrangement of probe, seven fiber probes was chosen to design the detection device, and when the number is seven, the detection device could make the best of the information of the detection region. The arrangement of reflectance probe is shown in Fig. 16.
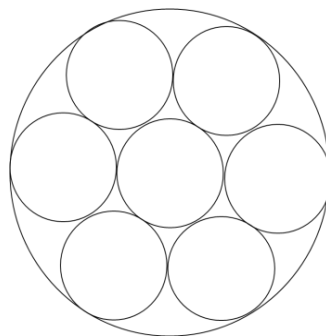


**Figure 16.** The arrangement of reflectance probe

The reflection probes were fixed in a device made up of a detection probe. The probe can acquire the spectral data from the pork cuts surface. Multi-point testing of the samples in different locations can be achieved through fiber multiplexer. Detection device was connected

with electric translation stage through connection frame. With the control of stepper motor, detection device could go up and down following the electric translation stage. The construct of connecting detection device is shown in Fig. 17.
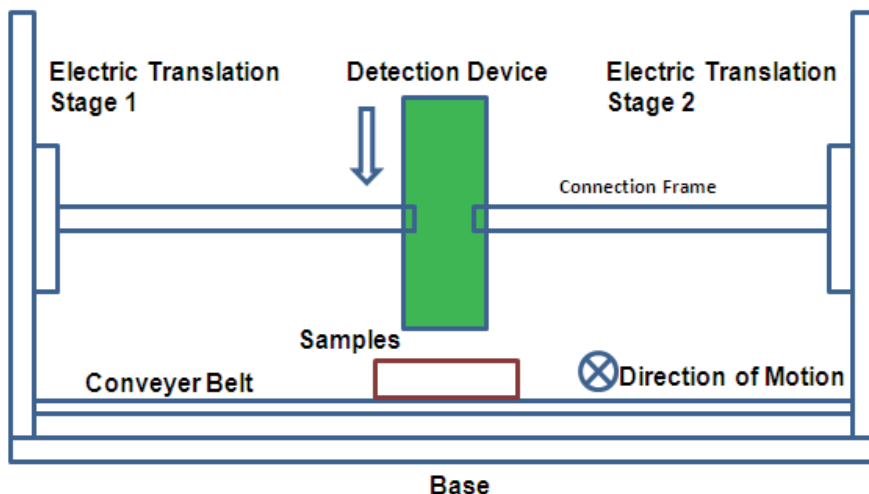


**Figure 17.** The construct of connecting detection device

Signal was transmitted and processed between the various parts of hardware by signal transmission system. The two spectrometers were connected with synchronization cable to ensure that the two spectrometers were synchronized. The second spectrometer was made the master spectrometer. The connected pattern between spectrometers makes them collect spectral data and display prediction results on the same software interface. Fiber multiplexer was connected with computer through the serial cable, so that computer could control the switching sequence of the fiber multiplexer. When sample approaches the required position, the photoelectric sensor produces an output signal to single chip microcontroller. The model of photoelectric sensor was E3Z-T61. Programmable System on Chip was used to receive signals from computer parallel port to control the stepper motor. With the control of stepper motor, the position of sample to be detected was controlled. Sample on arrival to the detection zone, signal is generated to control spectrometer and collect optical data with certain delay time. After collection of spectral data, control system retuned fiber multiplexer and detection device.

Motion system was used to deliver detection probe and samples and maintain constant distance between the detection probe and the surface of the sample to be detected. Motion system included motion parts of the conveyor belt and motion parts of detection device. Conveyor belt was designed to convey samples. Conveyor speed was adjustable. When testing the same batch of samples, the conveyor speed should remain constant. The detection device

moved up and down which was controlled by motor, and when the detection device was in contact with the sample surface, the spectral data collection procedure was started.

The initial software interface is shown as Fig. 18. Before collection of spectral data, the spectrometer was calibrated with black reference and white reference. The measurement of black reference which is dark current spectral data was measured by turning off the light source. And the white reference was measured by the use of the white reference tile. After connection of hardware device, the software was operated. After receiving signal from the serial port, with proper delay time, the software triggered spectrometer to collect the spectral data from the sample. The delay time was determined according to the hardware structure. The spectral data acquisition was achieved through switching sequence of multi-channel fiber multiplexer, and then the multi-point measurement results were averaged, and finally the diffuse reflectance of sample were calculated. After the pre-treatment of spectral data, the corresponding freshness detection prediction model was called in the software to assess every indicator of freshness, finally the prediction results were displayed in the software interface.
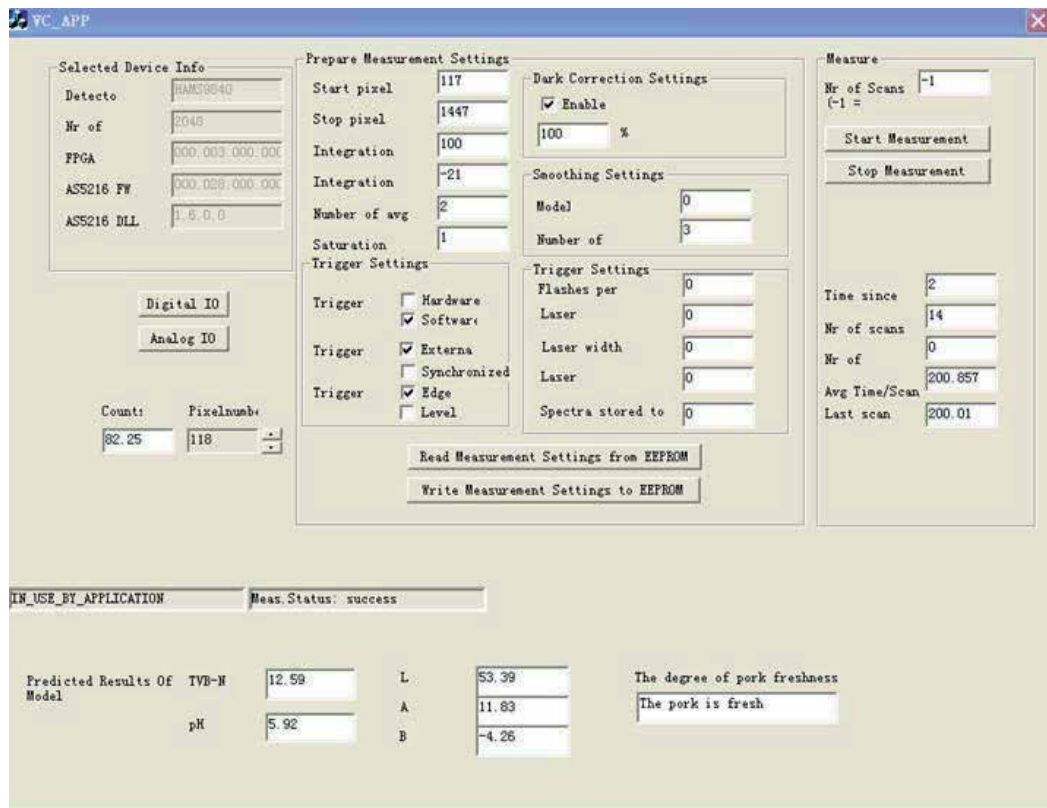


**Figure 18.** Start interface of software system

The prediction model was based on an experiment carried out under static environment. Diffuse reflectance spectroscopy data from the pork surface of 380-1080 nm was obtained by use of multi-channel visible near-infrared spectroscopy system. The pre-treatments of the spectral data were multiplicative scattering correction (MSC) and standard normal variables (SNV), then using partial least squares regression to establish pork freshness of prediction model, and then evaluated the freshness of pork. The results show that the partial least squares regression model after standard normal variables (SNV) treatment is relatively stable, and the performance is better. The correlation coefficient of TVB-N is 0.9. Finally, the accuracy rate of pork freshness assessment is 92.9% by this model.

## 3.2. Bacteria Contamination

Tao *et al* [34] made use of NIR hyperspectral imaging technique to realize determination of *Escherichia coli* contamination of pork. 31 fresh pork meat samples were purchased from a local market earlier on the day of the experiment and transported to the lab under refrigeration in 30 min. In order to avoid the effect from initial contamination, the surface pieces in 1-cm thickness were removed from all pork meat chops under sterile procedures. Then, all samples were trimmed to the size of 9 cm×5 cm×2.5 cm uniformly. The generic E. coli was provided by College of Food Science and Nutritional Engineering, China Agricultural University. The bacteria used were first activated by duplicate transfers and incubation in Nutrient Broth for 24 h at 37 °C respectively, and then delivered into 0.85% sterilized saline solutions to achieve series of bacterial suspensions. Pork meat samples with different E. coli loads were artificially contaminated by submerging into different concentrations of E. coli suspensions accordingly. Additionally, in order to ensure the adhesion of E. coli cells on pork meat samples, the samples were placed in the super clean bench for a certain time uniformly [35].

The cell counts of different E. coli suspensions were determined immediately after the sample preparation. Three original or diluted concentrations for each suspension were selected to be incubated on Nutrient Agar and two repetitions were performed on each concentration. All plates were incubated at 37°C for 48 h and the results were expressed in Log CFU/mL. The data of two repetitions was averaged and then used for further analysis. Then the images of pork samples were acquired by a hyperspectral imaging system in the spectral range of 400-1100 nm. This system was similar to that mentioned above. For each sample, an average image from four images was acquired for further analysis. In addition, 2×2 binning was performed when acquiring images to improve the signal-to-noise ratio. The final hyperspectral image was of 520×688 pixels. The hyperspectral image of pork meat was shown in Fig. 19.

Then Lorentzian distribution function and the modified Gompertz function were performed to fit the scattering profiles of pork in the spectral range of 400-1100 nm. Lorentzian distribution function can be mathematically expressed by Eq. (1).

$$R_{w_i} = a_{w_i} + \frac{b_{w_i}}{1 + \left(z / C_{w_i}\right)^2} \tag{1}$$
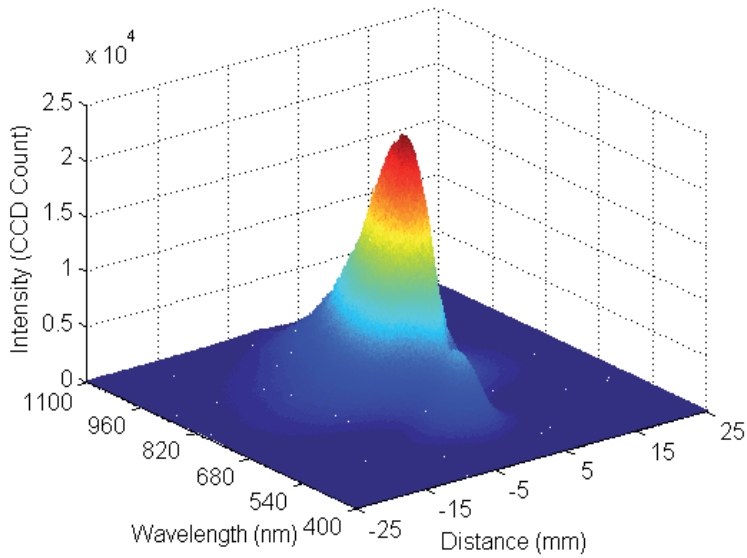
**Figure 19.** The hyperspectral image of pork meat in 3-D format

where $R$ represents the light intensity, in CCD count; $z$ means the scattering distance from the center of beam incident, in mm; $a$ is the asymptotic value of the light intensity; $b$ is the peak value of the scattering profile at $z$=0, in CCD count; $c$ is the full width of the scattering profile at $b/2$ (FWHM), in mm. The subscript $w_i$ represents one individual wavelength of the whole spectral range with $i$=1, 2, 3... N; and N is the total number of wavelengths. The modified Gompertz function with four parameters was shown in Eq. (2) [36].

$$R_{w_i} = \alpha_{w_i} + \beta_{w_i}\left(1 - e^{-\exp\left(\varepsilon_{w_i} - \delta_{w_i} z\right)}\right)$$

(2)

where $R$ represents the light intensity, in CCD Count; $z$ means the distance from the detected position to the light incident center, in mm; $\alpha$ is the asymptotic value of light intensity; $\beta$ is related to the upper value of estimated light intensity at the light incident center; $\varepsilon$ is the full scattering width at the inflection point; $\delta$ is the slope around the inflection point; $w_i$ represents the designated wavelength in the spectral range of 400-1100 nm in accordance with $i$=1, 2, 3... N; and N is the number of wavelengths [37].

Then extracted three individual Lorentzian parameters $a$, $b$, $c$, combined parameters of $(b-a)$, $(b-a)\times c$, $(b-a)/c$, $a\&b\&c$ and four Gompertz parameters $\alpha$, $\beta$, $\varepsilon$, $\delta$ were used to establish MLR models in the study. The extracted parameters $a$ and $b$ for pork samples were shown in Fig. 20. Gompertz parameters $\alpha$, $\beta$, $\varepsilon$, and $\delta$ from 31 pork meat samples were shown in Fig. 21.

(a)

(b)
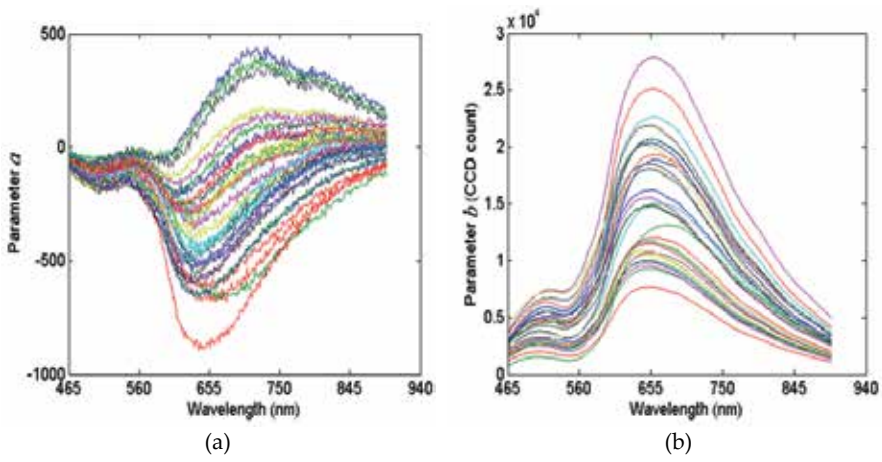
**Figure 20.** Lorentzian parameters extracted for 31 pork samples: (a) Parameter a (asymptotic value), (b) Parameter b (peak value)



(a)

(b)

(c)

(d)
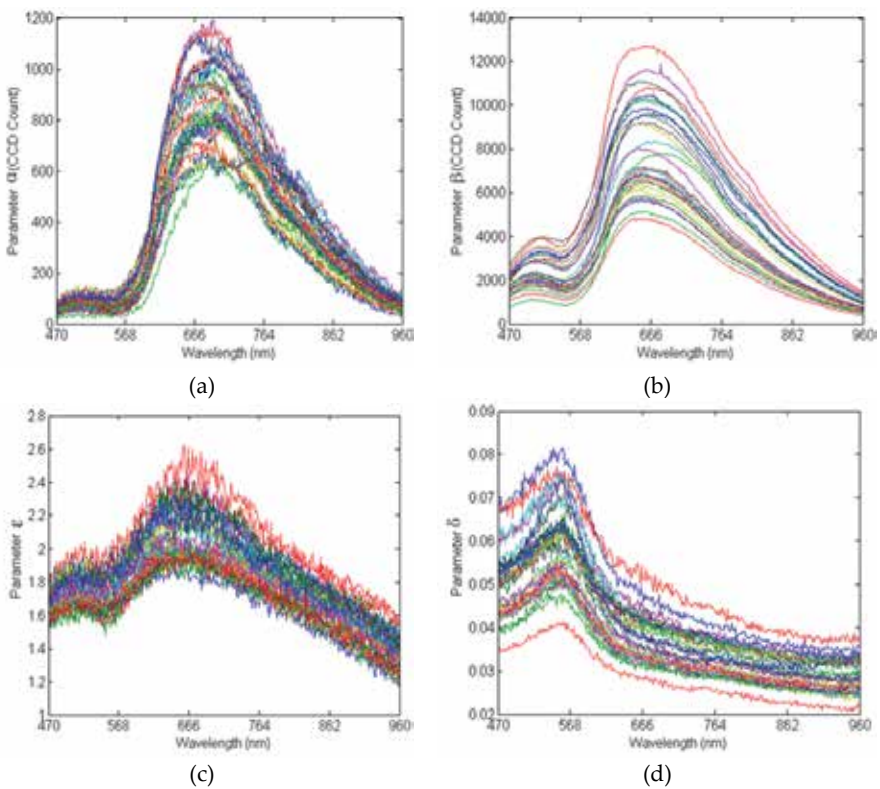
**Figure 21.** Gompertz parameters extracted from pork samples: (a) parameter $\alpha$, (b) parameter $\beta$, (c) parameter $\delta$, (d) parameter $\varepsilon$

For the Lorentzian function fitting, the models developed using parameter $a$ and integrated "$a\&b\&c$" variables determination method can give good validation result with Rv of 0.841. For the Gompertz function fitting, the model developed by parameter $\delta$ is superior to other parameters. In addition, the method of integrated parameter was also implemented to improve the model performance, and better validation results was obtained with Rv of 0.939 for pork E. coli contamination.

# 4. Conclusions and Future Outlook

The existing researches showed that when predicting the quality and safety attributes by NIR spectroscopy, minced samples present better results than intact tissue. It is mainly because minced samples are more homogeneous.. For intact samples, spectrum data obtained were affected by surface texture and inner component content. Meanwhile the spectrum data collected by surface diffuse method only represented the surface information. It was difficult to obtain internal spectrum because of the limit of depth, so it had great influence on the precision and stability of the model.The results of the present study verify that NIR spectroscopy is a suitable method to predict simultaneously several meat chemical properties. NIR shows superiorities not only in time and money consumption, but also in the detriment to body health or the environment. However, NIR spectroscopy didn't predict well when estimating some attributes of meat, for example WHC (water-holding capacity), mainly due to the low precision of the reference method. Therefore, better NIR models for such characteristics are required, mainly with respect to a better sampling procedure and improvement of the precision of the reference methods. Based on published results, NIR spectroscopy shows only limited ability for assessing the physical quality of meat.

Taking this limitation into consideration, it is difficult in this regard to envisage implementation at industrial level because of the low precision of the reference methods. More precise method and better control of other influential factors may be the fundamental way achieve improvements to this parameters.

NIR spectroscopy will be more and more popular in the meat detection industries. Nowdays, more effort has been made to reduce errors in reference methods, and more reliable models are developed by using larger sample sets which show wide ranges in reference values. In addition, the use of fiber optic probes may improve the ability of NIR to monitor and control meat processing using remote on-line detection. Furthermore, this technique does not require any consumables or supporting equipment once optimized and put into use, which has great advantage over the traditional techniques on solving the challenging quality control problems. More effort needs to be made to realize the implementation from off-line application to on-line approach [38].

## Acknowledgements

## Author details

Yankun Peng[*] and Wenxiu Wang

*Address all correspondence to: ypeng@cau.edu.cn

China Agricultural University, College of Engineering, Beijing, China

## References

[1] Lanza E (1983) Determination of Moisture, Protein, Fat, and Calories in Raw Pork and Beef by Near Infrared Spectroscopy. Journal of Food Science. j. 48: 471-474.

[2] Prieto N, Roehe R, Lavín P (2009) Application of Near Infrared Reflectance Spectroscopy to Predict Meat and Meat Products Quality: A review. Meat Science. j. 83(20): 175-186.

[3] Prieto N, Andres S, Giraldez FJ, Mantecon AR, Lavin P (2008) Ability of Near Infrared Reflectance Spectroscopy (NIRS) to Estimate Physical Parameters of Adult Steers (oxen) and Young Cattle Meat Samples. Meat Science. j. 79: 692-699.

[4] Su H, Sha K, Zhang L (2014) Development of Near Infrared Reflectance Spectroscopy to Predict Chemical Composition With a Wide Range of Variability in Beef. Meat Science. j. 98: 110-114.

[5] Xiong Z, Sun D, Zeng X, Xie A (2014) Recent Developments of Hyperspectral Imaging Systems and Their Application in Detecting Quality Attributes of Red Meats: A review. Journal of Food Engineering. j. 132: 1-13.

[6] Brondum J, Byrne DV, Bak LS, Bertelsen G, Engelsen SB (2000) Warm Edover Flavour in Porcine Meat-A Aombined Spectroscopic, Sensory and Chemometric Study. Meat Science. j. 54: 83-95.

[7] Nicola Y, Beullens K, Bobelyn E (2007) Nondestructive Measurement of Fruit and Vegetable Quality by Means of NIR Spectroscopy: A review. Postharvest Biology and Technology. j. 46: 99-11.

[8]  Williams PC (2008) Near-infrared Technology-Getting the Best Out of the Light -A short course in the practical implementation of near infrared spectroscopy for user. Nanaimo, Canada: PDK Projects, Inc.

[9]  Cen H, He Y (2007) Theory and Application of Near Infrared Reflectance Spectroscopy in Determination of Food Quality. Trends in Food Science and Technology. j. 18: 72-83.

[10]  Warriss PD (2004) Meat Science. An introductory text, Wallingford, Oxon, UK: CABI Publishing.

[11]  Williams PC (1987) Variables affecting near-infrared reflectance spectroscopic analysis. In Williams & Norris (Eds.), Near-infrared technology in the agricultural and food industries (pp.143-167). St. Paul: American Association of Cereal Chemists.

[12]  Alomar D, Gallo C, Castaneda M, Fuchslocher R (2003) Chemical and Discriminant Analysis of Bovine Meat by Near Infrared Reflectance Spectroscopy (NIRS). Meat Science. j. 63: 441-450.

[13]  Windham WR, Lawrence KC, Feldner PW (2003) Prediction of Fat Content in Poultry Meat by Near-infrared Transmission Analysis. Journal of Applied Poultry Research. j. 12: 69-73.

[14]  Viljoen M, Hoffman LC, Brand TS (2007) Prediction of The Chemical Composition of Mutton with Near Infrared Reflectance Spectroscopy. Small Ruminant Research. j. 69: 88-94.

[15]  Barlocco N, Vadell A, Ballesteros F, Galietta G, Cozzolino D (2006) Predicting Intramuscular Fat, Moisture and Warner-Bratzler Shear Force in Pork Muscle using Near Infrared Reflectance Spectroscopy. Animal Science. j. 82: 111-116.

[16]  Venel C, Mullen AM, Downey G, Troy DJ (2001) Prediction of Tenderness and Other Quality Attributes of Beef by Near Infrared Reflectance Spectroscopy between 750 and 1100 nm, Further Studies. Journal of Near Infrared Spectroscopy. j. 9: 185-198.

[17]  Geesink GH, Schreutelkamp FH, Frankhuizen R, Vedder HW, Faber NM, Kranen RW (2003) Prediction of Pork Quality Attributes from Near Infrared Reflectance Spectra. Meat Science. j. 65: 661-668.

[18]  Liao Y, Fan Y, Wu X (2010) Online Determination of pH in Fresh Pork by Visible/ Near-Infrared Spectroscopy. Spectroscopy and Spectral Analysis. j. 30(3): 681-684.

[19]  Zhang L, Peng Y, Dhakal S, Song Y, Zhao J, Zhao S (2013) Rapid Nondestructive Assessment of Pork Edibility by using VIS/NIR Spectroscopic Technique. SPIE/Defense, Security and Sensing 2013, Paper No. 8721-06, Proceedings of SPIE Vol. 8721, April 29-May 3, 2013, Baltimore, Maryland, USA

[20]  Zhang H, Peng Y, Wang W, Zhao S, Dhakal S (2012) Non-destructive Detection of Water Content in Fresh Pork Based on Visual/Near-Infrared Spectrum. ASABE An-

nual International Meeting, July 29-August 1, 2012, Paper No. 121341179, Dallas, Texas, USA

[21] Williams PC, Sobering DC (1993) Comparison of Commercial Near Infrared Transmittance and Reflectance Instruments for Analysis of Whole Grains and Seeds. Journal of Near Infrared Spectroscopy. j. 1: 25-32.

[22] Ma S, Tang X, Xu Y, Peng Y, Tian X, Fu X (2012) Nondestructive Determination of pH Value in Beef using Visible/near-infrared Spectroscopy and Genetic Algorithm. Transactions of the Chinese Society of Agriculture Engineering. j. 28(18): 263-268.

[23] Tian, X., Xu, Y., Peng, Y., Ma, S., Tang, M., Niu, L. (2012). Research on support vector machine evaluation of beef tenderness. *Journal of Food Safety and Quality.* 3(6): 613-616.

[24] Wu J, Peng Y, Li Y, Wang W, Chen J, Dhakal S (2012) Prediction of Beef Quality Attributes using VIS/NIR Hyperspectral Scattering Imaging Technique. Journal of Food Engineering. j. 109: 267-273.

[25] Tao F, Peng Y (2014) A Method for Nondestructive Prediction of Pork Quality and Safety Attributes by Hyperspectral Imaging Technique. Journal of Food Engineering. j. 126: 98-106.

[26] James B, Yang S (2011) Testing Meat Tenderness using an in Situ Straining Stage with Variable Pressure Scanning Electron Microscopy. Procedia Food Science. j. 1: 258-266.

[27] Park B, Chen YR, Hruschka WR, Shackelford SD, Koohmaraie M (1998) Near-infrared Reflectance Analysis for Predicting Beef Longissimus Tenderness. Journal of Animal Science. j. 76:2115-2120.

[28] Peng Y, Wu J, Chen J (2009) Prediction of Beef Quality Attributes using Hyperspectral Scattering Imaging Technique. ASABE Annual International Meeting. June 21-24, 2012, Paper No. 096424, Reno, Nevada, USA.

[29] Peng Y, Gao X, Chen J, Huang H (2009) Prediction of Beef Tenderness using VIS/NIR Hyperspectral Scattering Characteristics. Journal of Food Safety and Quality. 1(1): 10: 20-26.

[30] Abeni F, Bergoglio G (2001) Characterization of Different Strains of Broiler Chicken by Carcass Measurements, Chemical and Physical Parameters and NIRS on Breast Muscle. Meat Science. j. 57: 133-137.

[31] Thyholt K, Isaksson T (1997) Differentiation of Frozen and Unfrozen Beef using Near-infrared Spectroscopy. Journal of the Science of Food and Agriculture. j. 73: 525-532.

[32] Peng Y, Zhao S, Wang W, Zhang H (2012) Real-time Evaluation System of Pork Freshness based on Multi-channel Near-infrared Spectroscopy. ASABE Annual International Meeting, July 29-August 1, 2012, Paper No. 121341181, Dallas, Texas, USA.

[33] Cozzolino D, DeMattos D, Martins DV (2002) Visible/near Infrared Reflectance Spectroscopy for Predicting Composition and Tracing System of Production of Beef Muscle. Animal Science. j. 74: 477-484.

[34] Peng Y, Tao F, Wang W, Li Y, Chen J, Wu J, Zhang L (2010) Hyperspectral Scattering Technique for Assessment of Multi Quality Attributes of Pork. Proceedings of International Agricultural Engineering Conference 2010, 3, 9-19, Sep. 17-20, 2010, Shanghai, China

[35] Tao F, Peng Y, Li Y, Chao K, Dhakal S (2012) Simultaneous Determination of Tenderness and Escherichia coli Contamination of Pork using Hyperspectral Scattering Technique. Meat Science. j. 90: 851-857.

[36] Peng Y, Wang W (2008) Prediction of Pork Meat Total Viable Bacteria Count Using Hyperspectral Imaging System and Support Vector Machines. ASABE, 2008 Food Processing Automation Conference, Paper No. 085438, June 28-June 29, 2008, Providence, Rhode Island, USA

[37] Peng Y, Zhang J, Wu J, Hang H (2009) Hyperspectral Scattering Profiles for Prediction of the Microbial Spoilage of Beef. SPIE/Defense, Security and Sensing, Paper No. 7315-25, Proceedings of SPIE Vol. 7315, April 13-17, 2009, Orlando, Florida, USA

[38] Zhu Y, Dhakal S, Peng Y, Wang C (2013) Progress and trend of pork meat detection technology: A review. International Agricultural Engineering Journal. j. 22(4): 72-80.

*Edited by Theophanides Theophile*

This informative and state-of-the-art book on Infrared Spectroscopy is addressed to Researchers in Medicine as well as to Pharmaceutical Industry and Agriculture. It features 7 specialized chapters of MIRS and NIRS covering applications in proteins and biopolymers; food quality research and food safety applications; and medical applications, such as Down syndrome disorders of tooth, probing of brain oxygen, the role of $CO_2$ in blood pressure and diagnosis of metastatic cancer. This book highlights the span of modern Infrared applications.

Photo by Arsgera / iStock

IntechOpen

ISBN 978-953-51-5052-7

9 789535 150527